Heat and Mass Transfer

Daniel Livescu
Arash G. Nouri
Francine Battaglia
Peyman Givi *Editors*

Modeling and Simulation of Turbulent Mixing and Reaction

For Power, Energy and Flight

Springer

Heat and Mass Transfer

This book series publishes monographs and professional books in all fields of heat and mass transfer, presenting the interrelationships between scientific foundations, experimental techniques, model-based analysis of results and their transfer to technological applications. The authors are all leading experts in their fields.

Heat and Mass Transfer addresses professionals and researchers, students and teachers alike. It aims to provide both basic knowledge and practical solutions, while also fostering discussion and drawing attention to the synergies that are essential to start new research projects.

More information about this series at http://www.springer.com/series/4247

Daniel Livescu · Arash G. Nouri ·
Francine Battaglia · Peyman Givi
Editors

Modeling and Simulation of Turbulent Mixing and Reaction

For Power, Energy and Flight

Springer

Editors
Daniel Livescu
CCS-2, Computational Physics and Methods
Los Alamos National Laboratory
Los Alamos, NM, USA

Arash G. Nouri
School of Engineering
University of Pittsburgh
Pittsburgh, USA

Francine Battaglia
Mechanical and Aerospace Engineering
University at Buffalo, The State University of New York
Buffalo, NY, USA

Peyman Givi
School of Engineering
University of Pittsburgh
Pittsburgh, PA, USA

ISSN 1860-4846 ISSN 1860-4854 (electronic)
Heat and Mass Transfer
ISBN 978-981-15-2642-8 ISBN 978-981-15-2643-5 (eBook)
https://doi.org/10.1007/978-981-15-2643-5

This Springer imprint is published by the registered company Springer Nature Singapore Pte Ltd.
The registered company address is: 152 Beach Road, #21-01/04 Gateway East, Singapore 189721, Singapore

Preface

Computational modeling and simulation are rapidly growing in importance throughout the sciences and engineering. We are now in a new era where computational scientists and engineers are teaming to tackle grand challenge problems. Turbulent mixing and reactions are critical phenomena that remain as some of the most significant challenges in computational modeling, especially as industrial technologies continue to advance. Modern developments in computational platforms, numerical discretization techniques, chemical kinetics modeling, and turbulence closures have improved predictive capabilities and have contributed to our understanding of the complex physics of reactive turbulence. In turn, the advantages afforded by computational fluid dynamics have had a direct influence in many industries. With improved computational technologies, we are able to predict and parameterize complex reactive flows that are difficult and expensive to experimentally measure and study.

This book is inspired by bringing together several leading researchers in computational turbulence and combustion. The objective is to present some of the most recent results and achievements in important aspects related to these fields. The book features large-scale numerical simulations of canonical mixing layers with density variations and reacting flows; theoretical analyses of stratified downslope flows; and state-of-the-art modeling and computation of reactive flows, including combustion initiation, multiphase flows, and sprays. Included are some suggestions and guidelines to help chart future directions. The resulting volume is dedicated to Prof. Cyrus Koorosh (C.K.) Madnia, for the occasion of his 60th birthday. Professor Madnia is widely regarded as one of the present-day leading experts in several of the research fields covered in this book, including direct numerical simulation and large eddy simulation of turbulent mixing and reaction, turbulence–chemistry interactions, compressible turbulence, flame–vortex interactions, flow topology, and

turbulence structures. The legacy of Prof. Madnia will remain forever through his Ph.D. students (and their subsequent students and so on) who are, and will be, making advancements in these fields. The works of some of these students are featured in this book.

Los Alamos, USA — Daniel Livescu
Pittsburgh, USA — Arash G. Nouri
Buffalo, USA — Francine Battaglia
Pittsburgh, USA — Peyman Givi
November 2019

Acknowledgements

We are indebted to Prof. Cyrus Madnia for his leadership, friendship, mentorship, and collegiality. Several of the authors are also indebted to him for his review, comments and suggestions. This book project is part of an effort sponsored by the US National Science Foundation under Grant CBET-1603131 and Grant CBET-1609120; and by the Los Alamos National Laboratory which is operated by Triad National Security, LLC, for the National Nuclear Security Administration of the US Department of Energy (Contract no. 92689233218CNA000001).

Contents

Contributors

Amir Akbarzadeh J. Mike Walker ’66 Department of Mechanical Engineering, Texas A&M University, College Station, TX, USA

Nasser Ashgriz Department of Mechanical and Industrial Engineering, University of Toronto, Toronto, Canada

Jon R. Baltzer Los Alamos National Laboratory, Los Alamos, NM, USA

Iman Borazjani J. Mike Walker ’66 Department of Mechanical Engineering, Texas A&M University, College Station, TX, USA

Siyu Chen Department of Mechanical and Industrial Engineering, University of Toronto, Toronto, Canada

Tomasz G. Drozda NASA Langley Research Center, Hampton, VA, USA

J. Philip Drummond NASA Langley Research Center, Hampton, VA, USA

Sean C. Garrick Department of Mechanical Engineering, University of Minnesota, Minneapolis, MN, USA

Peyman Givi Department of Mechanical Engineering and Materials Science, University of Pittsburgh, Pittsburgh, PA, USA

Farhad Jaberi Department of Mechanical Engineering, Michigan State University, East Lansing, MI, USA

Reza Jahanbakhshi Department of Mechanical Engineering, Johns Hopkins University, Baltimore, MD, USA

Jonathan Komperda Department of Mechanical and Industrial Engineering, University of Illinois at Chicago, Chicago, IL, USA

Daniel Livescu Los Alamos National Laboratory, Los Alamos, NM, USA

Cyrus K. Madnia Department of Mechanical and Aerospace Engineering, State University of New York at Buffalo, Buffalo, NY, USA

Farzad Mashayek Department of Mechanical and Industrial Engineering, University of Illinois at Chicago, Chicago, IL, USA

Viktor Nikulin Lavrentyev Institute of Hydrodynamics SB RAS, Novosibirsk, Russia

Jesse R. Quinlan NASA Langley Research Center, Hampton, VA, USA

Zhuyin Ren Center for Combustion Energy/School of Aerospace Engineering, Tsinghua University, Beijing, China

Shervin Sammak Center for Research Computing, University of Pittsburgh, Pittsburgh, PA, USA

Serguei Savtchenko Department of Mechanical and Industrial Engineering, University of Toronto, Toronto, Canada

Harold Schock Department of Mechanical Engineering, Michigan State University, East Lansing, MI, USA

Inanc Senocak Department of Mechanical Engineering and Materials Science, University of Pittsburgh, Pittsburgh, PA, USA

Yifeng Tian Department of Mechanical Engineering, Michigan State University, East Lansing, MI, USA

Ahad Validi Department of Mechanical Engineering, Michigan State University, East Lansing, MI, USA

Everett A. Wenzel Department of Mechanical Engineering, University of Minnesota, Minneapolis, MN, USA

Cheng-Nian Xiao Department of Mechanical Engineering and Materials Science, University of Pittsburgh, Pittsburgh, PA, USA

Low-Speed Turbulent Shear-Driven Mixing Layers with Large Thermal and Compositional Density Variations

Jon R. Baltzer and Daniel Livescu

Abstract Low speed shear-driven mixing layers involving fluid streams of different densities due to temperature or compositional variations are described by remarkably similar equations with some differences in the formulations of the molecular transport terms. These differences are related to specifics of the heat conduction and mass diffusion operators, as well as viscosity dependence on mixture molar mass and temperature in the low Mach number limit. Direct numerical simulations are performed in incompressible/low-speed limits to study the differences and similarities in mixing behavior associated with these configurations. The results demonstrate both subtle and significant changes in the mixing behavior for variable composition versus variable temperature mixing. Higher-order statistics related to density field reveal greater differences than are apparent from mean profiles; these differences can be extremely important when the physics is sensitive to mixing, such as in combustion problems. Therefore, conclusions regarding the mixing dynamics drawn from variable temperature mixing are not necessarily applicable to multi-species mixing.

Keywords Shear layers · Low speed · Variable density · Turbulence · Mixing

1 Introduction

Variable-density shear-driven mixing layers appear in a number of applications, including combustion. In combustion, the mixing of both different species (e.g. fuel and oxidizer) and temperature variations can influence the spatial variations in density. Shear-driven mixing involving only a single fluid with negligible thermal variations has historically received a great deal of attention both experimentally (e.g., Refs. [1–3]) and in numerical simulations (e.g., Refs. [4–8]). The single-fluid configuration contains much of the physics governing the variable-density shear layer, but

J. R. Baltzer · D. Livescu (✉)
Los Alamos National Laboratory, MS D413, Los Alamos, NM 87545, USA
e-mail: livescu@lanl.gov

J. R. Baltzer
e-mail: jbaltzer@lanl.gov

D. Livescu et al. (eds.), *Modeling and Simulation of Turbulent Mixing and Reaction*, Heat and Mass Transfer, https://doi.org/10.1007/978-981-15-2643-5_1

significant differences have long been observed experimentally for variable-density mixing layers [9]. Local density variations exist as well in high-speed compressible mixing layers, which have also been studied extensively, particularly related to the strong reduction in mixing layer growth rate that occurs with increasing Mach number. Though density effects associated with compressibility were once thought to affect growth rate [9], direct numerical simulation (DNS) results have clarified how compressibility effects reduce the growth due to decreased turbulent kinetic energy production, as compressibility directly affects the pressure fluctuations, which decorrelates them from the strain (Refs. [10–13]). Recent simulations have further investigated the mixing characteristics of compressible mixing layers (e.g., Ref. [14]). However, low-speed mixing layers in which the two free streams have significantly different densities also have important applications, but have nonetheless been only scarcely studied. The low-speed configuration is the focus of the present study.

The pioneering 3D temporal simulations of Ref. [12] included an investigation of different free-stream densities within a broader study of compressible mixing layers. The differing densities were established by varying the temperature for a single fluid. They found that increasing Atwood number decreased the temporal thickness growth rate, though the extent depended on how thickness was defined. During self-similar growth, the Reynolds shear stress changed little in magnitude but its profile shifted to the light fluid side with increasing Atwood number. They also developed a model characterizing the shift of the mean velocity profile to the light fluid side and the associated decrease in momentum thickness growth rate. Mild compressibility effects were likely present because the convective Mach number was $M_c = 0.7$. More recently, Almagro et al. [15] performed DNS using a low-speed approximation for the flow of Ref. [12]. Two streams of a single fluid with different temperatures again create the density difference, but compressibility effects are considered negligible at low speeds. They also developed a semi-empirical model for the reduction in momentum thickness growth rate with density ratio.

Details of mixing layers with variable density due to differing fluid compositions are much less understood. Detailed studies of mixing layers involving two different miscible fluids have been rare, particularly when not complicated by other effects such as buoyancy or compressibility, despite earlier attention. The historic low-speed experiments of Ref. [9] using two gases with different densities found reductions in the growth rates as large as 50% for density ratios up to 7. These measurements were limited to mean density and streamwise velocity profiles and no details of the changes to turbulence and mixing properties are available. Our present investigation focuses on this flow but in a temporal configuration. Preliminary direct numerical simulations of mixing layers with miscible binary mixing at $A = 0.75$ are included in Ref. [16]; similar simulations using the same code and configuration are the basis for the present study.

The spatially-developing configuration, which is amenable to experimental studies, leads to thickening of the layer with downstream distance, while the temporal configuration, which is more convenient to address in numerical simulations, leads to a thickening of the layer in time at all streamwise locations. Though the symmetry associated with the periodic boundary conditions in the temporal configuration

changes the wave solutions relative to the spatially-developing set-up, there are also many similarities between the two flows, for example as related to the shear turbulence production.

2D simulations of early-time spatially-developing mixing layers show strong differences in entrainment depending on whether the low or high speed stream has lower or higher density [17]. Ashurts and Kerstein [18] studied variable density effects in temporal and spatial mixing layers using the one-dimensional turbulence stochastic simulation method; they captured many of the effects observed in Ref. [12].

Other studies have addressed variable-density shear-driven mixing layers with buoyancy or other complicating physics playing a significant role. Olson et al. [19] simulated mixing layers with mixed Rayleigh-Taylor (buoyant) and Kelvin-Helmholtz (shear) instability and Atwood numbers ranging up to 0.71 using the same governing as for our present study. Reference [20] simulated the mixing of vertical columns of fluid with different densities and perturbed interfaces. Gravity accelerates the perturbed heavy and light fluid columns in opposite directions within the triply-periodic domain to induce Kelvin-Helmholtz instability.

To understand the fundamental physics associated with density variations in a sheared flow, relevant mixing layers have been simulated with the same set-ups but using two different free-stream species with negligible thermodynamic variations [16] and using a single species with different temperatures of the two free streams [12, 15]. The present study briefly contrasts the governing equations, assumptions that lead to these equations, and mixing behavior based on DNS for these sets of governing equations. Effects of variations of species concentrations and temperature are also relevant to mixing layers appearing in combustion problems (e.g., Ref. [21]).

2 Governing Equations

The multicomponent compressible Navier-Stokes equations are applicable to all of the mixing layers considered here. Let partial derivatives be denoted by a subscript and the variable by which the partial derivative is taken follow a comma, with t representing the time variable and the index i representing the relevant spatial direction x_i. For a mixture of ideal gases in the low-Mach number limit, these equations become [22, 23]:

$$\rho_{,t} + \left(\rho u_j\right)_{,j} = 0, \tag{1}$$

$$\left(\rho u_i\right)_{,t} + \left(\rho u_i u_j\right)_{,j} = -\pi_{,i} + \tau_{ij,j}, \tag{2}$$

$$\left(\rho Y_\alpha\right)_{,t} + \left(\rho u_j Y_\alpha\right)_{,j} = -\left(\rho Y_\alpha V_{\alpha j}\right)_{,j} + \dot{\omega}_\alpha, \tag{3}$$

$$\rho h_{,t} + \rho u_j h_{,j} = p_{0,t} - \left(\lambda T_{,j}\right)_{,j} + \sum_\alpha \left(\rho Y_\alpha V_{\alpha j} h_\alpha\right)_{,j} + \Phi + \dot{Q}, \tag{4}$$

$$u_{j,j} = -\frac{1}{\gamma p_0} p_{0,t} + \frac{R}{c_p p_0}\left[-\sum_\alpha \left(\rho Y_\alpha V_{\alpha j}\right) h_{\alpha,j} + \left(\lambda T_{,j}\right)_{,j} + \Phi + \dot{Q}\right] - \frac{1}{\rho R}\sum_\alpha \left(\rho Y_\alpha V_{\alpha j} R_\alpha\right)_{,j} + \frac{1}{\rho}\left[\frac{\rho R}{c_p p_0}\dot{Q} + \sum_\alpha \left(\frac{R_\alpha}{R} - \frac{h_\alpha}{c_p T}\right)\dot{\omega}_\alpha\right], \tag{5}$$

where the viscous stress, assumed to be Newtonian, is

$$\tau_{ij} = \mu\left[u_{i,j} + u_{j,i} - \frac{2}{3}u_{k,k}\delta_{ij}\right]. \tag{6}$$

Equations (1) and (2) are the mass conservation and momentum equations governing the fields of density ρ, velocity components u_i, and dynamic pressure π. For the low-Mach number (M) approximation, the pressure p can be expanded in M and truncated to $p \approx p_0 + \pi$, where p_0 is thermodynamic pressure and π is the dynamic component [24]. Equation (3) governs the diffusion of species α, with Y_α representing each species' mass fraction. The diffusional velocity components are $V_{\alpha j}$. This system also includes the energy transport equation rewritten as a transport equation (Eq. 4) for enthalpy $h = e + p/\rho$, which is convenient for addressing a special case below [25]. Its transport is governed by the thermodynamic pressure change, thermal conduction, diffusion of species, and viscous dissipation Φ. The zeroth order pressure term p_0 can be shown to be spatially uniform but, in general, can vary with time [26]. Heat conduction is specified by Fourier's law with conduction coefficient λ. The diffusion velocities are given by the Maxwell relations [27]. For the binary case, they reduce to the Fickian form. Note that the Fickian and Fourier expressions of the mass diffusion and heat conduction terms are the low-Mach number limits of the full multicomponent operators. The low-Mach number limit leads to no further simplifications to the compressible form of the viscous stress tensor, as the divergence of velocity remains non-zero. A number of mechanisms can contribute to the divergence of velocity in Eq. (5). In general, non-zero divergence of velocity can be generated in the presence of background pressure changes, heat conduction, viscous dissipation, heat release, reactions between species with different molar masses, and mass diffusion. $\dot{Q}$ represents the rate of energy release from a heat source (such as from a chemical/nuclear reaction or radiation) and $\dot{\omega}_\alpha$ represents the rate of production associated with a scalar source for species α. The gas constant R for the ideal gas mixture is $R = \sum_\alpha R_\alpha Y_\alpha$.

For a mixture of ideal gases, the equations of state in the variable-density low-Mach number approximation is $p_0 = \rho R T$ and $h = \sum_\alpha Y_\alpha h_\alpha(T)$. Then the ideal gas relation simplifies to

$$\frac{1}{\rho} = \frac{T}{p_0}\sum_\alpha Y_\alpha R_\alpha, \tag{7}$$

where R_α and p_0 are constant. p_0 is approximated as spatially constant in many applications [26, 28], including mixing layers, and can also be shown to be temporally constant under certain circumstances described below.

Two special nonreacting cases that can sustain large density variations are here examined: (1) single species with variable temperature in the low-speed approximation and (2) two species with different molar masses in the incompressible limit.

2.1 Single-Fluid Case with Temperature Variations

The first case is based on the LMNOB (i.e. low-Mach number non-Oberbeck-Boussinesq) equations, which are recovered from the general low-Mach number equation set in Eqs. (1) and (5) by assuming a single species system. The LMNOB equations have been applied to a number of simulations including vertical convection in air [26, 29]. Similar sets of equations have also been applied to reacting flows [28, 30]. Though the evolution of p_0 is a consideration in more complex flows (e.g., Ref. [26]), in variable-density turbulent mixing layers it can be argued that p_0 remains constant in time because it is an open system [15].

If the viscous dissipation is neglected in Eq. (5), the velocity field divergence implied by the LMNOB equations with constant background pressure is

$$\nabla \cdot \mathbf{u} = \frac{1}{c_p} \nabla \cdot \left[\lambda \nabla \left(\frac{1}{\rho} \right) \right]. \tag{8}$$

The corresponding energy transport equation can be simplified from Eq. (4) for the single-fluid case as

$$(\rho T)_{,t} + (\rho u_i T)_{,i} = \tfrac{1}{c_p} \left(\lambda T_{,i} \right)_{,i}, \tag{9}$$

after neglecting the viscous dissipation. This equation is redundant with the divergence relation of Eq. (10) when p_0 is constant. This further simplified set of equations is denoted herein as the low-Mach number thermal density variation (LMTV) equations.

Studies addressing the case of a single fluid with temperature variations often simplify the LMNOB (or in some instances their simplified LMTV version) equations by assuming constant values for material transport properties such as c_p, thermal conduction coefficient λ, and viscosity μ. The simulations herein are restricted to the simplified case of the LMTV equations in which c_p and λ are constant. For constant material properties, the velocity field divergence simplifies to

$$\nabla \cdot \mathbf{u} = \frac{\lambda}{c_p} \nabla^2 \left(\frac{1}{\rho} \right). \tag{10}$$

The complete set of equations that must be solved in this case are comprised of mass conservation Eq. (1), momentum balance Eq. (2), and velocity divergence condition Eq. (10). As the former two equations are evolved in a numerical simulation, the divergence can be enforced using a fractional step method that solves a Poisson equation for the pressure terms involving π. This is the approach used for the simulations shown below. Alternatively, rather than solving for the flow in primitive variables, the approach of Ref. [15] satisfies this system of equations but solves for the momentum vector Helmholtz-decomposed into divergence-free and curl-free components. This approach solves for the π pressure term through a Poisson equation.

Current applications of LMNOB equations (in their simplified LMTV form) to mixing layers assume temperature-independent thermal conductivity and viscosity, such as in the variable-density mixing layer simulations of Refs. [12, 15]. While the emphasis in such studies was simply to attain the desired density differences, it also should be considered how these assumptions relate to real fluid behavior. If both streams of the same ideal gas are at the same pressure, the density ratio between them is inversely proportional to the streams' temperature ratio. Thus, $A = 0.75$ requires a temperature ratio of 7 to attain the density ratio of 7. Gases can experience significant changes in thermal conductivities and specific heats as well as viscosities over these ranges of temperatures. For instance, for streams of air at 273.15 and 1912.05 K and atmospheric pressure producing a density ratio of 7, the hotter stream has 24% greater c_p, 354% greater λ and 251% greater μ than the colder stream. In the variable-density mixing layers that are the present focus, the non-Oberbeck-Boussinseq (NOB) effect of interest is related to the inertial effects of density variations. In many other applications, the most prominent NOB effects are related to transport property changes that are dependent on temperature. Many examples are related to Rayleigh-Bénard and other convection problems, such as vertical convection. Those NOB effects first arise when the Oberbeck-Boussinseq (OB) approximation of temperature-independent material parameters (kinematic viscosity, thermal diffusivity, heat conductivity, isobaric specific heat capacity c_p, and isobaric thermal expansion coefficient β) is violated (e.g., Ref. [31]). Additional considerations in LMNOB flows exist due to the change of density with temperature and pressure: in a closed volume, these effects can be balanced to conserve mass [26], but in mixing layers, and particularly with reactions releasing energy, the boundary conditions can be specified to allow expanding fluid to flow outward [32]. The low-speed variable-density mixing layer simulations of Ref. [15] incorporated boundary conditions based on this work.

2.2 *Two-Species Variable-Density Incompressible Case*

For multi-species mixtures, the incompressible limit is now considered. The incompressible limit is obtained by taking the infinite speed of sound c limit [33]. For a mixture of ideal gases, this limit requires that $T \to \infty$ because $c^2 = \gamma RT$. Furthermore, in this limit, $p_0 \to \infty$ simultaneously to maintain a finite ρ, according

to the ideal gas law equation of state Eq. (7) [25]. This limit eliminates density effects caused by thermal variations.

For non-reacting materials, the resulting expression for the velocity divergence is $\nabla \cdot \mathbf{u} = -\frac{1}{\rho R} \sum_\alpha \left(\rho Y_\alpha V_{\alpha j} R_\alpha\right)_{,j}$. Maxwell's relations [27] are needed to solve for the diffusion velocities. For binary mixing [25, 33],

$$\nabla \cdot \mathbf{u} = -\nabla \cdot \left(\mathcal{D} \frac{\nabla \rho}{\rho}\right). \tag{11}$$

For binary mixing without any sources of species (i.e., reactions), Eq. (3) simplifies to

$$(\rho Y_\alpha)_{,t} + (\rho Y_\alpha u_i)_{,i} = \mathcal{D} \left(\rho Y_{\alpha,i}\right)_{,i}. \tag{12}$$

Defining the microdensities of the fluids as $\rho_\alpha = \frac{W_\alpha}{\mathcal{R}} \frac{p_0}{T}$, with W_α being the species molar mass and $\mathcal{R}$ the universal gas constant, the density of mixed fluid is related to species mass fractions as $\frac{1}{\rho} = \sum_\alpha \frac{Y_\alpha}{\rho_\alpha}$. For the incompressible limit considered above, it can be shown that $p_0/T = \rho R$ is constant in space and time, so the microdensities ρ_α are likewise constant [25]. For the binary mixing under consideration, the final relation between density and species mass fractions is

$$\frac{1}{\rho} = \frac{Y_1}{\rho_1} + \frac{Y_2}{\rho_2}, \tag{13}$$

where $Y_1 + Y_2 = 1$. More generally (i.e. for non-ideal gas equation of state), this mixing rule is valid when the microdensities ρ_1 and ρ_2 of the two fluids remain constant during mixing, such that the volume occupied by the mixture is equal to the volume occupied by the unmixed constituents at their respective microdensities. This condition is also satisfied by mixing liquids. Previously, the mixture relation of Eq. (13) was derived for two-liquid mixtures by Ref. [34] and used in the pioneering Rayleigh-Taylor simulation of Ref. [35].

For binary mixing, assuming that Eq. (13) holds, simply substituting Eq. (13) into Eq. (12) and combining with Eq. (1) also yields the divergence in Eq. (11). This derivation was given for two-fluid mixtures satisfying Eq. (13) by Ref. [36], while this same divergence was previously obtained by Ref. [34] for a two-liquid system. In contrast, the derivation described above began with the divergence given in Eq. (5) based on thermodynamic properties of the fluid and simplified to Eq. (11). The latter derivation based on the mass conservation produces the same divergence relation, which is a condition required for consistency [25, 33]. Thus, the species mass conservation equation is redundant with the divergence equation.

For the case of two-species variable-density incompressible mixing, mass conservation Eq. (1), momentum balance Eq. (2), and divergence relation Eq. (11) comprise a complete set of equations to describe the flow evolution. This may be referred to as the INBM (incompressible non-Boussinesq mixing) equations. In this application, the term "non-Boussinesq" is indicative of including the inertial effects associated

with large density fluctuations that would not be captured in the Boussinesq limit of two-species incompressible mixing. In this limit, the velocity divergence reduces to 0 and causes density to behave as a passive scalar in the absence of buoyancy [25].

Applications to Rayleigh-Taylor and related simulations (e.g., Refs. [19, 37, 38]) often assume that ν and $\mathcal{D}$ are constant. Under these assumptions, the velocity field divergence simplifies to

$$\nabla \cdot \mathbf{u} = -\mathcal{D}\nabla^2 (\ln \rho) . \tag{14}$$

Computationally, the INBM equations can be solved using a variant of the fractional step method that advances Eqs. (2) and (1) while requiring the velocity field to satisfy the divergence Eq. (14) [37, 39]. This is the same procedure as the first method described for the LMTV equations, except with the different divergence that now implicitly causes Eqs. (12) and (13) to be satisfied. This technique has been applied to a number of Rayleigh-Taylor turbulence two-species mixing simulations (e.g., Ref. [37]) and has been further discussed in related references. It should be noted that in the present simulations, the governing equations are solved without the buoyant terms, whereas these terms play important roles in many of the traditional applications (e.g. Rayleigh-Taylor instability).

2.3 Discussion

Despite the differing diffusion operators, there are notable similarities in the forms of the equations for the INBM and LMTV cases. One of the species mass fractions in the former case plays an analogous role to temperature in the latter case. The transport equations for these quantities, Eqs. (12) and (9), have similar forms. It should be noted again that different simplifications lead to these equations. For instance, the LMTV equations can include a term representing the conversion of kinetic energy to thermal energy through viscous dissipation, a mechanism that has no analogy in INBM nonreacting species mixing. However, this effect is typically small and virtually always neglected in practice. The most pronounced difference between these equations pertains to their diffusion terms: the outer gradient includes a density product for Eq. (12), whereas density does not appear in the diffusion of Eq. (9). In both cases, there is an inversely proportional relationship between density and mass fraction/temperature (aside from an additive constant). The final velocity divergence forms are similar, but the divergence is proportional to the Laplacian of $-\ln \rho$ versus the Laplacian of $1/\rho$. As it was shown that substituting the density-mass fraction relation into the species mass transport equation and combining with the overall mass conservation equation can be used to obtain the INBM divergence, likewise substituting the equation of state into the energy transport equation and combining with the overall mass conservation equation leads to the LMTV divergence.

Besides this difference in the governing equations, assumptions about the fluid properties play important roles in the flow development. Assumptions related to the conduction and diffusion coefficients, λ and $\mathcal{D}$, as applicable to each case, have been

discussed above, but the appropriate prescription for fluid viscosity ν can also depend on the flow case. In the incompressible INBM variable density shear mixing layer simulations described in Ref. [16], the kinematic viscosity ν and diffusivity $\mathcal{D}$ are assumed constant, such that the Schmidt number $Sc = \nu/\mathcal{D}$ remains uniform with a value of 1. This same assumption was used in the Rayleigh-Taylor simulations discussed above. The choice of constant ν implies that dynamic viscosity $\mu \sim \rho$, whereas with real fluids there is typically a weaker dependence on density such as $\mu \sim \sqrt{\rho}$ [40]. For the INBM case, Chapman-Enskog theory predicts that if the two gases remain at constant temperature and pressure, $\mathcal{D}$ would remain constant independent of the concentration [41].

In the LMTV simulations of Ref. [15] addressing mixing layers involving a single fluid at different temperatures, the dynamic viscosity μ is instead assumed to be constant. Thus, the heat transfer analog of Schmidt number, the Prandtl number $Pr = \nu/\alpha = c_p\mu/\lambda$, is uniform ($\alpha$ is the thermal diffusivity $\lambda/(\rho c_p)$).

Another study in Ref. [20] performed an incompressible simulation of two vertical streams with different species set in motion by buoyancy. Viscosity μ was assumed to be uniform and constant but a constant Schmidt number of 1 was also maintained. Kinematic viscosity $\nu = \mu/\rho$ therefore spatially varied with density, and $Sc = 1$ necessitated that diffusivity also behaved similarly as $\mathcal{D} = \mu/\rho$. Substituting the density-dependent diffusivity into Eq. (11) results in a velocity field divergence of

$$\nabla \cdot \mathbf{u} = \mu \nabla^2 \left(\frac{1}{\rho} \right), \tag{15}$$

where μ is constant. Thus, the form of the equation is the same as that in Eq. (10) for the LMTV case with constant λ. This example illustrates that both the governing equations and assumptions on the diffusion behavior play equally significant roles in determining the divergence of the velocity field.

The objectives of the simulations are to compare the cases outlined above and to assess the differences associated with the mixing of the scalar quantity that affects the density (interpreted as species mass fraction in INBM or temperature in LMTV) for several forms of transport properties. These are constant versus proportional to $1/\rho$ diffusion coefficients for the scalar (if both are interpreted in the species transport framework) and proportional to ρ versus constant dynamic viscosity.

3 Simulation Set-Up

Direct numerical simulations are performed of temporally-growing planar shear-driven mixing layers. Significant variable-density effects are introduced by adopting an Atwood number of $A = 0.75$, which corresponds to a density ratio of 7 between the free streams. The simulation methodology is that described in Ref. [16] for the $A = 0.75$ variable density mixing layer, including the same simulation code. However, only the INBM case with ν and $\mathcal{D}$ constant was performed in that work,

whereas several additional cases are here performed: LMTV with ν constant and λ/c_p constant, LMTV with μ constant and λ/c_p constant, and also INBM with μ and $\mathcal{D}$ constant. The INBM and LMTV governing equations are simulated by enforcing the applicable velocity field divergence through a fractional step method as the continuity and momentum equations are evolved. The constant μ simulations are prescribed by $\mu = \rho_0 \nu_0$ based on the average density of the two streams, ρ_0, and the same kinematic viscosity, ν_0, that is uniform and constant in the constant ν simulations. Likewise, the constant values of λ/c_p of the LMTV simulations are, when divided by ρ_0, equal to the constant value of $\mathcal{D}$ of the INBM simulations. Given the inverse/direct proportionality with density for some of the $\mathcal{D}$ and ν cases, the relatively large density ratio makes the effect of these transport properties significant.

For all of the present simulations, the domain size in the streamwise (x) and spanwise (z) directions is the same as in Ref. [16], while the cross-stream (y) dimension is thicker. The governing equations are supplemented by slip wall boundary conditions in the y direction and periodic boundary conditions in the x and z directions. The simulations use a resolution of $2048 \times 2048 \times 512$ grid points. Each simulation is initialized by a thin interface prescribed by aligned $\tan h$ profiles of mean streamwise velocity and density to maintain the required velocity difference ΔU and density difference $\Delta\rho$ between the two free streams. ΔU, $\Delta\rho$, and the average of the two free-stream densities, ρ_0, remain the same for each simulation. The initial velocity profile is perturbed to initiate the transition to turbulence (as described in Ref. [16]). Each simulation begins from the same initial conditions to minimize the statistical influence of the initial disturbance when comparing the differences produced by differing governing equations.

4 Results

The primary objective of the simulations is to determine how the flow evolution according to the different governing equations described above affects the most basic flow properties and mixing. This is evaluated after the flow has had time to develop and the mixing layer is growing in an approximately self-similar manner. Based on a number of indications, such as growth rate and peak Reynolds stress time histories, the time around $t\Delta U/h_0 = 284$ displays the best adherence to self-similar growth behavior. h_0 is the initial thickness of the mixing layer streamwise velocity profile. The Reynolds numbers are approximately $Re_\lambda = \tilde{k}\sqrt{20/(3\nu\varepsilon)} = 73$ during this time period, where $\tilde{k}$ is turbulent kinetic energy and ε is its dissipation rate. The statistical profiles (e.g., mean streamwise velocity and mean density) remain constant when y is scaled by the time-growing thickness h. h is defined to be the distance in y between the points at which the mean streamwise velocity $\tilde{U}_1$ is at 10% and 90% of the free-stream velocity difference ΔU. Momentum thickness $\delta_m = \int (\bar{\rho}/\rho_0)(1/4 - \tilde{U}^2/\Delta U^2)\, dy$ may alternatively be used to measure the mixing layer thickness; during self-similar growth, $h \approx 7.9\delta_m$ in the flows shown, but the relation varies with Atwood number and is not valid at early times. $\overline{f}$ denotes ensemble averaging of quantity f; in the

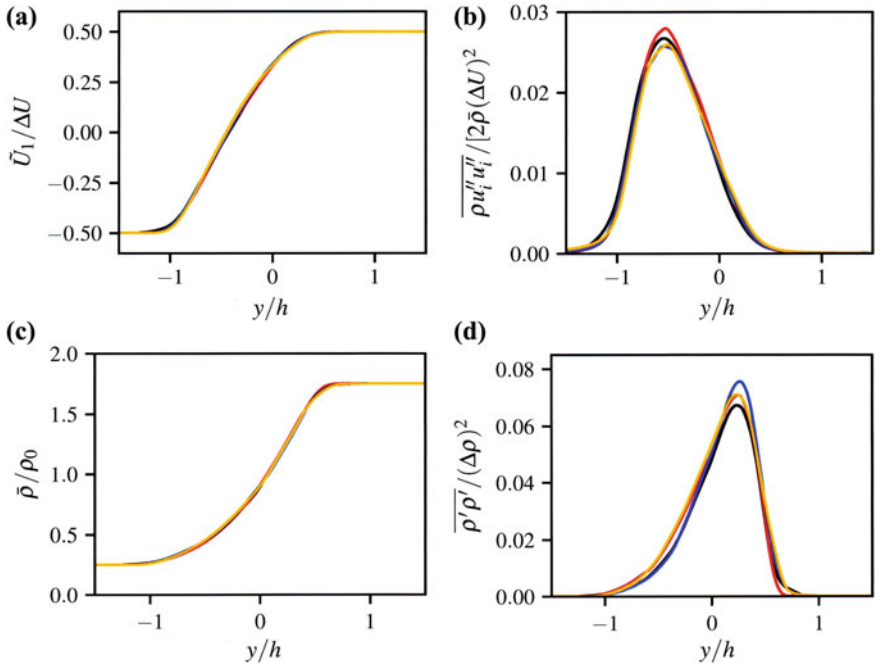

Fig. 1 Comparison of self-similar growth **a** mean streamwise velocity, **b** turbulent kinetic energy, **c** mean density, and **d** density variance profiles for (——) $\mathcal{D} = \text{const.}$ (INBM) and $\mu \propto \rho$, (——) $\mathcal{D} = \text{const.}$ and $\mu = \text{const.}$, (——) $\mathcal{D} \propto 1/\rho$ (constant-transport-property LMTV) and $\mu \propto \rho$, and (——) $\mathcal{D} \propto 1/\rho$ and $\mu = \text{const.}$

simulation data, it is approximated by area averaging over the homogeneous x and z coordinates. Self-similar averages are in addition averaged over the appropriate time period with y scaled by h. The mean streamwise velocity is Favre averaged as $\tilde{U}_1 = \overline{\rho u_1}/\bar{\rho}$. Fluctuations are defined relative to Reynolds averages as $f' = f - \bar{f}$ and relative to Favre averages as $f'' = f - \tilde{f}$. Statistical profiles are averaged between $t\Delta U/h_0 = 227$ and 341 to reduce statistical noise; profiles for mean density and streamwise velocity are shown in Fig. 1.

Overall, the most intense turbulence moves to the light-fluid (negative y) side, which causes the gradient in mean streamwise velocity to thicken more quickly to the light-fluid side. The turbulence intensity is quantified by turbulent kinetic energy. The associated position of strongest turbulent mixing also makes the mean density profile gradient shallower on the light fluid side and steeper on the heavy fluid side. The mean profiles for both density and streamwise velocity are nearly identical between INBM versus LMTV cases and constant ν versus μ cases. However, turbulent kinetic energy and density variance profiles weakly vary between cases, indicating some degree of mixing differences.

Table 1 y/h values for neutral points and peak values of density and velocity with $A = 0.75$

Equation Form	η_ρ ($\tilde{\rho} = \rho_0$)	η_2 ($\tilde{U}_2$ peak)	η_1 ($\tilde{U}_1 = 0$)	η_{12} ($\tilde{R}_{12}$ peak)
$\mathcal{D} =$ const. (INBM) and $\mu \propto \rho$	0.07	−0.36	−0.43	−0.55
$\mathcal{D} =$ const. and $\mu =$ const.	0.07	−0.27	−0.44	−0.54
$\mathcal{D} \propto 1/\rho$ (LMTV) and $\mu \propto \rho$	0.08	−0.31	−0.44	−0.54
$\mathcal{D} \propto 1/\rho$ and $\mu =$ const.	0.07	−0.37	−0.45	−0.53

For the same constant-$\mathcal{D}$ INBM and constant-λ and c_p LMTV cases shown in Fig. 1, the y/h values of the neutral points and peak values of various quantities are shown in Table 1. The points of interest include the neutral point of density (where the mean density is equal to the average of the free streams), the peak value of cross-stream velocity (the negative $\tilde{U}_1$ near the interface only is present in variable-density temporal mixing layers), the neutral point of streamwise velocity (where $\tilde{U}_1$ is equal to 0, the average of the free stream values), and the peak value of $\tilde{R}_{12}$. Reynolds stress $\tilde{R}_{12} = \overline{\rho u_1'' u_2''}/\bar{\rho}$ is an important quantity closely related to the growth of the mixing layer [10, 12]. The positions remain consistent among cases. The cross-stream mean velocity $\tilde{U}_2$ peak position varies the most, but statistical variation is likely more pronounced for this quantity as the $\tilde{U}_2$ component is relatively weak. In each case, $\eta_2 > \eta_1 . \eta_\rho$, the position of neutral density, changes the least from the initial interface $y = 0$ and moves slightly to the heavy fluid side. The streamwise velocity neutral points move significantly to the light fluid side and represent the drifts of each mixing layer, while the $\tilde{R}_{12}$ peaks associated with intense turbulence are consistently furthest to the light fluid side.

The density fluctuation mean squared statistics shown in Fig. 1 provide further information on the mixing. Besides the weak differences in peak magnitudes, the tails on the heavy fluid side decay more gradually for the constant ν cases. As it is shown below from density probability density functions (PDFs), stirring parcels of mostly-unmixed heavy fluid cause larger density fluctuations on the heavy fluid side, while more mixed fluid on the lighter-fluid side is associated with weaker fluctuation intensity.

For binary species mixing, analogies with reacting flows (e.g., combustion) suggest forming statistics based on the mass fraction of the heavy fluid. Based on Eq. (13) for the INBM case, this mass fraction is related to specific volume $v = 1/\rho$ as

$$Y_2 = \frac{-\rho_1 \rho_2}{\rho_2 - \rho_1} v + \frac{\rho_2}{\rho_2 - \rho_1}. \tag{16}$$

It follows that the means and variances can be written as $\bar{Y}_2 = -[\rho_1 \rho_2/(\rho_2 - \rho_1)]\bar{v} + \rho_2/(\rho_2 - \rho_1)$ and $\overline{Y_2'^2} = [\rho_1 \rho_2/(\rho_2 - \rho_1)]^2 \overline{v'^2}$. In the low Atwood number limit, the heavy fluid mass fraction plays a role approaching that of a passive scalar. For this reason, a scalar designated by ϕ will be used to represent Y_2, with the understanding

that this scalar affects variable-density flow dynamics. The analogy between INBM mass fraction and LMTV temperature suggests defining the scalar for the LMTV case as $\phi = (T - T_1)/(T_2 - T_1)$. Thus, ϕ also varies from 0 to 1 between the low density (high T) and high density (low T) fluid streams. Substituting T obtained from Eq. (7) into the above expression yields $\phi = (v - v_1)/(v_2 - v_1)$. Substituting $v_1 = 1/\rho_1$ and $v_2 = 1/\rho_2$ yields the same right-hand side as Eq. (16). Thus, this ϕ based on scaled temperature for the LMTV case obeys the same relation with specific volume as the incompressible INBM case.

These equivalencies suggest comparing statistics of the scalar between cases. The specific volume variance is normalized by dividing by $(v_1 - v_2)^2$, the difference in free-stream specific volumes squared; this is equivalent to the $[\rho_1\rho_2/(\rho_2 - \rho_1)]^2$ multiplicative factor above. The scalar statistics are shown in Fig. 2. Unlike the density variance, the scalar (and thus specific volume) variance peak is concentrated in the light fluid side and exhibits large differences among cases, which is indicative of variable density effects. The constant-μ simulation peak values are consistently greater than those of the constant-ν peaks, while the constant-$\mathcal{D}$ (INBM) peak is larger than

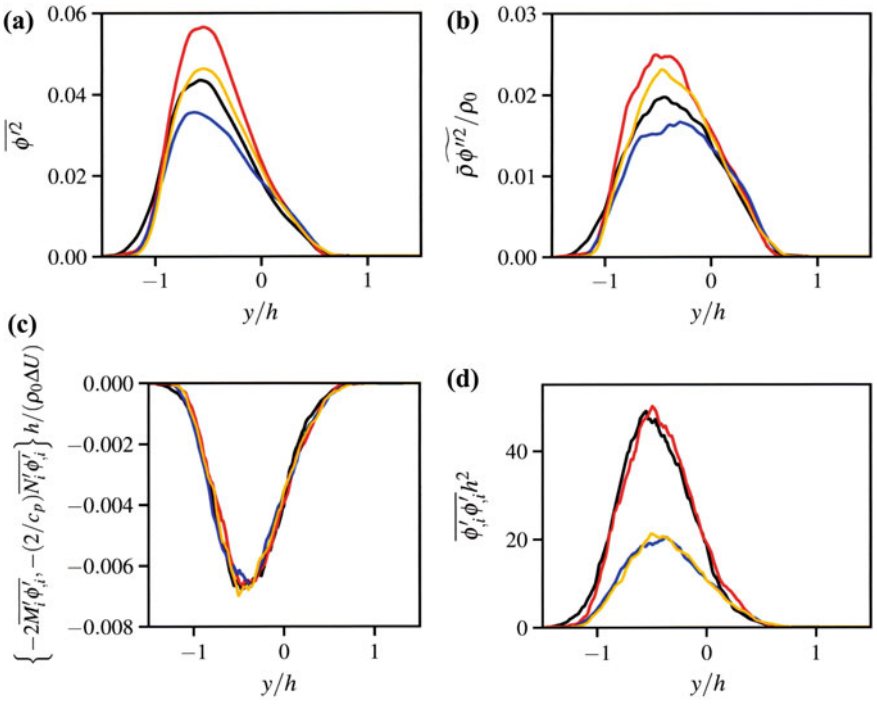

Fig. 2 Comparison of **a** self-similar growth scalar ϕ (or scaled specific volume) variance profiles, as well as $t\Delta U/h_0 = 284$, **b** density-multiplied Favre-averaged scalar variance, **c** scalar dissipation, and **d** scalar gradient intensity profiles. Colors are (——) $\mathcal{D} = \text{const.}$ (INBM) and $\mu \propto \rho$, (——) $\mathcal{D} = \text{const.}$ and $\mu = \text{const.}$, (——) $\mathcal{D} \propto 1/\rho$ (constant-transport-property LMTV) and $\mu \propto \rho$, and (——) $\mathcal{D} \propto 1/\rho$ and $\mu = \text{const.}$

the $\mathcal{D} \propto 1/\rho$ (LMTV) peak for a given viscosity prescription. The Favre scalar variance peak also moves to the light fluid side, however the cases with similar viscosity prescriptions yield closer magnitudes. Thus, the scalar variance is more sensitive to the viscosity variation than diffusion variation, though both of these effects influence the results, for the Reynolds number examined here. Given the linear relationship between specific volume and temperature, the variances for specific volume can also be compared with those for temperature reported in Ref. [15], which corresponds to the LMTV constant-μ case. The results are fully consistent with those shown here.

To clarify the factors that affect the scalar variance, its budget equation is frequently investigated. Starting from species conservation in Eq. (12), the budget equation for ϕ variance in the constant-$\mathcal{D}$ INBM cases can be expressed in the following form [42]

$$\begin{aligned}\left(\bar{\rho}\widetilde{\phi''^2}\right)_{,t} = &\underbrace{-\left(\bar{\rho}\tilde{U}_i\widetilde{\phi''^2}\right)_{,i}}_{\text{term I}} \underbrace{-2\bar{\rho}\widetilde{u_i''\phi''}\tilde{\phi}_{,i}}_{\text{term II}} \underbrace{-2\overline{M_i'\phi'_{,i}}}_{\text{term III}} \underbrace{-\left(\bar{\rho}\widetilde{u_i''\phi''^2}\right)_{,i}}_{\text{term IV}} \\ &+\underbrace{2\left(\overline{M_i'\phi'}\right)_{,i}}_{\text{term V}} + \underbrace{2\overline{\phi''}\bar{M}_{i,i}}_{\text{term VI}},\end{aligned} \tag{17}$$

where $M_i = \rho\mathcal{D}\phi_{,i}$. The terms contributing to the scalar variance evolution are (I) convection by mean velocity, (II) production, (III) dissipation, (IV) turbulent diffusion, (V) molecular diffusion, and (VI) compressibility. The scalar dissipation term is of particular interest because it represents the rate of mixing and also is directly related to reaction rate in simplified combustion problems with fast chemistry [43].

For LMTV cases, the scalar ϕ defined above as scaled temperature obeys a similar budget equation for its Favre variance. For constant c_p, this equation is:

$$\begin{aligned}\left(\bar{\rho}\widetilde{\phi''^2}\right)_{,t} = &\underbrace{-\left(\bar{\rho}\tilde{U}_i\widetilde{\phi''^2}\right)_{,i}}_{\text{term I}} \underbrace{-2\bar{\rho}\widetilde{u_i''\phi''}\tilde{\phi}_{,i}}_{\text{term II}} \underbrace{-\frac{2}{c_p}\overline{N_i'\phi'_{,i}}}_{\text{term III}} \underbrace{-\left(\bar{\rho}\widetilde{u_i''\phi''^2}\right)_{,i}}_{\text{term IV}} \\ &+\underbrace{\frac{2}{c_p}\left(\overline{N_i'\phi'}\right)_{,i}}_{\text{term V}} + \underbrace{\frac{2}{c_p}\overline{\phi''}\bar{N}_{i,i}}_{\text{term VI}},\end{aligned} \tag{18}$$

where $N_i = \lambda\phi_{,i}$. The budget terms have similar interpretations as above. The most important difference in the form of the budget equations between the INBM and LMTV cases is that M includes density but N does not.

Unlike the Favre-averaged scalar variance itself, the corresponding dissipation terms have very similar behavior, both in magnitude and spatial distribution, for all of the cases (Fig. 2). When the diffusion coefficient ($\mathcal{D}$ or λ) is constant, the scalar dissipation term is essentially the variance of the scalar gradient. When written for the constant-$\mathcal{D}$ INBM governing equations, it is weighted by density (in M_i), but that weighting is absent for the corresponding constant-c_p and λ LMTV case (in N_i).

Examining the scalar gradient fluctuation intensity directly (Fig. 2), without density weighting for any case, demonstrates a strong dependence in magnitude on the form of the diffusivity. The inertially-induced drift of the mean velocity profile relative to the mean density profile suggests that fluid in the region of strongest turbulence and mixing experiences larger diffusivity for constant λ LMTV relative to constant $\mathcal{D}$ INBM. This is a consequence of the mixing layers growing preferentially into the lighter stream, though the strongest shear and disturbance were initially positioned at the fluid interface. Since $\mathcal{D} \propto 1/\rho$ is equivalent to constant λ, this drifting implies that $\mathcal{D}$ is larger than average (i.e., the average of the two free streams) in this region. The diffusivity of the constant $\mathcal{D}$ simulations is only matched by the $\mathcal{D} \propto 1/\rho$ simulations where $\rho = \rho_0 = (\rho_1 + \rho_2)/2$. Since the strongest turbulence and mixing becomes centered where the local density is, on average, less than ρ_0, it follows that the local $\mathcal{D}$ is larger than that of a constant $\mathcal{D}$ simulation. Despite the differences in the ϕ gradients, however, the weighting by density results in similar magnitudes of scalar dissipation for the INBM and LMTV cases. Similar arguments can be made that, in the same region, the local viscosity ν of a constant μ simulation is somewhat larger than that of a constant ν simulation. However, the scalar gradients display less sensitivity to viscosity. The effects on mixing layers of streams having differing viscosities (but the same densities) has been studied in depth (e.g., Ref. [44]). The comparisons made in Fig. 2 indicate that the differing transport forms modify the flow structure, but a number of gross quantities (e.g., scalar dissipation, as well as the mean density and velocity profiles) are only weakly affected. In summary, in these simulations, the scalar variance is relatively sensitive to the forms of the scalar diffusion and fluid viscosity, but its dissipation is insensitive to both forms.

The differences in statistics involving higher-order quantities are indicative of differing mixing dynamics. The PDFs of the density shown in Fig. 3 for selected y positions further illustrate the differences. Since local density is related to specific volume as $v = 1/\rho$ and specific volume has a linear relationship to species mass fraction or temperature depending on the case, these plots can also be interpreted in terms of the latter quantities. While the distributions are similar among cases at each y location, details of the PDFs reveal significant differences. At $y/h = -0.47$, peaks for both of the $\mathcal{D} \propto 1/\rho$ (LMTV) cases are located at densities greater than that of the pure light fluid, indicating that mixed fluid dominates. Conversely, for each of the constant $\mathcal{D}$ (INBM) cases (black and red curves), a peak also occurs at the lightest fluid density ($\rho/\rho_0 = 0.25$); this tail indicates that measurable traces of light fluid have yet to begin mixing. As y increases slightly, the behavior that dominates the intensely mixed layer emerges: a single dominant PDF peak with position weakly biased toward heavier density at constant ν than constant μ but slightly lower probability of fluid at higher density, indicating that the heavier fluid mixes more for constant ν. In addition, there are lower probabilities of fluid at the lowest densities, indicating the lightest fluid is also more mixed. As y further increases, each constant $\mathcal{D} \propto 1/\rho$ (LMTV) PDF develops a tail of increasing value near the pure heavy fluid. This effect continues as y position increases, with the unmixed heavy fluid peak much larger for the $\mathcal{D} \propto 1/\rho$ cases at the highest y value shown.

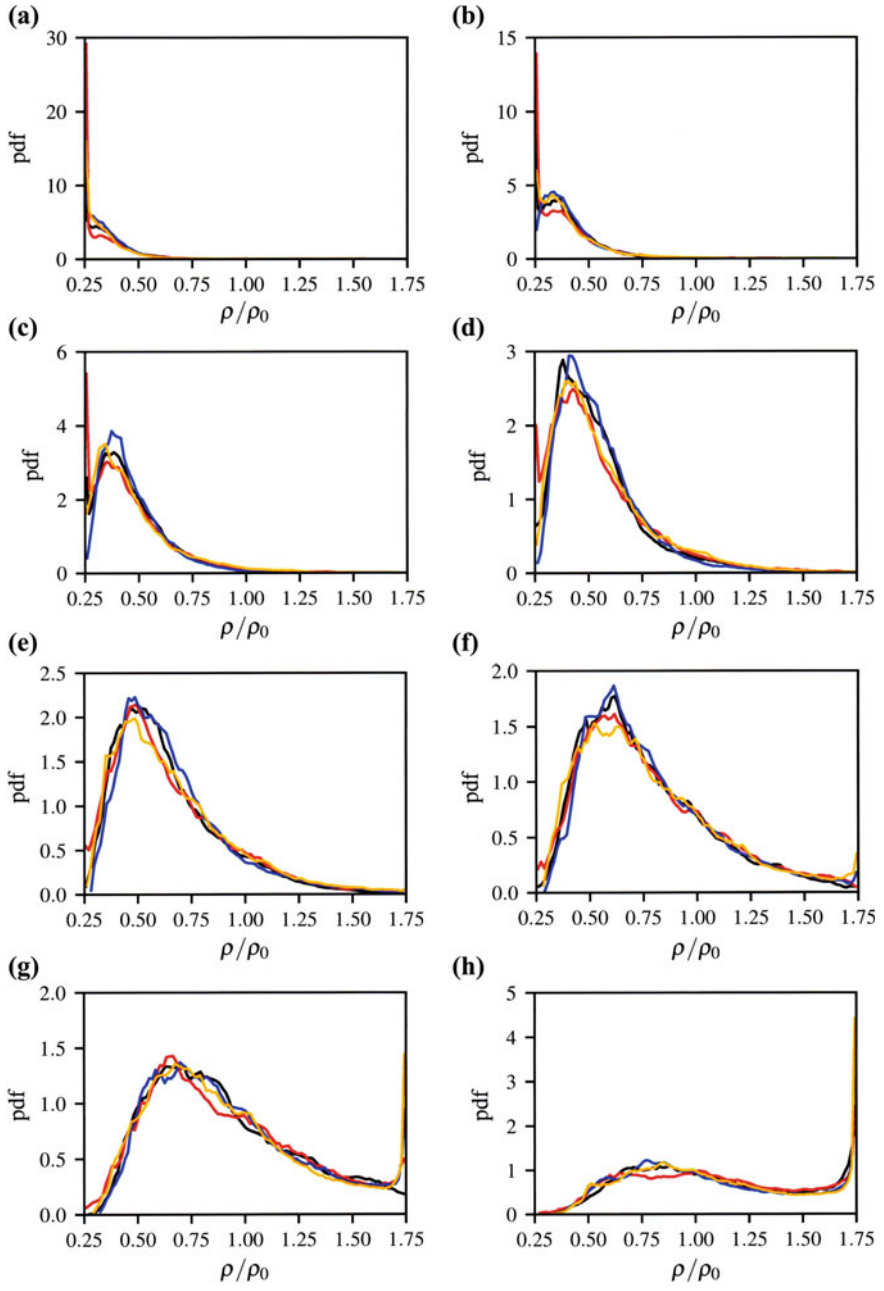

Fig. 3 Comparison of density PDFs at $t\Delta U/h_0 = 284$ and $y/h =$ **a** -0.70, **b** -0.58, **c** -0.47, **d** -0.35, **e** -0.23, **f** -0.12, **g** 0.00, and **h** 0.12. (——) $\mathcal{D} =$ const. (INBM) and $\mu \propto \rho$, (——) $\mathcal{D} =$ const. and $\mu =$ const., (——) $\mathcal{D} \propto 1/\rho$ (constant-transport-property LMTV) and $\mu \propto \rho$, and (——) $\mathcal{D} \propto 1/\rho$ and $\mu =$ const.

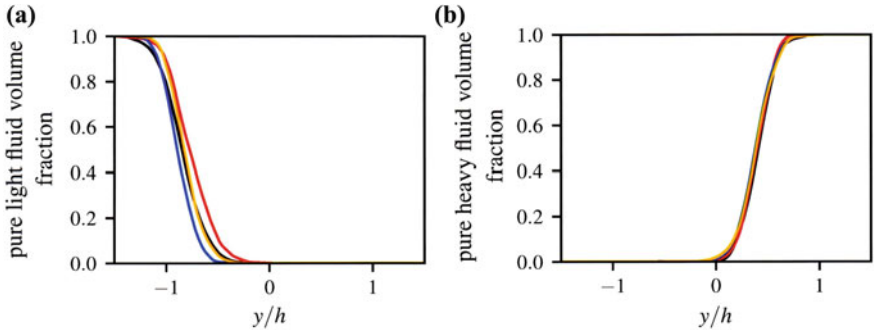

Fig. 4 Comparison of volume fractions of pure **a** light and **b** heavy fluid (defined as density within 1% of the total difference from each pure value) at $t\Delta U/h_0 = 284$. Colors are (——) $\mathcal{D} = \text{const.}$ (INBM) and $\mu \propto \rho$, (——) $\mathcal{D} = \text{const.}$ and $\mu = \text{const.}$, (——) $\mathcal{D} \propto 1/\rho$ (constant-transport-property LMTV) and $\mu \propto \rho$, and (——) $\mathcal{D} \propto 1/\rho$ and $\mu = \text{const.}$

The differences in the PDF tails can be compared by plotting the volume fractions of pure fluid as functions of y (Fig. 4). These comparisons show that the mixing behaviors involving the pure light sides are more significantly modified among the different cases than those involving the pure heavy fluid. On the light fluid side, the edge of the layer (where the pure light fluid fraction begins to decay from 1.0) is positioned at more strongly negative y values for the constant-ν cases than for the constant-μ cases. These extents are generally insensitive to the form of diffusivity. However, the PDFs include complicated peak behavior at positions where pure light fluid is beginning to mix. The 1% threshold used here does not correspond directly to the PDFs, which include bins of finer granularity that reveal features such as the weak peak of unmixed light fluid at $y/h = -0.47$ for the constant-ν INBM case. From each outer edge, Fig. 4 shows that the pure light fluid persists further into the mixing layer for the constant $\mathcal{D}$ cases than for the $\mathcal{D} \propto 1/\rho$ cases. In other words, the pure light fluid mixes more rapidly with respect to position towards the center of the layer with $\mathcal{D} \propto 1/\rho$. While caution must be observed in interpreting the curves as functions of the scaled coordinates y/h with the possibility of altered profile shapes and growth dynamics affecting how the curves lie in relation to each other, the growths and mean profiles are very similar between cases, which supports the validity of these comparisons. The behaviors of the pure light fluid curves suggest that the outer boundary of mixing is mainly controlled by the viscosity, but as the layer is entered, the scalar diffusivity controls how quickly mixing eliminates pure light fluid.

In regard to the pure heavy fluid side, mixing begins at (that is, only pure heavy fluid exists up to) similar points for all of the cases. Some amount of pure heavy fluid persists for slightly further distances into the mixing layer for the LMTV (or $\mathcal{D} \propto 1/\rho$) cases. Thus, diffusivity also affects how quickly the mixing eliminates pure heavy fluid.

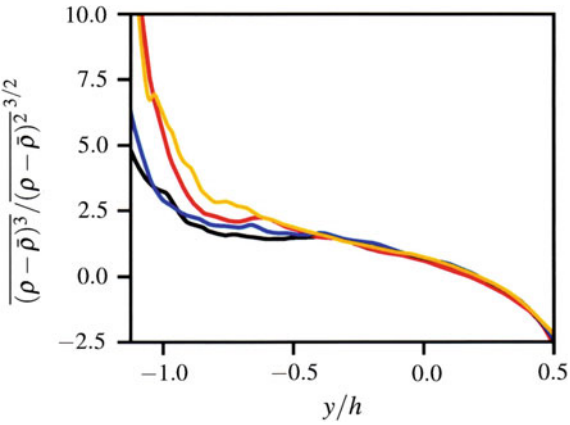

Fig. 5 Comparison of density skewness at $t\Delta U/h_0 = 284$. The y range is restricted to the interior of the layer where turbulent motions are most active. Colors are (——) $\mathcal{D} = \text{const.}$ (INBM) and $\mu \propto \rho$, (——) $\mathcal{D} = \text{const.}$ and $\mu = \text{const.}$, (——) $\mathcal{D} \propto 1/\rho$ (constant-transport-property LMTV) and $\mu \propto \rho$, and (——) $\mathcal{D} \propto 1/\rho$ and $\mu = \text{const.}$

The asymmetries of the density PDFs inside the layer can be quantified by their skewnesses. These are plotted across the layers in Fig. 5. All of the cases collapse near the heavy fluid side as the skewnesses becomes negative. This collapse occurs despite the significantly different magnitudes among cases of the squared density fluctuation $\overline{\rho'\rho'}$ in the tail on the heavy-fluid side (Fig. 1). Approaching the light-fluid side, the skewnesses behave similarly but diverge among cases. In general, the constant μ cases are more positively skewed as the light-fluid edge of the mixing layers is approached. This is consistent with their pure light fluid tails persisting further into the mixing layer and beginning to decay at smaller distances from the core.

The complex dependencies on diffusivity and viscosity suggest that the various scales of motion are affected differently. Spectra of density and scalar ϕ further clarify these effects. Figure 6 shows two-dimensional spectra of density for various cross-stream (y) positions. Though the flow is anisotropic between the x and z axes due to the mean shear, averaging implied by the two-dimensional spectra is sufficient to reveal the scale dependence. Particularly at the lowest y values, the low wavenumbers of the density field are more strongly affected by the fluid viscosity form, with the diffusivity form having little effect. At the highest wavenumbers, particularly around the location of the most intense turbulence (e.g., at $y/h = -0.23$), the spectra are strongly affected by the diffusivities (i.e., INBM with constant $\mathcal{D}$ versus LMTV with constant λ and c_p). This diverging behavior of spectra at high wavenumbers with respect to diffusivity is even more pronounced when the scalar is considered rather than the density, and this effect persists over all y positions shown (Fig. 7).

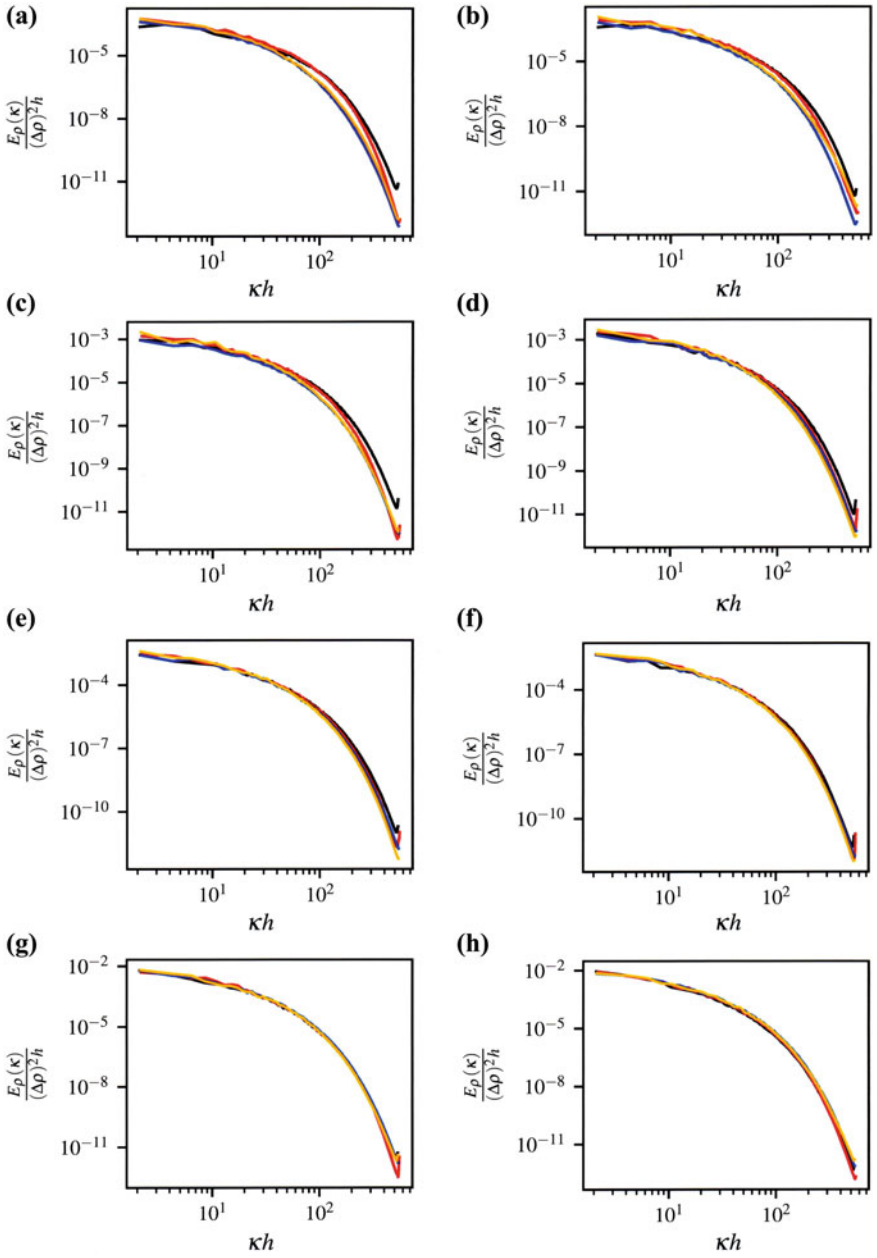

Fig. 6 Comparison of 2D spectra for density at $t\Delta U/h_0 = 284$ and $y/h =$ **a** −0.70, **b** −0.58, **c** −0.47, **d** −0.35, **e** −0.23, **f** −0.12, **g** 0.00, and **h** 0.12. (——) $\mathcal{D} =$ const. (INBM) and $\mu \propto \rho$, (——) $\mathcal{D} =$ const. and $\mu =$ const., (——) $\mathcal{D} \propto 1/\rho$ (constant-transport-property LMTV) and $\mu \propto \rho$, and (——) $\mathcal{D} \propto 1/\rho$ and $\mu =$ const.

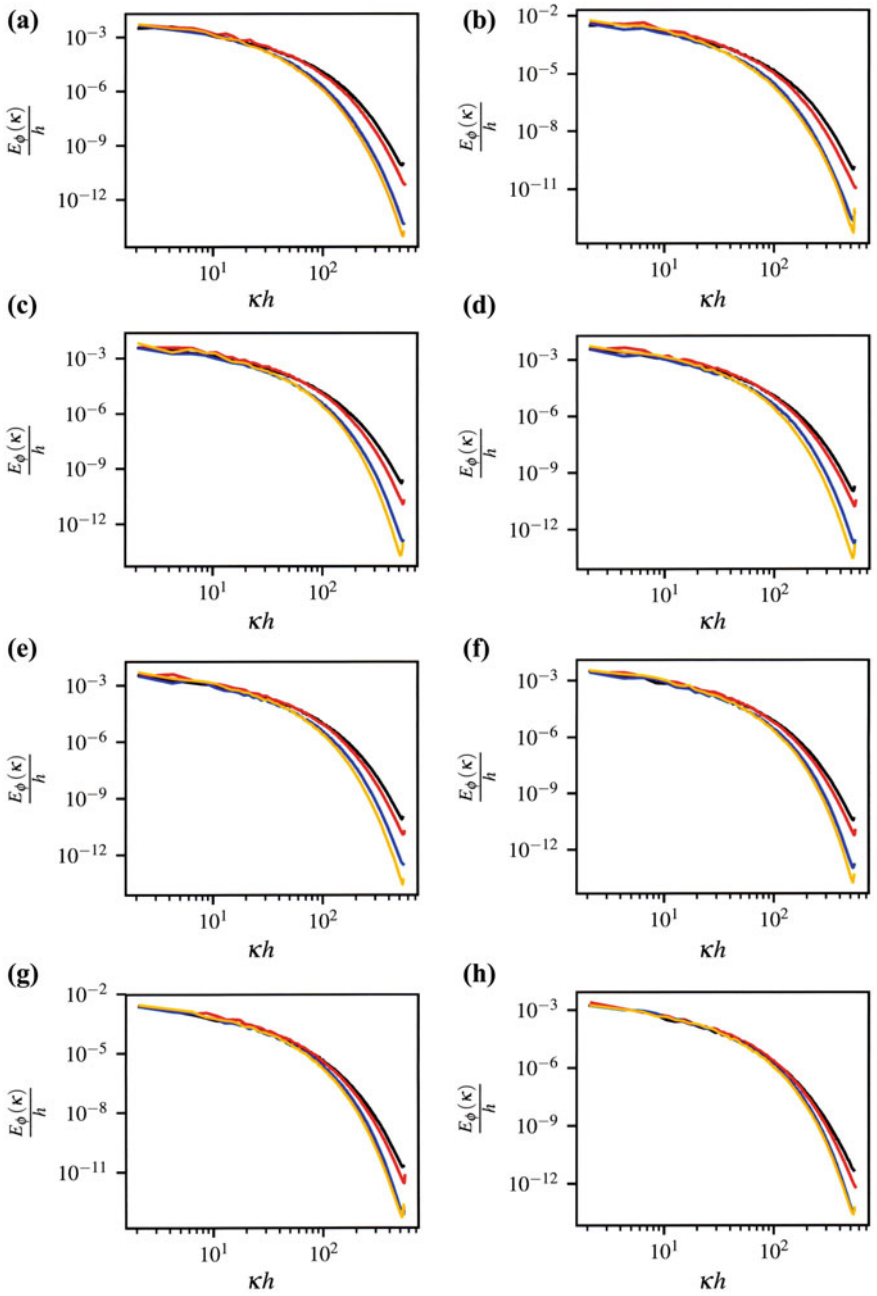

Fig. 7 Comparison of 2D spectra for scalar ϕ (heavy fluid mass fraction or scaled temperature) at $t\Delta U/h_0 = 284$ and $y/h =$ **a** -0.70, **b** -0.58, **c** -0.47, **d** -0.35, **e** -0.23, **f** -0.12, **g** 0.00, and **h** 0.12. (——) $\mathcal{D} =$ const. (INBM) and $\mu \propto \rho$, (——) $\mathcal{D} =$ const. and $\mu =$ const., (——) $\mathcal{D} \propto 1/\rho$ (constant-transport-property LMTV) and $\mu \propto \rho$, and (——) $\mathcal{D} \propto 1/\rho$ and $\mu =$ const.

5 Conclusions

Low- and zero-Mach number approximations have been employed for studying flows with large density variations in a variety of flows. In these limits, density variations can be related to two classes of flows: (a) single fluid flows with temperature fluctuations and (b) mixing between species with different densities (e.g. due to different molar masses). In addition, the associated changes in the fluid properties can also be important.

For temporal shear driven mixing layers, despite the similarities in the mean flow quantities, higher order statistics reveal significant differences in the mixing dynamics resulting from governing equations derived for density variations induced by species or thermodynamic variations. These changes are also indicative of modified turbulence structures. While the results shown are for a single Atwood number and the effects can be expected to increase in magnitude with Atwood number, they demonstrate that in general care must be taken to apply conclusions between dissimilar diffusion operators (e.g., LMTV or INBM) and other transport properties. In addition, very different physical conditions and simplifications (e.g., assuming that c_p and λ are constant despite large temperature variations) are necessary to reach the respective forms of governing equations for INBM (incompressible non-Boussinesq mixing) and LMTV (low-Mach number temperature variations), as they have been used in previous studies. Thus, though both the INBM and LMTV governing equations can be derived from the low-Mach number non-Oberbeck-Boussinesq equations for a multi-fluid mixture, distinct simplifications are required that have unique physical interpretations. Beyond the simplification to a single fluid or taking the infinite speed-of-sound incompressible limit, further assumptions on the transport properties (diffusivity or conduction coefficient) and their dependencies on density or temperature influence the flow evolution. These assumptions have differing fidelities relative to practical flow conditions. Physically obtaining high Atwood numbers in a LMTV configuration would imply large differences in temperature, which would result in large variations in fluid properties. Though these variations could be simulated as well, considering them weakens the connection to INBM flows and suggests that care is necessary in making analogies between practical flows. While the INBM equations solved herein assume a constant diffusivity, that assumption more closely matches the conditions experienced within a practical experiment. The results demonstrate that the differences between the LMTV or INBM governing equations, despite their close resemblance, can nevertheless significantly affect the mixing dynamics to which reacting flows are sensitive. Exploring the range of species- and temperature-induced density effects is thus necessary to gain the physical insight necessary to advance the prediction of the broad spectrum of flows in which mixing plays a critical role.

Acknowledgements This work has been authored by employees of Triad National Security, LLC which operates Los Alamos National Laboratory under Contract No. 89233218CNA000001 with the U.S. Department of Energy/National Nuclear Security Administration.

References

1. B.W. Spencer, B.G. Jones, Statistical investigation of pressure and velocity fields in the turbulent two-stream mixing layer. *AIAA Paper*, pp. 71–613 (1971)
2. J.H. Bell, R.D. Mehta, Development of a two-stream mixing layer from tripped and untripped boundary layers. AIAA J. **28**, 2034–2042 (1990)
3. R.B. Loucks, J.M. Wallace, Velocity and velocity gradient based properties of a turbulent plane mixing layer. J. Fluid Mech. **699**, 280–319 (2012)
4. M.M. Rogers, R.D. Moser, Direct simulation of a self-similar turbulent mixing layer. Phys. Fluids **6**, 903–923 (1994)
5. E. Balaras, U. Piomelli, J.M. Wallace, Self-similar states in turbulent mixing layers. J. Fluid Mech. **446**, 1–24 (2001)
6. M. Tanahashi, S. Iwase, T. Miyauchi, Appearance and alignment with strain rate of coherent fine scale eddies in turbulent mixing layer. J. Turbul. **2**(6), 1–17 (2001)
7. Y. Wang, M. Tanahashi, T. Miyauchi, Coherent fine scale eddies in turbulence transition of spatially-developing mixing layer. Int. J. Heat Fluid Flow **28**, 1280–1290 (2007)
8. A. Attili, F. Bisetti, Statistics and scaling of turbulence in a spatially developing mixing layer at $\mathrm{Re}_\lambda = 250$. Phys. Fluids **24**, 035109 (2012)
9. G.L. Brown, A. Roshko, On density effects and large structure in turbulent mixing layers. J. Fluid Mech. **64**, 775–816 (1974)
10. A.W. Vreman, N.D. Sandham, K.H. Luo, Compressible mixing layer growth rate and turbulence characteristics. J. Fluid Mech. **320**, 235–258 (1996)
11. S. Sarkar, On density and pressure fluctuations in uniformly sheared compressible flow, in *Proceedings IUTAM Symposium on Variable Density Low-Speed Flows, Marseille*, ed. by L. Fulachier, J.L. Lumley, F. Anselmet (Kluwer Academic Publishers, 1996)
12. C. Pantano, S. Sarkar, A study of compressibility effects in the high-speed turbulent shear layer using direct simulation. J. Fluid Mech. **451**, 329–371 (2002)
13. D. Livescu, C.K. Madnia, Small scale structure of homogeneous turbulent shear flow. Phys. Fluids **16**, 2864–2876 (2004)
14. R. Jahanbakhshi, N.S. Vaghefi, C.K. Madnia, Baroclinic vorticity generation near the turbulent/non-turbulent interface in a compressible shear layer. Phys. Fluids **27**, 105105 (2015)
15. A. Almagro, M. García-Villalba, O. Flores, A numerical study of a variable-density low-speed turbulent mixing layer. J. Fluid Mech. **830**, 569–601 (2017)
16. J.D. Schwarzkopf, D. Livescu, J.R. Baltzer, R.A. Gore, J.R. Ristorcelli, A two-length scale turbulence model for single-phase multi-fluid mixing. Flow Turbul. Combust. **96**, 1–43 (2016)
17. L. Joly, The structure of some variable density shear flows, in *Variable Density Fluid Turbulence*, ed. by P. Chassaing, R.A. Antonia, F. Anselmet, L. Joly, S. Sarkar, Chap. 8, pp. 201–234 (Springer, 2002)
18. W.T. Ashurst, A.R. Kerstein, One-dimensional turbulence: Variable-density formulation and application to mixing layers. Phys. Fluids **17**, 025107 (2005)
19. B.J. Olson, J. Larsson, S.K. Lele, A.W. Cook, Nonlinear effects in the combined Rayleigh-Taylor/Kelvin-Helmholtz instability. Phys. Fluids **23**, 114107 (2011)
20. I. Gat, G. Matheou, D. Chung, P.E. Dimotakis, Incompressible variable-density turbulence in an external acceleration field. J. Fluid Mech. **827**, 506–535 (2017)
21. C. Pantano, S. Sarkar, F.A. Williams, Mixing of a conserved scalar in a turbulent reacting shear layer. J. Fluid Mech. **481**, 291–328 (2003)
22. M.S. Day, J.B. Bell, Numerical simulation of laminar reacting flow with complex chemistry. Comb. Theor. Mod. **4**, 535–556 (2000)
23. A.S. Almgren, J.B. Bell, C.A. Rendleman, M. Zingale, Low Mach number modeling of Type Ia supernovae. I. Hydrodynamics. Astrophys. J. **637**, 922–936 (2006)
24. A. Majda, J. Sethian, The derivation and numerical solution of the equations for zero Mach number combustion. Combust. Sci. Tech. **42**, 185–205 (1985)
25. D. Livescu, Turbulence with large thermal and compositional density variations. *Annu. Rev. Fluid Mech.* **52**, 309–341 (2020)

26. D.R. Chenoweth, S. Paolucci, Natural convection in an enclosed vertical air layer with large horizontal temperature differences. J. Fluid Mech. **169**, 173–210 (1986)
27. F. Williams, *Combustion Theory* (Perseus Books, Cambridge, 1985)
28. P.A. McMurtry, W.-H. Jou, J. Riley, R.W. Metcalfe, Direct numerical simulations of a reacting mixing layer with chemical heat release. AIAA J. **24**, 962–970 (1986)
29. S. Paolucci, On the filtering of sound from the Navier-Stokes equations. Technical Report SAND82-8257 (Sandia National Laboratories, 1982)
30. A.W. Cook, J.J. Riley, Direct numerical simulation of a turbulent reactive plume on a parallel computer. J. Comput. Phys. **129**, 263–283 (1996)
31. G. Ahlers, E. Brown, F.F. Araujo, D. Funfschilling, S. Grossmann, D. Lohse, Non-Oberbeck-Boussinesq effects in strongly turbulent Rayleigh-Bénard convection. J. Fluid Mech. **569**, 409–445 (2006)
32. F.J. Higuera, R.D. Moser, Effect of chemical heat release in a temporally evolving mixing layer. Technical Report, 19–40, CTR (1994)
33. D. Livescu, Numerical simulations of two-fluid turbulent mixing at large density ratios and applications to the Rayleigh-Taylor instability. Phil. Trans. R. Soc. A **371**, 20120185 (2013)
34. D.D. Joseph, Fluid dynamics of two miscible liquids with diffusion and gradient stresses. Eur. J. Mech. B **6**, 565–596 (1990)
35. A.W. Cook, P.E. Dimotakis, Transition stages of Rayleigh-Taylor instability between miscible fluids. J. Fluid Mech. **443**, 69–99 (2001)
36. D.L. Sandoval, The dynamics of variable density turbulence. Ph.D. thesis, University of Washington, 1995. LANL Rep. LA-13037-T
37. D. Livescu, J.R. Ristorcelli, Buoyancy-driven variable-density turbulence. J. Fluid Mech. **591**, 43–71 (2007)
38. W.H. Cabot, A.W. Cook, Reynolds number effects on Rayleigh-Taylor instability with possible implications of Type-Ia supernovae. Nat. Phys. **2**, 562–568 (2006)
39. T. Wei, D. Livescu, Late-time quadratic growth in single-mode Rayleigh-Taylor instability. Phys. Rev. E **86**, 046405 (2012)
40. D. Livescu, J.R. Ristorcelli, M.R. Petersen, R.A. Gore, New phenomena in variable-density Rayleigh-Taylor turbulence. Phys. Scr. **T142**, 014015 (2010)
41. E.L. Cussler, *Diffusion: Mass Transfer in Fluid Systems* (Cambridge University Press, Cambridge, UK, 2009)
42. Y. Tian, F.A. Jaberi, Z. Li, D. Livescu, Numerical study of variable density turbulence interaction with a normal shock wave. J. Fluid Mech. **829**, 551–588 (2017)
43. R.W. Bilger, Some aspects of scalar dissipation. Flow Turbul. Combust. **72**, 93–114 (2004)
44. N. Taguelmimt, L. Danaila, A. Hadjadj, Effect of viscosity gradients on mean velocity profile in temporal mixing layer. J. Turbul. **17**, 491–517 (2016)

Scalar Transport Near the Turbulent/Non-Turbulent Interface in Reacting Compressible Mixing Layers

Reza Jahanbakhshi and Cyrus K. Madnia

Abstract Direct numerical simulations of temporally evolving compressible reacting mixing layers with Schmidt number equal to one are performed to examine the transport of a conserved scalar across the turbulent/non-turbulent interface (TNTI). The budgets of the scalar-gradient transport equation are used to study the effects of compressibility and heat release on the mixing. The simulations include a wide range of convective Mach number (M_c) from a subsonic and nearly incompressible case ($M_c = 0.2$) to a supersonic mixing layer at $M_c = 1.8$. Furthermore, the highest level of heat release for the reacting simulations is opted to correspond to hydrogen combustion in air. The results suggest that the primary influence of the compressibility and heat release on the mixing of a conserved scalar is felt in a thin interface layer close to the TNTI whose thickness scales with the scalar-Taylor length scale. This interface layer is a juxtaposition of two dynamically different sub-regions referred to as laminar superlayer (LSL) and turbulent sublayer (TSL), whose thicknesses are of order of Kolmogorov and scalar-Taylor length scales, respectively. The transport of scalar is predominately governed by the molecular diffusion inside the LSL, whereas the inertial turbulent production dominates the transport within the TSL. It is shown that as the level of compressibility or heat release increases the rate of scalar mixing decreases. Compressibility affects the scalar mixing via a weakened turbulent production mechanism in the turbulent sublayer part of the interface layer, while the molecular diffusion process remains dynamically unaffected. On the other hand, in reacting cases the molecular diffusion inside the laminar superlayer and the turbulent production across the adjacent turbulent sublayer are subdued, which result in a decreased mixing rate.

R. Jahanbakhshi (✉)
Department of Mechanical Engineering, Johns Hopkins University, Baltimore, MD 21218, USA
e-mail: reza.jahan@jhu.edu

C. K. Madnia
Department of Mechanical and Aerospace Engineering, State University of New York at Buffalo, Buffalo, NY 14260, USA
e-mail: madnia@buffalo.edu

D. Livescu et al. (eds.), *Modeling and Simulation of Turbulent Mixing and Reaction*, Heat and Mass Transfer, https://doi.org/10.1007/978-981-15-2643-5_2

Keywords Scalar mixing · Turbulent reacting flow · Compressible flow

1 Introduction

In many shear flows, the flow field can be divided into two dynamically different regions, a turbulent region, and an irrotational (potential) flow region. An important feature of these type of flows is a sharp and highly convoluted interface, referred to as the turbulent/non-turbulent interface (TNTI), that separates the two regions [1]. The mixing and mass transport between these two regions remains a practically demanding and scientifically intriguing problem. In particular, compared to non-reacting subsonic flows, the mixing between two streams with different velocities under supersonic and/or chemically reacting conditions is relatively less understood. In a series of previous studies by the authors the momentum and mass transport across the turbulent/non-turbulent interface of reacting and compressible turbulent mixing layers are examined in details [2–6]. The current work is the new installment of the series aiming to study the effects of compressibility and heat release on the mixing of a conserved scalar in a temporally evolving mixing layer.

1.1 Scalar Transport in Incompressible Free Shear Flows

Due to its crucial relevance to many engineering and geophysical flow applications such as chemical reactions inside combustion chambers and pollutant dispersion, turbulent mixing has continuously been a subject of interest in fluid dynamic research (see review by Dimotakis [7]). More recently, the study of turbulent mixing in the context of turbulent/non-turbulent interface and its dynamics have received much attention in the literature [8]. In this subsection, a summary of the recent studies in which conserved-scalar mixing near the TNTI is examined, is presented.

Silva and da Silva [9] performed a numerical analysis of the dynamics of a passive-scalar field near a TNTI in incompressible turbulent planar jets. In their simulations, different cases with Reynolds numbers ranging from $142 \leq \mathrm{Re}_\lambda \leq 246$ and Schmidt numbers $\mathrm{Sc} = 0.07, 0.7$, and 7 were examined. They reported that for low to moderate Schmidt numbers ($\mathrm{Sc} < 0.7$) cases, the bulk of the mixing occurs in the irrotational region. In contrast for the high Schmidt number case ($\mathrm{Sc} = 7.0$), the TNTI consists of a viscous-convective superlayer that closely matches the viscous superlayer and an inertial-convective sublayer, which is much thinner than the turbulent sublayer, corresponding to the vorticity transport mechanism. Similar observations of scalar transport mechanisms were made by Hunger et al. [10] in planar turbulent jets with $\mathrm{Sc} = 0.25$ and 1, Watanabe et al. [11] in temporally developing mixing layers under various Schmidt numbers ($\mathrm{Sc} = 0.25, 1, 4, 8$) conditions, and by Attili et al. [12] for a spatially developing turbulent mixing layer with $\mathrm{Sc} \approx 1$. High Schmidt number ($\mathrm{Sc} \geq 1.0$) results of the aforementioned numerical works are also confirmed

by the experimental measurements of a turbulent round submerged liquid jet with Sc = 2000 reported by Westerweel et al. [13].

In another work, Watanabe et al. [14] examined the characteristics of the passive scalar transport near the TNTI for three interface orientations: the cross-streamwise edge and the leading edge that face the cross-streamwise and streamwise directions respectively, and the trailing edge which is opposite to the leading edge. In this work, the conditional average of the advection term in scalar transport equation shows that the scalar in the non-turbulent region is frequently transported into the turbulent region across the cross-streamwise and leading edges by interface propagation toward the non-turbulent region. In contrast, scalar in the turbulent region is frequently transported into the non-turbulent region across the trailing edge. Other notable studies on the scalar mixing in free shear flows were performed by Gampert et al. [15, 16]. The focus of these works is placed on the effects of different TNTI detection approaches, namely vorticity or a scalar criterion, on the interface dynamics [16], and the scaling of the passive scalar thickness and the scalar dissipation near the TNTI [15].

1.2 Motivation and Objective

As is evident from the discussions in Sect. 1.1, while the scalar transport near the TNTI in incompressible non-reacting free shear flow configurations have received much attention in recent years, the effects of compressibility and heat release on this phenomenon are relatively less understood. Watanabe et al. [17] were the first to analyze the transport of a reactive-scalar field near the TNTI using the direct numerical simulations of a planar jet with an isothermal second order chemical reaction for Damköhler numbers ranging from 0.1 to 10. They reported that the conditional mean of the concentration of chemical species changes with a sharp jump across the TNTI, while the width of this jump is almost independent of the Damköhler number and the chemical species. Zhang et al. [18] have performed the first study of the passive scalar mixing near TNTI in compressible turbulent boundary layers at Ma = 0.8 and 1.6. In their work, some basic conditional statistics are calculated as a function of the distance from the TNTI and the results are compared with the turbulent core region. In current study, we perform the first detailed analysis of the effects of compressibility and heat release on the conserved-scalar transport across the turbulent/non-turbulent interface in a turbulent mixing layer. The main objective is to elucidate the aforementioned effects on the scalar mixing and to compare them with the momentum and mass transfer in the same configuration previously studied by the authors [2–5].

This work is organized as follows. In Sect. 2 a summary of the direct numerical simulations (DNS) results for the compressible reacting mixing layer is provided. In Sect. 3, the method used to detect the turbulent/non-turbulent interface is presented. The findings of the current work are discussed in detail in Sect. 4, and conclusions are summarized in Sect. 5.

2 Direct Numerical Simulations

A brief description of the direct numerical simulations carried out to achieve the objectives of the current work is provided in this section. More detailed information alongside exhaustive validation study can be found in previously published works [3, 19–21].

In order to obtain the flow-field variables corresponding to a compressible reacting flow, the non-dimensional form of the Navier-Stokes equations [22] (conservation for mass, momentum and energy), and mixture fraction

$$\frac{\partial(\rho Z)}{\partial t} + \nabla \cdot (\rho \vec{u} Z) = \frac{1}{\mathrm{Re}} \nabla \cdot \left(\frac{\mu}{\mathrm{Sc}} \nabla Z \right), \tag{1}$$

are solved. Infinitely fast chemistry approximation [23] is used to model a one-step irreversible global reaction that involves fuel (hydrogen), oxidizer (oxygen), and product (water). Therefore, the species mass fractions are computed using the Burke-Schumann relations [23] from the mixture fraction field. The diluent of the mixture is nitrogen whose mass fraction is computed from the mass balance. In Eq. (1), ρ is the density, $\vec{u}$ is the velocity vector, Re is the (reference) Reynolds number, and μ is the the dynamic viscosity. In the combustion model used in the current work the following assumptions are employed: the molecular diffusion processes are simplified by neglecting the Soret and Dufour effects [24], the Fick's law [25] without velocity correction is used to model the diffusion velocity of the species, and Schmidt number is assumed to be equal to one for all species. In addition, all external forces are assumed to be negligible. Equation (1) contains no source term, and therefore, Z is a passive scalar. In the present simulations, mixture fraction is equal to 1 in the fuel stream and to 0 in the oxidizer stream.

To non-dimensionalize the thermochemical parameters of the mixture the reference temperature of $T_1 = 298^\circ$ K and the specific heat of nitrogen at T_1 are used. In non-reacting simulations the temperature variation is small. Therefore, the thermochemical variable are assumed to be constant. In reacting simulations, however, the temperature dependence of viscosity, specific heat and thermal conductivity is taken into account. The specific heat of the species are assumed to vary linearly with temperature. According to the thermochemical data found in the literature [26], this assumption is valid for the range of temperature of interest in the present work. Moreover, Sutherland's law [27] is used to model the temperature dependence of viscosity. Finally, the thermal conductivity is found by assuming Prandtl number is constant in the flow, which is a reasonable approximation for the range of temperatures in our simulations [26]. The Prandtl number is assumed to be equal to one in all simulations which results in a unity Lewis number.

The flow configuration of current study, i.e. a temporally evolving mixing layer, is shown schematically in Fig. 1. In this figure x and z represent homogeneous streamwise and spanwise directions respectively, and y denotes the transverse direction. Velocity in upper stream, U_1, is the reference velocity scale, and the lower stream has a velocity $U_2 = -U_1$. For streams with equal ratio of the specific heats,

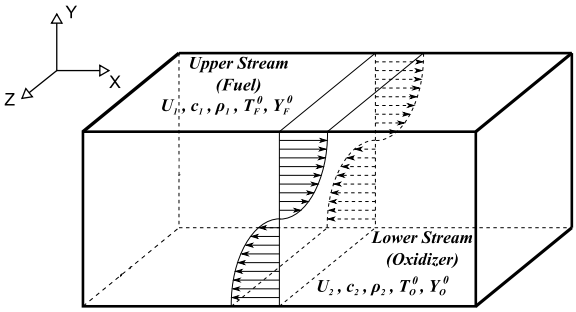

Fig. 1 Schematic configuration of a temporal mixing layer. All of the variables in the figure are defined in the text

Bogdanoff [28] proposed the convective Mach number as $M_c = \Delta U/(c_1 + c_2)$, where $\Delta U = U_1 - U_2$ is the velocity difference and c_1 and c_2 are the speeds of sound in each stream. Table 1 highlights the numerical and physical details of the cases of the present study. Computational domain lengths in x-, y- and z-directions are L_x, L_y and L_z, which are discretized with N_x, N_y and N_z grid points, respectively. Uniform-grid discretizations are used which resulted in equal grid size in all directions $\Delta x = \Delta y = \Delta z$. Periodic boundary conditions are imposed in homogeneous directions (x and z), whereas in transverse direction the boundaries are characteristic slip walls at which normal component of velocity is zero at all times while the other velocity components may be nonzero [22, 29]. In Table 1, the level of compressibility is altered by changing the value of convective Mach number, M_c, and the level of heat release is controlled by changing the parameter Q, which is a normalized heat release variable [23]. Thus, to study the effects of compressibility and heat release on turbulence several cases with different convective Mach numbers and heat release levels are simulated. The chosen values for convective Mach number cover a wide range of compressibility levels from subsonic and nearly incompressible (case $M02NR$) to supersonic and highly compressible flows (case $M18NR$). Moreover, several heat release levels are opted for the reacting cases with the highest level of heat release corresponding to hydrogen combustion in air, $Q = 8.1$. The reference length is the initial momentum thickness, δ_{θ_0}, in the present simulations.

The numerical method used to solve the governing equations is based on the Gottlieb-Turkel scheme [30]. In this method, spatial derivatives are computed through a forward-backward procedure with finite difference approach which results in fourth-order accuracy in space. The time integration is performed using a second-order MacCormack method [31]. The mean flow is initialized with hyperbolic tangent profile in streamwise direction, while the mean vertical and spanwise velocities are zero. The initial temperature is obtained from the Busemann-Crocco relationship [32] for the non-reacting cases, and from the Burke-Schumann relation [23] for the reacting cases. The pressure field is initially uniform, and the initial density is calculated from the equation of state for an ideal gas. The temperatures of the oxidizer, T_O^0, and fuel, T_F^0, streams are chosen such that for all the simulations the density of the two free streams is identical. This results in a temperature ratio of $T_F^0/T_O^0 = \Re_O/\Re_F$, where $\Re_F$ and $\Re_O$ are the gas constant in fuel and oxidizer streams, respectively.

Table 1 Numerical and physical parameters of the simulations. M_c is the convective Mach number, Q is the non-dimensional heat release parameter, Z_{st} is the stoichiometric mixture fraction, L_i & N_i are the domain length and number of grid points in i-direction, respectively, Re_λ is the Reynolds numbers based on Taylor scale at the final time of the self-similar state, and $\eta_{\min}$ is the minimum value of Kolmogorov length scale. δ_{θ_0} is the initial momentum thickness. Sc and Pr are equal to one in all simulations. "N/A" indicates "Not Applicable" and "NR" represents the non-reacting cases

Case	M_c	Q	Z_{st}	$\frac{L_x}{\delta_{\theta_0}} \times \frac{L_y}{\delta_{\theta_0}} \times \frac{L_z}{\delta_{\theta_0}}$	$N_x \times N_y \times N_z$	$\mathrm{Re}_{\lambda,\mathrm{final}}$	$\eta_{\min}/\Delta x$
M02NR	0.2	N/A	N/A	$300 \times 200 \times 100$	$1261 \times 841 \times 421$	230	0.772
M08NR	0.8	N/A	N/A	$250 \times 250 \times 100$	$1051 \times 1051 \times 421$	186	0.981
M12NR	1.2	N/A	N/A	$300 \times 250 \times 100$	$1261 \times 1051 \times 421$	195	1.112
M18NR	1.8	N/A	N/A	$300 \times 250 \times 100$	$1261 \times 1051 \times 421$	175	1.322
M02Q07Z05	0.2	0.7	0.5	$300 \times 210 \times 100$	$1261 \times 883 \times 421$	164	0.847
M02Q35Z05	0.2	3.5	0.5	$300 \times 210 \times 100$	$1261 \times 883 \times 421$	170	0.902
M02Q81Z05	0.2	8.1	0.5	$300 \times 210 \times 100$	$1261 \times 883 \times 421$	160	0.900

The conserved scalar is initialized with hyperbolic tangent profile. The mass fractions of the oxidizer and fuel in their corresponding streams, Y_O^0 and Y_F^0, are found from the equations of stoichiometric mixture fraction and normalized heat release variable for each case,

$$Z_{st} = \frac{Y_O^0}{sY_F^0 + Y_O^0} \tag{2}$$

and

$$Q = \frac{q_0 Y_F^0 Z_{st}}{C_{pN_2}^0 T_0 \nu_F \mathcal{W}_F}, \tag{3}$$

where $q_0 = \sum_\alpha \nu_\alpha \mathcal{W}_\alpha \Delta h_{f,\alpha}^0$ is the enthalpy of reaction [23], and ν_α and $\mathcal{W}_\alpha$ are the molar stoichiometric coefficient and the molecular weight of species α, respectively. The stoichiometric mixture fraction, Z_{st}, corresponds to the location at which the heat is released in the flame-sheet model [23]. To initiate turbulence, three dimensional perturbations are imposed on mean velocities. Velocity fluctuations are obtained using a digital-filter method [33]. This method generates fluctuations based on prescribed length scales and Reynolds stress tensor satisfying a locally given autocorrelation function.

Results from the DNS validations indicate that in all the simulations, flow reaches a universal self-similar state [34], in which the shear-layer growth rate approaches a constant value and the turbulent statistics show self-similarity. Present simulations have sufficient spatial resolution to capture the smallest scales in the flow and the domain size is large enough compared to the integral scales of the flow. Case $M02NR$ in Table 1 is the reference case which represents the lowest level of compressibility in our simulations and is an approximation to an incompressible non-reacting turbulent mixing layer. Figure 2 displays a sample flow visualization corresponding to case $M02Q81Z05$ at a time during the self-similar state. In this figure, the turbulent flow

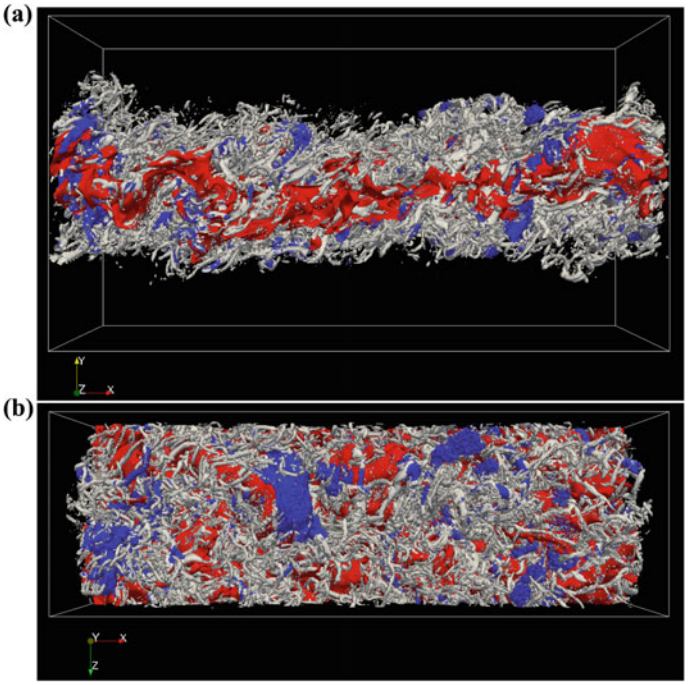

Fig. 2 Flow structures visualized by isosurfaces of discriminant of velocity-gradient tensor (gray), pressure (blue), and mixture fraction corresponding to flame (red) for case $M02Q81Z05$ at a time during the self-similar state. **a** side view, **b** top view

structures are visualized by the isosurfaces of discriminant of velocity-gradient tensor (gray) [6], pressure (blue), and mixture fraction corresponding to flame (red). The pressure isosurfaces represent some of the large flow structures, while the smaller structures are shown by the discriminant of velocity-gradient tensor isosurfaces. As Fig. 2 shows, the complex physics of the interaction between the flame and the structures of the turbulent flow, which is seen as stretching and wrinkling of the reaction zone due to turbulence in this figure, can be examined in detail in a three dimensional domain in our simulations. In the combustion model used in the present work, flame is a sheet with zero thickness. In other word, the heat release occur instantaneously as the reactants reach the stoichiometric ratio. Thus, the $Z = Z_{st}$ surface, which is depicted in Fig. 2 as the flame, is just for the purpose of visualization and an anecdotal observation of the location at which heat is released.

3 Turbulent/Non-turbulent Interface

In order to quantify the boundaries between the turbulent region and the irrotational region that encompasses it, several quantities including vorticity, velocity fluctuations, passive scalars, and the rate-of-strain have been used in the previous works [9, 13, 35–37]. The field of velocity derivatives is very sensitive to the non-Gaussian nature of turbulence or more generally to its structures, and hence reflects more of its physics [38]. On the other hand, it is sometimes preferred to use the mixture fraction (a conserved scalar) to differentiate between the turbulent and non-turbulent regions in situations at which three-dimensional velocity field can not be measured or in the flows of Schmidt number less than unity where the molecular diffusion of the conserved scalar is higher than the mixing due to turbulent motions. The comparison between the turbulent boundaries detected by the velocity-gradient field and the conserved-scalar-gradient field is examined previously for a variety of free-shear flow configurations [9–11, 39]. In these works, it is reported that for $\mathrm{Sc} \geq 1$ the two methods provide similar results. In order to compare the results of the current work with the results of previous works in our group [2–6, 19, 20], the vorticity magnitude, $\omega = \sqrt{\omega_i \omega_i}$, is used here to detect the turbulent/non-turbulent interface (TNTI). Since the Schmidt number is set to be equal to one in all the simulations, using mixture fraction to identify the TNTI only has a small quantitative effect on the results, while all the qualitative trends remain unchanged [19].

In order to examine the effect of the TNTI thresholds on the results of this work, the dependence of the volume fraction of the turbulent region on a given vorticity magnitude is depicted in Fig. 3 for all cases. This figure shows that the volume of the turbulent flow region, defined as the region where the vorticity magnitude is greater than a given threshold, exhibit a particular shape. As can be seen in Fig. 3, the volume fraction decreases with vorticity magnitude monotonically; however, there is a plateau of the volume fraction for a range of ω_{th} for all cases. For any threshold chosen from this plateau, a connected isosurface can be found that separates the turbulent and non-turbulent regions. Thus, any value of vorticity magnitude within the plateau region of Fig. 3 can, in principle, be used to detect the turbulent/non-turbulent interface. Similar to Taveira et al. [40], the thresholds used in the present work are chosen to be the inflection point on the plateau in Fig. 3. A detailed description of the physical and mathematical rationales for this choice of threshold is provided by da Silva et al. [41].

Figure 4 depicts the upper and lower TNTIs (contour colored surfaces) of the reference simulation of the current study ($M02NR$) at a time during the self-similar state and some of the turbulent flow structures (gray isosurfaces). The TNTIs are $\omega = \omega_{th}$ isosurfaces, and the turbulent structures are visualized by the isosurfaces of a constant value of discriminant of velocity-gradient tensor. As this figure shows, the TNTI is a highly protruded surface whose complexity can be traced back to the entire hierarchy of the scales from the smallest to the largest structures inside the turbulent region. The most prominent feature of the TNTIs in Fig. 4a, c is that the bulges and valleys of the upper and lower interfaces are similar in both streamwise

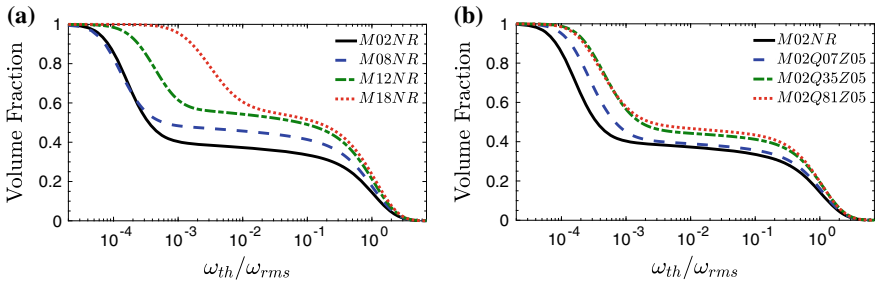

Fig. 3 The volume fraction of the turbulent region, identified as $\omega \geq \omega_{th}$, as a function of the vorticity magnitude threshold. Panel (**a**) presents the effect of convective Mach number, while panel (**b**) shows the effect of heat release

(x) and spanwise (z) directions. This observation is in accordance with the previous works on free-shear flow configurations [9, 42, 43], and is different from the TNTIs in wall-bounded flow configurations [36, 44, 45]. A detailed quantitative analysis of the effects of convective Mach number and heat release on the geometrical shape of the TNTI of the cases corresponding to the current study is presented in Chap. 3 of Jahanbakhshi [19].

Since its introduction by Bisset et al. [35], conditional sampling of statistics with respect to the distance from the TNTI are shown to be an effective tool to examine physics of entrainment and mixing in near TNTI regions, e.g. see review by Da Silva et al. [8]. A similar technique is adopted here, with one important modification to the original approach by Bisset et al. [35] in order to improve the quality of sampling; We define the distance from the interface, y_I, as the shortest distance in the direction normal to the TNTI, i.e. $y_I \parallel \hat{n}$ where $\hat{n} = \nabla\omega/|\nabla\omega|$ is the local unit vector normal to the TNTI in three-dimensional domain. Hereafter, the notation $\langle\bullet\rangle_I$ represents averages conditioned on the normal distances to the TNTI. Furthermore, the origin of the new coordinate system is placed on the TNTI, i.e. $y_I = 0$ is the location of the TNTI, $y_I > 0$ correspond to the turbulent region, and $y_I < 0$ are in the irrotational free-stream. Since the flow is homogeneous in spanwise (z) direction, the detection of the interface are done in x-y planes. In each plane, two interfaces are detected whose vorticity magnitudes are constant and equal to the predefined threshold—an interface between the turbulent region and the upper irrotational stream, and another interface separating the lower irrotational stream from the turbulent region. The shape of the interface can be quite complex, and as such, it is more common to use the interface envelope rather than the entire TNTI for calculating the conditional statistics. For each stream, the interface envelope is defined as the outermost point of the interface in the transverse direction. For a detailed description of the algorithm developed to sample the conditional statistics, the reader is referred to Chap. 3 of Jahanbakhshi [19]. It is observed that the results of the present work, conditioned on the distance from the TNTI, are similar for upper and lower TNTIs of the non-reacting simulations and the reacting cases in which the flame is in the middle of the mixing layer, i.e. $Z_{st} = 0.5$. Therefore, the reported plots and statistical values for these cases correspond to the average values of lower and upper TNTIs.

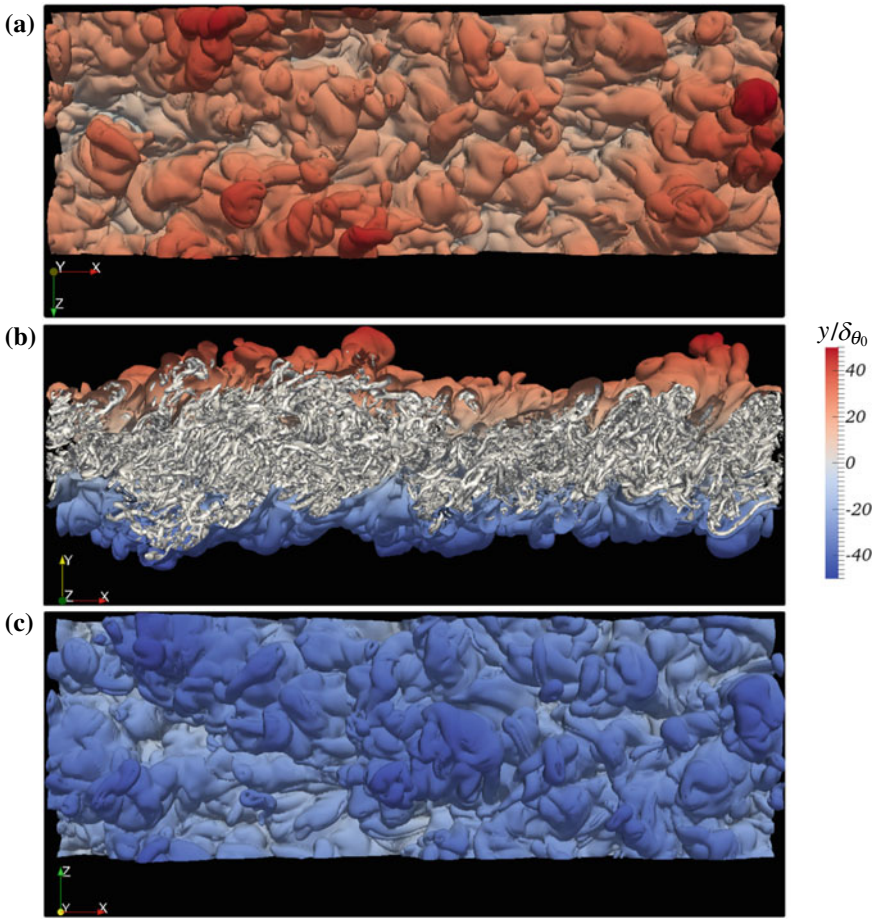

Fig. 4 The upper and lower TNTIs (contour colored surfaces) along with isosurfaces of a constant value of discriminant of velocity-gradient tensor (gray structures) for case $M02NR$ at a time during the self similar state: **a** top view, **b** side view, and **c** bottom view. The contour colors correspond to the local value of transverse location of the points on the TNTIs. δ_{θ_0} is the initial momentum thickness

4 Results and Discussions

In the current work, the mixing of the upper and lower streams, see schematic of Fig. 1, can be characterized using the mixture fraction quantity Z. Physically Z represents the local equivalence ratio of the mixture. Moreover, the scalar dissipation rate, which measures the molecular fluxes of the species towards the flame, is quantified as $\chi = 2D(\nabla Z \cdot \nabla Z)$ and the mixing layer thickness can be approximated as $\sqrt{D/\chi}$, where D is the mass diffusivity [22]. Therefore, the magnitude of the mixture fraction

gradient, $\sqrt{\nabla Z \cdot \nabla Z}$, is a good measure of the local degree of the mixing of the two streams. The square of this variable is used to quantify the mixing process in the rest of this work.

4.1 Evolution of Scalar-Gradient Magnitude Near the TNTI

Figure 5 depicts the conditional mean profiles of the magnitude of mixture fraction gradient squared, $\Psi = \nabla Z.\nabla Z$, in the coordinate system normal to the TNTI. As can be seen, the thickness of the region corresponding to sharp change of Ψ is characterized by the scalar-Taylor length scale defined as

$$\langle \lambda_Z \rangle_I = 2 \left(\frac{\left\langle Z''^2 \right\rangle_I}{\langle \nabla Z'' \cdot \nabla Z'' \rangle_I} \right)^{1/2}, \tag{4}$$

where $Z'' = Z - \langle \rho Z \rangle_I / \langle \rho \rangle_I$ is the fluctuation with respect to the density-weighted (Favre) average of the mixture fraction. The reference scalar-Taylor length scale, denoted by λ_Z hereafter, is chosen to be equal to the value of $\langle \lambda_Z \rangle_I$ at the inner edge of the corresponding interface layer. It is observed that λ_Z exhibits a good scaling for comparison of different cases in terms of providing Reynolds-number-independent results. Other possible choices, including velocity-Taylor and Kolmogorov scales, are also examined (not shown here).

For all the cases shown in Fig. 5, two distinct regions can be identified inside the turbulent region; (i) the scalar-interface-layer engulfing the TNTI, along which scalar-gradient magnitude changes with sharp increasing and decreasing slopes respectively, and (ii) the fully-turbulent region, in which $\langle \Psi \rangle_I$ increases at a much smaller rate. Figure 5 reveals that the thickness of the scalar-interface-layer, characterized by the sudden changes of scalar-gradient magnitude, is of the order of one scalar-Taylor length scale for all cases highlighting the good scalability of the scalar-mixing with

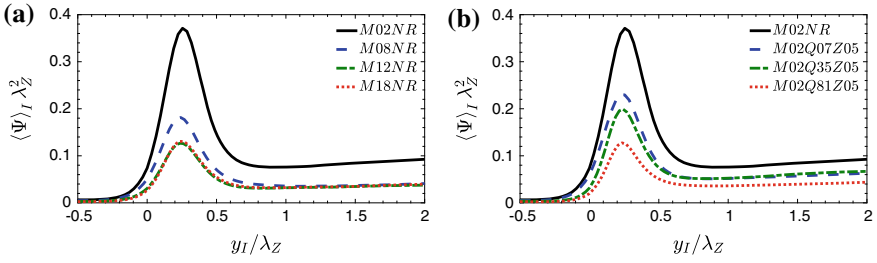

Fig. 5 Conditional averages of square of scalar-gradient magnitude, $\Psi = \nabla Z.\nabla Z$, in interface coordinate system. The effects of (**a**) convective Mach number and (**b**) heat release are investigated. Profiles are normalized with the reference scalar-Taylor length scale, λ_Z

this quantity. This thickness is approximately 70% of the thickness of velocity-interface-layer, which is commonly identified with a sharp jump of vorticity magnitude across the TNTI in the literature [2, 3] (not shown here). Furthermore, $\langle\Psi\rangle_I$ profiles show a distinct peak inside the scalar-interface-layer at around $y_I \approx 0.25\lambda_Z$ for all cases. The profile of case $M02NR$ is similar to previous observations in incompressible non-reacting shear flows with different Schmidt numbers [9, 11, 12, 14]. Figure 5a, b show that as the convective Mach number or the level of heat release increases, the conditional averages of square of scalar-gradient magnitude decreases. In other words, the degree of mixing of the lower and upper streams reduces with compressibility and heat release. In the next section, the effects of compressibility and heat release on the mixing is further investigated by examining the terms in the transport equation of scalar-gradient magnitude squared.

4.2 Budgets of Scalar-Gradient Magnitude Squared

The dynamics of scalar mixing of the two streams shown in Fig. 1 is studied by examining the budgets of the square of the mixture fraction gradient magnitude. By defining $\vec{G} = \nabla Z$ and $\Psi = \vec{G} \cdot \vec{G}$, taking the gradient of the mixture fraction equation (Eq. 1), and performing the dot product of the corresponding vector equation with the vector $\vec{G}$, the non-dimensional form of transport equation for Ψ in a variable density and viscosity flow is obtained as

$$\underbrace{\frac{D\Psi}{Dt}}_{\Psi_I} = \underbrace{-2\vec{G}\cdot\left[\vec{G}\cdot\nabla\vec{u}\right]}_{\Psi_{II}} + \underbrace{\frac{\nu}{\mathrm{Re\,Sc}}\nabla^2\Psi}_{\Psi_{III}} \underbrace{-\frac{2\nu}{\mathrm{Re\,Sc}}\nabla\vec{G}:\nabla\vec{G}}_{\Psi_{I\mathcal{V}}} \underbrace{-\frac{2\nu}{\rho\mathrm{Re\,Sc}}\vec{G}\cdot\left[\left(\nabla\cdot\vec{G}\right)\nabla\rho\right]}_{\Psi_{\mathcal{V}}}$$
$$+ \underbrace{\frac{1}{\rho\mathrm{Re\,Sc}}\left\{\nabla\Psi\cdot\nabla\mu + 2\vec{G}\cdot\left[\left(\nabla\cdot\vec{G} - \vec{G}\cdot\frac{\nabla\rho}{\rho}\right)\nabla\mu + \vec{G}\cdot\nabla\left(\nabla\mu\right)\right]\right\}}_{\Psi_{\mathcal{V}I}}. \tag{5}$$

In Eq. (5), the term on the left hand side is the total variation of the scalar-gradient magnitude squared at each point in the flow while moving with the fluid element. On the right hand side, term Ψ_{II} represents stretching/compression of the constant scalar-gradient lines which results in its increase/decrease, respectively. This term is usually referred to as turbulent production. Terms Ψ_{III} and $\Psi_{I\mathcal{V}}$ are the molecular diffusion and dissipation of the scalar-gradient magnitude squared, respectively. Term $\Psi_{\mathcal{V}}$ can be viewed as the change of $\vec{G}$ due to the variation of the molecular diffusion in a density-gradient field. In other words, as the local density changes, the effects of molecular diffusion becomes more or less intense. Term $\Psi_{\mathcal{V}I}$ represents the cumulative effects of viscosity variation on the change of scalar gradient.

Figures 6, 7 and 8 show the averages of the terms in Eq. (5) conditioned on the normal distance from the TNTI corresponding to all the cases of Table 1. The reference scalar-Taylor length scale as defined in Eq. (4), and the reference value of

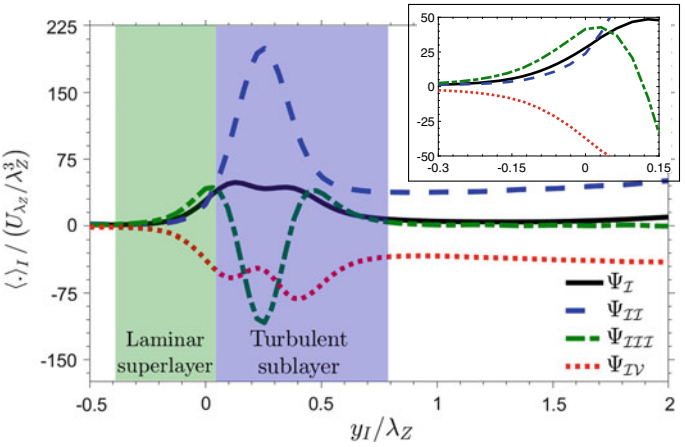

Fig. 6 Variation of the terms in Eq. (5) in interface coordinate system for case $M02NR$. Scalar-Taylor length scale, λ_Z, and scalar-Taylor velocity scale, U_{λ_Z}, are used to normalize the axes. The region very close to the TNTI is magnified in the zoomed figure

the scalar-Taylor velocity scale,

$$\langle U_{\lambda_Z}\rangle_I = \frac{2}{\langle\rho\rangle_I \,\mathrm{Re}} \left\langle \frac{\mu}{\mathrm{Sc}} \nabla Z'' \cdot \nabla Z'' \right\rangle_I \langle\lambda_Z\rangle_I \,, \tag{6}$$

are used to normalize the axes in these figures. Similar to λ_Z, the reference value U_{λ_Z} is considered to be equal to the value of $\langle U_{\lambda_Z}\rangle_I$ at the inner edge of the scalar-interface-layer. Figure 6 reveals that inside a statistically stationary fully-turbulent region, $y_I > 0.8\lambda_Z$, on the average the scalar mixing is basically controlled by the balance of the turbulent production term and the molecular dissipation term—a phenomenon that is also observed in the reacting and compressible cases. Along the scalar-interface-layer ($-0.3\lambda_Z < y_I < 0.8\lambda_Z$), however, terms Ψ_{II} and $\Psi_{I\mathcal{V}}$ are not balanced. Similar to the results of Fig. 5, the thickness of this layer is identified to be of the order of λ_Z in Fig. 6. Similar observations are reported by Watanabe et al. [11], Hunger et al. [10] and Silva and da Silva [9] for incompressible turbulent jets and mixing layers with Schmidt numbers ranging between 0.07 and 8. Inside the interface layer, depending on the level of compressibility and heat release, all the terms in Eq. (5) can have an appreciable contribution to the scalar mixing.

Figure 6 shows the budgets for the reference case ($M02NR$). Terms $\Psi_{\mathcal{V}}$ and $\Psi_{\mathcal{V}I}$ have a negligible contribution to the scalar transport in case $M02NR$, and are excluded from the results of Fig. 6. As can be seen, by moving from irrotational region towards fully-turbulent region, the molecular diffusion term Ψ_{III} dominates the transport process on the outer edge of the interface layer up to $y_I \approx 0.03\lambda_Z$. Whereas the turbulent production term Ψ_{II} contributes to most of the average positive rate of transport of Ψ deeper inside the interface layer and in the fully-turbulent region. The molecular dissipation term $\Psi_{I\mathcal{V}}$ is relatively large everywhere in the field. The

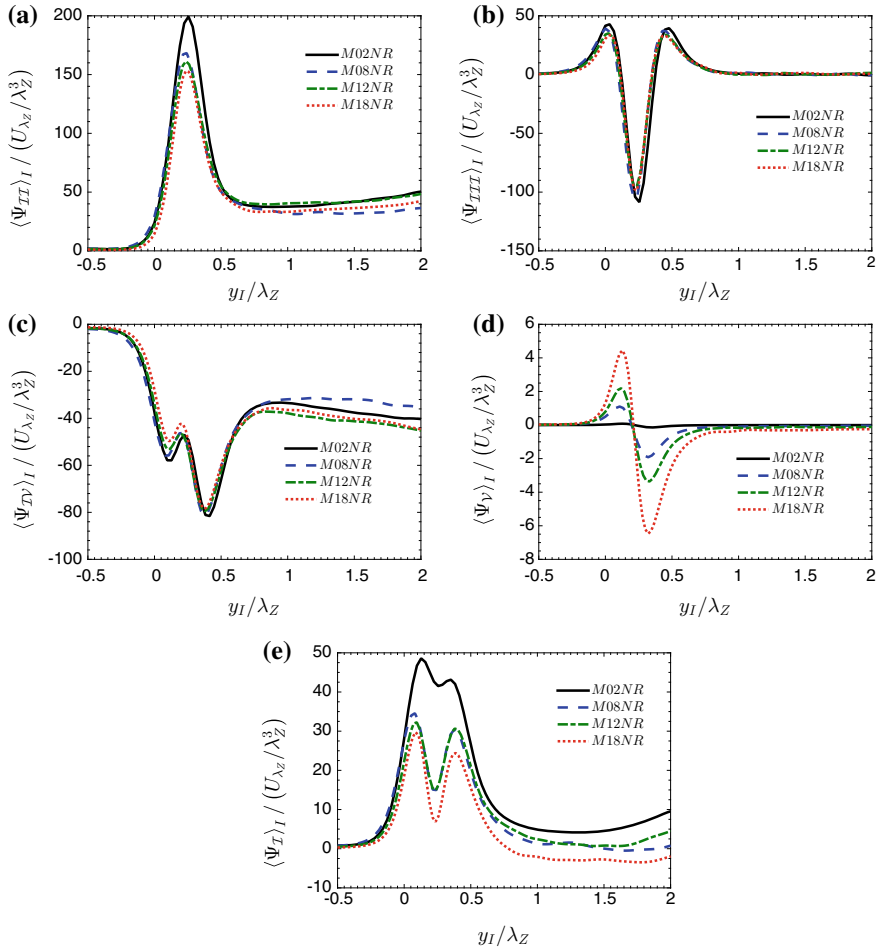

Fig. 7 The effect of convective Mach number (compressibility) on the budgets of scalar gradient squared in Eq. (5) in interface coordinate system. Scalar-Taylor length scale, λ_Z, and scalar-Taylor velocity scale, U_{λ_Z}, are used to normalize the axes

role of this term is to reduce (dissipate) positive rate of increase of scalar-gradient magnitude regardless of the source of this increase. It is also evident that the peak of $\langle\Psi\rangle_I$, observed in Fig. 5 at $y_I \approx 0.25\lambda_Z$, is caused by an intense stretching of constant scalar-gradient lines at this location. The results of Fig. 6 paint a picture of scalar transport across the TNTI that is similar to the enstrophy and momentum transport in mixing layers and jets [2, 4, 46, 47]. In these free shear flows transport mechanisms is initiated in a molecular-diffusion-dominated sub-region, commonly referred as the laminar superlayer (LSL) [1], sitting on the outer edge of the turbulent region. Along the laminar superlayer, the irrotational (potential) flow of the free-stream is seeded

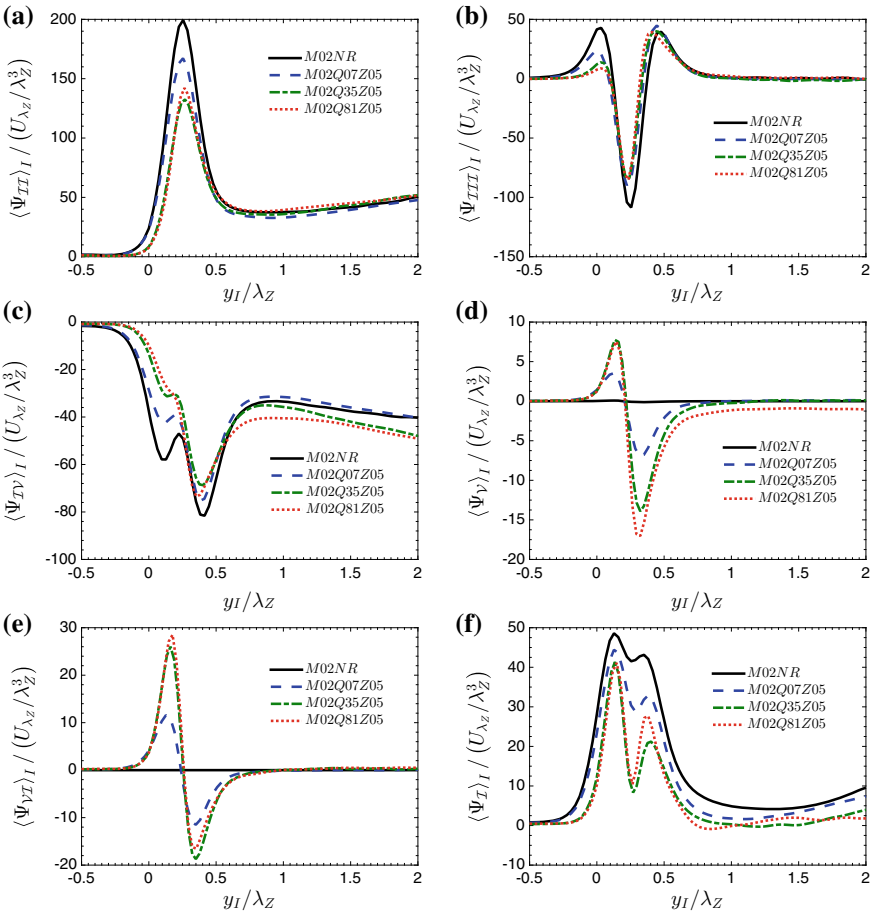

Fig. 8 The effect of heat release on the budgets of scalar gradient squared in Eq. (5) in interface coordinate system. The scalar-Taylor length scale, λ_Z, and scalar-Taylor velocity scale, U_{λ_Z}, are used to normalize the axes

with small-amplitude turbulent fluctuations by the molecular diffusion mechanism. It is well-established that an initially potential flow field seeded with small-amplitude disturbances exhibits, at least for a short time, an essentially positive mean turbulent production [38]. The fluctuations inside the LSL are subsequently amplified along an adjacent inertially-dominated sub-region, usually referred to as turbulent sublayer (TSL) [8], by the turbulent production mechanism. The approximate extents of the LSL and TSL for case $M02NR$ are marked in Fig. 6.

In the next two subsections, the effects of compressibility and heat release on the scalar mixing are examined by comparing the budgets of Eq. (5) corresponding to cases of the present study.

The Effects of Compressibility

The budgets of scalar-gradient transport in non-reacting cases are compared in Fig. 7 to highlight the effects of compressibility on them. Due to small variation of temperature in the non-reacting cases, the contribution of the viscosity variation term in Eq. (5), $\Psi_{\mathcal{V}\mathcal{I}}$, to the change of scalar gradient is negligible, and therefore, the profiles of this term are not included in Fig. 7. The overall contribution of terms $\Psi_{\mathcal{I}\mathcal{I}}$, $\Psi_{\mathcal{I}\mathcal{I}\mathcal{I}}$ and $\Psi_{\mathcal{I}\mathcal{V}}$ to the variation of scalar gradient in the high Mach number cases is similar to the nearly incompressible case. The main difference between the cases with different levels of compressibility is the amount by which the inertial term, $\Psi_{\mathcal{I}\mathcal{I}}$, contributes to the transport mechanism. From panels (*a*) to (*c*) of Fig. 7, it can be seen that as the convective Mach number increases the contribution of the stretching/compression of the constant scalar-gradient lines to the scalar mixing is subdued, while the molecular diffusion and dissipation are relatively unaffected by the compressibility. Therefore, while the diffusion of fluctuations into the free-stream along the laminar superlayer seems to remain unchanged, the amplification of these small-amplitude fluctuations by the turbulent production term inside the turbulent sublayer is weakened as a result of increasing the convective Mach number. Hence, the primary reason behind the attenuating effects of compressibility on the scalar mixing, observed in Figs. 5a and 7e, can be attributed to the "less-energetic" transport of the scalar by the advective turbulent motions inside the interface layer of high Mach number flows. Furthermore, Fig. 7d shows that as the level of compressibility increases the role of term $\Psi_{\mathcal{V}}$ in the scalar transport becomes more appreciable. The mechanism by which this term contributes to scalar mixing is similar to that of molecular diffusion term, i.e. seeding the potential flow with small amplitude fluctuations by transporting these fluctuations from the inner turbulent region to the LSL.

The Effects of Heat Release

In order to examine the effects of heat release on the scalar mixing, Fig. 8 compares the budgets of the terms in Eq. (5) for the reacting cases. Similar to the effect of compressibility, the results in panel *a* show a significant drop in the transport of scalar due to the inertial turbulent motions. However, unlike the effect of compressibility, panels *b* and *c* of Fig. 8 reveal an appreciable change in the molecular diffusion and dissipation terms. Most noticeably, these panels show that as the level of heat release increases the molecular-diffusion-dominated scalar transport sub-region close to the TNTI (LSL) seems to disappear. Therefore, the suppressed scalar mixing due to the effects of heat release, observed in Figs. 5b and 8f, can primarily be traced back to two sources; (i) The molecular diffusion process, whose primary role is to seed the free-stream potential flow with small-amplitude turbulent disturbances, becomes significantly weaker in the reacting cases—an issue that is clearly supported in Fig. 8b, c by the decline of the local maximum and minimum very close to the TNTI in the profiles of $\Psi_{\mathcal{I}\mathcal{I}\mathcal{I}}$ and $\Psi_{\mathcal{I}\mathcal{V}}$, respectively, and in Fig. 8a by the retardation in the location at which the profiles of $\Psi_{\mathcal{I}\mathcal{I}}$ start to rise in the reacting cases compared to the non-reacting reference case. (ii) The production term in Eq. (5), $\Psi_{\mathcal{I}\mathcal{I}}$, that is meant to amplify the small-amplitude perturbations to their fully-turbulent level,

is also suppressed as the level of heat release increases. Panels *d* and *e* of Fig. 8 suggest that as the level of heat release increases larger gradient of temperature and density across the interface layer is established which increases the contribution of terms $\Psi_{\mathcal{V}}$ and $\Psi_{\mathcal{V}I}$ to the scalar transport. These terms' role is mainly to seed the potential flow on the outer edge of interface layer with the turbulent fluctuations. The cumulative contribution of terms $\Psi_{\mathcal{V}}$ and $\Psi_{\mathcal{V}I}$ along the LSL seem to exceed that of the molecular diffusion term in the reacting case with the highest heat release level.

4.3 Heat Release Versus Compressibility Effects

In the previous section, the effects of compressibility and heat release on the average scalar transport are examined. It is shown that increasing the level of compressibility affects the turbulent sublayer portion of the interface layer by weakening the turbulent production along this region. On the other hand, increasing the level of heat release affects both the laminar superlayer and turbulent sublayer parts of the interface layer resulting in a subdued scalar mixing. In the present section, these effects are investigated from a local perspective by examining how the laminar superlayer and the turbulent sublayer change by increasing the levels of heat release or compressibility.

The Laminar Superlayer

Thus far, it is established that the primary difference between the mechanisms by which the compressibility and heat release suppress the scalar mixing, is their effects on the laminar superlayer located on the outer edge of the shear layer. In order to quantify this sub-region in reacting compressible flows, the correlation coefficient between terms $\Psi_{\mathcal{I}\mathcal{I}\mathcal{I}}$ and $\Psi_{\mathcal{I}\mathcal{V}}$ in Eq. (5) is shown to be a useful quantity [4]. The laminar superlayer is a region dominated by molecular diffusion of scalar, and thus the molecular dissipation which occurs in this region should predominantly be dissipating the diffused scalar gradient. Therefore, inside the laminar superlayer, the molecular diffusion term should have a high negative correlation with the molecular dissipation term.

Figure 9 shows the correlation coefficient between the molecular diffusion and the molecular dissipation terms in Eq. (5), $C\left(\Psi_{\mathcal{I}\mathcal{I}\mathcal{I}}, \Psi_{\mathcal{I}\mathcal{V}}\right)$, in interface coordinate system for all the cases. As can be seen in panel *a*, for the non-reacting cases except for a short length inside the interface layer, $\left|C\left(\Psi_{\mathcal{I}\mathcal{I}\mathcal{I}}, \Psi_{\mathcal{I}\mathcal{V}}\right)\right|$ is generally less than 0.5 everywhere in the flow field. The thin region engulfing the TNTI, along which the correlation coefficient between the molecular diffusion and the molecular dissipation terms is large, can be identified as the laminar superlayer. Figure 9a also shows that, for the chosen ω_{th}, the TNTI located at $y = 0$ is inside the LSL closer to the turbulent edge of this layer. This figure reveals that increasing the level of compressibility does not have a significant effect on the thickness of the region along which $\Psi_{\mathcal{I}\mathcal{I}\mathcal{I}}$ has a high inverse correlation with $\Psi_{\mathcal{I}\mathcal{V}}$. This is an indication that increasing M_c has a small effect on the thickness of the LSL in agreement with the observations in Fig. 7b, c. By defining the laminar superlayer as the region with $C\left(\Omega_{\mathcal{I}\mathcal{I}\mathcal{I}}, \Omega_{\mathcal{I}\mathcal{V}}\right) \leq -0.7$, the

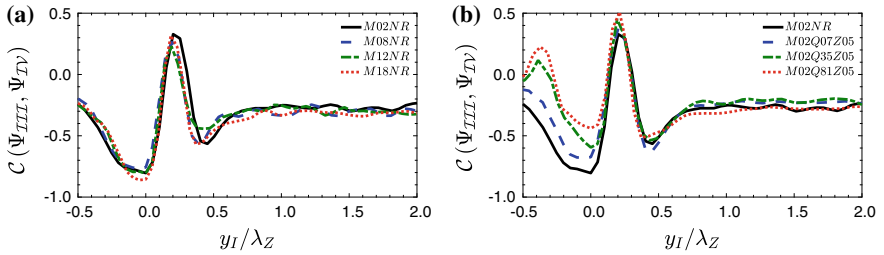

Fig. 9 The correlation coefficient between the molecular diffusion and molecular dissipation terms in Eq. (5), $C(\Psi_{II}, \Psi_{IV})$, in interface coordinate system: Effects of (*a*) compressibility and (*b*) heat release. Here λ_Z is the scalar-Taylor length scale

thickness of this layer is in the range $5\eta - 6\eta$ in non-reacting cases, where η is the Kolmogorov length scale at the inner edge of interface layer. It should be pointed out, since $\mathrm{Sc} = 1$ in our simulations, the Kolmogorov length scale is equal to the Batchelor scale. Figure 9b shows that as the level of heat release increases, the thickness of the region with large negative $C(\Omega_{II}, \Omega_{IV})$ decreases, which corresponds to a thinner laminar superlayer in reacting cases compared to the non-reacting ones. As can be seen in this figure, the values of $|C(\Psi_{II}, \Psi_{IV})|$ corresponding to the case with $Q = 8.1$ drop below 0.5 everywhere inside the flow field. Therefore, in accordance with the results of Fig. 8, Fig. 9b also provides evidence that as the level of heat release increases the molecular-diffusion-dominated scalar transport sub-region very close to the TNTI seems to diminish.

The Turbulent Sublayer

The primary feature of the turbulent sublayer is the dominant transport of scalar by the energetic inertial turbulent motions. This effect is quantified as the turbulent production term Ψ_{II} in Eq. (5). The velocity gradient dynamics holds the key to understanding of many turbulence phenomena, including the inertial transport of scalar. The production term in Eq. (5) can be rewritten as

$$\Psi_{II} = -2\vec{G} \cdot \left[\vec{G} \cdot \nabla\vec{u}\right] = -2\Psi\left[\alpha_1 \cos^2(\xi_1) + \alpha_2 \cos^2(\xi_2) + \alpha_3 \cos^2(\xi_3)\right], \quad (7)$$

where, $\alpha_1 > \alpha_2 > \alpha_3$ are the eigenvalues of the strain-rate tensor, i.e. $S = \frac{1}{2}[\nabla\vec{u} + (\nabla\vec{u})^{tr}]$, and ξ_1 to ξ_3 are the angles between the corresponding eigenvectors (principle directions) and the mixture fraction gradient vector. Therefore, the magnitude and the sign of the strain-rate eigenvalues determines the nature of the self-straining of the velocity gradients, and the orientation between the principle directions of S and the vector $\vec{G}$ governs the degree of the scalar-gradient magnification and ultimately the efficiency of mixing [48].

Figure 10 depicts the probability density function (PDF) of the normalized eigenvalues of S, panels *a* to *c*, and the angles between the corresponding eigenvectors and the vector $\vec{G}$, panels *d* to *f*, at a location near the TNTI inside the turbulent sublayer.

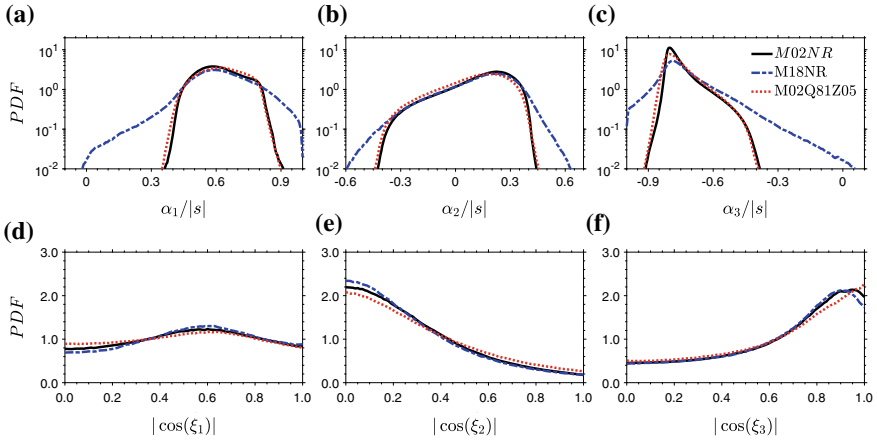

Fig. 10 The probability density functions of, $(a-c)$ the normalized eigenvalues of the strain-rate tensor and $(d-f)$ the orientation between the principle directions and the scalar-gradient vector. The results are computed at $y_I \approx 0.4\lambda_Z$ and $|s| = \sqrt{\alpha_1^2 + \alpha_2^2 + \alpha_3^2}$ is the magnitude of the strain-rate tensor

The results are shown for only three extreme cases of the present study. This figure reveals that for all cases the scalar-gradient increase due to the turbulent production (positive Ψ_{II}) is primarily caused by α_3 and ξ_3. Whereas α_1 and ξ_1 predominately result in a negative Ψ_{II}, i.e. the scalar mixing process is mostly suppressed by the first eigenvalue and principle direction. Since $\cos(\xi_2)$ is most probably zero and $|\alpha_2|$ is smaller than $|\alpha_1|$ and $|\alpha_3|$, the contribution of the term containing the second eigenvalue and eigenvector in Eq. (7) to turbulent production, and consequently scalar mixing, is relatively small. Comparing the PDFs of cases $M02Q81Z05$ and $M02NR$ in Fig. 10 indicates that heat release minimally affects the magnitude of the eigenvalues and the orientation of the principle directions of the strain-rate tensor. However, PDFs of case $M18NR$ show an appreciable change in the magnitudes of the eigenvalues as a result of increasing the convective Mach number.

The results of Figs. 9 and 10 reveal a clear distinction between the mechanisms by which the turbulent production is suppressed inside the turbulent sublayer due to the effects of heat release and compressibility. As the convective Mach number is increased, the turbulent production along the turbulent sublayer seems to be weakened by a change in the magnitude of the eigenvalues of the strain-rate tensor. In other words, compressibility seems to affect the flow by changing some of the inherent dynamics of the turbulent region characterized by local streamline topology and vortical structure [6, 49–51]. The effects of the heat release, on the other hand, are mostly felt in the laminar superlayer where the molecular diffusion process is significantly inhibited as a result of increasing the level of heat release. Thus, the change in the thermochemical properties of the mixture due to temperature-rise associated with the chemical reaction plays a key role in how heat release affects the mixing process.

5 Summary and Conclusions

Direct numerical simulations of temporally evolving turbulent mixing layers are performed to examine the mixing of a conserved-scalar across the turbulent/non-turbulent interface (TNTI). In order to study the effects of compressibility and heat release on turbulence several cases with different convective Mach numbers and heat release levels are chosen for the simulations. The chosen values for convective Mach number cover a wide range of compressibility levels from subsonic and nearly incompressible to supersonic and highly compressible flows. Moreover, several heat release levels are opted for the reacting cases with the highest level of heat release corresponding to hydrogen combustion in air. Infinitely fast chemistry approximation is used to model a one-step irreversible global reaction that involves fuel (hydrogen), oxidizer (oxygen), and product (water). The Schmidt number (Sc) in this study is chosen to be unity.

The mixing process is quantified using the magnitude of a conserved-scalar gradient vector, and the underlying mechanisms are examined using the transport equation of the norm of scalar gradient squared. It is shown that the effects of compressibility and heat release on the mixing are primarily felt in a thin interface layer engulfing the boundaries of the turbulent region. The results support a view of scalar transport that is dynamically similar to the momentum transport in similar flow configurations; The potential flow is first seeded with small-amplitude fluctuations in a molecular-diffusion-dominated sub-region (laminar superlayer) sitting on the outer edge of the turbulent region. These fluctuations are then amplified quickly along an adjacent layer (turbulent sublayer) in which the turbulent production (inertial turbulent motions) dominates the flow dynamics. It is also observed that as the level of compressibility or heat release increases the rate of scalar mixing decreases. Compressibility affects the mixing process by a subdued turbulent production in the turbulent sublayer—an effect that seems to be caused by a change in the magnitude of eigenvalues of the strain-rate tensor. On the other hand, it is argued that as the level of heat release is increased, the molecular diffusion inside the laminar superlayer and the turbulent production along the turbulent sublayer are weakened together to produce the aforementioned effect. It is shown that the heat release mostly affects the dynamics of laminar superlayer by shrinking its thickness, while the eigenvalues and principle directions of strain-rate tensor along the turbulent sublayer of the reacting cases remains dynamically unchanged.

Acknowledgements This work was supported by the National Center for Hypersonic Combined Cycle Propulsion sponsored by AFOSR and NASA under Grant FA-9550-09-1-0611, and by the donors of the Petroleum Research Fund administrated by the American Chemical Society (ACS) under Grant 51834-ND9. Computational resources were provided by the Center for Computational Research (CCR) at the State University of New York at Buffalo.

References

1. S. Corrsin, A. Kistler, Free-stream boundaries of turbulent flows, Tech. Rep. TN-1244 (NACA, Washington, DC, 1955)
2. R. Jahanbakhshi, C.K. Madnia, Entrainment in a compressible turbulent shear layer. J. Fluid Mech. **797**, 564–603 (2016)
3. R. Jahanbakhshi, C.K. Madnia, The effect of heat release on the entrainment in a turbulent mixing layer. J. Fluid Mech. **844**, 92–126 (2018)
4. R. Jahanbakhshi, C.K. Madnia, Viscous superlayer in a reacting compressible turbulent mixing layer. J. Fluid Mech. **848**, 743–755 (2018)
5. R. Jahanbakhshi, N.S. Vaghefi, C.K. Madnia, Baroclinic vorticity generation near the turbulent/non-turbulent interface in a compressible shear layer. Phys. Fluids **27**(10), 105105 (2015)
6. N.S. Vaghefi, C.K. Madnia, Local flow topology and velocity gradient invariants in compressible turbulent mixing layer. J. Fluid Mech. **774**, 67–94 (2015)
7. P.E. Dimotakis, Turbulent mixing. Annu. Rev. Fluid Mech. **37**, 329–356 (2005)
8. C.B. da Silva, J.C.R. Hunt, I. Eames, J. Westerweel, Interfacial layers between regions of different turbulence intensity. Annu. Rev. Fluid Mech. **46**, 567–590 (2014)
9. T.S. Silva, C.B. da Silva, The behaviour of the scalar gradient across the turbulent/non-turbulent interface in jets. Phys. Fluids **29**(8), 085106 (2017)
10. F. Hunger, M. Gauding, C. Hasse, On the impact of the turbulent/non-turbulent interface on differential diffusion in a turbulent jet flow. J. Fluid Mech. **802**, R5 (2016)
11. T. Watanabe, Y. Sakai, K. Nagata, Y. Ito, T. Hayase, Turbulent mixing of passive scalar near turbulent and non-turbulent interface in mixing layers. Phys. Fluids **27**(8), 085109 (2015)
12. A. Attili, J.C. Cristancho, F. Bisetti, Statistics of the turbulent/non-turbulent interface in a spatially developing mixing layer. J. Turbul. **15**(9), 555–568 (2014)
13. J. Westerweel, C. Fukushima, J.M. Pedersen, J.C.R. Hunt, Momentum and scalar transport at the turbulent/non-turbulent interface of a jet. J. Fluid Mech. **631**, 199–230 (2009)
14. T. Watanabe, Y. Sakai, K. Nagata, Y. Ito, T. Hayase, Enstrophy and passive scalar transport near the turbulent/non-turbulent interface in a turbulent planar jet flow. Phys. Fluids **26**(10), 105103 (2014)
15. M. Gampert, K. Kleinheinz, N. Peters, H. Pitsch, Experimental and numerical study of the scalar turbulent/non-turbulent interface layer in a jet flow. Flow Turbul. Combust. **92**(1–2), 429–449 (2014)
16. M. Gampert, V. Narayanaswamy, P. Schaefer, N. Peters, Conditional statistics of the turbulent/non-turbulent interface in a jet flow. J. Fluid Mech. **731**, 615–638 (2013)
17. T. Watanabe, Y. Sakai, K. Nagata, Y. Ito, T. Hayase, Reactive scalar field near the turbulent/non-turbulent interface in a planar jet with a second-order chemical reaction. Phys. Fluids **26**(10), 105111 (2014)
18. X. Zhang, T. Watanabe, K. Nagata, Passive scalar mixing near turbulent/non-turbulent interface in compressible turbulent boundary layers. Phys. Scripta. **94**, 044002 (2019)
19. R. Jahanbakhshi, *DNS of Compressible Reacting Turbulent Shear Layer*. Ph.D. thesis (State University of New York at Buffalo, 2016)
20. N. S. Vaghefi, *Simulation and modeling of compressible turbulent mixing layer*. Ph.D. thesis (State University of New York at Buffalo, 2014)
21. N.S. Vaghefi, M.B. Nik, P.H. Pisciuneri, C.K. Madnia, A priori assessment of the subgrid scale viscous/scalar dissipation closures in compressible turbulence. J. Turbul. **14**(9), 43–61 (2013)
22. T. Poinsot, D. Veynante, *Theoretical and Numerical Combustion* (RT Edwards, Inc., 2005)
23. F.A. Williams, *Combustion Theory* (Benjamin-Cummings, San Francisco, 1985)
24. A. Ern, V. Giovangigli, *Multicomponent Transport Algorithms*, vol. 24 (Springer Science & Business Media, Berlin, 1994)
25. K.K. Kuo, *Principles of Combustion* (Wiley, Hoboken, 2005)
26. W.M. Haynes, *CRC Handbook of Chemistry and Physics* (CRC Press, Boca Raton, 2014)

27. W. Sutherland, LII. The viscosity of gases and molecular force. Lond. Edinb. Dubl. Phil. Mag. **36**(223), 507–531 (1893)
28. D. Bogdanoff, Compressibility effects in turbulent shear layers. AIAA J. **21**(6), 926–927 (1983)
29. K.W. Thompson, Time-dependent boundary conditions for hyperbolic systems, II. J. Comput. Phys. **89**(2), 439–461 (1990)
30. D. Gottlieb, E. Turkel, Dissipative two-four methods for time-dependent problems. Math. Comput. **30**(136), 703–723 (1976)
31. R.W. MacCormack, Numerical solution of the interaction of a shock wave with a laminar boundary layer, in *Lecture Notes in Physics*, vol. 8, (Springer, Berlin, 1971), pp. 151–163
32. S.A. Ragab, J.L. Wu, Linear instabilities in two-dimensional compressible mixing layers. Phys. Fluids A-Fluid **1**(6), 957–966 (1989)
33. M. Klein, A. Sadiki, J. Janicka, A digital filter based generation of inflow data for spatially developing direct numerical or large eddy simulations. J. Comput. Phys. **186**(2), 652–665 (2003)
34. J.A. Redford, I.P. Castro, G.N. Coleman, On the universality of turbulent axisymmetric wakes. J. Fluid Mech. **710**, 419–452 (2012)
35. D.K. Bisset, J.C.R. Hunt, M.M. Rogers, The turbulent/non-turbulent interface bounding a far wake. J. Fluid Mech. **451**, 383–410 (2002)
36. K. Chauhan, J. Philip, C.M. de Silva, N. Hutchins, I. Marusic, The turbulent/non-turbulent interface and entrainment in a boundary layer. J. Fluid Mech. **742**, 119–151 (2014)
37. G. Borrell, J. Jiménez, Properties of the turbulent/non-turbulent interface in boundary layers. J. Fluid Mech. **801**, 554–596 (2016)
38. A. Tsinober, Vortex stretching versus production of strain/dissipation, in *Turbulence Structure and Vortex Dynamics*, pp. 164–191 (2000)
39. M. Gampert, J. Boschung, F. Hennig, M. Gauding, N. Peters, The vorticity versus the scalar criterion for the detection of the turbulent/non-turbulent interface. J. Fluid Mech. **750**, 578–596 (2014)
40. R.R. Taveira, J.S. Diogo, D.C. Lopes, C.B. da Silva, Lagrangian statistics across the turbulent/non-turbulent interface in a turbulent plane jet. Phys. Rev. E **88**(4), 043001 (2013)
41. C.B. da Silva, R.R. Taveira, G. Borrell, Characteristics of the turbulent/non-turbulent interface in boundary layers, jets and shear-free turbulence, in *Journal of Physics: Conference Series*, vol. 506 (IOP Publishing, 2014), p. 012015
42. R. Nagata, T. Watanabe, K. Nagata, Turbulent/non-turbulent interfaces in temporally evolving compressible planar jets. Phys. Fluids **30**(10), 105109 (2018)
43. R.R. Taveira, C.B. da Silva, Kinetic energy budgets near the turbulent/non-turbulent interface in jets. Phys. Fluids **25**(1), 015114 (2013)
44. J. Lee, H.J. Sung, T.A. Zaki, Signature of large-scale motions on turbulent/non-turbulent interface in boundary layers. J. Fluid Mech. **819**, 165–187 (2017)
45. X. Wu, J.M. Wallace, J.-P. Hickey, Boundary layer turbulence and freestream turbulence interface, turbulent spot and freestream turbulence interface, laminar boundary layer and freestream turbulence interface. Phys. Fluids **31**(4), 045104 (2019)
46. R.R. Taveira, C.B. da Silva, Characteristics of the viscous superlayer in shear free turbulence and in planar turbulent jets. Phys. Fluids **26**(2), 021702 (2014)
47. M. van Reeuwijk, M. Holzner, The turbulence boundary of a temporal jet. J. Fluid Mech. **739**, 254–275 (2014)
48. R.K. Bikkani, S.S. Girimaji, Role of pressure in nonlinear velocity gradient dynamics in turbulence. Phys. Rev. E **75**(3), 036307 (2007)
49. S. Arun, A. Sameen, B. Srinivasan, S. Girimaji, Topology-based characterization of compressibility effects in mixing layers. J. Fluid Mech. **874**, 38–75 (2019)
50. S. Suman, S.S. Girimaji, Velocity gradient invariants and local flow-field topology in compressible turbulence. J. Turbul. **11**(2), 1–24 (2010)
51. J. Wang, Y. Shi, L.P. Wang, Z. Xiao, X.T. He, S. Chen, Effect of compressibility on the small-scale structures in isotropic turbulence. J. Fluid Mech. **713**, 588–631 (2012)

Linear Instability of Stably Stratified Down-Slope Flows

Inanc Senocak and Cheng-Nian Xiao

Abstract Fluid instabilities in the Prandtl model for down-slope flows are studied using linear modal analysis as well as direct numerical simulations. Given Prandtl's analytical solution for uniformly cooled down-slope flows, we determine the point of instability initiation and the corresponding unstable flow modes. We show that down-slope flows are susceptible to transverse and longitudinal instability modes. The transverse mode consists of stationary longitudinal rolls whose axes are aligned parallel to the base flow direction, whereas the longitudinal mode emerges as transverse waves travelling along the streamwise direction. The emergence of these instabilities are controlled by the Prandtl number, the slope angle, and the stratification perturbation parameter, which is a measure of the strength of the surface buoyancy flux relative to the background stratification. When the other two dimensionless parameters are held constant, the stratification perturbation parameters determines whether the imposed surface buoyancy flux can overcome the stabilizing effect of the background stratification and give rise to dynamically unstable flow. Beyond the linear stability thresholds, these two type of instabilities coexist to form complex flow structures. The absence of strong non-normality of the operator is shown by calculating the pseudospectra for both types of instabilities.

Keywords Stable stratification · Flow instability · Prandtl slope flows · Katabatic winds · Linear modal analysis · Direct numerical simulation

1 Introduction

Katabatic winds, also referred to as drainage winds or slope flows, are gravity-driven winds that arise due to the horizontal temperature differences between the surface

I. Senocak (✉) · C.-N. Xiao
Department of Mechanical Engineering and Materials Science, University of Pittsburgh, Pittsburgh, PA 15261, USA
e-mail: senocak@pitt.edu

C.-N. Xiao
e-mail: chx33@pitt.edu

D. Livescu et al. (eds.), *Modeling and Simulation of Turbulent Mixing and Reaction*, Heat and Mass Transfer, https://doi.org/10.1007/978-981-15-2643-5_3

and the air adjacent to it [1, 2]. Slope flows can even be prevalent over terrains that seemingly look flat to the eye (e.g. nocturnal low-level jets over the Great Plains of the United States [3]). Katabatic winds are persistent over Greenland and play an important role in ablation of the ice sheet because turbulent fluxes of sensible heat appear in the energy budget [4]. Likewise, katabatic winds over Antarctica cover a large portion of the continent to the extent that they contribute significantly to the atmospheric circulation in high southern latitude, more specifically, to the development of the circumpolar vortex [5]. Parish and Bromwich [5] have suggested that global circulation models may benefit from a representation of the katabatic wind regime that is effective in close proximity of the surface.

Air quality in urban areas near mountainous terrain (e.g. Salt Lake City) are closely coupled to dynamics of slope flows. Pollutants can accumulate in valleys and foothills under strongly stratified conditions leading to inversion episodes [6]. Very-stable conditions during night time are known to exacerbate air pollution problems [7]. Prediction of nocturnal winds in mountainous terrain is also important for agriculture, aviation, wind energy harvesting, and various military operations. Despite the important implications of stable conditions in the atmosphere, its representation in numerical weather models has been a technical challenge for a long while. Ad-hoc remedies to improve its representation are known to erode the representation of other processes [8, 9].

Stable atmospheric boundary layer (SABL) is typically categorized as weakly-stable (WSABL) and very-stable (VSABL) regimes, but the classification lacks a quantitative criterion. This classification was originally introduced by Mahrt [8] to highlight the challenges in the very-stable regime. It is generally accepted that we have a reasonable representation of weakly stable boundary layer over flat, homogeneous terrain through the Monin-Obukhov similarity theory (MOST) [10] and the local scaling theory of Nieuwstadt [11]. However, a comprehensive understanding of atmospheric boundary layer for very-stable stratification and over non-flat terrain is still lacking [12, 13], which has been attributed to the intermittency of turbulence and mixing processes under very-stable conditions. The emergence and collapse of turbulence in periods of bursts has puzzled researchers and such events complicate the parameterization of surface fluxes of mass, momentum and energy. Several processes within an SABL interact nonlinearly to create the complex flow structure that is difficult to study by measurements alone. Extreme environments of polar regions also present major hurdles for field experiments. Hence, theoretical and numerical investigations that isolate the key processes are needed to elucidate the physics of SABL and katabatic winds.

Prandtl [14] was the first person to adopt a quantitative approach to explain the winds in mountains and valleys. He dedicated the last three pages of his famous book titled “Essentials of Fluid Dynamics” to the subject [15, p. 422]. By assuming that the one-dimensional flow is maintained solely by a balance between buoyancy and longitudinal shear forces, he was able to derive an analytic solution to explain mountain winds and valley flows. He considered a viscous stably-stratified ambient fluid layer over an infinitely-long and uniformly-cooled (or heated) planar surface with a constant slope to it. The buoyancy and velocity profile predicted by Prandtl’s

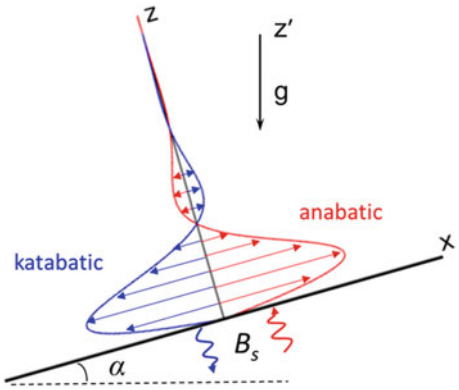

Fig. 1 Sketch of the Prandtl model for slope flow for katabatic and anabatic conditions and the rotated coordinate system. Profiles are drawn not to scale

laminar flow solution is a sinusoid exponentially damped with growing height [16]. The velocity profile produced by low-level jet along the slope descent that is capped by a weak reverse flow is depicted in Fig. 1. For laminar linearly stable conditions, the along-slope velocity profile (i.e. only the profiles only differ by sign) is symmetric about the slope normal direction for katabatic and anabatic conditions.

Fedorovich and Shapiro [16] conducted a direct numerical simulation of the turbulent analog of Prandtl model for anabatic and katabatic conditions. They proposed a dimensionless flow forcing parameter as a dynamic similarity constraint, which is a measure of the energy production at the surface and work against buoyancy and viscous forces. Mean profiles of katabatic flows were found to be structurally more similar to the laminar Prandtl model than the mean profiles of anabatic flows. Unlike flat terrains where a constancy of the turbulent fluxes led to the development of similarity theory, Fedorovich and Shapiro found no evidence of constancy of fluxes in slope flows, which casts doubt on the applicability of MOST based surface parameterizations for non-flat terrain. However, the issue of to what extent MOST is inapplicable to slope flows as a function of the slope angle and stratification remains unresolved. Giometto et al. [17] complemented the work of Fedorovich and Shapiro by conducting DNS of slope flows for prescribed surface buoyancy as opposed to the prescribed buoyancy flux used in Fedorovich and Shapiro. Giometto et al. performed a detailed budget analysis for turbulent kinetic energy (TKE) and fluxes, and they too did not observe a constant flux layer.

Several numerical and experimental studies on instabilities in stably-stratified flows have appeared in recent literature. Unlike classical works where direction of shear and stratification were the same, the distinguishing aspect of these recent efforts is that shear and stratification are not aligned in the same direction. Facchini et al. [18] carried out linear stability analysis for Couette flow with cross-flow stable stratification and verified the results with both experiments and DNS, whereas Chen et al. [19] investigated stably-stratified horizontal boundary layer on a vertical wall. In both of those configurations, the stratification was directed orthogonal to both the parallel base flow and main shear. In the case studied by [20], the direction of strat-

ification was orthogonal to the base flow but oblique to the plane of shear; inviscid instabilities generated by a Bickley jet ejected onto a sloping surface was identified via linear stability analysis. Prandtl model is distinct from the aforementioned works on instability of stratified flows because the direction of stratification forms an acute angle with both the base flow as well as the direction of shear due to the surface inclination. In this chapter, we will analyze the stability behaviour of this flow configuration, which has hitherto received little attention.

2 Governing Equations

Prandtl's model for incompressible flows over an infinite, uniformly cooled slope is displayed in Fig. 1, where α is the constant inclination angle with respect to the horizontal and gravity acts in the vertical direction. B_S is the constant surface heat flux, which is negative for katabatic slope flows. To facilitate analysis, the equations for the configuration are written in a Cartesian coordinate system rotated by α whose x axis is aligned with the slope surface. Under this coordinate system, u, v, w denote the along-slope (longitudinal), the cross-slope (transverse), and the slope-normal velocity components, respectively. Thus the notation $u_i = [u, v, w]$ represents the velocity vector. The gravity components in the rotated coordinate system are then given via $g_i = [g_1, g_2, g_3] = [\sin\alpha, 0, \cos\alpha]$. The Brunt-Väisälä frequency and buoyancy are denoted by N, b, respectively, and N^2 can be regarded as a measure of the stable background stratification. Following [16], the momentum and the buoyancy balance equations under the Boussinesq approximation are given as follows:

$$\frac{\partial u_i}{\partial t} + \frac{\partial u_i u_j}{\partial x_j} = -\frac{1}{\rho}\frac{\partial p}{\partial x_i} + \frac{\partial}{\partial x_j}\left(\nu \frac{\partial u_i}{\partial x_j}\right) + b g_i, \tag{1}$$

$$\frac{\partial b}{\partial t} + \frac{\partial b u_j}{\partial x_j} = \frac{\partial}{\partial x_j}\left(\beta \frac{\partial b}{\partial x_j}\right) - N^2 g_j u_j, \tag{2}$$

where ν is the kinematic viscosity and β represents the thermal diffusivity of the fluid. Mass conservation is ensured via the continuity equation

$$\frac{\partial u_i}{\partial x_i} = 0. \tag{3}$$

In the subsequent parts, we will also denote the position and velocity vectors x_i, u_i as $[x, y, z]^T$ and $[u, v, w]^T$, respectively. x, y and u, v represent the horizontal along-slope and cross-slope components and z, w represent the component vertical to the slope surface.

Equation (2) for buoyancy can be derived from the first law of thermodynamics, as described in Ref. [21]. Let θ be the potential temperature. Then according to the first law of thermodynamics, the energy balance written in an unrotated coordinate

system with components x_i', u_i' gives:

$$\frac{\partial \ln\theta}{\partial t} + \frac{\partial(\ln\theta\ u_j')}{\partial x_j'} = \frac{Q}{c_p T}, \tag{4}$$

where Q is the total amount of added heat and c_p is the heat capacity at constant pressure. Assuming that the potential temperature can be decomposed as the sum of a horizontally uniform background environment temperature θ_0 and a much smaller perturbation term, i.e. $\theta \approx \theta_0 + \theta'$ with $\theta' \ll \theta_0$, and that the only significant heat transfer mechanism is thermal conduction, Eq. (2) readily follows from a first order approximation of Eq. (4), invoking the relationship $b = g\frac{\theta'}{\theta_r}$ between buoyancy b and potential temperature perturbation θ', where θ_r is the reference potential temperature. The Brunt-Väisälä frequency N is related to the vertical gradient, the only non-negligible gradient component, of the background environmental potential temperature via the following definition

$$N = \sqrt{\frac{g}{\theta_r}\frac{\partial\theta_0}{\partial z'}}, \tag{5}$$

On the slope surface, i.e. $z = 0$, a negative buoyancy flux B_s is imposed to drive the downslope flow.

2.1 Prandtl Model for Slope Flows

Under Prandtl's model where flow is assumed to be laminar, the slope is infinite and B_S is constant as well as uniform, the momentum Eq. (1) simplifies to a balance between buoyancy force and along-slope inertial momentum; and the energy equation given by Eq. (2) expresses a balance between along-slope momentum and buoyancy diffusion. With these assumptions Eqs. (1) and (2) reduce to the following forms:

$$b\sin\alpha + \nu\frac{\partial^2 u}{\partial z^2} = 0, \tag{6}$$

$$-N^2 u\sin\alpha + \beta\frac{\partial^2 b}{\partial z^2} = 0. \tag{7}$$

These two equations above can be used to derive an exact solution to the idealized slope flow. For a constant uniform buoyancy flux at the surface and for any Prandtl number, the following one-dimensional exact solution is given in Shapiro and Fedorovich [22]:

$$u_n = \sqrt{2}\sin(z_n/\sqrt{2})\exp(-z_n/\sqrt{2}), \tag{8}$$

$$b_n = \sqrt{2}\cos(z_n/\sqrt{2})\exp(-z_n/\sqrt{2}), \tag{9}$$

where $z_n = z/l_0$, $u_n = u/u_0$, $b_n = b/b_0$ are nondimensional height, velocity, and buoyancy, respectively, and the corresponding scales governing the flow problem are given as [16]

$$l_0 = (\nu\beta)^{1/4} N^{-1/2} \sin^{-1/2}\alpha, \tag{10}$$

$$u_0 = (\nu\beta)^{-1/4} N^{-3/2} B_s \sin^{-1/2}\alpha, \tag{11}$$

$$b_0 = \nu^{1/4}\beta^{-3/4} N^{-1/2} B_s \sin^{-1/2}\alpha, \tag{12}$$

where $\mathrm{Pr} \equiv \nu/\beta$ denotes the Prandtl number. From the above scales, a characteristic time $t_0 = l_0/|u_0|$ and frequency $\omega_0 = t_0^{-1}$ can also be derived. Note that when the imposed surface boundary condition is constant buoyancy rather than buoyancy flux, the above flow scales will look quite differently.

2.2 Dimensionless Numbers

Dimensionless parameters are extremely useful to interpret data whether it has been collected numerically or experimentally. Richardson number (Ri), a measure of the relative importance of buoyancy to shear in the flow, dominates the analyses of SABL. However, it has been recognized that the set of dimensionless numbers governing the SABL is incomplete [12]. The slope flow depicted in Fig. 1 is dependent on the slope angle α, kinematic viscosity ν, thermal diffusivity β of the working fluid, surface buoyancy flux B_s, and the measure of the background stratification. There are five independent variables and a dependent variable such as the magnitude of the jet velocity, which makes a total of six variables and two primary dimensions (i.e., length and time). Thus, Buckingham π theorem predicts that there are four dimensionless parameters. This means that is the nondimensionalized dependent variable is a function of three independent dimensionless parameters. Shapiro and Fedorovich [23] recognized this fact, but hypothesized that the full katabatic flow is controlled by two dimensionless numbers, which are the Prandtl number and a modified Reynolds number. In their scaling analysis, the slope angle appeared as a stretching factor in the modified Reynolds numbers.

Application of the Buckingham π theorem gives the Prandtl number Pr, the slope angle α, and the **stratification perturbation parameter** Π_s which is a measure of the ratio between the imposed surface buoyancy gradient and the background stratification as follows:

$$\Pi_s \equiv \frac{|B_s|}{\beta N^2} = \frac{\left|\frac{\partial b}{\partial z}\right|_s}{N^2}. \tag{13}$$

Since the buoyancy flux at the surface, B_S, is negative for katabatic slope flows and positive for anabatic slope flows, the magnitude of B_S is used in the definition of Π_s. Note that for both katabatic and anabatic conditions, the slope flow becomes dynamically more unstable at higher Π_s [24].

For a constant buoyancy condition at the surface the stratification perturbation number takes the following form

$$\Pi_s \equiv \frac{|b_0|}{\sqrt{N^3 \beta}}, \tag{14}$$

where b_0 is the prescribed buoyancy at the surface. An interesting outcome of the above dimensional analysis is the following: Richardson and internal Froude numbers that are widely used in the study of stratified flows do not appear in the list of dimensionless parameters governing the Prandtl model for stratified slope flows. In hindsight, this is not surprising, but this observation deserves an explanation, and that is because there are no external velocity or length scales imposed in the Prandtl model. The flow along the slope self starts due to imposed surface buoyancy flux and not driven by an external flow field or confined by a length scale. However, using the internal length and velocity scales defined in Eqs. (10) and (11), we can relate Π_s to the so-called internal Froude number as $\Pi_s = \mathrm{Fr}\sqrt{\mathrm{Pr}}$, and to the bulk Richardson number as $\Pi_s = \sqrt{\mathrm{Pr}/\mathrm{Ri}}$. However, we do not recommend using Fr or Ri for the current slope flow problem in the absence of external shear. Our viewpoint is that relevant dimensionless parameters should identify and capture the interplay of competing variables that are essential to the physics of the flow problem.

3 Linear Modal Analysis

Assuming that solutions to Eqs. (1)–(3) can be written as the sum of Prandtl's laminar base flow profile given by Eqs. (8)–(9) plus a small disturbance term, and stipulating that those disturbances to the base flow are wave modes represented by $\mathbf{q}(x, y, z, t) = \hat{\mathbf{q}}(z) \exp\left\{i(k_x x + k_y y) + \omega t\right\}$, the disturbance equations become, after linearization of Eqs. (1)–(3) around Prandtl's profile for katabatic flows:

$$ik_x\hat{u} + ik_y\hat{v} + \frac{\partial \hat{w}}{\partial z} = 0, \tag{15}$$

$$\omega\hat{u} + iu_n k_x \hat{u} + u_n'\hat{w} = -ik_x\hat{p} - \frac{\mathrm{Pr}}{\Pi_s}\sin\alpha\left(-(k_x^2 + k_y^2)\hat{u} + \frac{\partial^2\hat{u}}{\partial z^2} + \hat{b}\right), \tag{16}$$

$$\omega\hat{v} + iu_n k_x \hat{v} = -ik_y\hat{p} - \frac{\mathrm{Pr}}{\Pi_s}\sin\alpha\left(-(k_x^2 + k_y^2)\hat{v} + \frac{\partial^2\hat{v}}{\partial z^2}\right), \tag{17}$$

$$\omega\hat{w} + iu_n k_x \hat{w} = -\frac{\partial\hat{p}}{\partial z} - \frac{\mathrm{Pr}}{\Pi_s}\sin\alpha\left(-(k_x^2 + k_y^2)\hat{w} + \frac{\partial^2\hat{w}}{\partial z^2} + \hat{b}\cot\alpha\right), \tag{18}$$

$$\omega\hat{b} + iu_n k_x \hat{b} + b_n' \hat{w} = -\frac{\sin\alpha}{\Pi_s}\left(-(k_x^2 + k_y^2)\hat{b} + \frac{\partial^2 \hat{b}}{\partial z^2} - (\hat{u} + \hat{w}\cot\alpha)\right), \quad (19)$$

where $\hat{u}(z)$, $\hat{v}(z)$, $\hat{w}(z)$, $\hat{p}(z)$, $\hat{b}(z)$ denote slope normal dependent flow disturbance quantities normalized by the characteristic flow scales given in Eqs. (10)–(12). (k_x, k_y) is a real wave vector on the $x - y$ plane, whereas ω is a complex frequency representing both growth rate as well as oscillation frequency. The normalized laminar Prandtl flow profile and its derivative in the slope normal z-direction in normalized coordinates are given by u_n, b_n and u_n', b_n', respectively. It can be easily deduced from Eqs. (8) and (9) that Prandtl's profiles for both velocity and buoyancy are sinusoidal oscillations dampened with growing height, thus containing infinitely many inflection points, which may enable the onset of inflection instabilities. Equations (15)–(19) also verify that there are three dimensionless parameters governing Prandtl's slope flow as determined in the previous section with the help of Buckingham's π theorem.

The above system of linearized equations can be formally recast as a generalised eigenvalue problem as follows:

$$A(k_x, k_y)\hat{\mathbf{q}}(z) = \omega \mathbf{M}\hat{\mathbf{q}}(z), \quad (20)$$

where $\hat{\mathbf{q}}(z) = [\hat{u}(z), \hat{v}(z), \hat{w}(z), \hat{p}(z), \hat{b}(z)]^T$ is the flow disturbance vector varying in the slope-normal direction. $\mathbf{M}$ is a singular matrix due to the primitive variable formulation; it is created by setting all diagonal entries in the identity matrix belonging to the continuity equation to zero. To be compatible with the physical boundary conditions of the original problem, the appropriate boundary conditions for this system of equations are no slip for disturbance velocities at the slope surface $z = 0$, free slip at infinite height $z \to \infty$, and the buoyancy disturbance must satisfy $\partial\hat{b}/\partial z|_0 = 0$, $\hat{b}|_{z\to\infty} = 0$. The normal gradient of pressure disturbance $\hat{p}$ is also set to be zero at both $z = 0$ and $z \to \infty$. The generalised eigenvalue problem Eq. (20) is discretized via a collocated spectral method using Chebychev polynomials, and an algebraic map is used to cover the semi-infinite domain $[0, \infty)$. To obtain sufficient accuracy, two hundred collocation points are used for discretization, and the resulting generalised eigenvalue problem is solved with the help of MATLAB routine `eigs`. Linear stability/instability of the problem is determined by the real part of the eigenvalues ω, where $\Re\{\omega\} > 0$ signifies a positive exponential growth for the corresponding eigenmode, thus implying instability. The imaginary part of ω represents the angular frequency of the temporal oscillation for the corresponding eigenmode, and hence $\Im\{\omega\} = 0$ implies a stationary mode.

3.1 Linear Temporal Growth Rates

To study the linear temporal instability mechanism, we calculate the eigenvalue with the maximal real part for a range of wave number pairs (k_x, k_y) at different specific

values of the slope angle α and the stratification perturbation parameter Π_s. We set Pr = 0.71. At an inclination angle of $\alpha = 30°$ and $\Pi_s = 5.6$ for katabatic conditions, the maximal normalized growth rates, i.e. the maximal eigenvalue real part, are displayed in Fig. 2a for the wave number pair $[k_x, k_y]$ within $[0, 0.1] \times [0, 0.5]$. Only the positive growth rates, signifying asymptotic unstable modes, are colored in the plots. We observe at any given transverse wave number k_y, the maximal temporal growth rate is found for $k_x = 0$, i.e. the most unstable modes are purely transverse modes without variation along the base flow direction; the most dangerous transverse wave number with maximal temporal growth rate is attained approximately $k_y \approx 0.33$, as observed from Fig. 2a. The imaginary part of the most unstable eigenvalues, not shown here, are all zero, which shows that these transverse instabilities are all stationary, they are vortex rolls aligned with the longitudinal axis. At first sight, this instability mode runs contrary to Squire's theorem which states that the most unstable mode of parallel flows must be two-dimensional and propagate along the direction of the base flow [25], such as for example the plane Poiseuille flow. Since Squire's Theorem is only strictly valid for flows in the absence of other external body forces, we deduce that the transverse instability mode must be caused by the buoyancy force acting simultaneously orthogonal as well as parallel to the base flow direction, which is similar to the role of the centrifugal force in other types of flow where similar instabilities exist, such as for example Görtler vortices or Taylor-Couette flow [25, 26]. The analogy between the normal buoyancy force and surface curvature effects has been established earlier [27], and both of these effects have been identified as key components for the initiation of longitudinal rolls on a curved, cooled surface. Our previous results, therefore, shows that even in the presence of background stable stratification of strength N^2, the surface cooling, hence the buoyancy force, can be strong enough to trigger the aforementioned instability mechanism, overcoming the stable background stratification. Stratification perturbation parameter Π_s captures this effect directly.

For a much steeper inclination angle of $\alpha = 70°$ and at a higher stratification perturbation number of $\Pi_s = 18.5$ under katabatic conditions, the real part of the most unstable eigenvalues for wave-numbers $[k_x, k_y]$ within $[0.1, 0.33] \times [0, 0.1]$ are shown in Fig. 2b. In clear contrast to Fig. 2a for the smaller angle $\alpha = 30°$, Fig. 2b indicates that the modes become more unstable with smaller k_y component such that the largest growth rates are located at $k_y = 0$; the longitudinal wave number of the most unstable mode is approximately $k_x \approx 0.24$, as shown in Fig. 2b. These modes are thus only varying along the slope direction, parallel to the main flow, hence they are longitudinal modes. This is much more in line with instability in other type of nearly parallel flows such as wakes behind a cylinder or Tollmien-Schlichting waves in boundary layers. This essential difference from the instability of slope flows at the lower angle of $\alpha = 30°$ could be explained by the larger along-slope buoyancy force component relative to the force orthogonal to the surface at steeper slope angles. As another substantial deviation from the case at $\alpha = 30°$, the imaginary part of the most unstable eigenvalues, i.e. normalized oscillation frequency of the most unstable modes, are nonzero. This means that the longitudinal instability modes on steep slopes are waves propagating along the slope direction, in contrast to the stationary

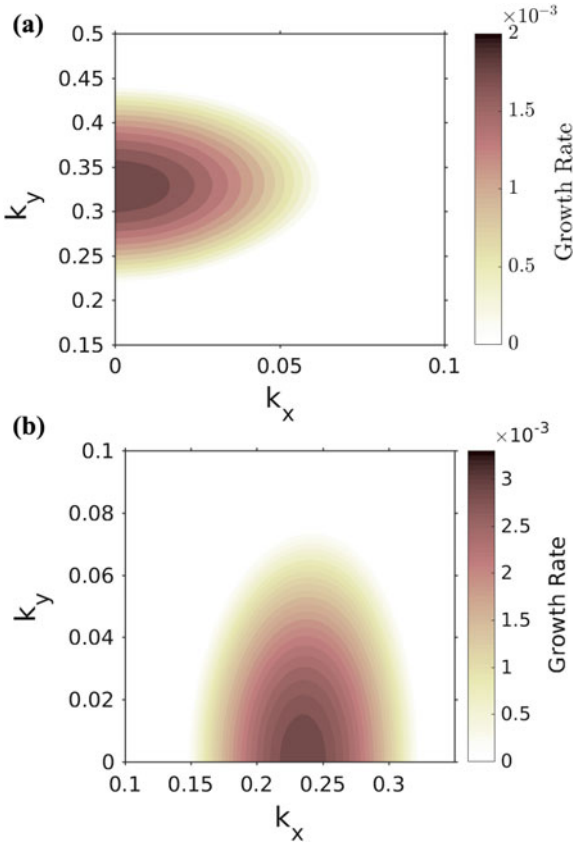

Fig. 2 Growth rate contours depending on wave number vectors k_x, k_y at different slope angles for Pr = 0.71: **a** $\alpha = 30°$, $\Pi_s = 5.6$; **b** $\alpha = 70°$, $\Pi_s = 18.5$

rolls found at moderate slope angles. It should be emphasised here that for both the moderate as well as the steep slope angles, the most unstable instability mode never propagates in an oblique direction ($k_x, k_y \neq 0$); it is either parallel ($k_y = 0$) or transverse ($k_x = 0$) to the main flow direction along the slope. This is a different to the spanwise-stratified Couette flow case in which oblique instabilities tend to be the most unstable modes [18].

3.2 Growth Rates for Pure Modes

The findings of the previous subsection led us to the observation that the most unstable modes at each slope angle α and stratification perturbation Π_s are pure and not oblique, which means that one component of the wave number pair $[k_x, k_y]$ must be zero in order to achieve maximal growth rate at fixed values for α and Π_s. This assertion implies that the critical threshold value of Π_s required for the initiation of

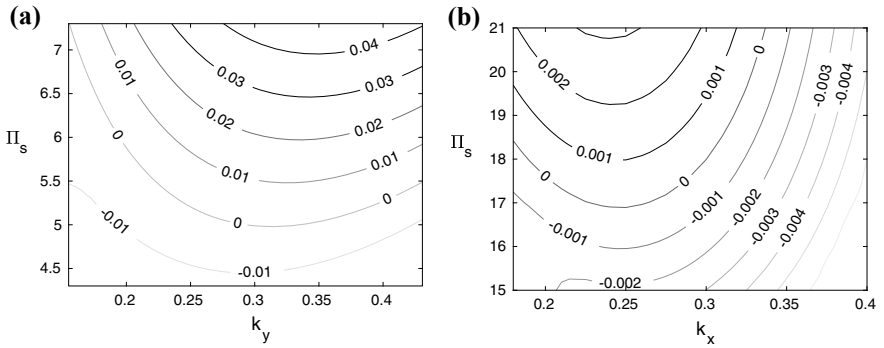

Fig. 3 Growth rate contours. **a** $\alpha = 30°$ for the transverse mode; **b** $\alpha = 70°$ for the longitudinal mode. The most unstable eigenvalue at slope angle 30° for $\Pi = 5.6$ is $\omega \approx 0.15$ and is attained for the transverse wave number $k_y = 0.32$. The most unstable eigenvalue at slope angle 70° for $\Pi = 18.5$ is $\omega \approx 0.001 + 0.115i$ at the longitudinal wave number $k_x = 0.25$

instability at a specific slope angle α and Pr number can be obtained by computing the growth rates over Π_s separately for each wave number k_x and k_y and setting the other wave number to zero. The Prandtl number is unchanged from the previous subsection (i.e. Pr = 0.71). For the lower slope angle of $\alpha = 30°$, where the transverse mode is expected to be dominant due to previous results, Fig. 3a displays the growth rate contours over the $k_y - \Pi_s$ domain. It can be observed that the minimal stratification perturbation parameter required for the transverse mode is approximately $\Pi_s \approx 5$.

In Fig. 3b, the results for the steeper angle of $\alpha = 70°$ are shown over the $k_x - \Pi_s$ domain, since the longitudinal mode is expected to be dominant in this case. We observe from Fig. 3b that the threshold for triggering the longitudinal mode is approximately $\Pi_s \approx 17$. In both cases, we conclude after inspecting Fig. 3 that, for the range of values shown here, the growth rate increases with increasing Π_s at any fixed wave number k_x or k_y. Hence, a larger stratification perturbation parameter is associated with a more dynamically unstable flow configuration.

3.3 Eigenfunctions and Spectra

The eigenfunctions for each instability type described in the previous section are computed and displayed in Fig. 4 for the transverse mode, and in Fig. 5 for the longitudinal mode. All flow components are normalized by the maximal buoyancy disturbance magnitude. The transverse mode is computed at $\alpha = 30°$, $\Pi_s = 5.6$, whereas the longitudinal mode is taken at $\alpha = 70°$, $\Pi_s = 18.5$. From the eigenfunction plots, it can be seen from the transverse mode is fully three dimensional because it has nonzero disturbances in all three velocity components, which can be up to almost three times larger than the maximal buoyancy disturbance. On the other hand, the

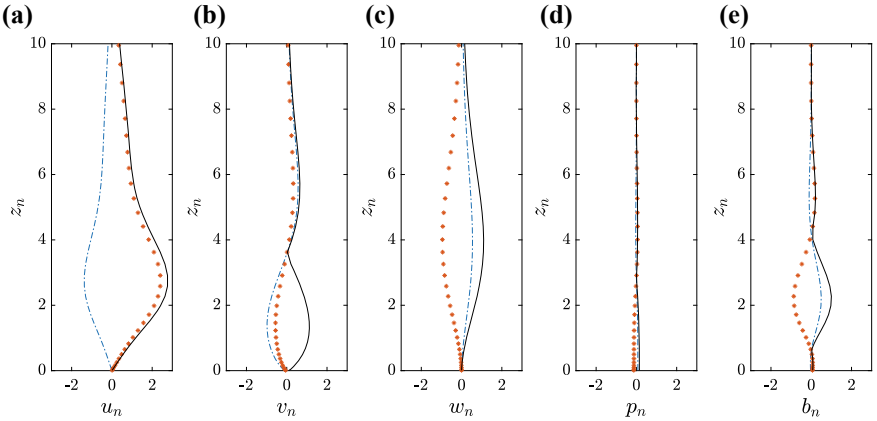

Fig. 4 Eigenfunctions of the linear stability problem for the transverse mode at $\alpha = 30°$. Dashed lines represent the real part, asterisks represent the imaginary part, and solid line is the magnitude. The disturbance magnitudes have been normalized with the maximal occurring buoyancy disturbance magnitude in each case

longitudinal flow velocity disturbance at steeper angle 70° is purely two-dimensional with zero cross-flow velocity component $v = 0$; its main flow and vertical flow disturbances are a lot weaker compared to its buoyancy disturbance. These differences appear to suggest that the transverse and longitudinal modes are instigated by two distinct instability mechanisms. Following the arguments made previously, the distinct flow disturbance characteristics of the transverse mode appears to be consistent with centrifugal instabilities such as longitudinal vortex rolls observed in Görtler or Taylor-Couette flows e.g. [26, 27]; on the other hand, the wave-like longitudinal mode is a conventional two-dimensional Squire mode and could be the result of a combination of Kelvin-Helmholtz mechanism as well as internal gravity waves in stably-stratified medium.

The spectra, as well as pseudospectra for a transverse mode at $\alpha = 30°$ and a longitudinal mode at $\alpha = 70°$, are displayed in Fig. 6a, b, respectively. which shows the complex plane after the conformal transformation $z \to 1/z$. It can be seen that the most unstable eigenvalue of the transverse mode, as shown in Fig. 6a, has zero imaginary part, implying stationarity, as explained earlier. On the other hand, the imaginary part of the most unstable eigenvalue for the longitudinal mode is nonzero (see Fig. 6b), thus indicating a travelling mode.

It is known that due to the non-normality of the stability operator, asymptotically stable modes can experience very large transient growth rates which could short-circuit the transition process [25, 28]. The pseudospectra have been computed with the help of the MATLAB routine `eigtool` [29] and serve a visual guide to judge the normality of the linearized stability operator [25]. The ϵ-pseudospectra contours shown in Fig. 6a, b closely follow the shape of the original spectrum at distance ϵ without major contortions, which is an indication for lack of strong operator non-

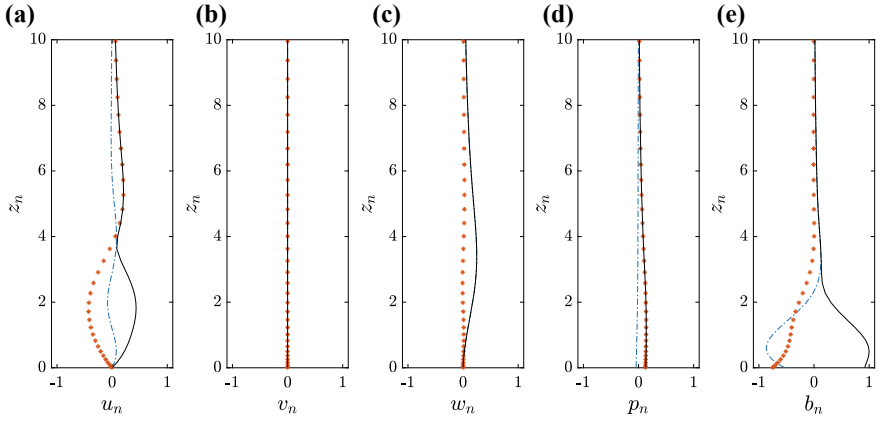

Fig. 5 Eigenfunctions of the linear stability problem for the longitudinal mode at $\alpha = 70°$. Dashed lines represent the real part, asterisks represent the imaginary part, and solid line is the magnitude. The disturbance magnitudes have been normalized with the maximal occurring buoyancy disturbance magnitude in each case

normality and hence absence of large transient growth rates dominating the most unstable asymptotic modes [25]. This has been supported by the analysis in [24] which found good agreement between the growth rate predicted by the most unstable mode and the simulation results. It is of interest that the plots displayed here bear strong resemblance with some of the pseudospectra for Taylor-Couette flows shown in [30].

3.4 Critical Stability Threshold and Map

Results from the analysis in previous subsections have shown a qualitative change in the flow instability as a result of different slope angles, which is exhibited by a transition from a transverse mode consisting of stationary rolls to two-dimensional waves propagating along the main flow direction at sufficiently large inclination angle. In order to obtain a detailed relation between slope angle α and the expected flow instability at α, we plot the critical threshold of Π_s for the onset of longitudinal and transverse modes as functions of α over the range $[30°, 80°]$ in Fig. 7a. It is obvious that whereas the critical threshold of stratification perturbation parameter for the transverse mode grows for increasing angle α, the corresponding value for the longitudinal mode hardly changes over the same slope angles. Thus the transverse mode becomes increasingly harder to be initiated with growing slope angle, and the angle at which its critical stability threshold equals that of the longitudinal mode is approximately $\alpha \approx 62°$, which is a very steep slope. From the relation $\Pi_s = \sqrt{\mathrm{Pr}/\mathrm{Ri}}$ between the stratification perturbation parameter and gradient Richardson

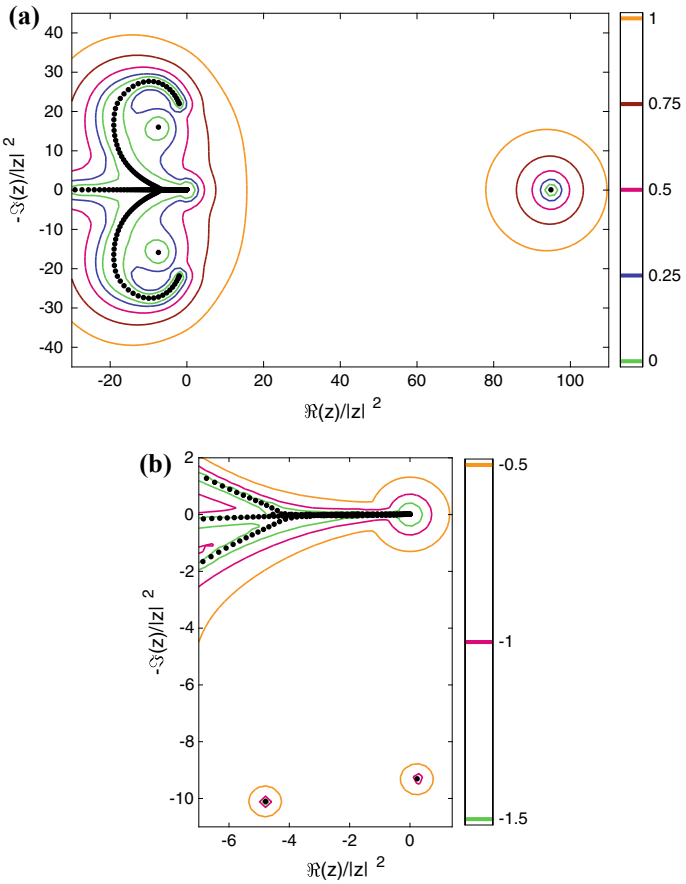

Fig. 6 Spectra and ϵ-pseudospectra. **a** $\alpha = 30°$, $\Pi_s = 18.5$ for the transverse mode; **b** $\alpha = 70°$, $\Pi_s = 20.5$ for the longitudinal mode. The original spectra are marked by dots, and unstable eigenvalues are located in the positive real half of the complex plane. ϵ-pseudospectra is shown by the color contours. The colorbar values are $\log_{10}\ \epsilon$

number [24], the value of Π_s that corresponds to the critical Richardson number of $\mathrm{Ri}_c = 0.25$ at the Prandtl number $\mathrm{Pr} = 0.7$ is $\Pi_s \approx 1.69$, as indicated by the dashed line in Fig. 7b. Figure 7a shows that at steep inclinations $\alpha > 62°$, the critical value of Π_s for each of the two instability modes is at least 17 and thus lies far above the $\mathrm{Ri}_c = 0.25$ line, and linearly stability is assured for an implied Ri that is as low as 2.5×10^{-3}.

From Fig. 7b showing the behaviour at low angles less than 9°, it can be observed that at such shallow slopes, the critical Π_s threshold for the transverse mode decreases with smaller angles such that at $\alpha \approx 5°$, the threshold value is as low as $\Pi_s \approx 1.61$. From the relation $\mathrm{Ri} = \mathrm{Pr}/\Pi_s^2$, it can be easily verified that at angles $\alpha \leq 5°$, the Prandtl base flow profile satisfies $\mathrm{Ri} > 0.25$. Thus the appearance of transverse insta-

bility mode in such a case apparently violates the stability criterion given by the celebrated Miles-Howard Theorem which is valid for parallel inviscid base flows under stable stratification [31]. However, this theorem, as explained in [32], requires the assumption of inviscid flow with buoyancy force only acting orthogonal to the base flow and surface; hence it completely neglects viscous shear as well as heat conduction effects as well as surface inclination. In an earlier work by [20], it has already been shown that when there is misalignment between shear and stratification, a stably stratified, inviscid flow can become linearly unstable even when the gradient Richardson number throughout the entire base flow field satisfies $\mathrm{Ri} > 0.25$. Further, as demonstrated by [33], heat conduction and viscous shear can also have a destabilizing effect on a parallel flow under stable stratification, such that linear instabilities may develop for base flows satisfying $\mathrm{Ri} > 0.25$ throughout. Thus, we are led to the conclusion that the presence of surface inclination as well as viscous and heat conduction combine to trigger the transverse instability mode at $\mathrm{Ri} > 0.25$ conditions, as shown in Fig. 7b.

3.5 Influence of Prandtl Number

The influence of the Prandtl number on the stability map $\alpha - \Pi_s$ is shown in Fig. 8, which plots the minimal threshold value of Π_s necessary to initiate each instability mode over the slope angle. A larger Prandtl number increases the stability threshold necessary for instability onset of both transverse and longitudinal modes. A plausible explanation for this observation is that when other flow parameters such as the fluid viscosity and Π_s are left unchanged, a larger value of Pr effectively implies a smaller thermal diffusivity, β, which then leads to a lower surface heat flux magnitude B_s at the same Π_s, as shown by Eq. (13). Figure 8 also clearly displays that the stability threshold of the transverse mode is influenced to a much larger degree by the Prandtl number than the longitudinal mode: Raising it from Pr = 0.7 for air to Pr = 6.7 for water at room temperature of 25°, the critical stability threshold of the transverse mode increases more than five times for all angles shown in the plot, whereas the threshold value of Π_s for the longitudinal mode only becomes about twice as large.

4 Results from Direct Numerical Simulations

Direct numerical simulations (DNS) are conducted to verify the results from the linear stability analysis as well as visualizing flow fields of the instabilities. Towards this end, the Navier-Stokes equations under a rotated coordinate system with buoyancy contributions modelled by the Boussinesq approximation given by Eqs. (1)–(3) are integrated via the second-order accurate three-dimensional solver GIN3D on a

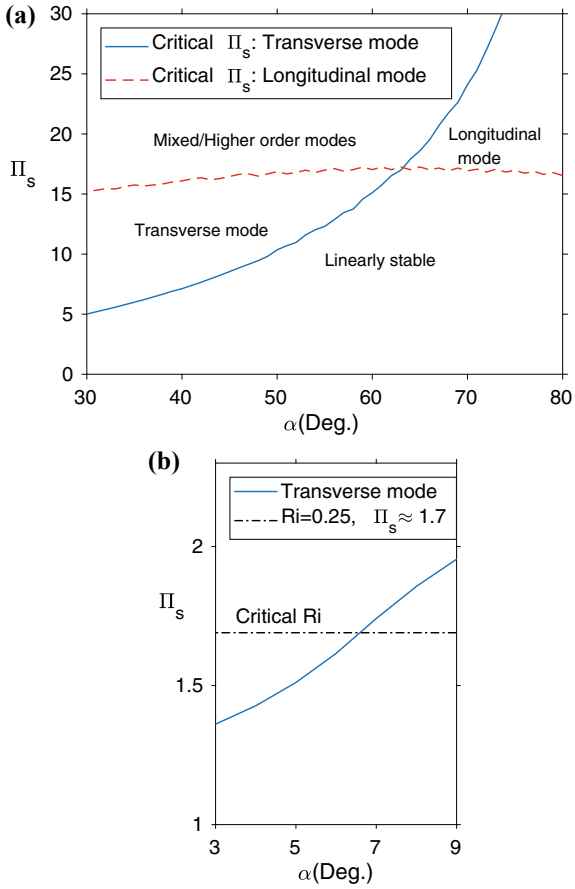

Fig. 7 Critical stability thresholds for longitudinal and transverse modes at different inclination angles: **a** for steep slopes with $\alpha > 30°$ and **b** for shallow slopes with $\alpha < 9°$. The line corresponding to the critical Richardson number Ri = 0.25 is drawn in the latter case

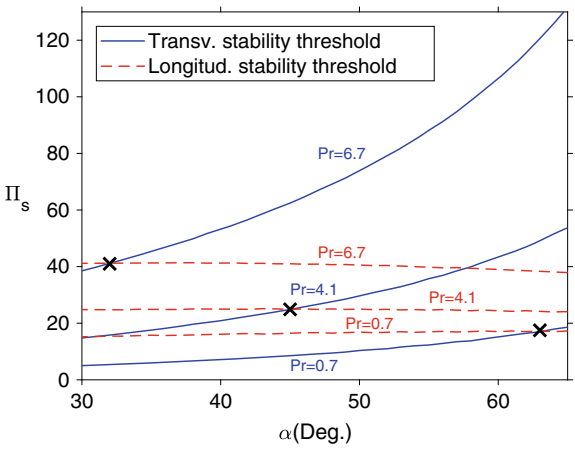

Fig. 8 Critical stability thresholds at different slope angles for different Prandtl numbers: for the transverse and the longitudinal mode. The locations where the thresholds for both modes are equal are marked with × symbol

Cartesian mesh [34]. The current version of GIN3D has been applied by Umphrey et al. [35] to simulate the Prandtl slope flows. The globally second-order accuracy of GIN3D was verified in that study.

4.1 Pure Instability Modes

We select rectangular boxes of dimensionless size $L_x \times L_y \times L_z$ as simulation domains for the katabatic slope flow problem. At least 3–4 points have been used to resolve one characteristic length scale l_0 along each direction in the simulated pure instability modes; for our last case, the mixed instability simulation, a coarser grid resolution has been applied due to the larger domain size which will be explained separately. We apply periodic boundary conditions in both the along-slope and cross-slope directions, whereas a no-slip condition with a constant buoyancy flux is imposed to the lower surface at $z = 0$; the upper boundary is assumed to be free-slip and adiabatic. The height of the simulation domain is set to be larger than 50 times the characteristic length scale l_0 computed from Eq. (10) to ensure nearly quiescent conditions on the top. There is substantial latitude in the choice of the longitudinal and transverse dimensions of the domain; we only need to ensure that the size in the relevant direction is somewhat approximately an integer multiple of the wave length of the most unstable mode as shown in Fig. 2. For initial conditions, we simply impose Prandtl's laminar flow profiles given by Eqs. (8) and (9). No initial disturbances are required to be added on since inaccuracies arising from interpolation of the Prandtl profile onto the discrete numerical grid as well as due to the iterative nature of computational schemes, augmented by massively-threaded finite-precision floating point arithmetics on graphics processing units were already enough to initiate the flow instabilities after sufficiently long simulation time.

After growing sufficient in amplitude, i.e. larger than 10% of the maximal base flow speed, nonlinear effects cause both modes to become saturated and reach a new supercritical steady state. The vertical velocity component of the unstable flow fields during the linear growth phase where the instability magnitude is many orders smaller than the mean flow magnitude and at the saturated steady state are both displayed in Figs. 9 and 10 for the transverse mode and longitudinal mode, respectively. A comparison between Fig. 9a, b indicates that for the transverse mode, which remains spatially stationary throughout, the shape of the flow field significantly changes after nonlinear saturation such that the symmetry between the uplift ($w_n > 0$) and downdraft ($w_n < 0$) flow regions is lost. In contrast, Fig. 10a, b show that there is no such major modification for the travelling longitudinal mode, which only displays some minor distortion of the flow field after reaching its supercritical steady state.

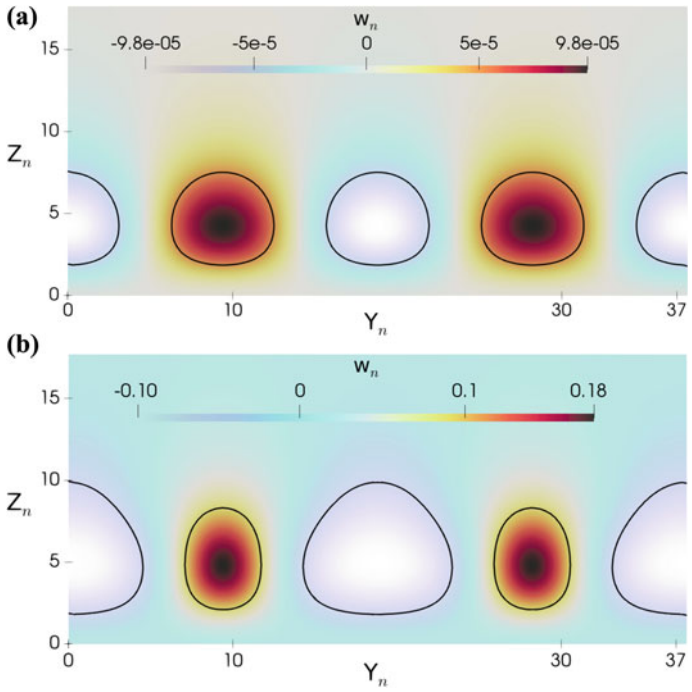

Fig. 9 Simulated unstable transverse mode of katabatic slope flow at $\alpha = 30°$, $\Pi_s = 5.6$. Instantaneous snapshot of vertical velocity component during (**a**) growth phase and (**b**) after saturation are shown. The contours are drawn for the normalized vertical velocity w_n at half of the maximal and minimal values, respectively

4.2 Mixed Instabilities Mode

At a slope angle $\alpha = 30°$, it can be seen from Fig. 7 that when the stratification perturbation parameter Π_s is larger than 20, the thresholds for both the transverse and longitudinal instabilities will be breached, suggesting that both modes could exist simultaneously under these conditions. In order to test this hypothesis, we carried out a simulation for $\alpha = 30°$, $\Pi_s = 21$ on a large domain of size $400l_0 \times 400l_0 \times 50l_0$ to ensure that multiple wavelengths along all directions are being captured. Due to the larger simulation domain size for this case, a slightly coarser grid resolution is chosen; it is ensured that about 2 grid points occupy each length scale l_0 in each direction. A snapshot of the instantaneous flow field is displayed in Fig. 11, which uses the isocontour of the Q-criterion at a fixed positive value for vortex structure identification [36]. It can be seen that both longitudinal rolls and along-stream waves, characterisitc of the transverse and longitudinal instability modes, simultaneously co-exist in the flow field and are delicately interwoven with each other, generating smaller, more intricate eddies along their evolution.

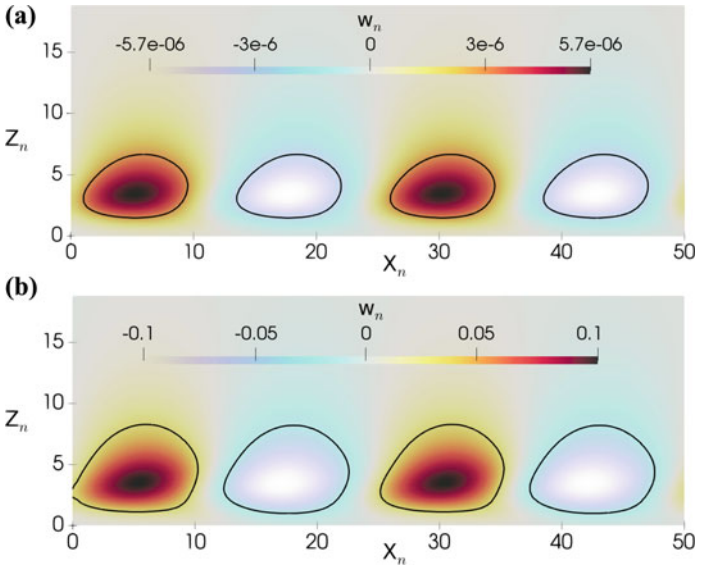

Fig. 10 Simulated unstable longitudinal mode of katabatic slope flow at $\alpha = 70°$, $\Pi_s = 18.5$. Instantaneous vertical velocity component during (**a**) growth phase and (**b**) after saturation are shown. The contours are drawn for the normalized vertical velocity w_n at half of the maximal and minimal values, respectively

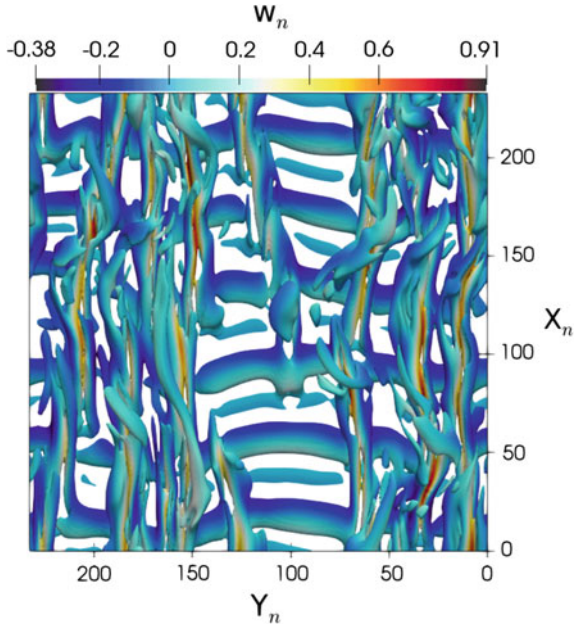

Fig. 11 Instantaneous contour for Q-criterion at $Q = 0.02$ at $\alpha = 30°$, $\Pi_s = 21$. The coloring is done via the normalized vertical velocity. In this view, the main downslope flow runs from top to bottom

5 Conclusions

As shown in this work and in Ref. [24], Prandtl model for down-slope flows is susceptible to different types of flow instabilities in response to infinitesimal perturbations. We used linear modal analysis and direct numerical simulations to uncover these instabilities. Pseudospectra of the generalized eigenvalue problem is used to explain the lack of strong non-normality of the linear stability operator, in contrast to other familiar cases such as Couette and pipe flows [25]. Slope flow instabilities are controlled by three dimensionless numbers, which are the inclination angle, the Prandtl number, and the stratification perturbation parameter, Π_s. This newly introduced dimensionless number captures the relative importance of the surface cooling to the background stratification.

For slopes that are not too steep, i.e. $\alpha < 62°$, a stationary, three-dimensional mode of instability characterized by longitudinal vortex rolls can be triggered for sufficiently high Π_s, despite the fact that Prandtl's laminar profile is an one-dimensional parallel flow. For gentle slopes satisfying $\alpha \lesssim 5°$, this instability can be initiated even for base flow profiles with implied gradient Richardson number value beyond the critical threshold of 0.25 given in the well-known Howard-Miles theorem for inviscid stratified shear flows.

At steep slope angles beyond 62°, however, a two-dimensional wave instability travelling along the slope develops. The onset of this instability can be explained by the more dominant along-slope gravity component in this configuration. For these slope angles, linear stability of the flow can be attained even at implied gradient Richardson number as low as 2×10^{-3}.

Discovery of these fluid instabilities in slope flows along with a set of dimensionless numbers controlling the dynamics are expected to lead to improved parameterization of turbulent surface fluxes of heat and momentum transfer and a better description of the very stable conditions in the atmospheric boundary layer.

Acknowledgements Research was sponsored by the Army Research Office and was accomplished under Grant Number W911NF-17-1-0564 with Dr. Julia G. Baryzk as the Program Manager. This research was supported in part by the University of Pittsburgh Center for Research Computing through the resources provided.

References

1. R.B. Stull, *An Introduction to Boundary Layer Meteorology* (Kluwer Academic Publishers, Dordrecht, 1988)
2. C.D. Whiteman, *Mountain Meteorology: Fundamentals and Applications* (Oxford University Press, Oxford, 2000)
3. E. Fedorovich, J.A. Gibbs, A. Shapiro, Numerical study of nocturnal low-level jets over gently sloping terrain. J. Atmos. Sci. **74**(9), 2813–2834 (2017)
4. A. Meesters, Dependence of the energy balance of the greenland ice sheet on climate change: Influence of katabatic wind and tundra. Q. J. Roy. Meteor. Soc. **120**(517), 491–517 (1994)

5. T.R. Parish, D.H. Bromwich, Continental-scale simulation of the antarctic katabatic wind regime. J. Climate **4**(2), 135–146 (1991)
6. H. Fernando, Fluid dynamics of urban atmospheres in complex terrain. Annu. Rev. Fluid Mech. **42**(1), 365–389 (2010)
7. J.A. Salmond, I.G. McKendry, A review of turbulence in the very stable nocturnal boundary layer and its implications for air quality. Prog. Phys. Geog.: Earth Environ. **29**(2), 171–188 (2005)
8. L. Mahrt, Stratified atmospheric boundary layers and breakdown of models. Theor. Comp. Fluid Dyn. **11**(3–4), 263–279 (1998)
9. I. Sandu, A. Beljaars, P. Bechtold, T. Mauritsen, G. Balsamo, Why is it so difficult to represent stably stratified conditions in numerical weather prediction (NWP) models? J. Adv. Model. Earth Sy. **5**(2), 117–133 (2013)
10. A. Monin, A. Obukhov, Basic laws of turbulent mixing in the atmosphere near the ground. Tr. Akad. Nauk SSSR Geofiz. Inst **24**(151), 163–187 (1954)
11. F.T.M. Nieuwstadt, The turbulent structure of the stable, nocturnal boundary layer. J. Atmos. Sci. **41**(14), 2202–2216 (1984)
12. H. Fernando, J. Weil, Whither the stable boundary layer? A shift in the research agenda. B. Am. Meteorol. Soc. **91**(11), 1475–1484 (2010)
13. L. Mahrt, Stably stratified atmospheric boundary layers. Annu. Rev. Fluid Mech. **46**, 23–45 (2014)
14. L. Prandtl, *Führer durch die Strömungslehre* (Vieweg und Sohn, Berlin, 1942)
15. L. Prandtl, *Essentials of Fluid Dynamics: With Applications to Hydraulics, Aeronautics, Meteorology and other Subjects* (Blackie & Son, 1953)
16. E. Fedorovich, A. Shapiro, Structure of numerically simulated katabatic and anabatic flows along steep slopes. Acta Geophys. **57**(4), 981–1010 (2009)
17. M. Giometto, G. Katul, J. Fang, M. Parlange, Direct numerical simulation of turbulent slope flows up to Grashof number $\mathrm{Gr} = 2.1 \times 10^{11}$. J. Fluid Mech. **829**, 589–620 (2017)
18. G. Facchini, B. Favier, P. Le Gal, M. Wang, M. Le Bars, The linear instability of the stratified plane Couette flow. J. Fluid Mech. **853**, 205–234 (2018)
19. J. Chen, Y. Bai, S. Le Dizès, Instability of a boundary layer flow on a vertical wall in a stably stratified fluid. J. Fluid Mech. **795**, 262–277 (2016)
20. J. Candelier, S. Le Dizès, C. Millet, Shear instability in a stratified fluid when shear and stratification are not aligned. J. Fluid Mech. **685**, 191–201 (2011)
21. J. Holton, *Introduction to Dynamic Meteorology*, 4th edn. (Academic Press, Cambridge, 2013)
22. A. Shapiro, E. Fedorovich, Unsteady convectively driven flow along a vertical plate immersed in a stably stratified fluid. J. Fluid Mech. **498**, 333–352 (2004)
23. A. Shapiro, E. Fedorovich, A boundary-layer scaling for turbulent katabatic flow. Bound.-Layer Meteorol. **153**, 1–17 (2014)
24. C.-N. Xiao, I. Senocak, Stability of the Prandtl model for katabatic slope flows. J. Fluid Mech. **865**, R2 (2019)
25. P.J. Schmid, D.S. Henningson, *Stability and Transition in Shear Flows* (Springer, New York, 2001)
26. G.I. Taylor, Stability of a viscous liquid contained between two rotating cylinders. Philos. Trans. Royal Soc. A **223**(605–615), 289–343 (1923)
27. H. Görtler, Über eine analogie zwischen den instabilitäten laminarer grenzschichtströmungen an konkaven wänden und an erwärmten wänden. Ingenieur-Archiv **28**(1), 71–78 (1959)
28. L.N. Trefethen, A.E. Trefethen, S.C. Reddy, T.A. Driscoll, Hydrodynamic stability without eigenvalues. Science **261**(5121), 578–584 (1993)
29. T.G. Wright, L. Trefethen, Eigtool, Software available at http://www.comlab.ox.ac.uk/pseudospectra/eigtool (2002)
30. H. Hristova, S. Roch, P.J. Schmid, L.S. Tuckerman, Transient growth in Taylor-Couette flow. Phys. Fluids **14**(10), 3475–3484 (2002)
31. P.G. Drazin, W.H. Reid, *Hydrodynamic Stability. Cambridge Mathematical Library*, 2nd edn. (Cambridge University Press, Cambridge, 2004)

32. J.W. Miles, On the stability of heterogeneous shear flows. J. Fluid Mech. **10**(4), 496–508 (1961)
33. J. Miller, K. Gage, Prandtl number dependence of the stability of a stratified free shear layer. Phys. Fluids **15**(5), 723–725 (1972)
34. D.A. Jacobsen, I. Senocak, Multi-level parallelism for incompressible flow computations on GPU clusters. Parallel Comput. **39**(1), 1–20 (2013)
35. C. Umphrey, R. DeLeon, I. Senocak, Direct numerical simulation of turbulent katabatic slope flows with an immersed boundary method. Bound.-Layer Meteorol. **164**(3), 367–382 (2017)
36. V. Kolář, Vortex identification: New requirements and limitations. Int. J. Heat Fluid Flow **28**(4), 638–652 (2007)

Shock-Turbulence Interaction in Variable Density Flows

Yifeng Tian, Farhad Jaberi and Daniel Livescu

Abstract Accurate numerical simulations of shock-turbulence interaction (STI) are conducted by a hybrid monotonicity preserving-compact finite difference scheme for a detailed study of STI in variable density flows. Numerical accuracy of the simulations has been established using a series of grid, particle, and linear interaction approximation (LIA) convergence tests. The results show that for current parameter ranges, turbulence amplification by the normal shock wave is much higher and the reduction in turbulence length scales is more significant when strong density variations exist in STI. The turbulence structure is strongly modified by the shock wave, with a differential distribution of turbulent statistics in regions with different densities. The correlation between rotation and strain is weaker in the multi-fluid case, which is shown to be the result of complex role density plays when the flow passes through the shock wave. Furthermore, a stronger symmetrization of the joint probability density function (PDF) of second and third invariants of the anisotropic velocity gradient tensor (VGT) is observed in the multi-fluid case. Lagrangian dynamics of the VGT and its invariants are studied and the pressure Hessian contributions are shown to be strongly affected by the shock wave and local density, making them important to the flow dynamics and turbulence structure.

Keywords Turbulence · Variable-density flows · Shock waves · Velocity gradient tensor

Y. Tian · F. Jaberi
Department of Mechanical Engineering, Michigan State University,
East Lansing, MI 48824, USA
e-mail: tianyife@egr.msu.edu

F. Jaberi
e-mail: jaberi@egr.msu.edu

D. Livescu (✉)
Los Alamos National Laboratory, Los Alamos, NM 87545, USA
e-mail: livescu@lanl.gov

D. Livescu et al. (eds.), *Modeling and Simulation of Turbulent Mixing and Reaction*, Heat and Mass Transfer, https://doi.org/10.1007/978-981-15-2643-5_4

1 Introduction

The interaction of a normal shock wave with multi-fluid isotropic turbulence is an extension of the canonical shock-turbulence interaction (STI) problem which includes strong variable density effects. This extended configuration can enhance our understanding of more complex flow problems such as fuel-air mixing in supersonic combustion, the interaction of supernova remnants with interstellar clouds, shock propagation through foams and bubbly liquids, inertial confinement fusion (ICF), and re-shock problem in Richtmyer-Meshkov instability (RMI). Most of the previous theoretical, numerical, and experimental studies of STI have been dedicated to the original canonical problem.

The early theoretical study in Ref. [1] has restricted the STI to the linear interaction regime with a large scale separation between the shock and turbulence, so that the nonlinear and viscous effects are assumed to be negligible during the interaction. By decomposing the pre-shock turbulence into independent modes (acoustic, vortical and entropy) using Kovaznay decomposition [2], the post-shock turbulence statistics can be theoretically derived from the linearized Rankine-Hugoniot jump conditions. This approach is referred to as the linear interaction approximation (LIA) and represents an important limiting case, since it provides analytical predictions for the jumps of fluctuating quantities through the shock.

Due to the challenges of accurate experimental measurements of the smallest time and length scales around the shock wave, numerical simulations have been more widely employed to investigate this interaction. Researchers have been using both shock-capturing and shock-resolving simulations to understand the post-shock amplification of Reynolds stress, vorticity variance, and turbulent length scales [3–10]. Earlier numerical studies have shown limited agreement with the LIA predictions because the parameter range was outside the linear regime. More recently, Ref. [11] have considered a wide range of parameters in their shock-resolving direct numerical simulations (DNS) to show that the DNS results converge to the LIA solutions when the ratio of the shock thickness (δ) to the pre-shock Kolmogorov length scale (η) becomes small. Replacing the actual shock interaction with the LIA relations can extend the reach of DNS to arbitrarily high shock Mach numbers and much larger Taylor Reynolds number (Re_λ) than otherwise computationally feasible, provided that the interaction parameters correspond to the linear regime. This method (named Shock-LIA by the authors) was used for detailed studies of the post-shock turbulent energy flux and vorticity dynamics [12, 13]. Reference [14] used shock-capturing simulation and LIA to study the thermodynamic field generated by STI. In a recent study, Ref. [15] showed, using shock-capturing turbulence-resolving simulations, that the LIA predictions for the Reynolds stresses can be approached (albeit at larger Re_λ values than in full DNS calculations) providing that the scale separation between numerical shock thickness (δ_n) and Kolmogorov length scale is large enough. Thus, when the scale separation is large enough, so that the numerical artifacts near the shock do not influence the flow, the shock-capturing method can properly simulate the STI.

As mentioned above, in many practical applications, STI may occur in a mixture of very different density fluids. This motivated our extension of the canonical STI problem to include variable density effects [15, 16] by considering the pre-shock turbulence as an isotropic mixture of two fluids with different molecular weights, as encountered in non-premixed combustion. Using turbulence-resolving shock-capturing simulations, we have examined the turbulence statistics, turbulence budgets, conditional statistics, and energy spectrum in the multi-fluid STI and found that the nonlinear effects from the density variations significantly change the turbulence properties in both physical and spectral spaces. In another study, Refs. [17, 18] considered a reactive shock wave in a premixed mixture and used LIA and shock-capturing simulations to study the detonation-turbulence interaction. However, there still exist many gaps in our knowledge of the variable density effects on the post-shock turbulence structure and flow topology.

The properties of the velocity gradient tensor (VGT) determine a wide variety of turbulence characteristics, such as the flow topology, deformation of material volume, energy cascade, and intermittency. Understanding both the VGT field immediately after the shock-wave and its dynamics as the flow evolves away from the shock wave are also crucial to the development of subgrid-scale models that can accurately describe the shock interaction and return-to-isotropy effects. Reference [19] has proposed an approach to classify the local flow topology and structure using the invariants of VGT. The dynamical behavior of the VGT has been studied for incompressible flows using the Lagrangian evolution of the invariants along conditional mean trajectories (CMT) [20]. The statistics regarding the invariants of VGT and their Lagrangian dynamics have been used to understand the structure of turbulence in many canonical flows, such as isotropic turbulence, turbulent boundary layer and mixing layers [21–23]. Previous studies on single-fluid STI have examined some of the statistics of the PDF of VGT. References [11, 12] took a step further to investigate the turbulence structure and vorticity dynamics based on the examination of VGT invariants. By taking advantage of the Shock-LIA procedure, they extracted the statistics of VGT and its invariants for a wide range of shock Mach numbers. On the other hand, the dynamics of VGT as the turbulence evolves away from the shock wave cannot be examined using the Shock-LIA procedure. Our preliminary numerical studies on variable density STI have revealed some important features of VGT [24, 25]. The relation between velocity and scalar field has also been studied by Ref. [26] to better understand mixing in this flow configuration. However, these studies have not yet fully revealed the variable density effects on the post-shock turbulence/scalar structure.

This chapter presents a comprehensive study of multi-fluid STI using the turbulence-resolving shock-capturing simulations. The chapter is organized as follows. Details of the simulations are described in Sect. 2 and the testing conducted to assess the accuracy of results are discussed in Sect. 3. Results are presented in Sect. 4.

2 Governing Equations and Solution Procedure

In this section, we will briefly discuss the governing equations and numerical approach used for shock-capturing turbulence-resolving simulations, from which we have extracted the Eulerian and Lagrangian statistics.

2.1 Eulerian Method

The conservative form of the dimensionless compressible Navier-Stokes equations for flows with two miscible species (i.e. continuity, momentum, energy, and species mass fraction transport equations) were solved numerically together with the perfect gas law using a high-order hybrid numerical method [15]. The inviscid fluxes for the transport equations were computed using the fifth-order monotonicity-preserving (MP) scheme, as described in Refs. [15, 27, 28]. The molecular transport terms were calculated using the sixth-order compact scheme [29]. The 3rd-order Runge-Kutta scheme was used for time advancement.

The physical domain for the simulations considered in this paper is a box that has a dimension of 4π in the streamwise direction (denoted as x) and $(2\pi, 2\pi)$ in the transverse directions (denoted as y and z), as shown in Fig. 1a. A buffer layer is used at the end of the computational domain from 4π to 6π to eliminate reflecting waves. In the transverse directions, periodic boundary conditions are used as the flow is assumed to be periodic and homogeneous in these directions. To provide inflow turbulence, pre-generated decaying isotropic turbulence is superposed on the uniform mean flow with Mach number = 2.0 and convected into the domain using Taylor's hypothesis. The inflow turbulent Mach number, Reynolds number and peak wavenumber are $M_t \approx 0.1$, $Re_\lambda \approx 45$, and $k_0 = 4$, respectively. For this M_t value, Taylor's hypothesis is appropriate for approximating spatially developing turbulence with temporally developing turbulence [30]. The variable density (multi-fluid) effects arise from compositional variations, by correlating the density to an isotropic scalar field. The scalar field is generated as a random field following a Gaussian spectrum with a peak at $k_s = 8.0$ and has double-delta probability density function distribution so that the scalar value initially is either 1.0 or 0.0. The initial scalar field is smoothed by solving a diffusion equation so that the scalar field can be fully resolved by the chosen mesh. The resulting scalar field is then allowed to decay in the fully developed isotropic turbulence setup for one eddy turn over time as a passive scalar. The mass fractions of the two fluids can be extracted from the density field using the infinite speed of sound relation [31, 32], which is approximately satisfied at low turbulent Mach numbers. The Atwood number, $A_t = (W_2 - W_1)/(W_2 + W_1)$, calculated from the molar weights of the two fluids, W_1 and W_2, is 0.28. This value of the Atwood number was chosen such that the variable density effects are non-negligible, yet the interaction with the shock wave is still in the wrinkled-shock regime. The Prandtl number, Pr, and Schmidt number, Sc, are the same and equal to 0.75. The mean flow Mach number, M_s, is 2.0. Immediately before the shock wave, M_t and Re_λ are around 0.09 and 42, respectively.

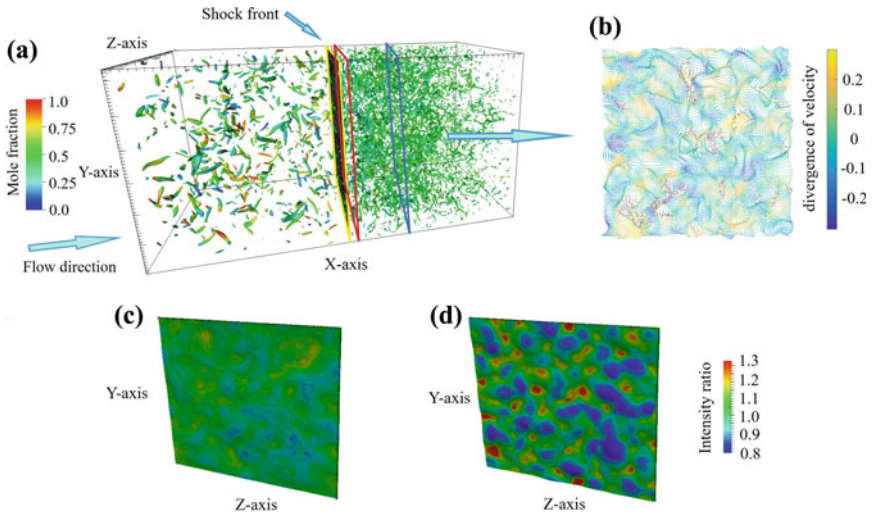

Fig. 1 Instantaneous contours of vorticity and shock surface in isotropic turbulence interacting with a shock wave and the shock Mach number is 2.0. **a** Vortex structure, identified by the Q criteria (i.e. isosurface of the second invariant of VGT: $Q = 2\langle Q_w \rangle$, where $\langle Q_w \rangle$ is the averaged magnitude of rotation tensor) and colored by the mole fraction of the heavy fluid. Fluid particles are initialized as a sheet that spans over the homogeneous directions at a given post-shock streamwise position and allowed to develop with the flow. **b** Visualized particle sheet, convected and distorted by the post-shock turbulence. The instantaneous shock surface is colored by the shock intensity across the shock for **c** single-fluid and **d** multi-fluid cases

2.2 *Lagrangian Method*

For the current study, we have tracked more than 4.5 million particles that are initialized uniformly at various streamwise positions $\vec{x}_0$, and calculated various turbulence structure statistics following their trajectories. The aim is to understand the evolution of flow structures following fluid particles. Figure 1a marks with red lines a typical streamwise plane where particles are initialized. The particles are then convected by the instantaneous turbulent velocity obtained by turbulence-resolving shock-capturing simulations [15] and moved to another plane marked by the blue lines. At this stage, the initially flat particle sheet is distorted by the turbulence as shown in Fig. 1b.

The fluid particles are non-inertial and follow the local flow velocity. The corresponding transport equations for particle positions x_i^+ are:

$$\frac{dx_i^+(t|\vec{x}_0, t_0)}{dt} = u_i^+(t|\vec{x}_0, t_0), \tag{1}$$

$$u_i^+(t|\vec{x}_0, t_0) = u_i(x_i^+, t), \tag{2}$$

where $x_i^+(t|\vec{x}_0, t_0)$ represents the positions of the particles at time t that are initialized at $\vec{x}_0$ and time t_0. The particle velocity $u_i^+(t|\vec{x}_0, t_0)$ can be obtained from the Eulerian velocity field $u_i(x_i^+, t)$ by interpolation. The interpolation is based on the cubic spline scheme, whose accuracy in predicting particle positions has been studied in Ref. [33]. In the STI configuration, there is a sharp change of the flow velocity at the shock, which deteriorates the interpolation accuracy. To achieve accurate interpolation of the particle velocity, the domain is partitioned into three different regions as shown in Fig. 1a: pre-shock, shock, and post-shock regions. The instantaneous shock surface is identified using the sensor: $s = -\theta/(|\theta| + \langle\omega_i\omega_i\rangle_{yz}^{0.5}) > 0.5$, where $\theta = \partial u_i/\partial x_i$ is the dilatation, $\omega_i = \epsilon_{ijk}\partial u_k/\partial x_j$ is the vorticity, and $\langle\rangle_{yz}$ represents the instantaneous average over the homogeneous directions. After the instantaneous shock region is identified, the pre- and post-shock turbulence fields can be separated for interpolation. Lagrangian dynamics of particles across the shock wave is not considered in this study.

3 Numerical Accuracy

The accuracy of the numerical results is addressed in this section through a series of convergence tests. To ensure that all the turbulence length scales are well resolved, a grid convergence test was conducted in Ref. [15]. Here, we summarize these results for completeness, together with additional convergence results for small-scale quantities. Figure 2 shows the velocity dissipation rate ε and mass fraction dissipation rate ε_ϕ as a function of the normalized streamwise direction k_0x for a series of meshes. The grey regions in the following figures indicate the unsteady shock region, inside which the results are affected by the shock wrinkling and unsteady shock movement. As the grid is refined in all three directions, both quantities display convergence,

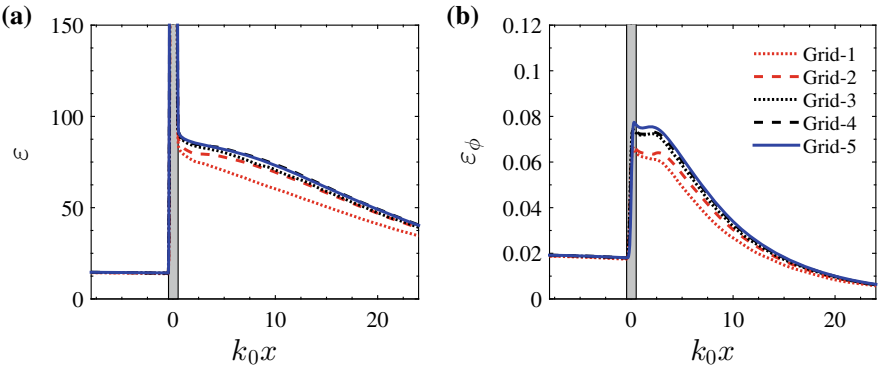

Fig. 2 Results of multi-fluid grid convergence tests at $Re_\lambda = 42$ and $M_t = 0.09$. Streamwise development of **a** velocity dissipation rate ε and **b** mass fraction dissipation rate ε_ϕ is shown. The region of unsteady shock movement is marked in grey. Grid numbers for Grid 1–5 are $256 \times 256 \times 1024$, $384 \times 384 \times 1024$, $384 \times 384 \times 1536$, $512 \times 512 \times 1536$, $512 \times 512 \times 2048$

proving the accuracy of the turbulence database. Another aspect that needs to be considered is the scale separation between the numerical shock thickness δ_n and the Kolmogorov length scale η as suggested in our previous study [15]. With the finest mesh ($512 \times 512 \times 2048$), the scale separation ratio (η/δ_n) is around 1.9, which is sufficient for resolving the interaction between the numerical shock wave and small-scale turbulent motions. Therefore, in the current study, we have obtained all the statistics from the turbulence field based on the finest grid to ensure accuracy. Secondly, LIA convergence tests were conducted following Ref. [11] to show that the shock-capturing simulations can capture the correct limits. Turbulent Mach number (M_t) and Taylor Reynolds number (Re_λ) were varied for the canonical single-fluid simulations, covering a wide range of parameter space. The shock-capturing simulation results do converge to LIA predictions for individual Reynolds stress components as long as certain conditions are satisfied [15]. This was the first time that the asymptotic values for individual Reynolds stresses were approximated using shock-capturing simulations.

Statistical convergence is another important factor that needs to be addressed before any further analysis. To reduce the statistical variability, all the results that are based on the Eulerian data are space-averaged over homogeneous directions and time-averaged for around two pass-over times.

For the Lagrangian statistics, the number of fluid particles needs to be large enough for statistical convergence, especially for conditional averaged statistics. The conditional statistics are obtained by ensemble averaging over all the fluid particles that fall into the bins (see Eq. (14)). The number of samples needed to achieve statistical convergence will be examined for different bin sizes. Figure 3 shows the convergence of two important conditional Lagrangian statistics $\langle \frac{DQ}{Dt} \rangle / \langle Q_w \rangle^{3/2}$, $\langle \frac{DR}{Dt} \rangle / \langle Q_w \rangle^2$ and their standard deviation (see Sect. 4.3 for definitions), depending on the number of particles in each bin. For the multi-fluid case, we note that the convergence of both conditional means and standard deviations can be achieved when using around

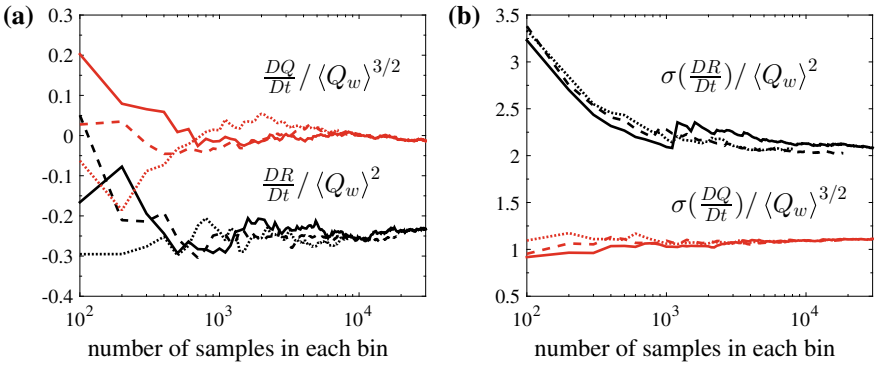

Fig. 3 The statistical convergence for **a** $(DQ/Dt)/\langle Q_w \rangle^{3/2}$ and $(DR/Dt)/\langle Q_w \rangle^2$ and **b** their standard deviations conditioned at point (3.0, 3.0) in the (Q, R) phase plane for multi-fluid case. The number of bins are 30×30 (solid), 40×40 (dashed) and 60×60 (dotted)

10,000 particles. The effects of the bin sizes are also examined by comparing three different set of bin numbers 30×30, 40×40 and 60×60 in the (Q, R) phase plane at the same point (3.0, 3.0). These bin numbers correspond to the following bin sizes: (1.3, 1.3), (1.0, 1.0) and (0.67, 0.67). Our analysis indicate that the statistics converge to almost the same value when the sample size is large enough. In the present study, we uniformly sampled more than 4.5 million particles and made sure that there are at least 10,000 particles in each sample bin with the number of bins being 40×40 ($(\Delta Q, \Delta R) = (1.0, 1.0)$).

4 Results and Discussions

In this section, the effects of density variations on STI are examined in detail by comparing the results obtained from variable density (VD) or "multi-fluid" cases with those obtained from a reference 'single-fluid' simulation. The single-fluid reference simulation was conducted using the same inflow conditions for turbulent variables except density. In this reference case, the mass fraction of the heavy fluid is set to 1.0. At the same time, a passive scalar equation, which is the same as the mass fraction equation in the multi-fluid case, is solved for comparison. This case is referred to as just the single-fluid case and used as a reference to study the effects of VD on STI. For all cases, the turbulence is allowed to adjust itself to the scalar field in the pre-shock region before interacting with the normal shock. Statistical averages are computed over homogeneous directions to obtain statistics of the flow. Reynolds averages are denoted by an overbar, $\overline{f}$, while Favre averages are denoted by a tilde, $\widetilde{f}$; the corresponding fluctuations around these averages are denoted by f' and f''.

4.1 General Effects of Density on STI

Averaged flow statistics are compared in Fig. 4 for single-fluid and multi-fluid cases. Before the shock wave, all cases yield the same results. This observation not only confirms that the inflow conditions are somewhat similar in these cases, but also implies that for current simulation, the effect of density variations on turbulence is small in the pre-shock region. When comparing the multi-fluid turbulent kinetic energy and vorticity variance with the corresponding single-fluid values in Fig. 4a, d, it is noted that the amplification in these turbulent statistics is much more significant in the multi-fluid cases. Furthermore, the multi-fluid turbulent kinetic energy reaches a peak around $k_0 x \approx 2.0$, which is closer to the shock than $k_0 x \approx \pi$ for single-fluid case. Figure 4b, c show the comparison for streamwise turbulence Taylor micro length scale, λ_1, and Kolmogorov length scale, η. The reduction in turbulence length scales across the shock wave is evident in these figures; the multi-fluid cases show more reduction than the single-fluid case. Note that the changes in turbulence statistics

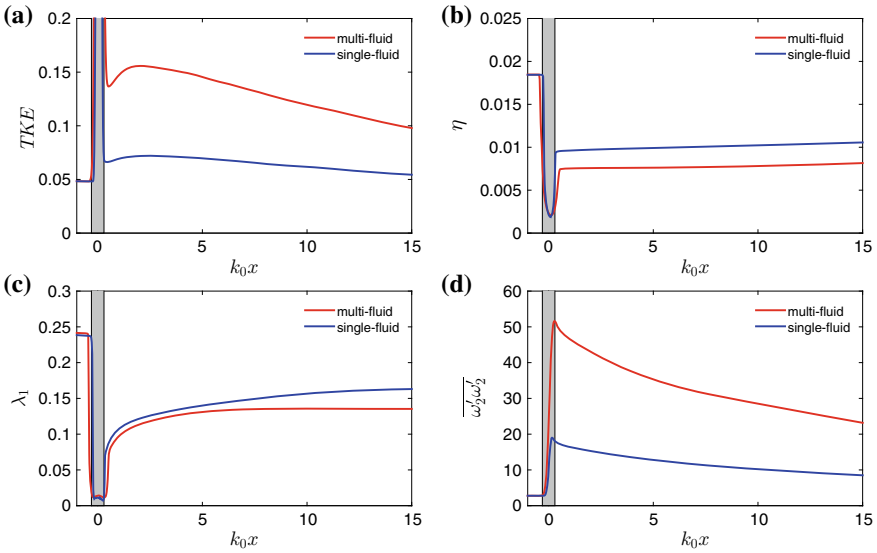

Fig. 4 Plots of **a** turbulent kinetic energy, **b** Kolmogorov length scale, **c** Taylor micro scale and **d** transverse vorticity variance for multi-fluid (red) and single-fluid (blue) simulations. Figure reprinted with permission from Tian et al. [15]

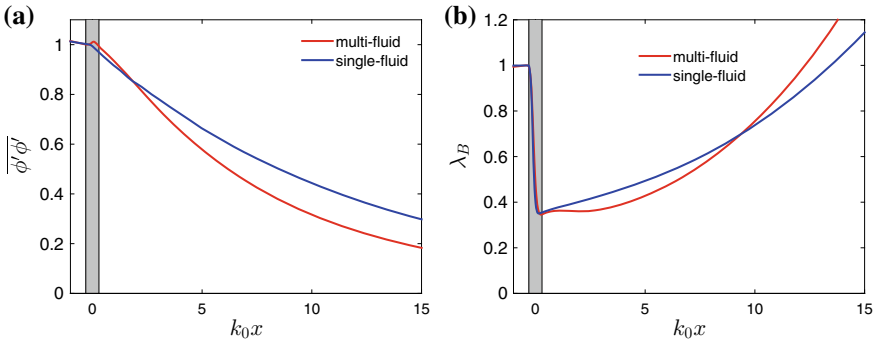

Fig. 5 Plots of normalized **a** scalar variance, **b** Batchelor scale for multi-fluid (red) and single-fluid (blue) simulations. Figure reprinted with permission from Tian et al. [15]

in multi-fluid cases are expected to depend on the scalar structure and the Atwood number [34]; these are not discussed in this paper.

In Fig. 5, statistics related to the scalar field (heavy fluid mole fraction for multi-fluid case and passive scalar for the single-fluid case) and mixing are compared. Both scalar variance $\overline{\phi'\phi'}$ and Batchelor scale λ_B are shown. λ_B is calculated based on the scalar dissipation and is the representative of the smallest scales in the scalar field. The scalar statistics are normalized by the values immediately before the shock wave. After passing through the shock wave, the faster decay of scalar variance for the multi-

fluid case indicates stronger shock enhancement of scalar mixing. The Batchelor scale, however, shows a more complex behavior. Unlike the Kolmogorov length scale, the same reduction ratio of Batchelor scale across the shock wave is observed between the multi-fluid and single-fluid cases. After passing through the shock wave, the Batchelor scales of multi-fluid cases exhibit a transient process of decreasing before returning to the pre-shock value, during which an even smaller structure of the scalar field is generated. In the single-fluid case, however, the Batchelor scale increases monotonically back to its pre-shock value. We also note that after $k_0 x \approx 10.0$, the multi-fluid λ_B values are larger than the single-fluid values as the faster mixing immediately after the shock smooths out the small scalar scales.

To further understand the variable density effects, conditional expectations of several turbulence quantities, conditioned on the density, are calculated and examined. In Fig. 6a, the conditional expectation of the turbulent kinetic energy, TKE, is shown. We note that TKE has a preferential distribution in the relatively high or low density regions in the post-shock regions. One possible explanation is that in high and low density regions, the local sound speed has different values from that of average sound speed, so that the local shock velocity, $u_{1,s}$ becomes nonzero (in the reference frame of the laminar shock wave) and changes significantly. The local movement of the shock surface then further changes the post-shock velocity, $u_{1,d}$ and makes it deviate from the averaged post-shock velocity $\overline{u_{1,d}}$. The deviation from $\overline{u_{1,d}}$ or u_i' in low and high density regions is much larger in magnitude than that in regions with moderate density, which results in larger TKE in the high and low density regions. We have computed the conditional average of u_i' on density. Results agree very well with our explanation for conditional TKE. We also note that TKE is larger in the light fluid regions compared to heavy fluid regions. This is due to the low inertia of the light fluid, which responds faster to the changes in the local strain and, thus, accelerates faster [35, 36]. This explanation is also applicable to Fig. 6b for single-fluid case, which shows a preferential distribution of TKE in the lower density fluid region before the shock wave. After passing through the shock

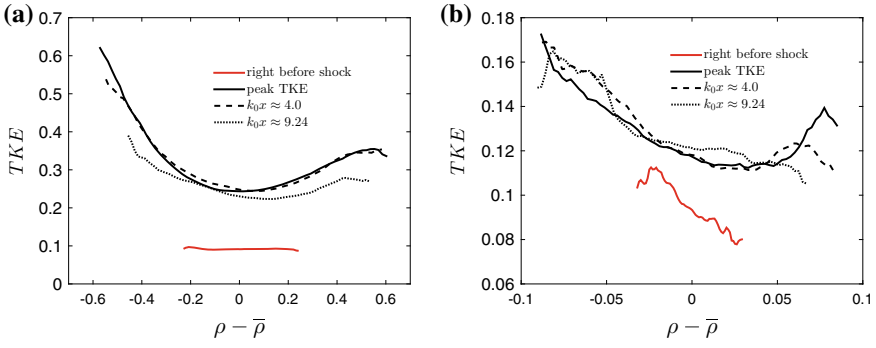

Fig. 6 Conditional expectation of TKE as a function of density at various streamwise location for: **a** multi-fluid and **b** single-fluid case. Figure reprinted with permission from Tian et al. [15]

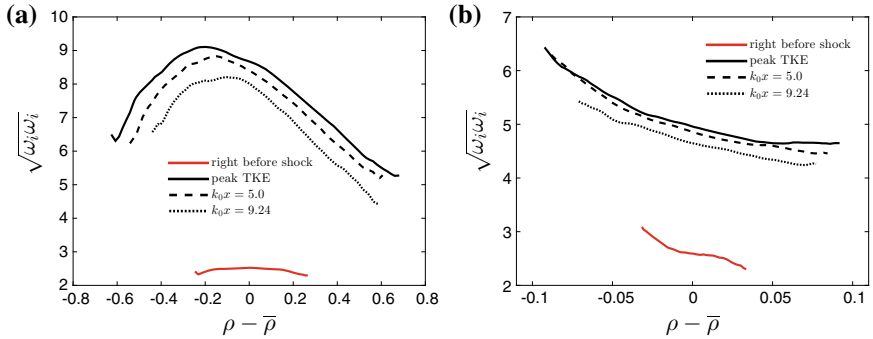

Fig. 7 Conditional expectation of enstrophy as a function of density at various streamwise location for: **a** multi-fluid and **b** single-fluid case. Figure reprinted with permission from Tian et al. [15]

wave, a stronger amplification in the high and low density regions is noted but this is relatively weak.

The correlation between vorticity and density has a completely different behavior than TKE. Evidently, Fig. 7 shows that more vorticity is generated in the mixed fluid regions. Before reaching the shock wave, the mixing process is relatively slow, so that there are still large regions with pure or partially mixed fluids and only narrow regions with fully mixed fluids. In these regions, the density gradients remain large. Through the interaction with the shock wave, the large density gradients lead to the generation of vorticity through the baroclinic torque. For the single-fluid case (Fig. 7b), the distribution of vorticity is not affected much by the shock because of the absence of large density variations.

4.2 Structure and Topology of the Post-shock Turbulence

References [1, 3, 9, 12] showed that STI leads to a two-dimensionalization of the flow immediately after the shock, i.e. the flow becomes locally axi-symmetric. The vortex stretching term is therefore the smallest immediately after the shock. This term then increases as the flow evolves away from the shock and returns to a 3-D structure. Following the expression of the vortex-stretching term in Ref. [12], the turbulent stretching term can be decomposed into contributions from eigenvectors and eigenvalues of strain rate. After normalizing the turbulent stretching term in the enstrophy equation using $\overline{\omega_2'\omega_2'}$ and the turbulence time scale TKE/ϵ (where ϵ is the rate of dissipation), the effects of the eigenvectors and eigenvalues of the strain rate can be isolated. As shown in Fig. 8, the magnitude of turbulent stretching decreases to around zero across the shock wave. During the transient post-shock process, the multi-fluid case exhibits a faster return to 3-D isotropic turbulence structure, indicated by the faster increase in the normalized turbulent stretching term. Further

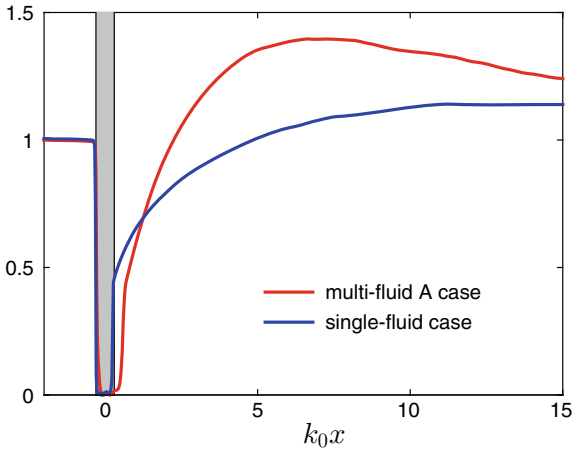

Fig. 8 Vortex-stretching term in the enstrophy equation, normalized by $\overline{\omega_2\omega_2}$ and turbulence time scale TKE/ϵ. Figure reprinted with permission from Tian et al. [15]

downstream, the multi-fluid case reaches its peak value much sooner than the single-fluid case. The behavior of the normalized turbulent stretching term indicates that the contributions to the return to 3-D turbulence not only come from increased enstrophy amplification, but also from the change of alignment between vorticity and strain rate tensor eigenvectors.

The preferential amplification of the transverse components of the rotation and strain rate tensors is a well-known effect in STI and has been extensively studied for the canonical single-fluid flows [7, 11, 12]. This amplification can lead to an increase in the correlation between the two quantities. When density variations are introduced, Ref. [15] showed that the transverse components of vorticity variance are further enhanced across the shock wave while the streamwise component retains almost the same value. To better understand the variable density effects on post-shock turbulence, the PDF of the strain-enstrophy angle, Ψ, is considered in Fig. 9. Ψ is calculated using $\Psi = tan^{-1}(S_{ij}S_{ij}/(W_{ij}W_{ij}))$, where $S_{ij} = 1/2(A_{ij} + A_{ji})$ and $W_{ij} = 1/2(A_{ij} - A_{ji})$ are the strain and rotation tensors and $A_{ij} = \partial u_i/\partial x_j$ is the velocity gradient tensor. In isotropic turbulence, the PDF of Ψ peaks at 90° [37], indicating a strain dominated flow. In single-fluid post-shock turbulence, the PDF of Ψ exhibits a shift of the peak from 90° to around 45°, as the shock Mach number increases. This has been observed by Livescu and Ryu [12] and is interpreted as the increase in correlation of strain and rotation. However, in the multi-fluid case, the peak still occurs at relatively large angles and the increase in correlation is not as pronounced as that in the single-fluid case, at the same shock Mach number. Figure 9 implies that the rotation and strain are amplified differently by the shock when large density variations are present, which compromises the correlation between the above two quantities.

To understand the effects of the density variations on the strain and rotation tensors as the flow interacts with the shock wave, the pre- and post-shock values of the conditional expectations of the magnitudes of the two tensors are shown in Fig. 10 for

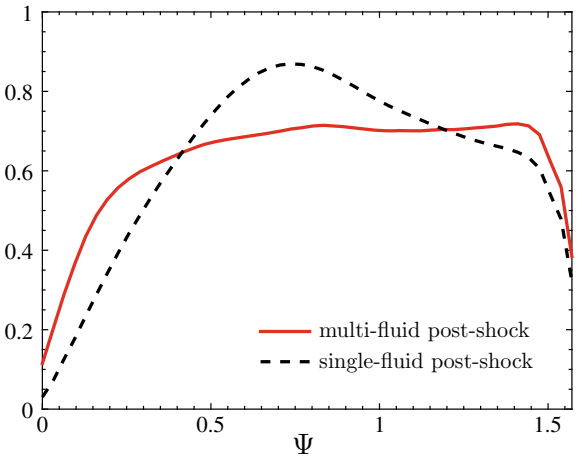

Fig. 9 PDF of the strain-enstrophy angle Ψ in degrees for post-shock turbulence

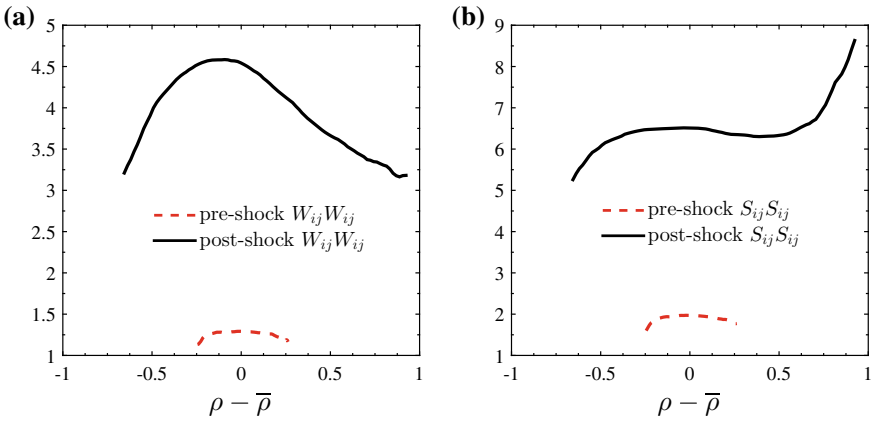

Fig. 10 Conditional expectation of the magnitude of **a** rotation tensor and **b** strain rate tensor as a function of density before and after the shock

the multi-fluid case. The amplification of vorticity is stronger in the mixed fluid region as shown and explained in the last section. On the other hand, Fig. 10b shows that the magnitude of the strain rate tensor tends to be stronger in the heavy fluid regions and weaker in the light fluid region. This trend is hypothesized to be related to the dependence of shock strength on the pre-shock density. Reference [15] showed that shock strength is positively correlated with density. In the highest density regions, the shock compression is also stronger, while it is weaker in the smallest density regions, leading to the observed trend in the amplification of the strain rate tensor magnitude. This trend is different from that observed for the vorticity, which is explained above. As a result, the trend of the strain-enstrophy angle PDF peaking around 45°, observed

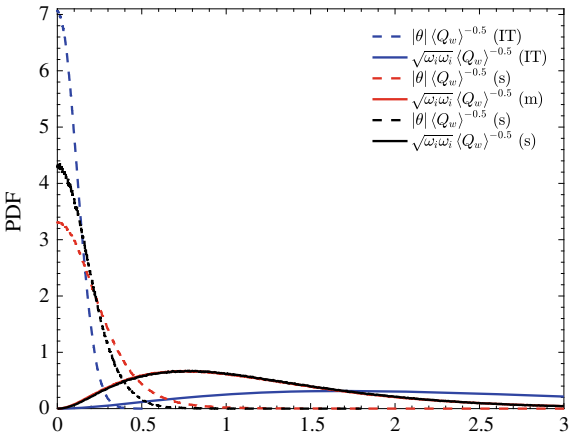

Fig. 11 PDFs of the normalized dilatation and vorticity for isotropic turbulence (IT), single-fluid post-shock turbulence, and multi-fluid post-shock turbulence

in the single fluid case at higher shock Mach numbers is weakened in the multi-fluid case.

To further characterize the turbulence structure behind the shock wave, we have analyzed the invariant space of the VGT. The second and third invariants (denoted by Q^* and R^*) of the anisotropic/deviatoric part of the VGT can reveal important features of the flow topology [38]. In highly compressible turbulence, there exits a richer set of flow topologies due to the dilatational part of the velocity gradient tensor [39]. For the parameter range considered in this study; however, the compressibility effects are weak. This is demonstrated in Fig. 11, where the normalized PDFs of the dilatation and vorticity for pre-shock isotropic turbulence, single-fluid, and multi-fluid post-shock turbulence are shown. The pre-shock isotropic turbulence has a very low magnitude of dilatation. The shock wave expectedly amplifies the dilatation magnitude, and more so when variable density effects exist, but the dilatation values are still considerably lower than those studied in Refs. [39–41]. Considering that the focus of this study is on the variable density effects, here we only present the topological structure of the anisotropic velocity gradient tensor, using data points where $P \approx 0$. These regions encompass about 60% of the flow. The anisotropic part of the VGT is calculated using the formula $A^*_{ij} = A_{ij} - \theta/3I$. Correspondingly, the second and third invariants can be calculated from:

$$Q^* = -\frac{1}{2}A^*_{ij}A^*_{ji}, \tag{3}$$

$$R^* = -\frac{1}{3}A^*_{ij}A^*_{jk}A^*_{ki}, \tag{4}$$

Based on the local values of Q^* and R^*, four types of local flow topologies can be identified: stable-focus/stretching (SFS), unstable-focus/contracting (UFC), stable-node/saddle/saddle (SN/S/S) and unstable-node/saddle/saddle (UN/S/S). For isotropic turbulence, the joint PDF of (Q^*, R^*) has the well-known tear-drop shape.

This has been further observed in other fully developed turbulent flows, such as boundary layers, mixing layers, and channel flows [38, 42]. This type of distribution of Q^* and R^* is an indicator that the turbulence is more likely having a local topology of stable-focus/stretching or an unstable-node/saddle/saddle. In Fig. 12a, it is shown that the joint PDF of normalized second and third invariants, $Q^*/\langle Q_w \rangle$ and $R^*/\langle Q_w \rangle^{3/2}$, has the same tear-drop shape in the pre-shock flow. Using shock-LIA and DNS data, Ref. [11] showed that for single-fluid STI, the (Q^*, R^*) distribution is significantly modified by the shock wave, with a tendency towards symmetrization of the joint PDF. This indicates that the regions with stable-focus/compression and stable-node/saddle/saddle (first and third quadrant) are more likely to occur as turbulence develops a 2-D axisymmetric flow structure. To understand the variable density effects on this shock-induced symmetrization, the joint PDFs of (Q^*,R^*) for both single-fluid and multi-fluid post-shock turbulence are compared in Fig. 12b, c.

Figure 12b shows the joint distribution for the single-fluid post-shock turbulence. The dashed lines denote the locus of zero discriminant of A^*, where Q^* and R^* satisfy $27R^{*2}/4 + Q^{*3} = 0$. Compared to the pre-shock joint PDF, there is a tendency towards symmetrization, with more points located in the first and third quadrants. This agrees very well with previous shock-LIA results [11]. Similar to single-fluid STI, multi-fluid STI demonstrates a tendency towards symmetrization of the (Q^*, R^*) distribution. However, the multi-fluid distribution is slightly more symmetric and has a larger variance, with more points away from the axes. This implies that more extreme "events" exist in the post-shock multi-fluid turbulence. It also agrees with previous results on multi-fluid STI that shows amplification of TKE to be stronger when there are significant density variations [15, 16].

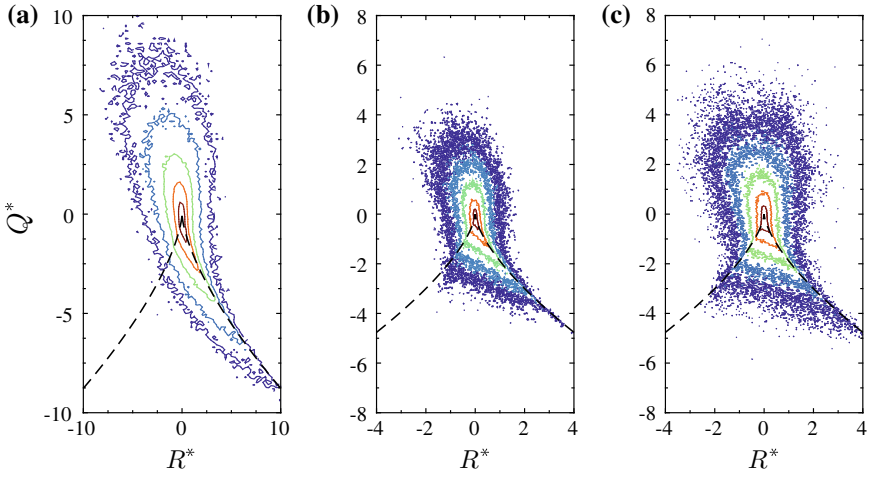

Fig. 12 Iso-contour lines of joint PDFs of normalized second and third invariants of the anisotropic part of the velocity gradient tensor, (Q^*,R^*), for **a** pre-shock, **b** single-fluid post-shock turbulence, and **c** multi-fluid post-shock turbulence. The lateral lines denote the locus of zero discriminant

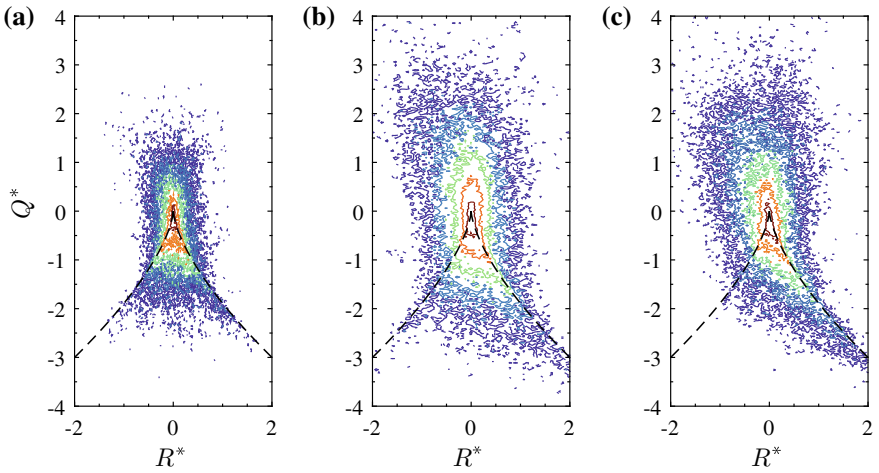

Fig. 13 Iso-contour lines of post-shock ($k_0 x \approx 0.44$) joint PDF of second and third invariants of the anisotropic part of the velocity gradient tensor, (Q^*,R^*), in regions with different densities. **a** Regions with high density values, $\rho > (\overline{\rho} + 90\%\rho'_{rms})$, **b** regions with density around the post-shock mean value, and **c** regions with low density values, $\rho < (\overline{\rho} - 90\%\rho'_{rms})$

The density effects on the post-shock joint PDF of second and third invariants are further explored by comparing the conditional distribution, conditioned on regions with different densities, in Fig. 13a–c. Figure 13a corresponds to regions with relatively high density ($\rho > (\overline{\rho} + 90\%\rho'_{rms})$), Fig. 13b to regions with density around the post-shock mean value, and Fig. 13c to low density regions ($\rho < (\overline{\rho} - 90\%\rho'_{rms})$). For consistency check, the joint PDFs corresponding to these regions are also computed for the pre-shock flow (not shown) and found to be close to the single-fluid PDFs. After the shock wave, the joint PDFs demonstrate significant differences between regions with different densities. In regions with density closer to that of post-shock mean density, the distribution of invariants appears to be very similar to that shown in Fig. 12c. But for regions with higher density (Fig. 13a), the joint PDF becomes more symmetric compared to the overall flow or single-fluid case. There is a much larger portion of data points having a local topology of stable-node/saddle/saddle, and fewer data points fall into the first and second quadrants, indicating larger strain-dominated regions. On the other hand, the post-shock regions with low-density values (Fig. 13c) exhibit features similar to that of isotropic turbulence, with almost the same tear-drop shape, only with a larger variance or a wider distribution. The quantitative difference is hypothesized to be related to the higher shock strength variation in the multi-fluid case. It was observed in our previous studies [43], that the local shock strength is positively correlated with the pre-shock density. With a stronger shock, the two-dimensionalization effect on the post-shock turbulence should also appear stronger in the high-density regions [12]. For low-density regions, the smaller two-dimensionalization effect reduces the symmetrization trend. Moreover, the relatively lower inertia in these regions leads to a faster response to

the local strain field [36], which could make a faster return to isotropic turbulence. The different characteristics of (Q^*, R^*) joint PDF in regions with different densities provide additional evidence for the previous argument made about the density role on the preferential amplification of the strain and rotation tensors.

4.3 Lagrangian Dynamics of VGT

Lagrangian equations of the VGT and its invariants can be used to understand the evolution of turbulence structure. The time evolution of A_{ij} for fluid particles can be obtained by taking the spatial derivatives of the Navier-Stokes equations. In dimensionless form, it can be written as [40]:

$$\frac{DA_{ij}}{Dt} = \frac{\partial A_{ij}}{\partial t} + u_k \frac{\partial A_{ij}}{\partial x_k} = -A_{ik}A_{kj} - H_{ij} + \mathcal{T}_{ij}, \tag{5}$$

with

$$H_{ij} = \frac{\partial}{\partial x_j}\left(\frac{1}{\rho}\frac{\partial p}{\partial x_i}\right) = -\frac{1}{\rho^2}\frac{\partial \rho}{\partial x_j}\frac{\partial p}{\partial x_i} + \frac{1}{\rho}\frac{\partial p^2}{\partial x_i \partial x_j} = H^b_{ij} + H^p_{ij}, \tag{6}$$

$$\mathcal{T}_{ij} = \frac{\partial}{\partial x_j}\left(\frac{1}{\rho}\frac{\partial \sigma_{ik}}{\partial x_k}\right),\ \sigma_{ij} = \frac{\mu}{Re_0}\left(\frac{\partial u_i}{\partial x_j} + \frac{\partial u_j}{\partial x_i} - \frac{2}{3}\frac{\partial u_k}{\partial x_k}\delta_{ij}\right), \tag{7}$$

where Re_0 is the reference Reynolds number. From here, the dynamic equations for the three invariants of the VGT, P, Q, and R can be derived in the following form [40]:

$$\frac{DP}{Dt} = (P^2 - 2Q) + H^p_{ii} + H^b_{ii} - \mathcal{T}_{ii}, \tag{8}$$

$$\frac{DQ}{Dt} = (PQ - 3R) + (PH^p_{ii} + A_{ij}H^p_{ji}) + (PH^b_{ii} + A_{ij}H^b_{ji}) + (-P\mathcal{T}_{ii} - A_{ij}\mathcal{T}_{ji}), \tag{9}$$

$$\frac{DR}{Dt} = PR + (QH^p_{ii} + PA_{ij}H^p_{ji} + A_{ij}A_{jk}H^p_{ki}) + (QH^b_{ii} + PA_{ij}H^b_{ji} + A_{ij}A_{jk}H^b_{ki}) + (-Q\mathcal{T}_{ii} - PA_{ij}\mathcal{T}_{ji} - A_{ij}A_{jk}\mathcal{T}_{ki}), \tag{10}$$

where the three invariants of VGT are defined as:

$$P = -tr(A_{ij}), \tag{11}$$

$$Q = \frac{1}{2}(tr(A_{ij})^2 - tr(A_{ij}A_{jk})), \tag{12}$$

$$R = -det(A_{ij}), \tag{13}$$

Here, $tr(A_{ij})$ and $det(A_{ij})$ denote the trace and determinant of a tensor. Note that instead of the deviatoric part of the VGT, the dynamic equations for the full VGT are considered. The reason is that due to the variable density effects and shock compression, the incompressibility condition is not satisfied especially when M_t and A_t become large. Even though M_t and A_t in this study are small, we still consider the full equations for any future comparisons. The contributions from the dilatational part of the VGT and their coupling with the variable density effects in highly compressible turbulence are still unknown and need to be explored for STI in future studies.

The dynamical equations can be divided into contributions by four different parts: (I) mutual-interaction among invariants, (II) pressure Hessian, H_{ij}^p, (III) baroclinic, H_{ij}^b and (IV) viscous term $\mathcal{T}_{ij}$. The statistics regarding these terms can be extracted from the Lagrangian data.

The Lagrangian dynamics of the turbulence and the evolution of flow topology are examined by considering the conditional mean rate of change of Q and R in the invariants plane [22]. The rates of change are used to form a vector at each point in the invariants plane. The trajectories implied by these vectors can be followed to understand the return-to-isotropy. In fully compressible turbulence, the (P, Q, R) invariant space becomes three-dimensional [39–41] and there exists an out-of-plane (Q, R) component of the trajectory due to the contribution from compressibility (P) effect. Due to the low compressibility effect in this work, however, it would be more appropriate to consider only the in-plane (Q, R) dynamics and leave the compressibility effects for future study. Therefore, the results presented below correspond to the data points with small magnitude of P ($|P|/\langle Q_w\rangle^{0.5} < 0.1$) for the relatively "incompressible" region of the flow. These points comprise approximately 60% of the flow. The procedure used to obtain the conditional mean vectors (CMVs) in this study is similar to that in Ref. [22]. The condition averages are computed using the formula:

$$\langle X|(A = A_0, B = B_0)\rangle = \langle X|(A_0 - \frac{1}{2}\Delta A) \le A < (A_0 + \frac{1}{2}\Delta A), \\ (B_0 - \frac{1}{2}\Delta B) \le B < (B_0 + \frac{1}{2}\Delta B)\rangle, \tag{14}$$

therefore, $X(Q, R)$ represents a statistical quantity that is conditioned on Q and R.

The normalized conditional mean vectors $(DQ/Dt/\langle Q_w\rangle^{3/2}, DR/Dt/\langle Q_w\rangle^2)$ for different flows are shown in Fig. 14. The vectors obtained from isotropic turbulence data are shown in Fig. 14a for reference. It can be seen that the CMVs exhibit a circulating behavior in the (Q, R) plot around the origin in the clockwise direction, indicating that the flow evolves from SFS to UFC, UN/S/S, SN/S/S then back to SFS on average. This circulating behavior represents the Lagrangian dynamics in fully developed turbulence that maintains the tear-drop shape of the (Q, R) distribution. This has been observed in many incompressible/compressible canonical turbulent flows [22, 40]. The CMVs for single-fluid and multi-fluid post-shock turbulence are shown in Fig. 14b, c. Evidently, the joint PDF of (Q, R) becomes more symmetric due to shock compression. From the Lagrangian point of view, the circulating

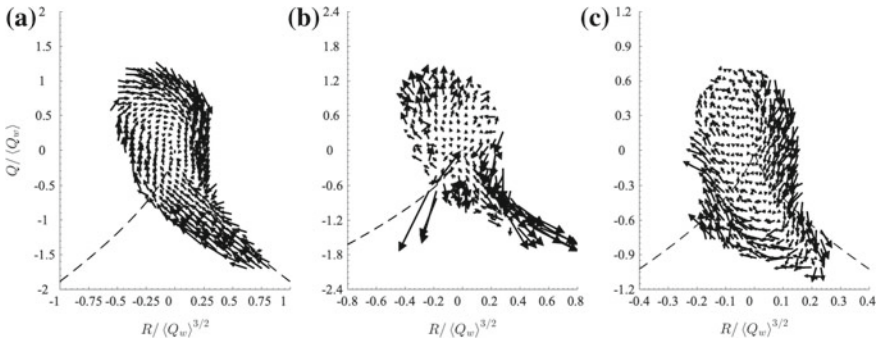

Fig. 14 Conditional mean rate of change vectors of $(DQ/Dt/\langle Q_w\rangle^{3/2}, DR/Dt/\langle Q_w\rangle^2)$ in the (Q, R) plane for **a** isotropic turbulence, **b** single-fluid post-shock turbulence, and **c** multi-fluid post-shock turbulence at streamwise location of $k_0x \approx 0.5$. To ensure that the vectors can be properly visualized, their sizes are re-scaled by multiplying with a constant of 0.3. This applies to all the following vector plots

behavior as seen in Fig. 14a isotropic turbulence is weakened. The particles in Q_2 tend to have an increasing Q and decreasing R, resulting in an overall trend of getting away from the original point, instead of circulating and then moving toward Q_1. This trend in the second quadrant represents an increase of enstrophy. The particles in Q_1 have similar dynamics as in isotropic turbulence and tend to move downward in the (Q, R) plane toward the zero discriminant curve. The particles in Q_3 are more likely to move straight up towards Q_2, while those in Q_4 are likely to move away from the original point following the direction of the zero discriminant line and then circulate back to Q_3. The overall behavior formed by these particles demonstrates the return-to-isotropy process, with an enlarging head in the second quadrant and elongating tail in the fourth quadrant, anticipating the formation of the classic tear-drop shape.

The density effects can be further examined by conditioning the $(DQ/Dt, DR/Dt)$ vector field on the local density. Figure 15a shows the CMVs for the light fluid regions. The light fluid particles retain the circulating motion, except that the particles in Q_3 and Q_4 are likely to go straight left instead of following the zero discriminant line. In general, the flow dynamics in the light fluid regions are less affected by the shock wave. For the medium density fluid regions (Fig. 15b), the circulating motion disappears. On the right side of the (Q, R) plane $(R > 0)$, which is the strong dissipation-production region, the fluid particles tend to move downward, resulting in lower Q values. On the left side of the (Q, R) plane $(R < 0)$, which is the enstrophy-production dominated region, the fluid particles tend to move to the left, indicating an increased enstrophy-production. The overall downward-moving behavior of the medium density fluid particles is indicative of decreasing vorticity. This is possibly due to the fact that vorticity is preferentially amplified in the medium density region across the shock wave. After passing the shock wave, the vorticity will decrease as the correlation between density and vorticity vanishes. Figure 15c shows the CMVs for the heavy fluid regions. Interestingly, the heavy fluid particles exhibit

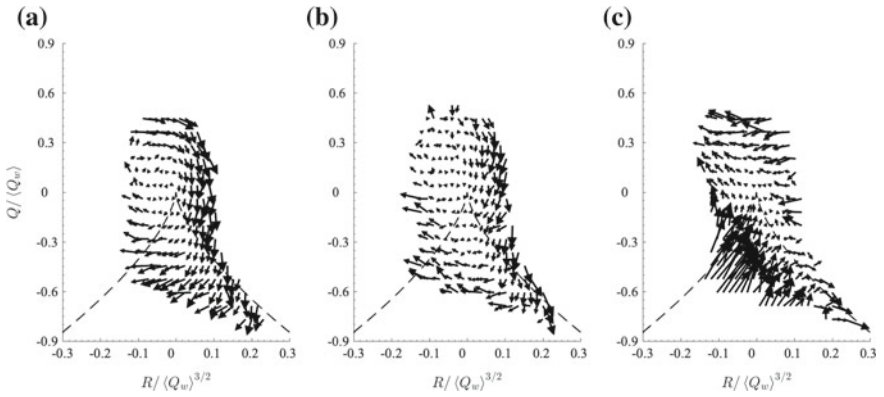

Fig. 15 Conditional mean vectors in the (Q, R) invariants plane for **a** light fluid, **b** medium density fluid and **c** heavy fluid at streamwise location of $k_0 x \approx 0.5$

counterclockwise motion. The heavy particles start from Q_3 and move to Q_4, Q_1, and finally to Q_2. This implies that they become vorticity dominated due to the fast depletion of strain. Evidently, density plays an important role in the development of the flow topology in the post-shock region, so special attention should be made to the modeling of variable density STI.

To better understand the underlying mechanisms that cause the behavior highlighted above, the dynamic Eqs. (9) and (10) governing the vector $(DQ/Dt, DR/Dt)$ are examined. The Lagrangian dynamics of the flow can be understood better by considering the conditional mean vectors of different terms in the (Q, R) plane. As a reference, these terms are shown in Fig. 16 for isotropic turbulence. The variable Q tends to be amplified in the enstrophy-production dominated region due to the effects of vortex stretching mechanism and is decreased in the dissipation-production dominated region due to self-amplification of the strain rate tensor. On the other hand, the mutual effects on R are small because the first invariant P is usually small and the positive and negative values are likely to cancel each other. The contributions from the pressure Hessian (Fig. 16b) tend to move the particles away from an asymptotic line, ending up amplifying the magnitude of R. This result agrees well with that observed in turbulent boundary layers [40]. For the current simulation, the asymptotic line starts from Q_2 and ends in Q_4 with a slope of around -2.5. The baroclinic contributions are very small in the post-shock turbulence as shown in Fig. 16c. The viscous effects as shown in Fig. 16d and as expected are reducing the magnitudes of Q and R and pushing the particles towards the origin. This has been observed in various types of turbulence [22, 40]. The combined effects from the four above mechanisms determine the circulating behavior of the conditional mean of $(DQ/Dt, DR/Dt)$ vectors.

For multi-fluid post-shock turbulence, the pressure Hessian term is also the only term that is qualitatively different than that in isotropic turbulence (Fig. 17). Despite the increased density and pressure gradient in the multi-fluid case, the baroclinic term

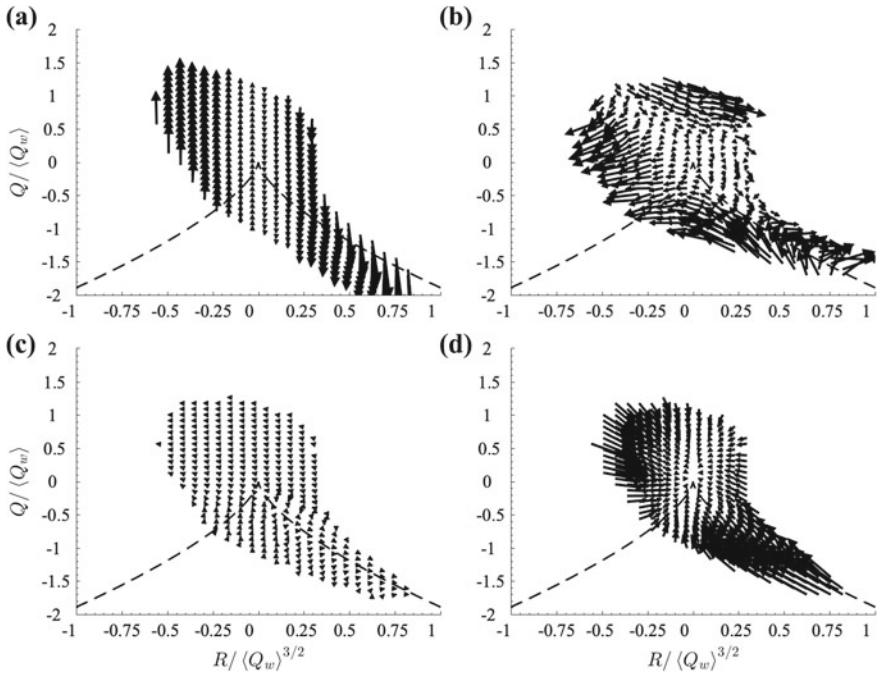

Fig. 16 Contributions to the transport equations of the VGT invariants by different terms for isotropic turbulence. **a** Mutual interaction among invariants, **b** pressure Hessian term, **c** baroclinic term, and **d** viscous term

is still considerably smaller than all the other terms. In Q_2 and Q_3, an asymptotic line similar to that in isotropic turbulence seems to exist, which "repels" the vectors away from it, causing an increase in $|R|$ values. In Q_1 and Q_4, the magnitude of pressure hessian term becomes much smaller. The further conditioned pressure Hessian term based on the local densities in Fig. 18 indicates that fluid particles with different densities have very different behaviors with respect to pressure Hessian dynamics. Specifically, the pressure Hessian generally moves the heavy particles toward the regions with larger Q values. In Q_3 and Q_4, it also moves the heavy fluid particles towards the $R > 0$ plane. For the light fluid particles, the pressure Hessian term tends to make them move towards regions with larger $|R|$ values in the first and second quadrant. In Q_3 and Q_4, the fluid particles move from Q_4 to Q_3. Last but not the least, the fluid particles with medium density seem to exhibit similar behavior to light fluid particles, except in Q_1, where the pressure Hessian contribution is moving the fluid particles towards the regions with large Q values. Examining Figs. 15 and 18 together, we observe that the differences in particle dynamics in the (Q, R) plane in regions with different densities are mainly due to differences in the pressure Hessian contributions.

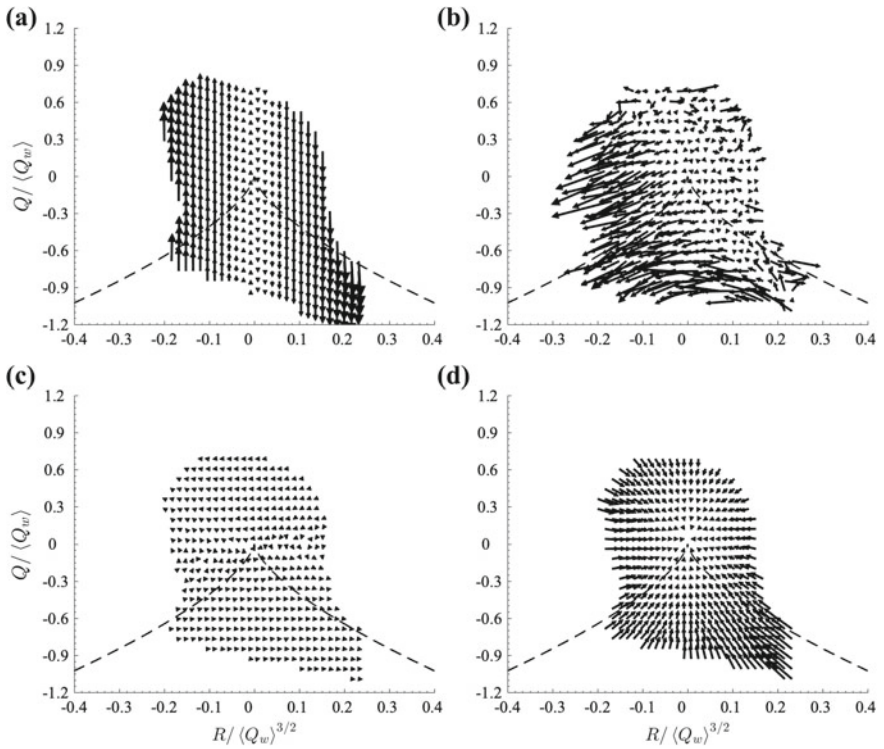

Fig. 17 Contributions to the dynamics of the VGT invariants by different terms for multi-fluid post-shock turbulence. **a** Mutual interaction among invariants, **b** pressure Hessian term, **c** baroclinic term, and **d** viscous term

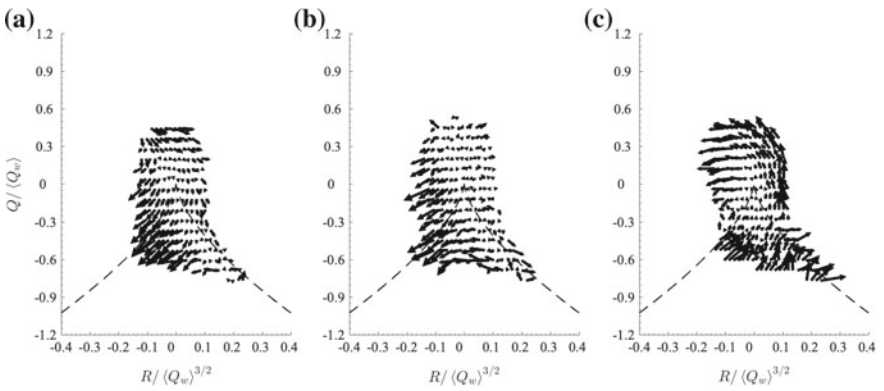

Fig. 18 Contributions from pressure Hessian to the dynamics of the VGT invariants in **a** light fluid region, **b** medium density fluid region and **c** heavy fluid region

Acknowledgements This work was performed under the auspices of DOE. YT and FJ were supported by Los Alamos National Laboratory, under Grant No. 319838. Los Alamos National Laboratory is managed by Triad National Security, LLC, for the National Nuclear Security Administration of the U.S. Department of Energy under contract 89233218CNA000001. Computational resources were provided by the High Performance Computing Center at Michigan State University and Texas Advanced Computing Center (TACC) at The University of Texas at Austin.

References

1. H.S. Ribner, Convection of a pattern of vorticity through a shock wave. NACA TR-1164 (1954)
2. L.S.G. Kovasznay, Turbulence in supersonic flow. J. Aeronaut. Sci. **20**, 657–674 (1953)
3. S. Lee, S.K. Lele, P. Moin, Direct numerical simulation of isotropic turbulence interacting with a weak shock wave. J. Fluid Mech. **251**, 533–562 (1993)
4. R. Hannappel, R. Friedrich, Direct numerical simulation of a Mach 2 shock interacting with isotropic turbulence. Appl. Sci. Res. **54**(3), 205–221 (1995)
5. K. Mahesh, S. Lee, S.K. Lele, P. Moin, The interaction of an isotropic field of acoustic waves with a shock wave. J. Fluid Mech. **300**, 383–407 (1995)
6. S. Lee, S.K. Lele, P. Moin, Interaction of isotropic turbulence with shock waves: effect of shock strength. J. Fluid Mech. **340**, 225–247 (1997)
7. K. Mahesh, S.K. Lele, P. Moin, The influence of entropy fluctuations on the interaction of turbulence with a shock wave. J. Fluid Mech. **334**, 353–379 (1997)
8. S. Jamme, J.-B. Cazalbou, F. Torres, P. Chassaing, Direct numerical simulation of the interaction between a shock wave and various types of isotropic turbulence. Flow Turbul. Combust. **68**(3), 227–268 (2002)
9. J. Larsson, S.K. Lele, Direct numerical simulation of canonical shock/turbulence interaction. Phys. Fluids **21**(12), 126101 (2009)
10. J. Larsson, I. Bermejo-Moreno, S.K. Lele, Reynolds- and Mach-number effects in canonical shock-turbulence interaction. J. Fluid Mech. **717**, 293–321 (2013)
11. J. Ryu, D. Livescu, Turbulence structure behind the shock in canonical shock-vortical turbulence interaction. J. Fluid Mech. **756**, R1 (2014)
12. D. Livescu, J. Ryu, Vorticity dynamics after the shock-turbulence interaction. Shock Waves **26**(3), 241–251 (2016)
13. R. Quadros, K. Sinha, J. Larsson, Turbulent energy flux generated by shock/homogeneous-turbulence interaction. J. Fluid Mech. **796**, 113–157 (2016)
14. Y.P.M. Sethuraman, K. Sinha, J. Larsson, Thermodynamic fluctuations in canonical shock-turbulence interaction: effect of shock strength. Theor. Comp. Fluid Dyn. **32**(5), 629–654 (2018)
15. Y. Tian, F. Jaberi, Z. Li, D. Livescu, Numerical study of variable density turbulence interaction with a normal shock wave. J. Fluid Mech. **829**, 551–588 (2017)
16. Y. Tian, F.A. Jaberi, D. Livescu, Z. Li, Numerical simulation of multi-fluid shock-turbulence interaction, in *AIP Conference Proceedings*, vol. 1793, p. 150010 (AIP Publishing, 2017)
17. T. Jin, K. Luo, Q. Dai, J. Fan, Simulations of cellular detonation interaction with turbulent flows. AIAA J. **54**(2), 419–433 (2015)
18. C. Huete, T. Jin, D. Martínez-Ruiz, K. Luo, Interaction of a planar reacting shock wave with an isotropic turbulent vorticity field. Phys. Rev. E **96**(5), 053104 (2017)
19. M.S. Chong, A.E. Perry, B.J. Cantwell, A general classification of three-dimensional flow fields. Phys. Fluids A-Fluid **2**(5), 765–777 (1990)
20. C. Meneveau, Lagrangian dynamics and models of the velocity gradient tensor in turbulent flows. Annu. Rev. Fluid Mech. **43**, 219–245 (2011)
21. M.S. Chong, J. Soria, A.E. Perry, J. Chacin, B.J. Cantwell, Y. Na, Turbulence structures of wall-bounded shear flows found using DNS data. J. Fluid Mech. **357**, 225–247 (1998)

22. A. Ooi, J. Martin, J. Soria, M.S. Chong, A study of the evolution and characteristics of the invariants of the velocity-gradient tensor in isotropic turbulence. J. Fluid Mech. **381**, 141–174 (1999)
23. L. Wang, X.Y. Lu, Flow topology in compressible turbulent boundary layer. J. Fluid Mech. **703**, 255–278 (2012)
24. Y. Tian, F. Jaberi, D. Livescu, Z. Li, Numerical study of shock–turbulence interactions in variable density flows, in *Proceedings of TSFP-10 (2017) Chicago, vol. 3 of International Symposium on Turbulence and Shear Flow Phenomena*, pp. 8C–3 (2017)
25. Y. Tian, F. Jaberi, D. Livescu, Density effects on the flow structure in multi-fluid shock-turbulence interaction, in *2018 AIAA Aerospace Sciences Meeting*, p. 0374 (2018)
26. R. Boukharfane, Z. Bouali, A. Mura, Evolution of scalar and velocity dynamics in planar shock-turbulence interaction. Shock Waves **28**(6), 1117–1141 (2018)
27. A. Suresh, H.T. Huynh, Accurate monotonicity-preserving schemes with Runge-Kutta time stepping. J. Comput. Phys. **136**, 83–99 (1997)
28. Z. Li, F.A. Jaberi, A high-order finite difference method for numerical simulations of supersonic turbulent flows. Int. J. Numer. Meth. Fl. **68**, 740–766 (2012)
29. S.K. Lele, Compact finite difference schemes with spectral-like resolution. J. Comput. Phys. **103**, 16–42 (1992)
30. S. Lee, S.K. Lele, P. Moin, Simulation of spatially evolving turbulence and the applicability of Taylor's hypothesis in compressible flow. Phys. Fluids A-Fluid **4**(7), 1521–1530 (1992)
31. D. Livescu, J.R. Ristorcelli, Buoyancy-driven variable-density turbulence. J. Fluid Mech. **591**, 43–71 (2007)
32. D. Livescu, Numerical simulations of two-fluid turbulent mixing at large density ratios and applications to the Rayleigh-Taylor instability. Phil. Trans. R. Soc. A **371**, 20120185 (2013)
33. P.K. Yeung, S.B. Pope, An algorithm for tracking fluid particles in numerical simulations of homogeneous turbulence. J. Comput. Phys. **79**(2), 373–416 (1988)
34. M. Lombardini, D.J. Hill, D.I. Pullin, D.I. Meiron, Atwood ratio dependence of Richtmyer-Meshkov flows under reshock conditions using large-eddy simulations. J. Fluid Mech. **670**, 439–480 (2011)
35. D. Livescu, J.R. Ristorcelli, Mixing asymmetry in variable density turbulence, in *Advances in Turbulence XII*, ed. by B. Eckhardt, vol. 132 of *Springer Proceedings in Physics*, pp. 545–548 (Springer, 2009)
36. D. Livescu, J.R. Ristorcelli, M.R. Petersen, R.A. Gore, New phenomena in variable-density Rayleigh-Taylor turbulence. Phys. Scripta **T142**, 014015 (2010)
37. F.A. Jaberi, D. Livescu, C.K. Madnia, Characteristics of chemically reacting compressible homogeneous turbulence. Phys. Fluids **12**(5), 1189–1209 (2000)
38. S. Pirozzoli, F. Grasso, Direct numerical simulations of isotropic compressible turbulence: influence of compressibility on dynamics and structures. Phys. Fluids **16**(12), 4386–4407 (2004)
39. S. Suman, S.S. Girimaji, Velocity gradient invariants and local flow-field topology in compressible turbulence. J. Turbul. **11**(2), 1–24 (2010)
40. Y.B. Chu, X.Y. Lu, Topological evolution in compressible turbulent boundary layers. J. Fluid Mech. **733**, 414–438 (2013)
41. N.S. Vaghefi, C.K. Madnia, Local flow topology and velocity gradient invariants in compressible turbulent mixing layer. J. Fluid Mech. **774**, 67–94 (2015)
42. J. Wang, Y. Shi, L.P. Wang, Z. Xiao, X.T. He, S. Chen, Effect of compressibility on the small-scale structures in isotropic turbulence. J. Fluid Mech. **713**, 588–631 (2012)
43. Y. Tian, F. Jaberi, D. Livescu, Shock propagation in media with non-uniform density, in *International Symposium on Shock Waves*, pp. 1167–1175 (Springer, 2017)

Novel Method for Initiation and Control of Combustion

Ahad Validi, Harold Schock and Farhad Jaberi

Abstract Turbulent jet ignition (TJI) is a novel ignition enhancement method which facilitates the combustion of lean and ultra-lean mixtures in propulsion systems including internal combustion engines. An overview of numerical study of TJI-assisted combustion in different systems is presented in this chapter. The numerical simulations are conducted by direct numerical simulation (DNS) and hybrid Eulerian-Lagrangian large eddy simulation (LES)-filtered mass density function (FMDF) methods. DNS of TJI-assisted combustion of lean hydrogen-air mixture in a planar jet for various thermo-chemical conditions reveals fundamental features of TJI systems such as localized flame extinction and re-ignition processes. LES-FMDF of TJI-assisted combustion in a rapid compression machine (RCM) reveals three main phases: (1) cold fuel jet, (2) turbulent hot product jet, and (3) reverse fuel-air/product jet. The simulated results are in good agreement with the experimental data.

Keywords Turbulent jet ignition · DNS and LES · Turbulent reaction · Lean combustion

1 Introduction

Turbulent jet ignition (TJI) systems can be used to initiate and control chemical reactions in lean and ultra-lean fuel-air mixtures by providing sufficient initial energy through high temperature turbulent jets [1, 2]. These systems typically consist of a relatively small pre-chamber (PCh), a main chamber (MCh), and a nozzle connecting

A. Validi · H. Schock · F. Jaberi (✉)
Department of Mechanical Engineering, Michigan State University,
East Lansing, MI 48824, USA
e-mail: jaberi@egr.msu.edu

A. Validi
e-mail: validiab@msu.edu; ahad.validi@ansys.com

H. Schock
e-mail: schock@egr.msu.edu

D. Livescu et al. (eds.), *Modeling and Simulation of Turbulent Mixing and Reaction*, Heat and Mass Transfer, https://doi.org/10.1007/978-981-15-2643-5_5

them. The hot product turbulent jet, which is created by a low spark ignition energy in the PCh, efficiently initiates and controls the MCh combustion much better than the conventional ignition systems [3]. TJI-assisted combustion of premixed mixtures have been studied before by focusing on the transition and the viability of practical configurations [4–6]. More recently, Validi and his collaborators [7–9] studied TJI in various combustion systems via direct numerical simulation (DNS) and large eddy simulation (LES) methods. This included a geometrically simple fundamental flow configuration and a complex configuration relevant to internal combustion (IC) engines. A thorough review of these studies are presented here.

The physical and chemical processes involved in TJI-assisted combustion of a well characterized turbulent planar jet (TPJ) [10–14] are investigated by DNS. The simulated TPJ-TJI configuration (Fig. 1), composed of hot products of combustion of stoichiometric and rich hydrogen-air mixtures injected into a lean and relatively cooler premixed hydrogen-air coflow, is designed such that it reaches a "stable" condition after a sufficiently long time. This allows the collection of stationary turbulence/flame statistics and provides fundamental insights on the flame and turbulence structures in TJI-assisted combustion systems. The TPJ-TJI associated DNS data are used to investigate the development of flame/turbulence structures and various combustion zones in such systems. Different coflow compositions are considered, from ultra-lean to moderately-lean mixtures with equivalence ratios ranging from $\phi = 0.1$ to 0.5. Numerical results show that TJI is capable of maintaining ultra-lean flames and decreasing the low flammability limit by constantly exposing the mixture to high temperature jet species despite the presence of strong localized flame extinction. The premixed flame propagation, the turbulent jet development, and consequently the flame-turbulence interactions are shown to be significantly affected by the coflow mixture composition. There is also a significant change in flame structure when the jet composition is changed from the combustion products of lean to stoichiometric, to rich mixtures. Even though the flame is mostly of premixed type, in the case of hot product jet with unburned fuel, simultaneous premixed and diffusion flames are developed, resulting in significant changes in the flame structure.

TJI has been applied in rapid compression machines (RCMs) [15–20], which are used for studying autoignition and combustion kinetics by compressing fuel-air mixtures uniformly to engine-like conditions. In the simulated RCM-TJI combustion system (Fig. 12a), a PCh is normally installed at the end side of the RCM, referred to as the MCh. The PCh is connected to the MCh through a nozzle (or several nozzles), creating one or more high speed hot product jets rapidly propagating into the MCh [21]. Ideally, the incoming jet(s) initiates "nearly homogeneous" premixed combustion in which the hot pockets of energy sources ignite the main charge as the flame/combustion products propagate throughout the system. This method enables the implementation of highly efficient lean burned technology in various combustion systems including IC engines. The lean burned TJI-assisted combustion systems operate in low temperature range which significantly reduce the pumping loss, improve the engine drive cycle efficiency, extend the knock limits, and decrease the carbon and NOx emissions.

The performance of TJI-assisted combustion systems particularly RCM-TJI is dependent on the complicated and often coupled effects of various factors such as the initial thermo-chemical conditions, the PCh and MCh geometries, the ignition parameters (timing, location, amount, and duration of discharged energy), the fuel-air-products mixing, and the fuel chemistry. It is not trivial to experimentally predict the system behaviour for various operating conditions. High-fidelity computational models such as those based on LES [13, 22–25] can greatly help with the development and assessment of such systems. However, LES models have not been fully utilized for this purpose partly due to computational demands and partly due to the challenges in modeling subgrid scale (SGS) correlations [26]. The numerical challenges of simulating TJI-assisted combustion arise from the strong coupling of the turbulent flow and thermo-chemical variables over a wide range of temporal and spatial scales, and the highly nonlinear, multicomponent, and unsteady nature of the heat and mass transport and chemical reactions in the hybrid jet-flame setup [13, 27]. Additionally, in the TJI-assisted combustion systems a broad range of flame types could exist simultaneously [8]. The combustion models developed for one type of flame are not often able to predict the other types, and therefore the overall behaviour of TJI-assisted combustion systems. Probability density function (PDF) methods [28, 29] are able to simulate different types of combustion regimes in the TJI systems.

The models developed for LES based on the solution of the transport equation of SGS PDF, known as the filtered density function (FDF), have been successfully used in simulating turbulent reacting flows. FMDF is the variable density verion of FDF [27, 29–38]. The main advantage of the single-point FMDF is that all single-point statistics, including the reaction terms appear in a closed form in its formulation regardless of their complexity and nonlinearity, even though modelling for multi-point correlations is still needed. This allows the natural inclusion of turbulent-combustion interactions into the model for different multicomponent fuels and makes it possible to simulate various types of flames (non-premixed, premised, flamelet, distributed, etc.) for every mode of system operation. FMDF has a strong mathematical/physical foundation and can be continuously improved without any major changes in its basic structure. With FMDF, LES solvers directly compute large-scale unsteady flow structures, while also accounting for complex processes at subgrid level. FMDF provides all higher moments of the species and temperature. The Lagrangian solution of FMDF is free of numerical diffusion error and overshoot/undershoot which it may cause fictional ignition. LES/FMDF solvers have been applied to and tested for extreme turbulent combustion conditions (e.g. blowout, local extinction/reignition, compressible combustion [29, 39–41]) and relatively complex geometries [41–43]. LES/FMDF model is used here to study TJI in RCM.

The rest of this chapter is organized as follows. In Sect. 2, the governing equations and numerical methodology used for DNS and LES/FMDF are described. In Sect. 3, the flow configuration and numerical results of our DNS study are presented. In Sect. 4, the RCM-TJI flow configuration and some of the results obtained by the LES/FMDF are described. The main findings and conclusions are summarized in Sect. 5.

2 Governing Equations and Numerical Methodology

For DNS, fully compressible, three-dimensional continuity, momentum, energy, and species equations are solved with high order numerical methods [7]. In these equations, the viscous stress tensor and heat flux vector are obtained by Newtonian, and Fourier models. The heat transfers due to radiation and Dufour effects have been neglected. The mixture-averaged thermal conductivity is calculated from the thermal conductivities of individual species. The species diffusion term is evaluated based on the Fick's model with binary diffusion coefficient between species and diffusion velocity of each individual species included. The mass flux due to temperature gradient (Soret diffusion) and the differential diffusion effects [44], important effects in hydrogen combustion, are also included. The conservation equations are closed by the equation of state. The Chemkin thermodynamic database [45] is used to obtain species thermodynamics and transport properties. The combustion of hydrogen-air is modeled with the detailed chemical kinetics mechanism developed by Stahl and Warnatz [46]. This mechanism, which is used in several previous studies on hydrogen combustion [47–50], consists of 38 elementary reactions and 9 species (H_2, O_2, O, OH, H_2O, H, HO_2, H_2O_2, and N_2).

The LES/FMDF computational model has two major components: (i) LES-FD solver, and (ii) FMDF-MC solver. The filtered LES velocity and pressure are obtained by solving the filtered continuity and momentum equations with the Eulerian finite difference (FD) method, while the species mass fractions and temperature are computed using the FMDF method. In this method, the modeled scalar FMDF equation is obtained indirectly via equivalent stochastic differential equations (SDEs) and their solution by a Lagrangian Monte Carlo (MC) procedure. So, the hybrid compressible LES/FMDF methodology involves two sets of Eulerian and Lagrangian equations, which are solved conjointly for velocity and scalar (species mass fractions and enthalpy) fields.

The primary LES/FMDF variables are the filtered density $\bar{\rho}$, the Favre-filtered velocity $\tilde{u}_i$, and the Favre-filtered scalar vector $\tilde{\boldsymbol{Y}} \equiv y_{\alpha(\alpha=1,\ldots,N_s+1)}$ (N_s represents the number of species), which includes the Favre-filtered species mass fraction $\tilde{y}_{\alpha(\alpha=1,\ldots,N_s)}$ and the Favre-filtered sensible enthalpy $\tilde{y}_{\alpha(\alpha=N_{s+1})} = \tilde{h}$. These are partly obtained by solving the Favre-filtered continuity, momentum and energy equations [9]. The filtered viscous stress tensor is assumed to be a linear function of the Favre-filtered strain rate and the filtered heat flux vector and species diffusion are evaluated based on Fourier and Fick's assumptions. The filtered form of the ideal gas equation of state is used to close the system of equations. The unclosed subgrid terms which appear in the filtered equations are closed by gradient type closures [42, 43]. The molecular viscosity and specific heat capacity of each species are calculated by polynomial functions of temperature where the polynomial coefficients are given in Ref. [51]. The combustion heat and mass source/sink terms are obtained from the scalar FMDF. The scalar FMDF is the joint SGS PDF of the scalar vector and is defined as:

$$P_L(\Psi; X, t) = \int_{-\infty}^{+\infty} \rho(X', t)\, \sigma\left[\left(\Psi, \boldsymbol{Y}(X', t)\right)\right] \boldsymbol{G}(X' - X)\, dX', \tag{1}$$

where $\boldsymbol{G}$ represents the filter function, Ψ is the scalar vector in the sample space and the fine-grained density, σ, is defined based on a series of delta functions, δ, as:

$$\sigma\left[\left(\Psi, \boldsymbol{Y}(X', t)\right)\right] = \prod_{\alpha=1}^{N_s+1} \delta\left(\psi_\alpha - y_\alpha(X, t)\right). \tag{2}$$

The FMDF transport equation is derived from the unfiltered scalar equation [29]. This equation is not solvable due to three unclosed terms: the convection term, the molecular diffusion term, and the compressibility term. The convection term is decomposed into resolved and residual or SGS parts, where the SGS part is modeled via a gradient type closure. The molecular diffusion term is decomposed to molecular transport and SGS dissipation terms, where the SGS dissipation is modeled with the linear mean square estimation (LMSE) or the interaction by exchange with the mean model (IEM) [29, 36, 41, 43]. The pressure effect [41, 52] is not fully included in the FMDF formulation and only the effect of filtered pressure on the scalar FMDF is considered by decomposing the compressibility term into resolved and SGS parts and by ignoring the SGS part [41].

In the LES/FMDF solver, an equivalent set of stochastic differential equations (SDE)s are solved by the MC method. The stochastic processes are collectively represented by a Fokker-Planck equation, which is a PDF equation identical to the FMDF transport equation. Each MC particle is spatially transported in the physical space due to large-scale convection, SGS turbulence, and molecular diffusion for the solution of SDEs. The number of MC particles used are managed via a procedure involving nonuniform weights. In this procedure, smaller and larger number of particles are allowed in low and high degree variability, respectively. The variable weighting allows the particle number to vary between certain minimum and maximum values. The modeled scalar FMDF transport equation provides all single-point statistics of reactive species and temperature. However, to check the mathematical consistency between the FMDF and the conventional LES methods, the transport equations for the filtered fuel and oxygen mass fractions are also solved directly by a grid-based conventional FD method. In the modeled scalar FMDF equation, the gas velocity and pressure fields are unknown and are obtained from the FD data.

The discretization of unfiltered DNS equations and filtered LES gas dynamics equations is based on the compact FD scheme [53, 54], which yields up to sixth order spatial accuracy. In order to avoid numerical instabilities and remove the numerical noises generated by the growth of numerical errors at high wave number modes, a low pass, high order, spatial implicit filtering operator is used [54]. The time differencing is based on a third order low storage Runge-Kutta method [42, 55].

The numerical method utilized in this work has been used previously in DNS and LES of low speed and high speed turbulent reacting flows [9, 33, 41–43] and is

proven to be quite accurate. However, the MC particle search and locate calculations could become computationally intensive when the LES/FMDF method is incorporated for simulating flows in complex geometries [41–43]. The computational cost of the MC method can be substantially reduced by using a structured, Eulerian Cartesian grid. With this grid, it is possible to morph the computational mesh to the physical boundaries by a version of immersed boundary (IB) method compatible with the LES/FMDF [9]. The solution algorithm is modified locally by enforcing the desired boundary conditions for both FD grids and MC particles. With the IB method, the LES/FMDF model retains its accuracy and provides a high level of flexibility for two reasons. First, the MC particle search and locate procedure requires less calculations. Second, the computational load is almost equally divided between the processors, which facilitates the maximum utilization of available parallel computational processors with a simpler and less expensive communication procedure.

3 DNS of Planar Turbulent Jets

The computational configuration considered in DNS study of TPJ-TJI consists of a spatially developing, three-dimensional planar jet [56] issuing hot combustion products into a combustible lean premixed ambient coflow. A schematic of the flow configuration, together with the specifications of physical dimensions are presented in Fig. 1. The flow evolves spatially in the stream-wise direction, (x). The free stream boundary conditions are imposed in the cross-stream direction, (y), and periodic boundary conditions are implemented in the span-wise direction, (z). In the simulated TPJ-TJI, the jet expansion is highly affected by the coflow momentum, fuel-air equivalence ratio, and turbulence-controlled flame speed. Therefore, the flow hydrodynamics and geometry have been designed such that a stable and statisti-

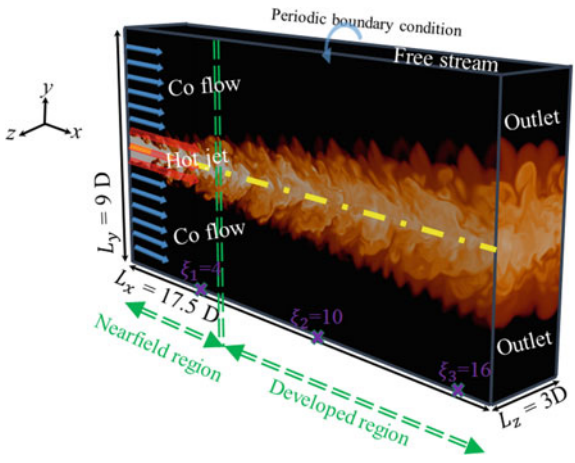

Fig. 1 Schematic of turbulent jet ignition (TJI) in a turbulent plane jet (TPJ) configuration

Table 1 Thermo-chemical properties of the incoming jets and coflows for different cases

Case #	T_j (K)	T_{co} (K)	ϕ_{i_j}	ϕ_{co}	y_{H_j}	$y_{H_{co}}$
Case 1	2556	850	1.0	0.10	0.0285	0.0403
Case 2	2556	850	1.0	0.20	0.0285	0.0774
Case 3	2556	850	1.0	0.35	0.0285	0.1280
Case 4	2556	850	1.0	0.50	0.0285	0.1730
Case 5	2050	850	0.5	0.35	0.0144	0.1280
Case 6	2350	850	2.0	0.35	0.0554	0.1280
Case 7	2350	850	2.0	0.10	0.0554	0.0403

cally "stationary" combustion is established and time-averaging is made possible. The selected configuration allows the understanding of TPJ-TJI physical features that are believed to be invariant of the geometry and common in other TJI-assisted combustion systems.

Table 1 provides the jet and the coflow thermo-chemical properties for different cases, where T_{co}, U_{co}, $y_{H_{co}}$, and ϕ_{co} represent the temperature, stream-wise velocity, elemental mass fraction of radical H, and equivalence ratio of the coflow. The equivalent variables for the incoming jet are denoted by T_j, U_j, y_{H_j}, and ϕ_{i_j}. The variable ϕ_{i_j}, however, is the equivalence ratio of an initial hydrogen-air mixture at temperature of 1000 (K) before it burns and gets injected as combustion products with higher temperature at TPJ-TJI inflow. The temperature value of 1000 (K) is selected in order to create a hot product jet with about three times of the coflow temperature (i.e. $T_j \approx 3T_{co}$) and consequently a stable and statistically stationary flame within the selected computational domain. In Case 1–Case 4, the coflow premixed mixture compositions vary from ultra-lean to moderately-lean (i.e. $\phi_{co} = 0.1$, 0.2, 0.35, and 0.5) with the same coflow temperature and velocity of $T_{co} = 850$ (K) and $U_{co} = 150$ (m/s). In these cases, the same hot product jet with $\phi_{i_j} = 1.0$ and $T_j = 2556$ (K) is injected so that the coflow composition effects on the turbulence-combustion interactions can be studied independent of the jet condition. The effects of jet composition (lean and rich initial mixtures with $\phi_{i_j} = 0.5$ and 2.0) are investigated by considering Case 5, Case 6, and Case 7. Note that by changing the initial jet mixture equivalence ratio from 0.5 to 2.0, the fuel (Hydrogen) concentration in the products is changed from 1.9e−7 to 2.7e−2 and also the jet temperature is changed from $T_j = 2050$ to 2350 (K). In these cases, the same coflow conditions as those in Case 3 are considered. In Case 7, the coflow equivalence ratio is the same as that in Case 1 but the jet composition is similar to that in Case 6. This case is considered to study the effects of the extra fuel in jet on the diffusion and premixed flames in the ultra-lean coflow mixtures. In all the cases, the pressure is atmospheric and the jet velocity is set to be three times of the coflow velocity, $U_j = 3U_{co} = 450$ (m/s). To calculate the statistics, the simulations are advanced for three flow-through time, τ_0, before averaging the variables up to $17\tau_0$. The flow through time, $\tau_0 = 218.75$ (μs), is calculated based on the average velocity, $U_{ref} = \dfrac{U_j + U_{co}}{2} = 300$ (m/s), and the

stream-wise domain length, $L_x = 17.5 \times D = 65.625 \times 10^{-3}$ (m) ($D = 3.75$ (mm) denotes the incoming jet width).

3.1 Flow-Flame Structure

To describe the complex flame and turbulence fields in the TJI-TPJ, it is useful to divide the entire flow into different regions and combustion zones. Primarily, the flow is divided spatially into separate regions based on the physical flame structures, identified by the heat of reaction. The combustion heat release rate, $\dot{Q}_e$, is a critical quantity to discern flames and their locations in turbulent reacting flows. Figure 2 shows the instantaneous contours of heat release rate at time $17\tau_0$. This figure indicates that the flow field can indeed be divided into two regions in the stream-wise direction: (i) near-field ($\xi = x/D \leq 4$) and (ii) developed ($\xi \geq 4$) regions with very different flame-turbulence features. In the near-field region, the hot incoming jet essentially causes auto-ignition at the jet shear layer and surrounding areas, where the jet heats the premixed coflow and ultimately sustains the flame even for ultra-lean condition. In addition to the combustion, highly distorted turbulent structures are developed in this region which enhance the mixing. The process of flame-turbulence interactions and mixing of the incoming hot jet with premixed coflow in the reacting shear layer creates relatively thick and geometrically complex flames, as the distributed $\dot{Q}_e$ values suggest. Marching in the stream-wise direction, a spatially continuous and distorted flame is developed. While the flame moves away from the main turbulent jet and spreads in the coflow, it becomes much thinner. The $\dot{Q}_e$ contour plots in Fig. 2 clearly show the separation of the unburned and burned zones in the developed region with the cross-stream spreading of the distorted turbulent flame front. The lower contours in this figure show the $\dot{Q}_e$ distribution in the span-wise direction in a $x - z$ plane at $y = D/2$. It is observed that the distributed high heat release rate values virtually vanish from the main jet as the flow moves away from the near-field to the developed region. Even though the flame and turbulence features vary over time, they appear to be well stabilized in the developed region.

In the developed region of the simulated TJI-TPJ, the flow can be divided into four main zones based on the flame/turbulence parameters. Figure 3 shows the schematic of these four zones:

I. hot product jet zone,
II. burned-mixed zone,
III. flame zone, and
IV. premixed coflow zone.

In order to identify the above zones, we primarily consider the temperature, the H radical mass fraction, and the heat release rate even though other quantities such as vorticity, $\overrightarrow{\omega}$, and Baroclinic torque, $\overrightarrow{\beta}$, may also be used. The probability density functions (PDF) of temperature, $\mathcal{P}(T)$, and H radical mass fraction, $\mathcal{P}(y_H)$, and the scatter plot of y_H versus T are shown in Fig. 4a–c. The PDF plots are useful in

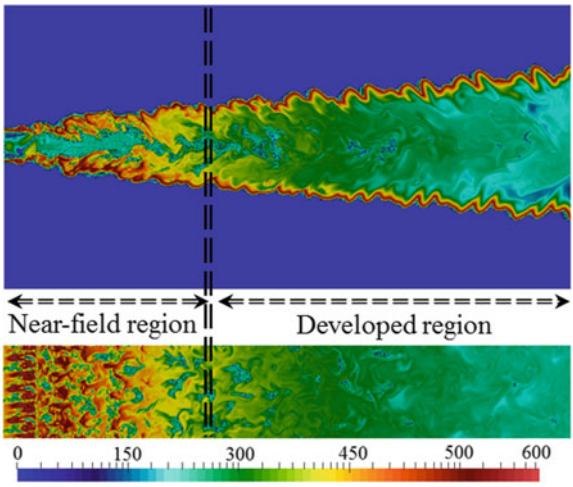

Fig. 2 Instantaneous heat release rate (KJ/s) contours at time $17\tau_0$. (Contours presented in the lower figures are for the $y = 0.5 \times D$ plane)

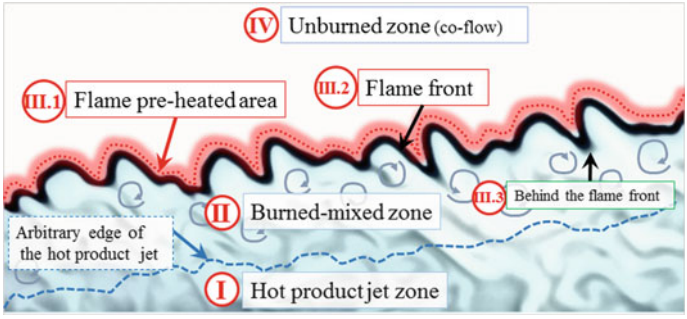

Fig. 3 Various zones in the developed region of the simulated turbulent planar jet with turbulent jet ignition

delineating the flow in different zones as shown in Fig. 3. The three distinguishable peaks of $\mathcal{P}(T)$ and $\mathcal{P}(y_H)$ in Fig. 4a, b are related to the three active combustion zones. The data associated with the coflow are not included in these figures. It is worthwhile to mention that details of the flow and flame may vary with changes in thermo-chemical and hydrodynamics conditions, but the general characteristics of various zones identified in the TJI-TPJ configuration stay the same.

The hot product jet zone (labeled as zone I) is identified by the $\mathcal{P}(T)$ peak located at the highest temperature values in Fig. 4a and by the $\mathcal{P}(y_H)$ peak located at the moderate y_H values in Fig. 4b. In the non-reacting flow, the jet temperature decreases by 30% in about $16D$ from the jet inlet due to heat transfer and mixing of hot jet with the cooler coflow [7]. There is also a temperature reduction in the reacting jet because the flame temperature of the lean coflow mixture is considerably lower than

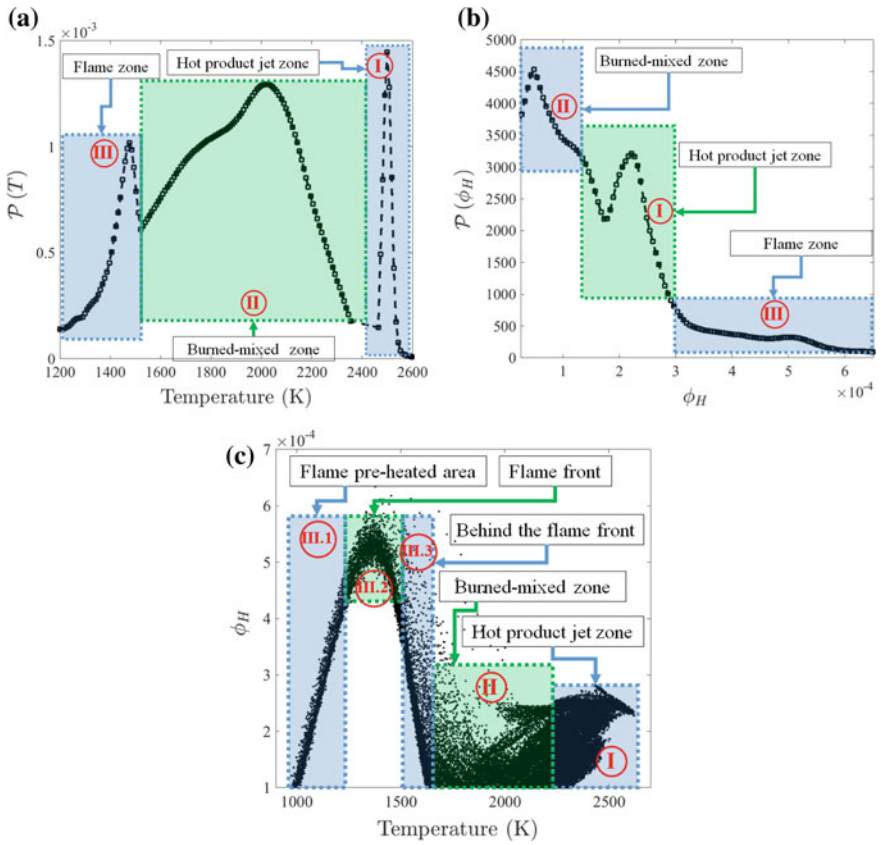

Fig. 4 Marginal PDFs of **a** temperature and **b** H radical mass fraction. **c** Scatter plot of H radical mass fraction and temperature

the temperature of the hot product incoming jet. However, the temperature reduction is less than 10%, due to heating of the remnant hot product jet zone by the reaction. The initial value of y_H in the hot product jet is also increased from 0.4×10^{-4} to 2.1×10^{-4}, which is consistent with the amount of H radical generated through combustion of the lean coflow mixture.

The $\mathcal{P}(T)$ peak in the intermediate temperature range in Fig. 4a and the $\mathcal{P}(y_H)$ peak in the lowest y_H range in Fig. 4b are both associated with the burned-mixed zone, which is labeled as zone II. There is a significant interaction between turbulence and flame and, as it can be observed in the scatter plot of y_H versus T in Fig. 4c, there may not be well defined and fine boundaries between zone II and its neighboring zones, particularly, the hot product jet zone. The $\mathcal{P}(T)$ peak falls in between the adiabatic flame temperature of the lean coflow and the hot product jet temperature. This clearly indicates that on average the coflow mixture is exposed to a sufficient amount of heat to initiate and sustain the combustion as zone II is significantly

affected by the hot product jet. In contrast, the peak of $\mathcal{P}(y_H)$ occurs at the smallest y_H values. As a reliable variable to identify the flame front, the maximum values of y_H occur at the flame front. The y_H values in the burned-mixed zone are less than their values in the hot product jet and flame front zones as the lean premixed combustion heat and products are diffused toward the main inner jet and coflow. The burned-mixed zone in the TJI-TPJ is similar to the burned zone appearing in standard turbulent premixed flames [57–59], where the fuel is consumed and the composition consists of the high temperature products. But, this region of TJI-TPJ consists of relatively higher temperature and higher concentration of products due to the interactions with incoming hot product jet. The complexity of this zone arises from the strong interactions of the inner hot product jet turbulence and composition fields with the lean premixed turbulent flame.

The $\mathcal{P}(T)$ peak in the lowest temperature range or zone III of Fig. 4a and the $\mathcal{P}(y_H)$ peak in the highest y_H range in Fig. 4b (identified by the marginal increase in $\mathcal{P}(y_H)$ around $y_H \simeq 5 \times 10^{-4}$) are associated with the flame temperature and y_H at the flame front of combustion of lean hydrogen-air mixture (with equivalence ratio of 0.35 and initial temperature of 850 (K)). These two peaks clearly identify the flame zone. Similar to what has been suggested for standard turbulent premixed flames [57–61], three areas in the flame zones can be identified:

(III.1) Preheated zone which is located very close to the flame front but inside the unburned fresh coflow mixture. This zone is shown in Fig. 4c and also in Fig. 3 by a shadow area on top of the flame front.

(III.2) Flame front which is identified by the highest y_H values and a relatively higher temperature than the adiabatic flame temperature of lean mixture. This zone is a thin wrinkled flame sheet separating unburned zone form the other zones as shown in Figs. 3 and 4c.

(III.3) Behind the flame front in burned-mixed zone which has a y_H level less than that in the flame front (Fig. 4c). It is worthwhile to emphasize that the temperature and H mass fraction in area III.3 and the entire flame zone are greater than those expected for a standard turbulent premixed flame [62–66] because of the heat transfer and mixing with the hot product jet.

In addition to detailed study of heat release, temperature, pressure and species fields in TPJ-TJI, we have also studied the behaviour of turbulent variables like vorticity [7]. DNS results suggest a similar vorticity field in reacting and non-reacting flows, even though the small-scale turbulent structures are depleted by the combustion. In the near-field region, the vortex stretching and compressibility are the sources of the vorticity production. Further downstream in the developed region, the significant variations in density and pressure cause the Baroclinic torque to play a more important role in generating vorticity. Close to the flame zone, the Baroclinic torque and the vortex stretching are the main sources of generating vorticity. However, in the combustion zones the vorticity field is negatively affected by the heat release induced volumetric flow expansion and increased viscosity. The jet spread rate in the reacting flow is considerably greater than that in the non-reacting flow, mainly, because of the turbulent burning velocity. Also, it is observed that the turbulence intensity con-

stantly decreases along the jet, as the jet spreading and combustion simultaneously dissipate turbulent structures inside the jet and at the flame front. It is also shown that the turbulent flame speed is directly correlated to the turbulence intensity; the higher turbulence intensity, the higher turbulent flame speed. These results are consistent with previous studies [67, 68]. However, contrary to the standard turbulent premixed flames, in the studied TJI-TPJ configuration a high temperature and momentum turbulent flow exists behind the flame front in the burned zone, which enhances the combustion at the flame zone and increases the flame burning velocity.

3.2 Effects of Various Flow Parameters

Having various combustion zones in the flow/flame fields identified, the effects of coflow and jet equivalence ratio on the TPJ-TJI are studied next. These are the most important parameters affecting the flow and combustion besides the jet velocity and turbulence intensity. Figure 5a–f present the instantaneous temperature contours at the mid span-wise plane of the three-dimensional computational domain and at time $t = 17\tau_0$ for six different cases with conditions provided in Table 1. For Case 3, Case 5, and Case 6 with different jet temperatures and compositions but the same coflow conditions, temperature contours in Fig. 5c, e, and f confirm that the nearfield flame/flow structures are indeed influenced more by the incoming jet than the coflow combustion.

In the developed region ($\xi \succeq 4$) the flame expansion and the growth rate of the jet "thermal width" are highly dependent on the coflow mixture conditions. The weak reaction of ultra-lean mixtures in Case 1 and Case 2 with equivalence ratios of 0.1 and 0.2 (Fig. 5a, b) hardly establishes stable and distinguishable combustion zones, suggesting significant localized flame extinction and re-ignition. However, for Case 3 and Case 4, with coflow equivalence ratios of 0.35 and 0.5, the flame is stable and widely spreads in the cross-stream directions, leading to separation of flame from the core jet turbulence (Fig. 5c, d). Despite different jet thermo-chemical conditions, the growth and structure of combustion zones for Case 5 and Case 6 (Fig. 5e, f) are almost the same as those for Case 3 (Fig. 5c), suggesting that the initial energy provided by the incoming hot product jet is sufficient to initiate a stable combustion in coflow mixtures with equivalence ratio of 0.35. These results confirm that the combustion in the developed region is very sensitive to the coflow composition, but is less influenced by the incoming jet composition particularly at sufficiently high equivalence ratios. The lower jet temperature in Case 5 (Fig. 5e), slightly affects the flame growth. The unburned hot fuel in the injected jet in Case 6 (Fig. 5f) mixes with the available oxidizer in the coflow and establishes stable diffusion flames within the main jet surrounded by the premixed flames. However, the heat release by the diffusion flames has a little effect on the overall jet behavior and the surrounding premixed flame in Case 6.

The overall effects of the coflow and incoming jet parameters are further examined in Fig. 6, where the mean and confidence intervals of time and $y - z$ plane averaged

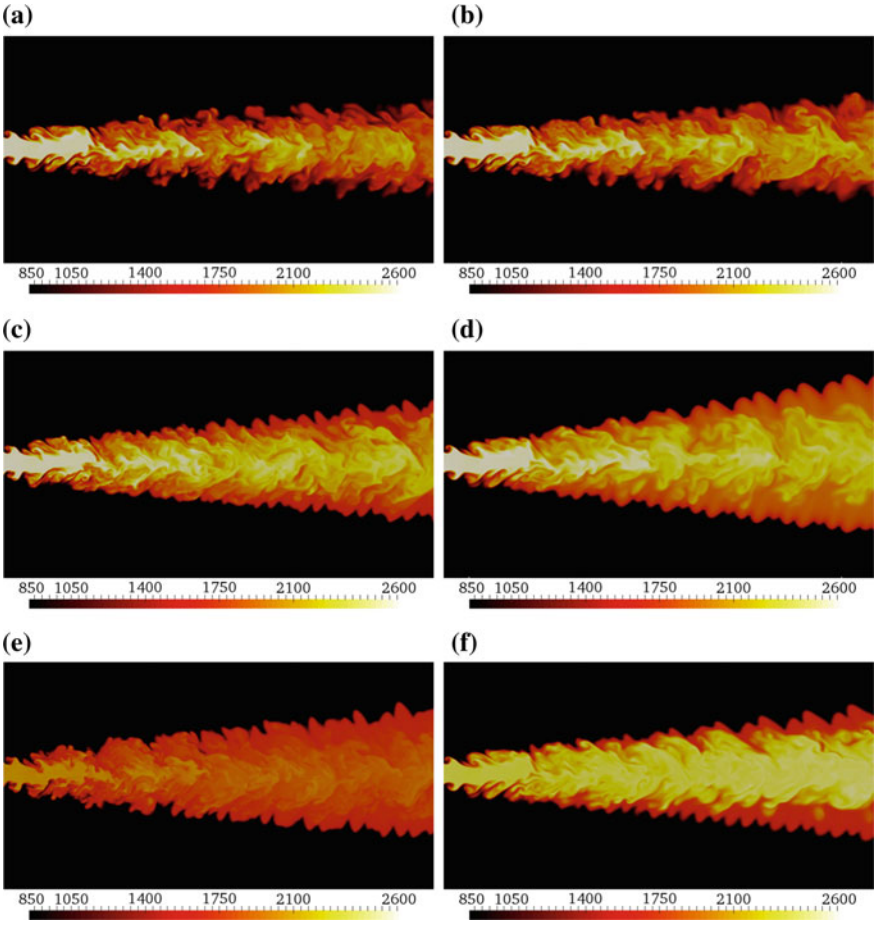

Fig. 5 Instantaneous temperature contours at the mid span-wise plane ($z = 1.5D$) and time $t = 17\tau_0$ for **a** Case 1 with $\phi_{co} = 0.1$ and $\phi_{i_j} = 1$, **b** Case 2 with $\phi_{co} = 0.2$ and $\phi_{i_j} = 1$, **c** Case 3 with $\phi_{co} = 0.35$ and $\phi_{i_j} = 1$, **d** Case 4 with $\phi_{co} = 0.5$ and $\phi_{i_j} = 1$, **e** Case 5 with $\phi_{co} = 0.35$ and $\phi_{i_j} = 0.5$, and **f** Case 6 with $\phi_{co} = 0.35$ and $\phi_{i_j} = 2$

temperature, $\mu(\langle\overline{T}\rangle_{yz}) \pm \sigma(\langle\overline{T}\rangle_{yz})$, are plotted at different stream-wise locations for six cases. The time-averaged statistics are calculated from the data gathered for $17\tau_0$. In these calculations, the coflow data are excluded, but the preheated zones of the premixed flame are included, which potentially lower the reported mean temperatures. Evidently, the results associated with the nearfield region are very similar in Case 1 to Case 4, which show the importance and dominance of the incoming jet properties and turbulent mixing of the hot jet with the coflow. In fact, the time and span-wise averaged profiles of the temperature versus the cross-stream direction at different stream-wise locations (not shown here) are found to be nearly identical

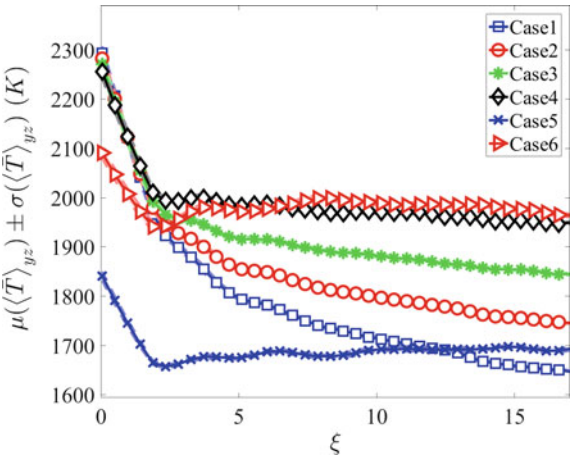

Fig. 6 Mean and confidence intervals of time and $y-z$ plane averaged temperature, $\mu(\langle\overline{T}\rangle_{yz}) \pm \sigma(\langle\overline{T}\rangle_{yz})$, in the combustion zones at different stream-wise locations, ξ, for Case 1 (□), Case 2 (○), Case 3 (∗), Case 4 (◇), Case 5 (×), and Case 6 (▷)

in cases with similar incoming jet thermo chemical conditions (Case 1–4). In the nearfield region, the maximum temperature, located at the jet centerline, is lower in Case 5 and Case 6 with lean and rich product jet mixtures. The temperature profiles in the shear layer seem to be dependent more on the coflow composition than the incoming jet composition.

The transition from the nearfield region to the developed region approximately starts at $\xi \approx 3$. In the developed region, the averaged temperature values continuously decrease along the stream-wise direction but with a much higher rate in Case 1 in comparison to Case 4. This is expected and is due to weaker and lower temperature combustion in the cases with low coflow equivalence ratios. Case 5 with a lean initial jet mixture, $\phi_{i_j} = 0.5$, exhibits rather different trend in comparison with other cases. For this case, the averaged temperature is initially lower compared to other cases and further decreases in the nearfield region before increasing again in the developed region and reaching to a plateau at downstream locations. A comparison between Case 5 and Case 3 indicates that even though the flow and combustion are similar in the nearfield region, the temperature is generally lower in Case 5 since the temperature of the incoming jet is lower. In the developed region of Case 6 with a rich initial jet mixture, ($\phi_{i_j} = 2.0$), the averaged temperature profile plateaus after a small increase, which is similar to that for Case 5 but is due to different reasons. The incoming jet temperature in Case 6 is lower than that in Case 3, but unlike Case 5, there is a stable diffusion flame with higher averaged temperature in this case. The presence of non-premixed flame in Case 6 is evident in Fig. 5f, where the temperature inside the combustion zones is shown to be considerably higher than those in other cases. The diffusion flame evidently increases the averaged temperature even higher than that in Case 3, despite the same coflow conditions.

It has been suggested in Ref. [8] that the approximate location of the flame or the jet thermal half width, D_{half}, in TPJ-TJI can be obtained from the peak temperature root mean square (rms), $T_{rms} = (\overline{T^2} - \overline{T}^2)^{1/2}$, since high temperature variations usually

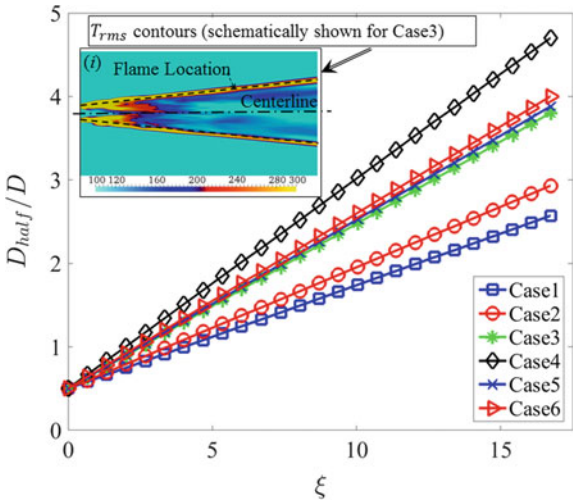

Fig. 7 Thermal half jet width, normalized by the incoming jet width (D_{half}/D), versus stream-wise direction (ξ). **a** Contours of rms of temperature, T_{rms}, at the mid span-wise plane, ($z = 1.5D$), for Case 3

occur at the flame zone. Figure 7a shows the temperature rms contours at the mid plane for Case 3, representing "high value T_{rms} zones" in the nearfield region, an indication of approximate location of relatively thick premixed/diffusion flames in this region. These high T_{rms} zones also occur in the periphery of the jet at the lean premixed flame zone in the developed region. The jet thermal half width (D_{half}) is measured simply by fitting a straight line (dashed black line shown in Fig. 7a to the locally maximum T_{rms} values. Figure 7 shows the stream-wise variations of the thermal half width jet, normalized by the incoming jet width, D_{half}/D, for different cases. The maximum and minimum D_{half} values correspond to Case 4 and Case 1 with the highest and the lowest coflow equivalence ratios. Evidently, D_{half} may not be altered significantly by changing the thermo-chemical properties of the incoming jet or by adding extra fuel or oxygen to the jet. Nevertheless, D_{half} for Case 6 is slightly greater than that for Case 3, which suggests a small effect of the inner jet diffusion combustion on D_{half}. For the conditions that the combustion is strong and premixed flames are moved far away from the incoming jet, D_{half} is unlikely to be affected by the interactions with the main jet turbulence. It can be concluded that D_{half} is mainly controlled by the premixed flame propagation.

Figures 8a–d present the contours of H mass fraction for Case 1 to Case 4. It can be observed that the maximum value of y_H occurs right at the lean premixed flame front while its values inside the incoming jet, in contrast to y_{OH}, are relatively low. This suggests that the radical H is a better flame marker in the TJI-assisted hydrogen combustion than OH. The H contours are in fact similar to the heat release rate, $\dot{Q}_e$, contours, especially in the developed region. Note that the color contour maps in Fig. 8 are scaled differently for better capturing of H radical behavior. For all coflow conditions considered in Case 1 to Case 4, the high values of y_H occur at the edges of the incoming jet in the nearfield region as shear layers develop and generate relatively thick flames. In the developed region of Case 4, y_H values are comparable to those

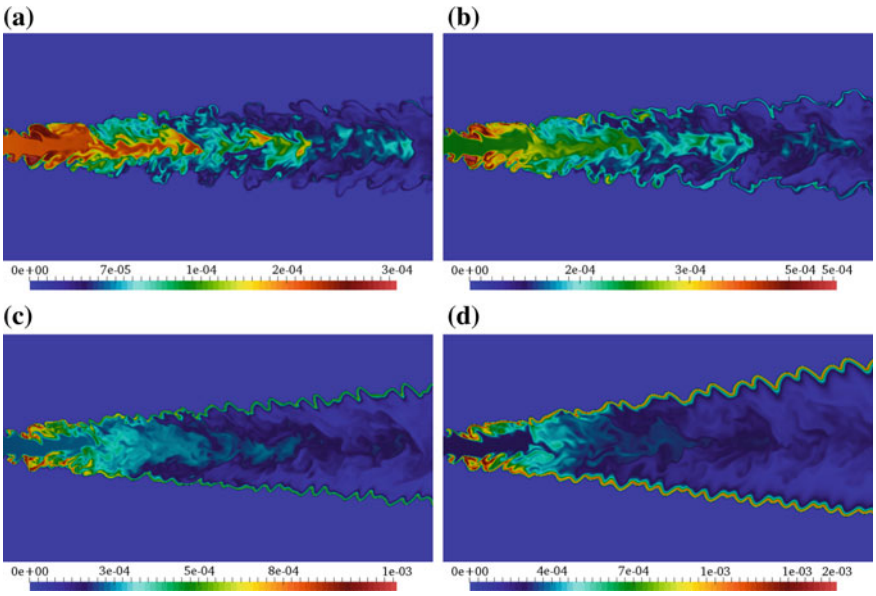

Fig. 8 Instantaneous contours of the H mass fraction, y_H, at the mid span-wise plane ($z = 1.5D$) and $t = 17\tau_0$ for **a** Case 1, **b** Case 2, **c** Case 3, and **d** Case 4 (Note that the scale limits are set to the available values in each contour and are not the same)

in the nearfield region and maximize at the flame front before dropping to very low values in the burned-mixed and hot product zones. Similar trend is observed in Case 3, Case 2, and Case 1 but with smaller local maximum y_H values at the flame front. In Case 1 (and to a lesser extent in Case 2) the local values of y_H in the flame zone are considerably lower than those in the nearfield and there are some discontinues in the flame front due to localized flame extinction.

As explained before, the mixing of the incoming hot jet with cooler premixed coflow in the nearfield region at the reacting shear layer creates relatively thick and geometrically complex flame structure in the TPJ-TJI. The flame structure in the nearfield region might be similar to the corrugated and distributed burning zones in standard premixed flames, where the turbulent eddies are strongly coupled with the thickened and wrinkled flame front. The somewhat distributed and strong reaction virtually vanishes from the main jet as the flow transitions from the nearfield to the developed region and the combustion removes the small scale turbulence. Moving in the stream-wise direction, a spatially continuous, distorted, and concentrated flame is developed in Case 4 and Case 3 (and to lesser extend in Case 2). While the flame propagates in the cross-stream direction into the coflow and moves away from the incoming jet, it becomes thinner and much less affected by the jet turbulence.

The H contours in Fig. 8b–d clearly show the separation of unburned and burned-mixed zones and the relatively thin distorted premixed turbulent flame in the developed region. Even though the flame and turbulence variables significantly fluctuate

in time, they appear to be well stabilized in the developed region. For Case 1, the H contours in Fig. 8a illustrate relatively high and very low values along the flame front, indicating that the coflow composition in this case is indeed very lean and close to lower flammability limit of hydrogen-air mixtures. The lean flammability limit for hydrogen-air mixture at $T = 359\,(\mathrm{K})$ is reported to be about 0.14 [69]. Considering that the coflow temperature in Case 1 is higher than the reported value in experimental measurements, the TJI-assisted premixed combustion can reach a lower lean flammability limit (0.1 in Case 1) than the standard premixed combustion, since the fuel-air mixtures are continuously exposed to a high temperature jet.

The flame stability and extinction are effectively controlled by the interplay of the heat loss from the flame due to turbulent mixing, and the combustion heat release. The heat release is comparatively small in Case 1 (and to a lesser extent in Case 2), making the TPJ-TJI to operate close to lean flammability limit. This is shown in Fig. 9, where the contours of $\dot{Q}_e$ for Case 1 are considered together with a magnified view of a section of flow/flame field in the developed region. The local extinction and re-ignition events are illustrated by e and r, respectively. The spatial and temporal variations in turbulent velocity (particularly at small scales) have significant effects on the flame stretching and folding. With a local increase in stretching effects of turbulence, the gap between the two sides of the flame decreases which leads to local flame extinction and incomplete combustion. As observed in the magnified image, the local flame extinction events are accompanied by a drop in heat release to near-zero values. When the flame front is pushed further away from the hot incoming jet, more local flame extinction events occur. Also, more re-ignition events are observed at locations close to the hot product jet zone, where relatively high heat release values reappear among the extinct flame zones. These confirm that in situations where the

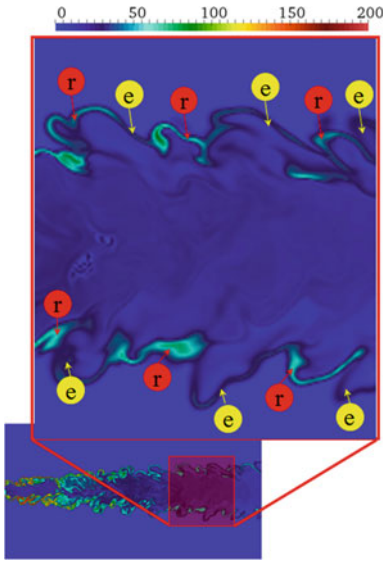

Fig. 9 Localized extinction e and re-ignition r events around the flame in Case 1 with the ultra-lean coflow, identified based on heat release and a magnified view of flow by a factor of 5 : 1

premixed flame is close to the hot product jet, the intense interactions and heat transfer from the incoming jet help the flame to continuously re-ignite after extinction. As long as the flame front is connected, lean coflow mixtures stay largely separated from the flame front and hot product inside burned-mixed zone.

To better understand the flame structure and the local extinction and re-ignition in the TPJ-TJI, the scatter plots of $\dot{Q}_e$ versus $\mathcal{R}$ are shown in Fig. 10 for Case 1 to Case 4. The results for various sections of the flow are included by dividing the flow into three sections: Sec1, (□), representing the nearfield region $0 \leq \xi \leq \xi_1$, Sec2, (◇), representing the initial part of the developed region $\xi_1 \leq \xi \leq \xi_2$, and Sec3, (∗), representing the end part of the developed region $\xi_2 \leq \xi \leq \xi_3$. In this figure, a modified non-normalized "progress variable", $\mathcal{R}$ defined for the TPJ-TJI as:

$$\mathcal{R} = \left(\frac{T_j - T}{T_j - T_{co}} \right) \phi,$$

is used, where ϕ is the local equivalence ratio. The general behavior in Fig. 10 is that the flame becomes much more intensive and the heat release rate roughly doubles

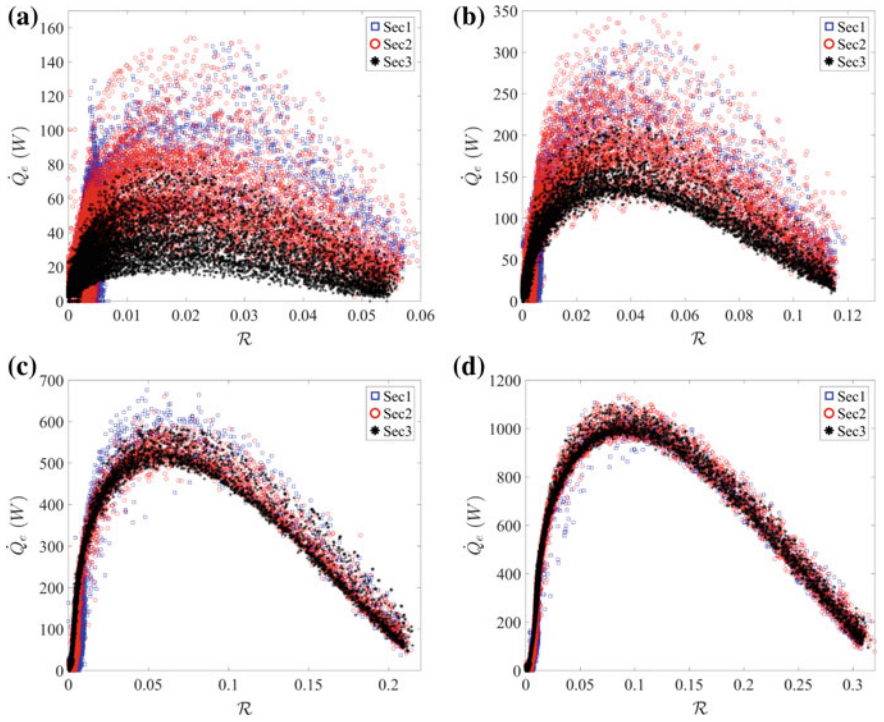

Fig. 10 Scatter plots of the heat release rate, $\dot{Q}_e$ (W), versus TJI progress variable, $\mathcal{R}$, for **a** Case 1, **b** Case 2, **c** Case 3, and **d** Case 4 at different stream-wise sections represented by (□) Sec1, (○) Sec2, and (∗) Sec3

on average with the increase in coflow equivalence ratio from 0.1 to 0.5 in Case 1 to Case 4. The maximum heat release happens at $\mathcal{R}$ values corresponding to the flame front, i.e. $\mathcal{R} = 0.02$, 0.04, 0.065, and 0.1. The areas with greater $\mathcal{R}$ values correspond to the preheated zone of the premixed flame. The areas with smaller $\mathcal{R}$ values represent either the hot product zone or the burned-mixed zone. The extent of scatter in the $\dot{Q}_e - \mathcal{R}$ plot also shows finite-chemistry effects and the level of local flame extinction. The very wide scatter in $\dot{Q}_e - \mathcal{R}$ data for the ultra-lean Case 1 (with $\phi_{co} = 0.1$) indicates that the finite rate chemistry effects are indeed very important and the local heat loss is more than the heat release so that a stable and continuous flame can hardly be maintained. This becomes more clear when the results at different sections of the flow are compared. As stated before, the flame behavior in Case 1 changes in the stream-wise direction from a complex thick flame in the nearfield region to a localized thin discontinuous flame in the developed region. In the nearfield region, as shown in Fig. 10a, the flame is stable and continuously provides sufficient amount of heat. This is represented by high $\dot{Q}_e$ at low $\mathcal{R}$ values. Moving in the stream-wise direction to Sec2, lower $\dot{Q}_e$ values at a given $\mathcal{R}$ are observed. In Sec3, the extinction is dominant and scatter in data is extensive in all flame regions. A somewhat similar but with less extensive scatter in the $\dot{Q}_e - \mathcal{R}$ data is observed for the Case 2 (with $\phi_{co} = 0.2$) in Fig. 10b. For Case 3 (with $\phi_{co} = 0.35$) and Case 4 (with $\phi_{co} = 0.5$), the relatively small scatter in the $\dot{Q}_e - \mathcal{R}$ data in all sections or jet locations supports the existence of a strong, continuous, and stable premixed combustion.

The effects of incoming jet thermo-chemical conditions on the TPJ-TJI are investigated by comparing the results for Case 3, Case 5, and Case 6. In these cases the equivalence ratio of the initial jet mixture, and consequently the incoming jet composition and temperature, are different while the coflow conditions are the same. In Case 3, the inflow jet composition is that of the combustion products of a stoichiometric mixture with no extra fuel or oxidizer with $T_j = 2556\,(\mathrm{K})$. In Case 5, the initial mixture equivalence ratio is chosen to be on the lean side with $\phi_{i_j} = 0.5$, thus the jet mainly consists of O_2 and H_2O with relatively lower (compared to Case 3) temperature of $T_j = 2050\,(\mathrm{K})$. In Case 6, a rich initial jet mixture is considered, therefore the incoming jet carries significant unburned hot fuel along with the combustion products (mainly H_2O) with temperature of $T_j = 2350\,(\mathrm{K})$. This makes the flame a combination of premixed and diffusion type, very different than that in Case 3 and Case 5. The jet and the coflow hydrodynamics are considered to be the same in these three cases. Cases 1 and 7 also have similar (but lower equivalence ratio) coflow but different jet composition.

Comparison of results for Cases 5 and 6 and Cases 1 and 7 (not shown) indicate the existence of both premixed and non-premixed flames in the TPJ-TJI which can be captured by the heat release or H radical. The nearfield results show that significant H radicals are generated by the very complicated, thick, and distributed combustion in all cases, even though the H radical generation in the product jet with extra fuel is much more significant. In Case 5 (similar to Case 1–Case 4), the maximum value of y_H in the developed regions are located at the lean premixed flame front, while y_H values are relatively very low in other zones. In Case 6, the H radical

concentration is significant not only at the premixed flame zones, but also inside the hot product jet zone, where strong diffusion flames exist. The trends are the same for the heat release contours. As shown in Fig. 5c the overall combustion zone temperature in Case 5 is lower than that in Case 3 due to less heat transfer from the incoming jet to its surroundings. However, since the combustion in the developed region is mainly controlled by the coflow conditions, almost the same amount of heat is generated by the premixed combustion in this region. Despite the overall similarities of the thermal half width jet growth in Case 6 with those in Case 5 and Case 3, the flame type and combustion behavior in this case are quite different. In Case 6, the flame-turbulence interactions in the nearfield region are more complex due to the existence of unburned hot fuel in the incoming jet and significant diffusion combustion in the jet zone. The wide and high level $\dot{Q}_e$ in the nearfield region indeed represents the extensive overlap of thick and distributed premixed flame with the diffusion flame. Moving in the stream-wise direction, a spatially continuous and distorted premixed flame is developed in Case 6 which gradually propagates and gets separated from the jet. This is similar to what we observed for Case 3 and Case 5 and is represented by a moderate level of $\dot{Q}_e$ at the edge of the flow. However there is still heat (and H and OH) generation in the inner core jet in the developed region which is due to diffusion flames. The premixed and non-premixed flames are somewhat separated in physical space due to propagation of premixed flame and confinement of the main jet. This can change if the premixed flame becomes weaker for much lower coflow equivalence ratio or ultra-lean conditions such as those considered in Case 1. As discussed above, the highly unsteady and unstable premixed flame in this case experiences significant finite-rate chemistry effects and considerable local extinction and re-ignition. The extra fuel in the incoming jet and the developed diffusion flame may however, has a significant effect on the ultra-lean TPJ-TJI combustion. This is investigated by considering the heat release contours for Case 7 in Fig. 11a with a magnified view of a section of the flow/flame field. The magnified section which is located in the developed region, is the same spacial TPJ-TJI section considered for Case 1 in Fig. 9. The highest values of $\dot{Q}_e$ mainly occur in the nearfield region, hence, for a better visualization, a relatively low contour maximum value of 200, representing the heat release values in the developed region, is considered. The premixed and diffusion flames are shown with dot and dashed lines, respectively. Since the coflow involves an ultra-lean fuel-air mixture, the premixed flame propagation in the cross-stream direction is weak. This leads to an extensive overlap between premixed and diffusion flames and smaller burned-mixed zone. The interactions of the weak premixed flame and high temperature diffusion flame develop a fairly stable premixed flame in the ultra-lean fuel-air mixture. Therefore, much less flame extinction and reignition events (as compared to Case 1 in Fig. 9) occur. This can be further investigated by comparing the mean and confidence intervals of $y-z$ plane averaged heat release rate, $\mu(\langle\dot{Q}_e\rangle_{yz}) \pm \sigma(\langle\dot{Q}_e\rangle_{yz})$, at $t = 17\tau_0$ at different stream-wise locations, ξ, for Case 7 and Case 1 (Fig. 11b). Similar to previous cases the maximum values of $\mu(\langle\dot{Q}_e\rangle_{yz}) \pm \sigma(\langle\dot{Q}_e\rangle_{yz})$ occur in the nearfield region for the reasons explained before. However, the observed higher values of $\dot{Q}_e$ at further downstream locations, confirm less localized extinction in the premixed flame of

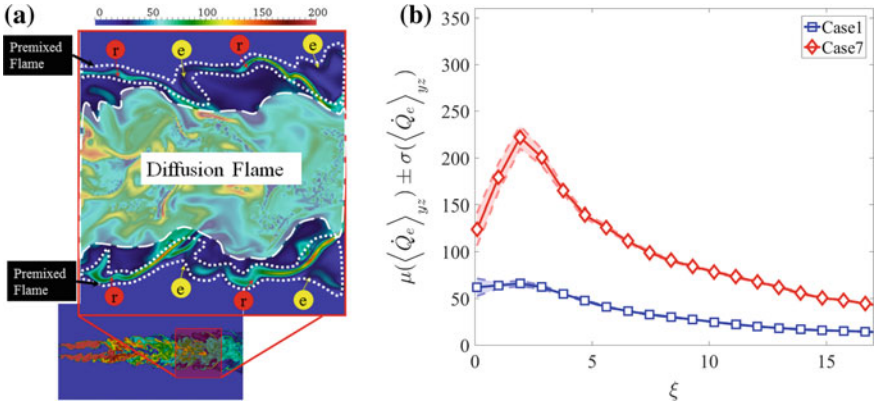

Fig. 11 **a** Simultaneous existence of diffusion and premixed flames along with localized extinction (e) and re-ignition (r) events at the premixed flame surrounding the diffusion flame in Case 7 with the ultra-lean coflow and rich incoming jet, identified based on heat release and a magnified view of flow by a factor of 5 : 1. **b** Mean and confidence intervals of $y - z$ plane averaged heat release rate, $\mu(\langle \dot{Q}_e \rangle_{yz}) \pm \sigma(\langle \dot{Q}_e \rangle_{yz})$, at $t = 17\tau_0$ at different stream-wise locations, ξ, for Case 1 (□) and Case 7 (◇)

fuel-rich jet Case 7. The premixed flame in this case experiences much less localized extinction even at very high strain rate locations, showing the uniqueness of the simulated ultra-lean hybrid premixed-diffusion flame.

4 LES/FMDF of RCM with TJI

The simulated RCM-TJI configuration is similar to the experimental RCM-TJI device built at Michigan State University, operating with a compression ratio of 8.5 [21]. This machine is mainly composed of three separate pneumatic, hydraulic, and combustion cylinder pistons, which are mechanically coupled. Initially, the RCM cylinder is evacuated and then filled with a fuel and air mixture at a specified equivalence ratio and preheated to 353 (K). The mixture is then rapidly compressed to the desired (elevated) temperature and pressure. At the end of the compression process, the fuel and air mixture is well and (ideally) homogeneously mixed. This mixture is held at a constant volume, while the spark plug in the pre-chamber (PCh) is being charged for a duration of about 5 (ms). The PCh is a relatively small chamber (about 2% of the MCh volume) with separate fuel and air injectors, igniter, and a pressure transducer (Fig. 12a). After a successful ignition and combustion in the PCh, a highly unsteady hot product turbulent jet is generated, which initiates the main chamber combustion.

As shown in Fig. 12b, the LES/FMDF equations are solved on the orthogonal uniform mesh with a uniform grid spacing of 2.5×10^{-4} (m) in all directions along with the immersed-boundary method to handle the curved surfaces. A Neumann bound-

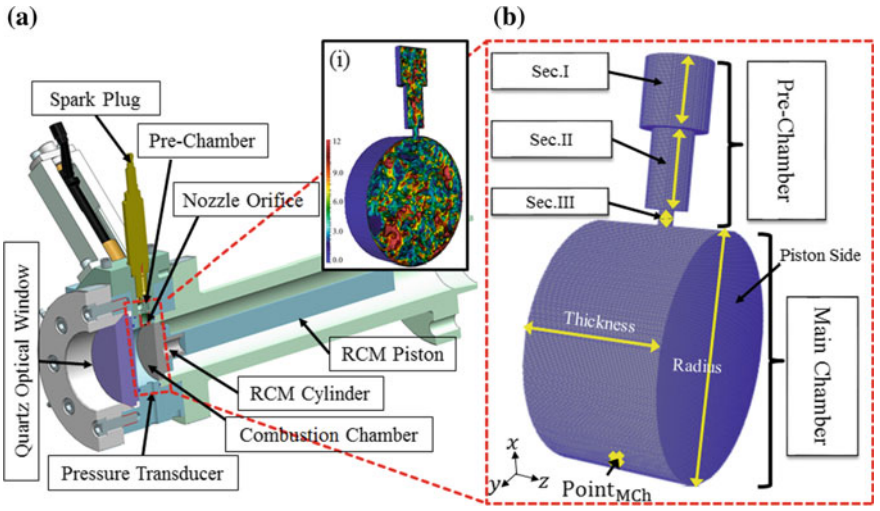

Fig. 12 **a** RCM-TJI combustion system and **b** three-dimensional view of the RCM-TJI mesh. **i** Iso-surfaces of velocity magnitude in half of the domain at the end of compression when piston reaches the top dead center

ary condition is imposed for the density, ($\frac{\partial \rho}{\partial n} = 0$, where n is the direction normal to the immersed surface) and no-slip boundary condition is used for the velocity components at the approximated boundaries. Since heat transfer at the combustion chamber wall is expected to be moderate [41, 42, 70], adiabatic wall condition is mainly considered. A conductive heat transfer model based on the energy balance between the flow and inner and outer walls is also developed and used [9]. The value of y^+ is calculated as $y^+ = \frac{\rho u_\tau y}{\mu}$, where the friction velocity and the wall shear stress are calculated by $u_\tau = \sqrt{\tau_w/\rho}$ and $\tau_w = \mu \frac{du}{dn}$, respectively. The values of y^+ at the TJI-RCM walls in compression and combustion stages are less than 8, where most part of the boundary layer can be captured.

In the RCM-TJI system, the transition from a non-reacting flow to a reacting flow is very fast and complex. The combustion is initiated by a spark plug installed inside and top section of the PCh. The PCh ignition process is a crucial phase in the generation of a stable flame and it depends, rather very significantly, on the turbulence and mixture homogeneity in the PCh prior to the ignition [71]. A successful flame kernel initiation does not necessarily lead to a stable flame and a successful TJI-assisted combustion. For instance, flame kernels may be generated in the PCh but they might be blown off due to intensive flow/turbulence and high strain rate field [72]. Here, the igniter is modeled by an energy deposition model (EDM) [71], in which the ignition source term, Q_{ig}, is defined to be an exponential function of both space and time. In the FD-based LES models, the SGS models have to capture the spark effects on the gas mixture as the ignition energy has to be discharged in an area smaller than the LES grid size. However, in the LES/FMDF model this energy

is deposited on the MC particles, which can capture the local effects. It is found that the selected spark energy value of 150 (mj) is sufficient for a successful ignition. The duration of the spark energy deposition is 200 μs.

The fuel considered in this study (and also used in the experiments) is methane (CH_4). The fuel and air combustion is modeled with one-step and two-step mechanisms provided in Ref. [73]. In the one-step mechanism, the reaction rate is modeled as $K_r = A\, e^{\frac{-E_a}{RT}} [CH_4]^a [O_2]^b$, where $[CH_4]$ and $[O_2]$ are the molar concentrations of CH_4 and O_2 per unit volume of solution. The exponents a and b are called partial orders of reaction, A is the pre-exponential factor (or frequency factor), E_a is the activation energy, and R is the universal gas constant. The flame speed, S_u, is sensitive to the fuel concentration exponent, a, while the oxidizer concentration exponent, b, determines the lean flammability limit. The variation of flame speed with pressure is also considered, where the flame speed decreases by increasing pressure. This can be expressed in the form of $S_u = S_0 p^{-c}$, where S_0 and c are constants. In this type of kinetics model, the flame speed varies as a function of pressure as $S_u \propto p^{(a+b-2)/2}$. Several fuel and oxidizer concentration exponents values were tested. The values of $a = 0.2$ and $b = 1.3$ are selected to give a pressure dependence of $p^{-0.5}$ which are consistent with the flame speed calculations obtained by a detailed mechanism [73]. In order to account (in part) for the effects of incomplete conversion to CO_2 and H_2O, and to include the sequential nature of the hydrocarbon oxidation, a two-step mechanism is also used. The rate of the CO oxidation reaction, $CO + 1/2O_2 = CO_2$, has the value $K_{f,CO} = 10^{14.6}\, e^{\frac{-40}{RT}} [CO]^1 [H_2O]^{0.5} [O_2]^{0.25}$. In order to reproduce both the proper combustion heat and the pressure dependence of the $[CO]/[CO_2]$ equilibrium, a reverse reaction is defined with a rate $K_{r,CO} = 5 \times 10^8\, e^{\frac{-40}{RT}} [CO_2]^1$. As it will be shown in the next section, the main and detailed experimental features of the RCM-TJI flow/combustion can be captured by the above reaction models.

One of the important features of the Lagrangian-Eulerian LES/FMDF solver is that scalars can be computed by two solvers independently to check the consistency and accuracy of them. The correlation coefficients for temperature and fuel mass fraction obtained by two solvers during the entire compression stage are equal to 1. These values for the entire combustion stage are equal to 0.99 and 0.98, showing the very good consistency and accuracy of both solvers. The predicted MCh and PCh pressure traces during the compression stage are compared with the experimental data [9, 21] and are found to be very close to the experimental pressure values throughout the compression stage before TDC ($t \approx 28$ ms). This trend continues up to the ignition point ($t \approx 36$ ms) when the conductive wall heat transfer model is used. As expected, the pressure stays constant between TDC and ignition when adiabatic walls are used. Nevertheless, the experimental and numerical pressures at the ignition point are less than 2% different for the case with adiabatic walls and less than 0.3% different for the case with conductive walls. It should be noted that the measured pressures are obtained by pressure transducers located at the bottom of MCh and top of the PCh, while the LES pressures are volume-averaged pressures.

A comparison between the experimental data [74] and LES/FMDF temperature contours is shown in Fig. 13. The LES thermo-chemical conditions for the reference

case with the MCh and PCh equivalence ratios of $\phi_{MCh} = 0.485$ and $\phi_{PCh} = 0.787$ are the same as those in the experiment. The experimental images shown in Fig. 13a_1–a_3 represent the MCh luminosity at different times. The high speed camera used in the experimental setup captures the luminosity of the flow/flame in the MCh which correlates with temperature (not necessarily the chemical species). Here, t_j is the time where the tip of the hot product jet reaches the middle of the MCh in both experiment and simulation as shown in Fig. 13a_1, b_1, and c_1. The contrast and brightness of the experimental color images were enhanced using Image-J software [75]. The experimental images effectively show the depth-averaged (or span-wise averaged) results in the MCh. Figures 13b_1 to b_3 show the span-wise averaged LES temperature contours, which are more similar to the experimental images. Figure 13c_1–c_3 also show the LES temperature contours at the mid plane in the MCh. It can be seen in Fig. 13a_2, b_2, and c_2 that at time $t_j + 0.2$ ms the measured and computed hot product jets both reach to the lower part of the MCh. The predicted tip jet velocity, consistent with the experiment, is about 125 m/s. After $t_j + 0.4$, combustion is already initiated and sufficiently propagated in the MCh in the span-wise and cross stream directions (Fig. 13a_3, b_3, and c_3).

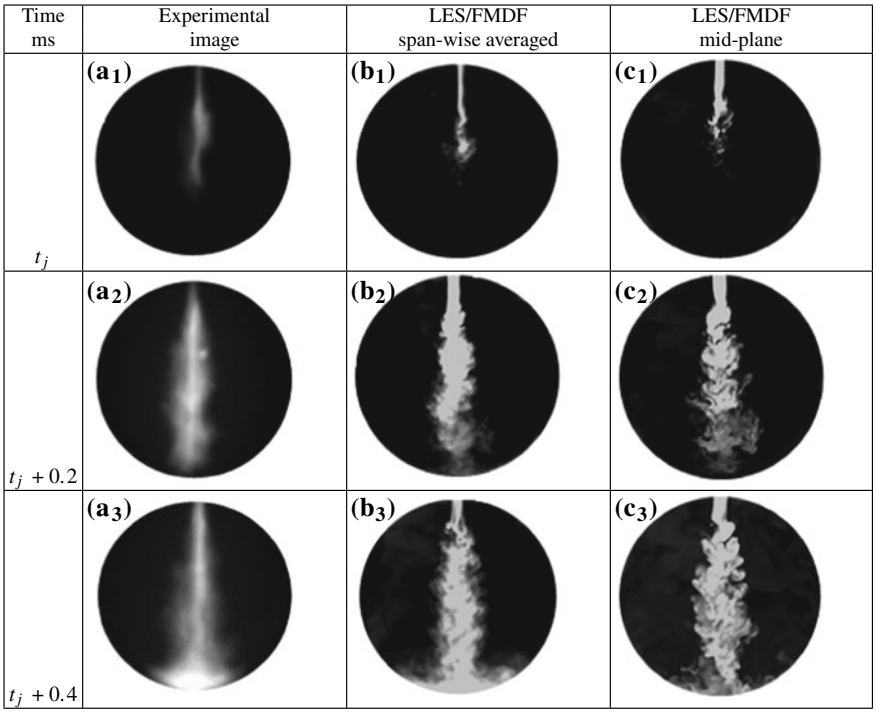

Fig. 13 $\mathbf{a_1}$–$\mathbf{a_3}$ Experimental images, $\mathbf{b_1}$–$\mathbf{b_3}$ LES/FMDF span-wise averaged temperature contours, and $\mathbf{c_1}$–$\mathbf{c_3}$ LES/FMDF instantaneous temperature contours at the middle plane in the MCh

The qualitative comparison between the experimental and numerical results clearly shows the reliability of the computational model used in this study. A quantitative comparison has also been made between the available experimental pressure data [74] and the LES pressures for similar thermo-chemical conditions with one-step and two-step mechanisms and two different wall models. During the early phases of the RCM-TJI combustion, the experimental and numerical pressure values are found to be in reasonably good agreement. In the later phases of the combustion, however, the pressure traces deviate from each other. This behavior might be due to the chemical kinetics and/or wall condition used in the simulations. The discrepancies between the reported and actual initial experimental conditions for the mixture equivalence ratio, temperature, pressure, and/or auxiliary amount of fuel, as well as the possible leakage in the experimental setup might also be the cause for the pressure differences. Despite these differences, the simulated pressure traces are found to follow the corresponding experimental values with less than 8% difference.

Figure 14a–d and e–h show the velocity magnitude iso-surfaces colored by temperature and fuel mass fraction. Figure 15 shows the variations of zy-plane averaged temperature (solid blue line), and fuel mass fraction (dashed red line) at the orifice in time, marked by the direction of the stream-wise filtered velocity component, $\overline{u}$. The jet moving from the PCh into the MCh (i.e. $\overline{u} \geq 0.0$) is shown by yellow squares (■) and the jet going in the opposite direction from the MCh into the PCh (i.e. $\overline{u} \leq 0.0$) is shown by green circles (●). The stream-wise jet velocity values at the orifice are also displayed on the temperature plot. The results in this figure represent the overall behavior of RCM-TJI, as well as the mixture composition and directions of the developed jets passing through the orifice from/to the PCh. It is to be emphasized that Figs. 14a–h and 15 represent the results associated with the same thermo-chemical conditions as those in the experiment (Fig. 13). Generally, three main phases are delineated in the TJI-assisted RCM combustion stage. The detailed features of each phase may vary for different thermo-chemical conditions, but the overall characteristics are believed to remain the same. The three main phases are: (I) cold fuel jet phase, (II) turbulent hot product jet phase, and (III) reverse fuel-air/product jet phase. The important features of each phase are described below.

I. Cold fuel jet phase: The first phase of the RCM-TJI combustion stage consists of the ignition, PCh gas expansion, and formation of the unburned fuel jet. It can be observed in Fig. 15 that at early part of Phase I, with the discharge of the igniter energy and sudden temperature and density changes, a low velocity stream of slightly fluctuating fuel-air mixture is generated at the orifice pushing the unburned charge from the PCh to the MCh. The generated low speed flow is mainly dependent on the amount and the duration of the discharged energy and vanishes rapidly. Having a successful ignition process, turbulent flames form and propagate throughout the PCh and accordingly the PCh pressure rise pushes the "cold" fuel jet into the MCh through the orifice. Figure 15 shows the properties of the cold fuel jet at the orifice; the gas temperature is about $T \simeq 750\,\mathrm{K}$, and the fuel mass fraction is about $y_{\mathrm{CH_4}} \simeq 0.05$ which is close to the stoichiometric value (also shown in Fig. 14a, e). Evidently, a relatively cold and fuel rich (in

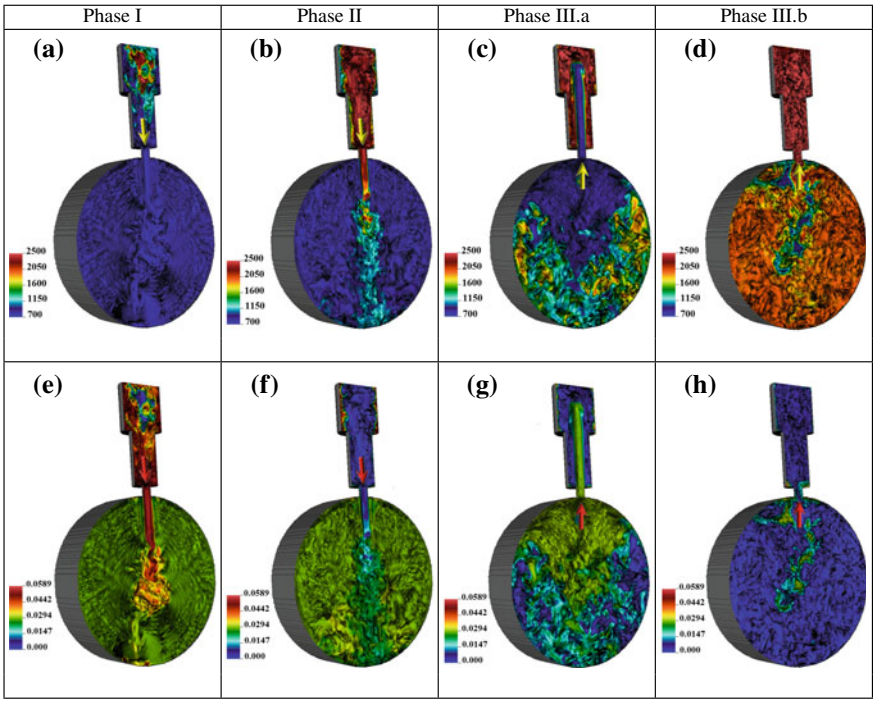

Fig. 14 Instantaneous iso-surfaces of velocity magnitude colored by **a**–**d** temperature, T, and **e**–**h** fuel mass fraction, y_{CH_4} in the RCM-TJI system

comparison to the MCh) jet passes through the orifice. Since the fuel mass fraction of the cold fuel jet is nearly the same as the PCh fuel mass fraction (which is much higher than that in the MCh), it can be easily distinguished from the MCh in Fig. 14e. However, the temperatures in the PCh and MCh are almost the same, making the tracking of the cold fuel jet based on its temperature difficult (Fig. 14a). The main characteristics of this jet are dependent on the PCh composition and turbulence intensity as well as the parameters involved in the ignition. For example, higher equivalence ratio and turbulence intensity in the PCh generally lead to higher velocity of the cold fuel jet. The amount of fuel leaking to the MCh is an important factor in designing the auxiliary air and fuel injectors. The main role of the auxiliary fuel injector is to improve the PCh combustion initiation by providing close to stoichiometric mixture in the PCh. Ideally, all the fuel inside the PCh must participate in the PCh combustion. However, in practice some of the auxiliary fuel escapes the PCh to the MCh. The escaped fuel has a little effect on the MCh combustion, but could be much more effective if it burns inside the PCh. As it will be explained in the next section, locating the igniter close to the nozzle inside the PCh effectively prevents most of the cold fuel leaking to the MCh.

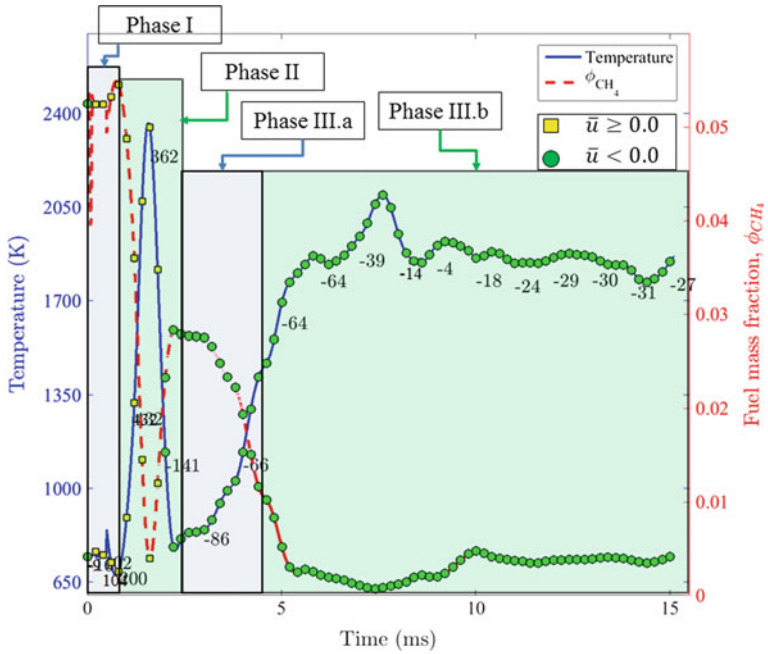

Fig. 15 RCM-TJI combustion phases identified based on the composition, temperature, and direction of the flow at the nozzle

II. Turbulent hot product jet phase: After a successful ignition process and with the development of the PCh combustion, a turbulent hot product/fuel jet is developed passing through the orifice from the PCh to the MCh. The physical and chemical features of this jet, which is controlled by various parameters including PCh and MCh thermo-chemical conditions, are important to the MCh combustion. Figure 14b and f show the jet temperature and composition contours, when it hits the lower section of the MCh. Unlike the cold fuel jet, the hot product jet can also be identified by the velocity magnitude iso-surfaces colored by the temperature. It can be seen in Fig. 15 that the jet temperature rapidly increases from $T \simeq 750\,(\mathrm{K})$ to $T \simeq 2400\,(\mathrm{K})$ and the fuel mass fraction drops to zero in Phase II. Initially, the jet velocity suddenly increases and reaches to very high values (about 500 m/s) at the orifice due to significant PCh-MCh pressure difference. Later on when the MCh combustion is initiated, the jet confronts relatively higher pressure in the MCh, while the PCh combustion becomes less effective. Therefore, the driving force to sustain the high velocity hot product jet is quickly weakened.

III. Reverse fuel-air/product jet phase: The hot product turbulent jet developed during Phase II of the PCh and MCh combustion provides high energy content ignition sites throughout the MCh. Since the fuel-air mixture residence time is relatively high at the lower section of the MCh, combustion mainly starts at this location.

The combustion and pressure rise lead to the development of inverse jet(s) from the MCh to the PCh. This phase of the combustion can be divided into two sub-phases, based on the composition and temperature of the reverse jet(s). Ideally, all of the available fuel must be burned in the MCh. However, as it can be observed in Phase III.a part of Fig. 15 and also in Fig. 14c, g, an unburned fuel stream with relatively low temperature and velocity of about −100 m/s is passing the orifice from the MCh to PCh in form of an inverse jet. The inverse jet properties change in time to higher temperatures and lower fuel mass fractions, an indication of the hot combustion product propagating back into the PCh. The temporal variations of the jet composition, temperature, and velocity are shown in Phase III.b part of Fig. 15. As it can also be observed in Fig. 14d, h, the transition from low temperature inverse fuel rich jet to high temperature inverse product jet depends on the extent of combustion in the MCh.

It is expected that all the fuel in the MCh to be burned by the end of Phase III, however, some of the unburned fuel leaked from the MCh to the PCh stays unburned for a long time and, negatively, affects the performance of the RCM-TJI system. At the very end of the RCM-TJI combustion stage, the remainder unburned fuel-air trapped in the PCh during the previous phases might generate a mixture of unburned fuel-air and product stream from the PCh to the MCh. Since the temperature of this jet is relatively high and its residence time is short, it burns quickly as it gets into the MCh. This jet might help with the combustion sustainability at the later times, however, it also stretches the RCM-TJI combustion period. Preventing the fuel from escaping the PCh by changing the PCh and MCh mixture compositions may not be trivial. However, lowering the igniter position in the PCh shortens the combustion duration and eventually prevents the unburned fuel at the upper section of the MCh to leak into the PCh.

Figure 16a–e show the instantaneous contours of heat release at the mid-plane at different times. To better understand the combustion/flame propagation, the temperature contours are also shown in Fig. 16f–j. After ignition, standard premixed flames are developed propagating in the PCh (Fig. 16a). During the hot product jet phase weak premixed flames are developed at the jet shear layers releasing relatively low heat, despite the generation of a high temperature jet (Fig. 16b, f). This is mainly because of the high jet speed and low fuel-air residence time. When the hot product jet reaches the low section of the MCh, a nearly homogeneous (distributed) combustion is created. Simultaneously, the reversed cold fuel-air jets from the MCh to the PCh develop premixed flames at the reversed jet shear layers inside the PCh (Fig. 16d, i). These indicate the necessity of the computational method of being able to simultaneously capture thick distributed flames in the MCh and the premixed flames in the PCh. The LES/FMDF model is able to do that. Later on during the propagation of the hot products to the upper section of the MCh, localized premixed flame pockets are created inside the unburned air-fuel mixtures. These premixed flame pockets inside the already burned zones are clearly well captured (Fig. 16e, j).

The main idea behind the TJI is to expose the lean MCh mixture to hot ignition sources for a sufficiently long time. However, as we have observed in the previous

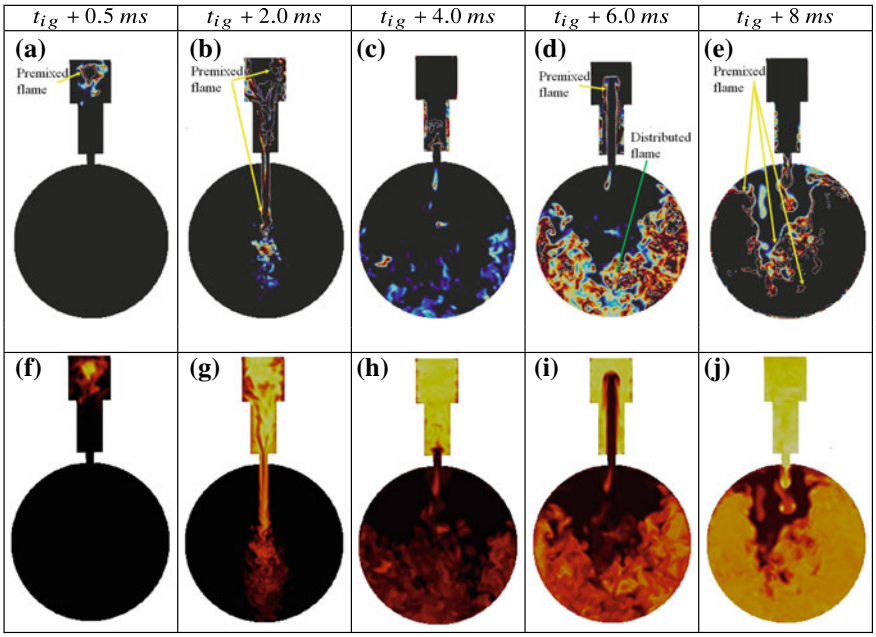

Fig. 16 Instantaneous contours of heat release **a–e** and temperature **f–j** at the mid-plane

figures, during the ignition process a cold fuel jet is developed and exits out to the MCh, slightly changing the leanness of the MCh mixture. Since this jet consists of a cold fuel stream, it unlikely helps the initiation of the MCh combustion, even though, it participates in the MCh combustion at later phases. This jet, however, negatively affects the PCh combustion and the RCM-TJI performance. The PCh ignition process (transition of a non-reacting flow to a reacting flow) determines the speed and amount of the cold fuel jet pushed out from the PCh into the MCh, which otherwise could participate in the PCh combustion. Among the charge/discharge timing and amount of energy and location of the igniter, we found that the spark location is the most influential parameter on the RCM-TJI combustion process. Hence, we consider various cases with different igniter locations which are possible to experimentally replicate. Lowering the igniter location in the PCh, for example, leads to earlier development of a hot turbulent jet and also an effective separation of the PCh mixture in two sections. The mixture at the upper section of the PCh is trapped by the premixed flame in the lower section, but gradually participates in the PCh com-

bustion. With a better understanding of the PCh flow and combustion, an effective TJI-assisted combustion can be established.

5 Conclusions

The studies presented in this chapter cover main features of initiating and controlling combustion via turbulent jet ignition (TJI) process which are important in designing high-performance TJI-based combustion systems. Direct numerical simulations (DNS) of a hot product turbulent planar jet (TPJ) injected into a lean premixed hydrogen-air coflow are performed with detailed chemical kinetics in a three-dimensional configuration. The TPJ-TJI system is spatially divided into nearfield and developed regions. In the nearfield region, the hot incoming jet rapidly auto ignites the lean hydrogen-air mixture at the developing jet shear layer, creating a complex flame structure and providing significant energy for a sustainable ultra-lean combustion. The jet "thermal width" is shown to be dependent more on the coflow thermo-chemical conditions than the incoming jet composition. However, the flame structure is still highly affected by the incoming turbulent jet temperature and composition. The interactions between the premixed flame zone and the hot turbulent inner jet are shown to be much more intense in ultra-lean coflow mixtures, generating extensive localized flame extinction and re-ignition events. The lean flammability limit is shown to be considerably lowered by TJI despite the existence of localized flame extinction. In the case of rich burned incoming product jet, hybrid diffusion-premixed flames are developed.

The application of TJI in a rapid compression machine (RCM), composed of a pre-chamber (PCh) and a main-chamber (MCh), is also simulated for various thermo-chemical and hydrodynamics conditions by the large eddy simulation/filtered mass density function (LES/FMDF) methodology. Three main combustion phases are identified in the RCM-TJI system: (i) cold fuel jet phase, (ii) turbulent hot product/fuel jet phase, and (iii) reverse fuel-air/product jet phase. As a result of the successful ignition of a stoichiometric or rich mixture in the PCh, a turbulent hot product/fuel jet is developed, initiating the lean MCh combustion by providing hot ignition sites throughout the chamber. The MCh combustion initiation and evolution depend on the PCh and MCh initial conditions, as well as the amount of heat transferring through the walls. In the PCh ignition process, a jet of unburned fuel exits out to the MCh, which is an undesirable effect of locating the igniter far away from the nozzle. Effectively, by igniting the PCh charge close to the nozzle much less unburned fuel leaks out into the MCh since the developed premixed flames inside the PCh act as barriers trapping the PCh charge in the upper side, which constantly and gradually burns in the PCh. It can be concluded that hotter, more turbulent, and longer burning jets would be more effective to initiate and maintain the combustion. A properly designed TJI system could generate a fast and nearly volumetric combustion of ultra lean fuel-air mixtures in various combustion systems.

Acknowledgements This study was conducted with the support of NSF and DOE under Grant CBET-1258581. The authors would also like to thank the Texas Advanced Computing Center at the University of Texas-Austin and the Institute for Cyber-Enabled Research at Michigan State University for providing high performance computational resources.

References

1. T. Jin, K. Luo, S. Lu, J. Fan, DNS investigation on flame structure and scalar dissipation of a supersonic lifted hydrogen jet flame in heated coflow. Int. J. Hydrogen Energy **38**(23), 9886–9896 (2013)
2. C. Madnia, F. Jaberi, P. Givi, Large eddy simulation of heat and mass transport in turbulent flows, in *Handbook of Numerical Heat Transfer*, pp. 167–189 (2000)
3. K. Grogan, S. Goldsborough, M. Ihme, Ignition regimes in rapid compression machines. Combust. Flame **162**(8), 3071–3080 (2015)
4. R. Sadanandan, D. Markus, R. Schießl, U. Maas, J. Olofsson, H. Seyfried, M. Richter, M. Alden, Detailed investigation of ignition by hot gas jets. Proc. Combust. Inst. **31**(1), 719–726 (2007)
5. N. Djebaili, R. Lisbet, G. Dupré, C. Patillard, Ignition of a combustible mixture by a hot unsteady gas jet. Combust. Sci. Technol. **104**, 273–285 (1995)
6. H. Phillips, Ignition in a transient turbulent jet of hot inert gas. Combust. Flame **19**(2), 187–195 (1972)
7. A. Validi, F. Jaberi, Numerical study of turbulent jet ignition in a lean premixed configuration. Flow Turbul. Combust. **10**(1), 197–224 (2018)
8. A. Validi, High fidelity numerical simulations of turbulent jet ignition and combustion. Ph.D. thesis, Michigan State University, 2016
9. A. Validi, H. Schock, F. Jaberi, Turbulent jet ignition assisted combustion in a rapid compression machine. Combust. Flame **186**, 65–82 (2018)
10. H. Gunnar, Hot-wire measurements in a plane turbulent jet. J. Appl. Mech. **32**(4), 721–734 (1965)
11. S. Gordeyev, F. Thomas, Coherent structure in the turbulent planar jet. Part 1. Extraction of proper orthogonal decomposition eigenmodes and their self-similarity. J. Fluid Mech. **414**, 145–194 (2000)
12. S. Pope, Calculation of a plane turbulent jet. AIAA J. **22**(7), 896–904 (1983)
13. S. Pope, *Turbulent Flows* (Cambridge University Press, New York, 2000)
14. J. Hinze, *Turbulence* (McGraw-Hill, New York, 1975)
15. E. Toulson, H. Schock, W. Attard, A review of pre-chamber initiated jet ignition combustion systems, in *SAE Technical Papers Series* (SAE Int., 2010)
16. S. Schlatter, B. Schneider, Y. Wright, K. Boulouchos, Comparative study of ignition systems for lean burn gas engines in an optically accessible rapid compression expansion machine, in *SAE Technical Papers Series* (SAE Int., 2013)
17. J. Maxson, D. Hensinger, K. Hom, A. Oppenheim, Performance of multiple stream pulsed jet combustion systems, in *SAE Technical Papers Series* (SAE Int., 1991)
18. E. Murase, S. Ono, K. Hanada, A.K. Oppenheim, Pulsed combustion jet ignition in lean mixtures, in *SAE Technical Papers Series* (SAE Int., 1994)
19. M. Gholamisheeri, I. Wichman, E. Toulson, A study of the turbulent jet flow field in a methane fueled turbulent jet ignition (TJI) system. Combust. Flame **183**, 194–206 (2017)
20. W. Attard, H. Blaxill, A single fuel pre-chamber jet ignition powertrain achieving high load, high efficiency and near zero NOx emissions. SAE Int. J. Engines **5**, 734–746 (2011)
21. G. Gentz, B. Thelen, M. Gholamisheeri, P. Litke, A. Brown, J. Hoke, E. Toulson, A study of the influence of orifice diameter on a turbulent jet ignition system through combustion visualization and performance characterization in a rapid compression machine. Appl. Therm. Eng. **81**, 399–411 (2015)

22. T. Poinsot, D. Veynante, *Theoretical and Numerical Combustion* (R. T. Edwards, Philadelphia, 2001)
23. N. Peters, *Turbulent Combustion* (Cambridge University Press, New York, 2000)
24. R. Fox, *Computational Models for Turbulent Reacting Flows* (Cambridge University Press, New York, 2003)
25. E. Oran, J. Boris, *Numerical Simulation of Reactive Flows* (Cambridge University Press, New York, 2001)
26. F. Williams, *Combustion Theory* (Benjamin/Cummings, Menlo Park, CA, 1985)
27. S. James, F. Jaberi, Large scale simulations of two-dimensional nonpremixed methane jet flames. Combust. Flame **123**(4), 465–487 (2000)
28. S. Pope, PDF methods for turbulent reactive flows. Prog. Energy Combust. Sci. **11**(2), 119–192 (1985)
29. F. Jaberi, P. Colucci, S. James, P. Givi, and S. Pope, Filtered mass density function for large-eddy simulation of turbulent reacting flows. J. Fluid Mech. **401**, 85–121 (1999)
30. M. Yaldizli, K. Mehravaran, H. Mohammad, F. Jaberi, The structure of partially premixed methane flames in high-intensity turbulent flows. Combust. Flame **154**(4), 692–714 (2008)
31. F. Jaberi, Temperature fluctuations in particle-laden homogeneous turbulent flows. Int. J. Heat Mass Transfer **41**(24), 4081–4093 (1998)
32. F. Jaberi, S. James, A dynamic similarity model for large eddy simulation of turbulent combustion. Phys. Fluids **10**(7), 1775–1777 (1998)
33. Z. Li, A. Banaeizadeh, S. Rezaeiravesh, F. Jaberi, Advanced modeling of high speed turbulent reacting flows. *50th AIAA Aerospace Sciences Meeting* (2012)
34. F. Jaberi, D. Livescu, C. Madnia, Characteristics of chemically reacting compressible homogeneous turbulence. Phys. Fluids **12**(5), 1189–1209 (2000)
35. L. Gicquel, P. Givi, F. Jaberi, S. Pope, Velocity filtered density function for large eddy simulation of turbulent flows. Phys. Fluids **14**(3), 1196–1213 (2002)
36. P. Colucci, F. Jaberi, P. Givi, S. Pope, Filtered density function for large eddy simulation of turbulent reacting flows. Phys. Fluids **10**(2), 449–515 (1998)
37. M. Sheikhi, M. Safari, F. Hadi, Entropy filtered density function for large eddy simulation of turbulent flows. AIAA J. **55**(9), 2571–2587 (2015)
38. P. Givi, Filtered density function for subgrid scale modeling of turbulent combustion. AIAA J. **44**(1), 16–23 (2006)
39. M. Sheikhi, T. Drozda, P. Givi, F. Jaberi, S. Pope, Large eddy simulation of a turbulent nonpremixed piloted methane jet flame (Sandia flame D). Proc. Combust. Inst. **30**(1), 249–556 (2005)
40. S. Yilmaz, M. Nik, P. Givi, P. Strakey, Scalar filtered density function for large eddy simulation of a Bunsen burner. J. Propul. Power **26**(1), 84–93 (2010)
41. A. Banaeizadeh, Z. Li, F. Jaberi, Compressible scalar filtered mass density function model for high-speed turbulent flows. AIAA J. **49**(10) (2011)
42. A. Banaeizadeh, A. Afshari, H. Schock, F. Jaberi, Large-eddy simulations of turbulent flows in internal combustion engines. Int. J. Heat Mass Transfer **60**, 781–796 (2013)
43. A. Afshari, F. Jaberi, T. Shih, Large-eddy simulations of turbulent flows in an axisymmetric dump combustor. AIAA J. **46**(7), 1576–1592 (2008)
44. F. Jaberi, R. Miller, F. Mashayek, P. Givi, Differential diffusion in binary scalar mixing and reaction. Combust. Flame **109**(4), 561–577 (1997)
45. R. Kee, F. Rupley, J. Miller, Chemkin-II: A Fortran chemical kinetics package for the analysis of gas-phase chemical kinetics (1989)
46. G. Stahl, J. Warnatz, Numerical investigation of time-dependent properties and extinction of strained methane and propane-air flamelets. Combust. Flame **85**, 285–299 (1991)
47. Y. Ju, T. Niioka, Reduced kinetic mechanism of ignition for nonpremixed hydrogen/air in a supersonic mixing layer. Combust. Flame **99**, 240–246 (1994)
48. C. Vagelopoulos, F. Egolfopoulos, C. Law, Further considerations on the determination of laminar flame speeds with the counterflow twin-flame technique. Symp. (Int.) Combust., [Proc.] **25**(1), 1341–1347 (1994)

49. C. Arndt, R. Schiel, J. Gounder, W. Meier, M. Aigner, Flame stabilization and auto-ignition of pulsed methane jets in a hot coflow: influence of temperature. Proc. Combust. Inst. **34**(1), 1483–1490 (2013)
50. L. Bezgin, V. Kopchenov, A. Sharipov, N. Titova, A. Starik, Evaluation of prediction ability of detailed reaction mechanisms in the combustion performance in hydrogen/air supersonic flows. Combust. Sci. Technol. **185**(1), 62–94 (2013)
51. G. Smith, D. Golden, M. Frenklach, N. Moriarty, B. Eiteneer, M. Goldenberg, C. Bowman, R. Hanson, S. Song, W. Gardiner, V. Vitali, Z. Qin, GRI-Mech 3.0 chemical kinetics mechanism
52. B. Delarue, S. Pope, Application of PDF methods to compressible turbulent flows. Phys. Fluids **9**(9), 2704–2715 (1997)
53. T. Poinsot, S. Lele, Boundary conditions for direct simulations of compressible viscous flows. J. Comput. Phys. **101**(1), 104–129 (1992)
54. S. Lele, Compact finite difference schemes with spectral-like resolution. J. Comput. Phys. **103**(1), 16–42 (1992)
55. C. Kennedy, M. Carpenter, R. Lewis, Low-storage, explicit Runge-Kutta schemes for the compressible Navier-Stokes equations. Appl. Numer. Math. **35**(3), 177–219 (2000)
56. C. Steinberger, T. Vidoni, P. Givi, The compositional structure and the effects of exothermicity in a nonpremixed planar jet flame. Combust. Flame **94**(3), 217–232 (1993)
57. S. Pope, Turbulent premixed flames. Annu. Rev. Fluid Mech. **19**, 237–270 (1987)
58. C. Rutland, A. Trouve, Direct simulations of premixed turbulent flames with nonunity Lewis numbers. Combust. Flame **94**(1–2), 41–57 (1993)
59. P. Clavin, Dynamic behavior of premixed flame fronts in laminar and turbulent flows. Prog. Energy Combust. Sci. **11**(1), 1–59 (1985)
60. J. Driscoll, Turbulent premixed combustion: Flamelet structure and its effect on turbulent burning velocities. Prog. Energy Combust. Sci. **34**(1), 91–134 (2008)
61. M. Boger, D. Veynante, H. Boughanem, A. Trouvé, Direct numerical simulation analysis of flame surface density concept for large eddy simulation of turbulent premixed combustion. Proc. Combust. Inst. **27**(1), 917–925 (1998)
62. O. Gicquel, N. Darabiha, D. Thevenin, Liminar premixed hydrogen/air counterflow flame simulations using flame prolongation of ILDM with differential diffusion. Proc. Combust. Inst. **28**(2), 1901–1908 (2000)
63. A. Lipatnikov, J. Chomiak, V. Sabelnikov, S. Nishiki, T. Hasegawa, Unburned mixture fingers in premixed turbulent flames. Proc. Combust. Inst. **35**(2), 1401–1408 (2015)
64. R. Griffiths, J. Chen, H. Kolla, R. Cant, W. Kollmann, Three-dimensional topology of turbulent premixed flame interaction. Proc. Combust. Inst. **35**(2), 1341–1348 (2015)
65. D. Lee, K. Huh, DNS analysis of propagation speed and conditional statistics of turbulent premixed flame in a planar impinging jet. Proc. Combust. Inst. **33**(1), 1301–1307 (2011)
66. A. Lipatnikov, J. Chomiak, Effects of premixed flames on turbulence and turbulent scalar transport. Prog. Energy Combust. Sci. **36**(1), 1–102 (2010)
67. Y. Lin, P. Jansohn, K. Boulouchos, Turbulent flame speed for hydrogen-rich fuel gases at gas turbine relevant conditions. Int. J. Hydrogen Energy **39**(35), 20242–20254 (2014)
68. D. Beerer, V. McDonell, P. Therkelsen, R.K. Cheng, Flashback and turbulent flame speed measurements in hydrogen/methane flames stabilized by a low-swirl injector at elevated pressures and temperature. J. Eng. Gas Turbines Power **136**, 20242–20254 (2014)
69. M. Zabetakis, Flammability characteristics of combustible gases and vapors (U.S. Bur. Mines. Bull. 627, 1965)
70. G. Lodier, C. Merlin, P. Domingo, L. Vervisch, F. Ravet, Self-ignition scenarios after rapid compression of a turbulent mixture weakly-stratified in temperature. Combust. Flame **159**(11), 3358–3371 (2012)
71. G. Lacaze, E. Richardson, T. Poinsot, Large eddy simulation of spark ignition in a turbulent methane jet. Combust. Flame **156**(10), 1993–2009 (2009)
72. S. Ahmed, E. Mastorakos, Spark ignition of lifted turbulent jet flames. Combust. Flame **146**(1–2), 215–231 (2006)

73. C. Westbrook, F. Dryer, Simplified reaction mechanisms for the oxidation of hydrocarbon fuels in flames. Combust. Sci. Technol. **27**(1), 31–43 (1981)
74. A. Validi, H. Schock, E. Toulson, F. Jaberi, LES/FMDF of turbulent jet ignition in a rapid compression machine. Bull. Am. Phys. Soc. **60**(21), 100 (2015)
75. C. Schneider, W. Rasband, K. Eliceiri, NIH Image to ImageJ: 25 years of image analysis. Nat. Methods **9**(7), 671–675 (2012)

Flamelet Modeling for Supersonic Combustion

Tomasz G. Drozda, Jesse R. Quinlan and J. Philip Drummond

Abstract Flamelet models have proven useful in enabling fast and accurate simulations of subsonic turbulent combustion. However, in supersonic combustion, these models face many challenges. The current work presents an a priori analysis of the steady flamelet model using the HIFiRE Direct Connect Rig (HDCR) dual-mode scramjet combustor. The analysis uses Reynolds-averaged simulation (RAS) data obtained with a finite-rate reaction mechanism to assess some of the flamelet model assumptions. Two flight conditions are numerically simulated: Mach 5.84 and Mach 8. These conditions cover a range of combustion phenomena that could be expected to occur in a scramjet engine during flight. The analysis reveals that both nonpremixed and premixed combustion occur in the HDCR combustor. In addition, under some conditions, strong finite-rate effects are also present. These physical aspects could be readily modeled with existing flamelet techniques, however, the effects of variable pressure, wall heat transfer, and flamelet equation boundary conditions are more challenging to address. The latter three elements present the key barriers to utilizing flamelets for supersonic combustion simulations. Although techniques to address these additional challenges are limited, a few perspectives are provided highlighting physics-based requirements in the context of flamelet modeling.

Keywords Flamelet modeling · Combustion modeling · Turbulent reacting flows · Supersonic flows · Reynolds average simulation · HIFiRE 2

1 Introduction

Accurate numerical simulations of supersonic, turbulent, reacting flows present some of the most challenging problems encountered today in fluid mechanics. This is

T. G. Drozda (✉) · J. R. Quinlan · J. P. Drummond
NASA Langley Research Center, Hampton, VA 23666, USA
e-mail: tomasz.g.drozda@nasa.gov

J. R. Quinlan
e-mail: jesse.r.quinlan@nasa.gov

J. P. Drummond
e-mail: j.p.drummond@nasa.gov

D. Livescu et al. (eds.), *Modeling and Simulation of Turbulent Mixing and Reaction*, Heat and Mass Transfer, https://doi.org/10.1007/978-981-15-2643-5_6

because, unlike subsonic combustors, supersonic combustors contain complex and coupled interactions of compressible flow features, such as shocks and expansions, with other elements of the flow like laminar, transitional, and turbulent boundary layers, turbulence itself, mixing-layers, large-scale vorticity, and combustion. These nonlinear interactions can drastically alter the flow behavior and lead to: shock-induced flow transition and/or separation, which change the effective flow area and alter the shock structure in the combustor; shock-turbulence interactions, which can amplify turbulence intensity; shock-mixing-layer interactions, which introduce baroclinic torque that can change fuel-air mixing and therefore rates of chemical reactions; and strong flow-chemistry coupling, which is responsible for potentially significant and rapid pressure rise due to the heat release. Furthermore, unlike subsonic combustors, which are typically designed with a specific combustion mode in mind, supersonic combustors often exhibit regions of nonpremixed, partially premixed, and premixed combustion. This is because low combustor temperatures and pressures increase ignition delay time, while at the same time, fast flow through times decrease residence times. Both effects result in partial premixing of the fuel and air in a high-speed combustor. In addition, flameholding devices utilize areas of flow recirculation that may contain fully and/or partially premixed burning fuel-air mixtures. All of these difficult to model and simulate flow elements are compounded onto the challenges of subsonic combustion, which includes turbulence and turbulence-chemistry interaction modeling, radiation modeling, and chemical kinetics modeling. As a final challenge of supersonic combustion, it should be noted that, unlike their subsonic counterparts, supersonic combustors are typically an order of magnitude larger in length and cross section area, operate at higher Reynolds numbers, and are highly integrated into the vehicle airframe [1]. Because of the above challenges, numerical simulations of supersonic combustors typically require an order-of-magnitude or more dynamic range of scales and therefore more computational resources (i.e., grid points). One aspect of supersonic flow simulations that is simpler than that of subsonic simulations is the specification of the boundary conditions [2], e.g., a supersonic inflow boundary does not exhibit an outward-traveling characteristic, and a supersonic outflow does not exhibit an inward-traveling characteristic. By contrast, subsonic flow typically requires physically consistent treatment of the outgoing and incoming flow characteristics [2] to ensure that simulations are well-posed, stable, and accurate.

The computational resources needed for reacting simulations also rapidly increase with the number of species transport equations and chemical reactions that must be solved for a given chemical kinetics model, which depend on the complexity of the fuel. A typical chemical kinetics model for even a simple fuel like hydrogen can have 9 species and 19 reactions [3], which more than doubles the number of solved transport equations for a three-dimensional Reynolds-averaged simulation (RAS) of a turbulent flow with a 2-equation turbulence model [4] typically used in practice. Chemical kinetics models for complex hydrocarbon fuels can contain 1,000s of species and 10,000s of chemical reactions [5] making numerical simulations all but intractable except for simple zero- and one-dimensional flame simulation configurations [6, 7]. For these reasons, the vast majority of computational simulations of

turbulent supersonic combustion have relied on only the most simplified or reduced mechanisms [8, 9] and/or phenomenological models of combustion [10], both of which limit predictive capability. In addition to increasing the number of needed equations, reaction rate constants found in most chemical kinetics models follow the Arrhenius form, which is expensive to evaluate numerically and introduces numerical stiffness, thereby further increasing the simulation time.

For numerical simulations to accurately and effectively contribute to the engineering design process, the simulation times must be kept to a minimum. Because chemical kinetics have such a strong influence on the overall simulation cost, often increasing it by an order of magnitude or more as compared to the corresponding nonreacting simulation, it is natural to seek models that reduce the number of needed species transport equations while simultaneously maintaining, to the extent possible, the fidelity of a complex chemical kinetics model. In general, the basis for the reduction hinges on the assumptions about the important chemical reactions [11] and/or the state of the underlying combustion physics. The laminar flamelet model introduced by Peters [12–14] follows the latter and assumes that local combustion processes progress much faster than those corresponding to the bulk flow motions that tend to strain and extinguish the local flame. Conceptually, this leads to a thin flame or a reaction front (called a flamelet) that is convected, distorted, and wrinkled by the otherwise nonreacting, often turbulent, flowfield [15, 16]. Although this flowfield is capable of warping the thin flame that it is convecting, it does not significantly alter the internal structure of the flame. Therefore, under the flamelet model, only the flow gradients in a single dimension normal to the flame can influence the local reaction chemistry. Consequently, complex three-dimensional (3D), wrinkled, turbulent flames may be approximated using an ensemble of local one-dimensional (1D), laminar flames. This phenomenology effectively allows the 1D laminar flame and its underlying chemical kinetics to be decoupled from the flowfield and solved independently using a set of simplified partial differential equations called the flamelet equations. The flamelet equations are derived from the conservation equations for the species mass, momentum, and energy (i.e., Navier-Stokes with species transport) by transforming the spatial coordinates into a coordinate normal to the flame surface and simplifying [17] or by utilizing a Crocco-type transformation to transform the spatial coordinate into a state-space variable called a mixture fraction [12, 14]. The fundamental property of the mixture fraction is that it is a nonreacting (passive) scalar quantity that can be used to track the local state of the mixture because it represents a fraction of mass that originated in the fuel stream. The mixture fraction is also the key element of the flamelet model because it parameterizes, independently of the type of fuel used, the complete thermochemical state of the flame by a single scalar quantity. This allows the flamelet model to retain many elements of the realistic chemistry and significantly reduces the computational costs of reacting simulations, especially for complex hydrocarbon fuels. Indeed, the laminar flamelet model was developed to enable any combustion simulation, at a time when the available computational resources were prohibitively limited. Currently, the laminar flamelet models continue to be useful by enabling practical combustion simulations with large eddy

simulations (LES) [18, 19] and optimization and uncertainty quantification studies with RAS [20].

Conventional flamelet modeling typically involves a tabulation step that provides relationships between the mixture fraction and the rest of the thermochemical state-space. This tabulation may be performed as a simulation preprocessing step or in situ [21]. The flamelet model may further be augmented by the assumed probability density function (PDF) turbulence-chemistry interaction (TCI) model [22–25] whose contribution can be included in the flamelet table. Including the assumed PDF model in the flamelet table requires an additional lookup parameter, typically mixture fraction variance, that identifies the level of turbulence intensity in the TCI model. The resulting lookup table contains all the species and thermodynamic state variables over the range of turbulence intensities needed to execute the simulation, and completely eliminates the need to computationally evaluate expensive reaction rates during the simulation, which also results in the removal of numerical stiffness associated with the Arrhenius reactions rate constants.

In practice, to generate a flamelet lookup table, the flamelet equations must be solved subject to certain boundary conditions. These boundary conditions specify the mixture composition of the fuel and oxidizer streams, and their respective temperatures. In addition, a constant value of the pressure experienced by the flame is needed as well as an equation of state, e.g., the ideal gas law. The characteristic strain imposed by the flowfield on the flame is also needed. For the flamelet equations transformed into the flame-normal coordinate, the "strain" is provided by specifying the 1D computational domain length, and fuel and oxidizer stream velocities normal to the flame. For the flamelet equations transformed into the mixture fraction state-space, the flame strain is replaced by the scalar dissipation rate. The strain and scalar dissipation rate are important parameters because they control the extent to which the 1D laminar flame can burn. Small strain leads to near-equilibrium combustion, whereas large strain can lead to a fully extinguished mixing solution. Therefore, to fully encompass the range of potential flamelet states, the strain rate or scalar dissipation rate can be included as an additional independent table parameter. However, the strain and the scalar dissipation rate are not directly related to the combustion process and lead to multivalued parameterization of the combustion state-space. To overcome this issue, either one of these quantities can be replaced in the flamelet table by a progress variable [26], which is usually a linear combination of one or more combustion product species [27]. Unlike the mixture fraction, the progress variable cannot be a passive scalar because it must be able to track the progress of combustion from near-equilibrium conditions to flame extinction and vice versa. In addition, the specific definition of the progress variable, together with the mixture fraction, must offer a unique mapping of the combustion state-space [27].

The above narrative describes the most computationally efficient steady laminar flamelet (SLF) model, where the word steady indicates that the flamelet equations have been integrated to steady-state and those results tabulated. The key limitations of this model are the inability to treat partially-premixed or premixed combustion systems, and for nonpremixed systems, the inability to model multifuel or multioxidizer streams with different stream temperatures or at different pressures. In

addition, the SLF model cannot accurately capture autoignition processes [28] nor heat transfer effects to the combustor walls. Despite the attractive and significant computational cost savings, the limitations of the SLF model significantly narrow, in theory, its range of practical applicability. Nevertheless, flamelet models, in general, have often been found to perform acceptably even for cases that are a priori known to violate some of the theoretical bounds of the model. This may be because flow regions containing unsupported physics do not drive the leading flow behavior for a particular case or that some limitations are not as restrictive as others. For example, the requirement of constant pressure is of no consequence for subsonic combustion where pressure variations within a combustor are small or at hypervelocity Mach numbers, where the heat release does not significantly raise the combustor pressure. Even pressure variations by a factor of 2 only produce reaction rate changes of the order 4, which may be within the error bound of a typical chemical kinetics model. However, other limitations may be critical; for example, in multiphase fuel spray combustion systems, the temperature of the gaseous oxidizer surrounding the evaporating liquid fuel droplet increases as the evaporated fuel mixes and reacts with the oxidizer. Modeling the latter process with steady flamelet equations would require (at the least) a variable oxidizer boundary condition, whose range is difficult to estimate a priori. Nevertheless, many of the limitations of the steady flamelet model have been addressed, albeit often at the expense of increased computational cost, by several new classes of the flamelet approach, namely: the unsteady flamelet model (also known as the representative interactive flamelet (RIF) model) [28–30], the flamelet progress variable (FPV) model [26, 31, 32], and the flamelet-generated manifolds (FGM) model [33–35].

In supersonic combustion, three physical effects complicate the formulation and implementation of the flamelet model. The first is the heat-release-induced pressure rise, which increases the pressure experienced by the flame as the reactions progress, thereby altering the chemical kinetics. The second is the viscous heating, which increases local mixing-layer and boundary layer temperatures and at higher Mach numbers may lead to oxidizer and fuel dissociation via endothermic reactions, processes that are not included in the flamelet equations. These two effects are important at opposite ends of the flight Mach number range; that is, for flight Mach numbers up to about 6–8, the heat-release-induced pressure rise is significant but its importance begins to decrease as the flight Mach number begins to exceed 10–12. The opposite is true for viscous heating, which is not significant compared to the heat release at Mach numbers less than about 4, but can lead to dissociation at Mach numbers in excess of about 7–8. Viscous heating is also much more difficult to account for using the flamelet methodology because it represents physical processes that are typically explicitly excluded from the energy equation when deriving the flamelet equations. Nevertheless, these effects could be qualitatively incorporated into the tabulation process or the unsteady flamelet model by allowing variations in the flamelet boundary conditions (e.g., temperature and composition of fuel and oxidizer streams). The third physical effect is the significant heat transfer that could occur to the combustor walls. For both supersonic and subsonic combustors, heat transfer to the wall is a result of flame-wall interactions and combustion products

being convected and/or diffused toward the cold walls. In addition, for high Mach number supersonic combustors, the heat transfer is also the result of viscous heating of the near-wall mixture. This mixture could contain pure fuel or pure air, or a burned or unburned mixture of the two. In all cases, the cooling process results in the decrease in the enthalpy of the mixture to states not accounted for in the flamelet table.

To demonstrate the extent of the applicability of the flamelet model to supersonic combustion, the Hypersonic International Flight Research Experimentation (HIFiRE) Direct Connect Rig (HDCR) [36, 37] dual-mode supersonic combustion ramjet (scramjet) combustor is used in this work. To accomplish this, 3D RAS are performed of the HDCR geometry using a 22-species finite-rate reduced reaction mechanism for a JP-7 fuel surrogate [38]. Although designed for academic and collaborative purposes, the HDCR is representative of a practical cavity-stabilized scramjet combustor. TCI modeling is omitted in the current work to focus the analysis on the flamelet model performance rather than the coupled performance of the flamelet and TCI models. Two HDCR flight conditions are analyzed: a Mach 5.84 dual-mode supersonic combustion mode, which exhibits both subsonic and supersonic combustion regions; and a Mach 8 scramjet mode, which consists of primarily supersonic combustion. Both flight conditions are analyzed to characterize the fundamental nature of the combustion. The current combustion mode analysis may not reveal the true nature of all combustion modes potentially present in the HDCR because modeling errors introduced by the turbulence and chemical kinetics models and the absence of various other physics submodels (e.g., TCI model), nevertheless, previous work [39] showed that the current simulations correctly reproduce the experimentally obtained HDCR combustor pressure rise and therefore heat release distribution.

This chapter is organized as follows. First, the governing equations applicable to high-speed compressible turbulent reacting flows are introduced, followed by the concept of the mixture fraction and its transport equation, the flamelet equations, and the progress variable. Second, some of the phenomenology observed in supersonic combustion is described and combustion mode analysis is utilized to identify the range of relevant phenomena present in the HDCR simulations. Third, the challenges of accounting for the variable pressure, wall heat transfer, and changing flamelet equation boundary conditions are discussed. The chapter concludes by discussing some of the challenges that continue to face the flamelet modeling approach in supersonic combustion.

2 Governing Equations

The details of the derivation of the transport equations governing fluid flows in thermodynamic equilibrium are documented in many undergraduate and graduate texts [2, 40–45] and will not be repeated here. Flows in thermodynamic non-equilibrium and multiphase flows are not considered, but common practical

approaches to treating these flows are discussed by Gnoffo et al. [46], Park [47] and Faeth [48]. The derivations of the governing equations for the motion of a fluid in thermodynamic equilibrium lead to a set of elegant nonlinear partial differential equations (PDEs) governing the transport of several conserved quantities: species mass, momentum, and energy. One of the earliest complete discussions of these equations with an application to high speed reacting flows is offered by Drummond [49]. These equations can also be further manipulated to obtain other transport equations for quantities such as vorticity, enthalpy, or (combining with the second law of thermodynamics) entropy that have been found useful in elucidating physical behaviors of flows [50].

The governing conservation equations encompass a wide range of physical fluid flow phenomena. One particularly complex phenomena is that of a turbulent flow. The discussion of turbulence physics is beyond the scope of this text, but several excellent texts are available [51–54] with many more describing computational [2, 49, 55–60] and modeling [61–65] treatments. Nevertheless, a few words relevant to the current discussion are warranted. Foremost, it should be stated that one characteristic of turbulent flows, which is responsible for the difficulty encountered in theoretical and numerical analysis, is the multiscale nature of turbulence. That is, the fluid motions in a turbulent flow occur over a wide range of both time and length scales with the ratio of large to small turbulence flow scales proportional to the 3/4 power of the Reynolds number [54]. For a problem of practical interest, this leads to the required number of computational cells for direct numerical simulation (DNS) to be on the order of $1 - 10 \times 10^9$ (i.e., three orders of magnitude in each of the three spatial dimensions). By contrast, the grid resolutions that are used in simulations of practical interest on capacity cluster hardware and in the amount of time required to make a programmatic impact are typically on the order of $10 - 100 \times 10^6$. That is, the typical current capability for numerical simulations of turbulent flows is almost two to three orders of magnitude smaller than that required for the corresponding direct simulations. Therefore, even before the flamelet model is introduced to reduce the computational cost of combustion, any numerical simulation involving turbulent flow must be set up to utilize the existing computer hardware in a reasonable amount of time and still be able to investigate and analyze turbulent reacting flows of interest.

One approach is to reduce the effective dynamic range of turbulent length and time scales to that which can be reasonably considered for simulations on a current computer. Unfortunately, this constrains the simulations to only a portion of the turbulence length scales with the removed portions requiring a mathematical model for the effects they have on those being simulated. This is called the closure problem and such modeling has been a topic of research for the past century [66] with significant developments in the last 50 years. In the current work, a common form of the governing conservation equations are presented. These equations can be obtained by either time-averaging (or ensemble-averaging) [62] to derive transport equations used for RAS, or spatial-averaging (or filtering) [63] to derive the LES equations. Despite the very different approach of these two methods to the turbulence scale reduction, the mathematical operations of time-averaging and spatial-averaging produce the exact same set of transport equations. What differs are the interpretations of

the terms, their closures, and the numerical implementation requirements, with the spatially-averaged transport equations for LES typically requiring unsteady, high-order accurate numerical schemes to properly resolve the turbulence length scales near the filter scale.

In what follows, the nondimensional form of the Favré-averaged transport equations are presented. These equations arise as a result of applying the time-average operator to the governing transport equations. The time-average and Favré-average of an arbitrary quantity, f, are denoted by an $\overline{f}$ and $\widetilde{f}$, respectively, and they are related to each other via the density, i.e., $\overline{\rho}\widetilde{f} = \overline{\rho f}$. The resulting Favré-averaged equations are commonly used to perform RAS of high-speed, turbulent, reacting flows. Applying the Favré-averaging operator to the governing equations for mass, species mass fractions, momentum, and energy results in:

$$\frac{\partial \overline{\rho}}{\partial t} + \frac{\partial \overline{\rho}\widetilde{u}_k}{\partial x_k} = 0, \tag{1}$$

$$\frac{\partial \overline{\rho}\widetilde{Y}_\alpha}{\partial t} + \frac{\partial \overline{\rho}(\widetilde{u}_k + \widehat{V}_k^c)\widetilde{Y}_\alpha}{\partial x_k} = \frac{\partial}{\partial x_k}\left(\frac{\widehat{\mu}}{\widehat{Sc}_\alpha}\frac{\partial \widetilde{Y}_\alpha}{\partial x_k}\right) + \dot{\omega}_\alpha(\overline{p}, \widetilde{Y}_\alpha, \widetilde{T}) \\ \underbrace{- \frac{\partial}{\partial x_k}\left(\widetilde{\overline{\rho}u_k Y_\alpha} - \overline{\rho}\widetilde{u}_k\widetilde{Y}_\alpha\right)}_{\text{Turbulence Flux}} + \underbrace{\left(\widetilde{\dot{\omega}_\alpha(p, Y_\alpha, T)} - \dot{\omega}_\alpha(\overline{p}, \widetilde{Y}_\alpha, \widetilde{T})\right)}_{\text{Turbulence Chemistry Interaction (TCI)}}, \\ \alpha = 1, 2, \ldots, N, \tag{2}$$

$$\frac{\partial \overline{\rho}\widetilde{u}_i}{\partial t} + \frac{\partial \overline{\rho}\widetilde{u}_k\widetilde{u}_i}{\partial x_k} = -\frac{\partial \overline{p}}{\partial x_i} + \frac{M_r}{Re_r}\frac{\partial}{\partial x_k}\left(\widehat{\mu}\left(\frac{\partial \widetilde{u}_i}{\partial x_k} + \frac{\partial \widetilde{u}_k}{\partial x_i}\right) - \frac{2}{3}\widehat{\mu}\frac{\partial \widetilde{u}_j}{\partial x_j}\delta_{ik}\right) \\ \underbrace{- \frac{\partial}{\partial x_k}\left(\widetilde{\overline{\rho}u_k u_i} - \overline{\rho}\widetilde{u}_k\widetilde{u}_i\right)}_{\text{Turbulence Stress}}, \tag{3}$$

$$\frac{\partial \overline{\rho}\widetilde{e^t}}{\partial t} + \frac{\partial \overline{\rho}(\widetilde{u}_k + \widehat{V}_k^c)\widetilde{h^t}}{\partial x_k} = \frac{M_r}{Re_r}\frac{\partial}{\partial x_k}\left(\widetilde{u}_i\left(\widehat{\mu}\left(\frac{\partial \widetilde{u}_i}{\partial x_k} + \frac{\partial \widetilde{u}_k}{\partial x_i}\right) - \frac{2}{3}\widehat{\mu}\frac{\partial \widetilde{u}_j}{\partial x_j}\delta_{ik}\right)\right) \\ + \underbrace{\frac{M_r}{Re_r}\frac{\partial}{\partial x_k}\left(\widetilde{u_i\tau_{ik}} - \widetilde{u}_k\widetilde{\tau_{ik}}\right)}_{\text{Velocity-Shear Stress Correlation}} + \frac{M_r}{Re_r Pr_r}\frac{\partial}{\partial x_k}\left(\frac{\widehat{\mu}}{\widehat{Pr}}\frac{\partial \widetilde{h}}{\partial x_k} - \frac{\widehat{\mu}}{\widehat{Pr}}\sum_\alpha\left(\frac{\widehat{Le}_\alpha - 1}{\widehat{Le}_\alpha}\right)\widetilde{h}_\alpha\frac{\partial \widetilde{Y}_\alpha}{\partial x_k}\right) \\ + \frac{\partial \overline{\rho}(\widetilde{k} + k)\widehat{V}_k^c}{\partial x_k} \underbrace{- \frac{\partial}{\partial x_k}\left(\widetilde{\overline{\rho}u_k h} - \overline{\rho}\widetilde{u}_k\widetilde{h}\right)}_{\text{Turbulence Enthalpy Flux}} \underbrace{- \frac{\partial}{\partial x_k}\left(\widetilde{\overline{\rho}u_k\frac{u_i u_i}{2}} - \overline{\rho}\widetilde{u}_k\widetilde{\frac{u_i u_i}{2}}\right)}_{\text{Turbulent Kinetic Energy Flux}}, \tag{4}$$

where ρ, Y_α, u_i, V_k^c, e^t, h^t, h, h_α, k, p, T, μ, τ_{ij}, and $\dot{\omega}_\alpha$ are the density, mass fraction of species α, velocity, differential diffusion correction velocity, total energy, total enthalpy, enthalpy, enthalpy of species α, kinetic energy, pressure, temperature, mixture molecular viscosity, shear-stress, and reaction rate of species α, respectively. Temporal and spatial coordinates are denoted by t, and x_i. The equations are also nondimensionalized with M_r, Re_r, Pr_r, denoting reference Mach, Reynolds, and Prandtl numbers, respectively. Pr, Sc_α, and Le_α are the mixture Prandtl number, and the Schmidt and Lewis numbers for species α. In addition, the "hat" over an arbitrary quantity, $\widehat{f}$, denotes a nonlinear function quantity evaluated using the Favré averaged variables, for example,

$$\widehat{V}_k^c = \sum_\alpha \frac{\widehat{\mu}}{\widehat{Sc}_\alpha} \frac{\partial \widetilde{Y}_\alpha}{\partial x_k}, \ \widehat{\mu} = \mu(\widehat{T}), \ \widehat{Sc}_\alpha = \frac{\widehat{\mu}}{\overline{\rho}\widehat{D}_\alpha}. \tag{5}$$

It should be noted that the mixture Pr, Sc_α, and Le_α quantities in Eqs. (2), and (4) are denoted with a "hat" because, although they could be constants, in general, they are nonlinear functions of both the thermodynamic and transport properties of the mixture. In addition, the temperature is also denoted with the "hat" because, for noncalorically perfect gases, it is obtained by iteration from the Favré averaged mixture enthalpy. Furthermore, it should also be noted that when the species diffusivities are all equal, i.e., $Sc_\alpha = Sc$, then the differential diffusion correction velocity, $\widehat{V}_k^c$ is identically zero. This assumption is commonly used when simulating turbulent reacting flows.

The various forms of energies are related by the first law of thermodynamics,

$$\begin{aligned} \widetilde{e^t} &= \widetilde{e} + \widetilde{k} + k, \ \widetilde{h^t} = \widetilde{h} + \widetilde{k} + k, \\ \widetilde{k} &= \frac{1}{2}\widetilde{u}_i\widetilde{u}_i, \ k = \frac{1}{2}\left(\widetilde{u_i u_i} - \widetilde{u}_i\widetilde{u}_i\right), \end{aligned} \tag{6}$$

where e is the internal energy.

All of the terms within the underbraces in Eqs. (1–4) and the turbulent kinetic energy are unclosed and must be modeled. The above equations further require a time-averaged form of the equation of state, which for an ideal gas becomes,

$$\overline{p} = \overline{\rho}\widetilde{RT} = \overline{\rho}\sum_\alpha \frac{Ru}{W_\alpha}\widetilde{Y}_\alpha\widetilde{T} + \underbrace{\overline{\rho}\sum_\alpha \frac{Ru}{W_\alpha}\left(\widetilde{Y_\alpha T} - \widetilde{Y}_\alpha\widetilde{T}\right)}_{\text{Scalar-Temperature Correlation}}, \tag{7}$$

where R, R_u, and W_α are the mixture gas constant, universal gas constant, and molecular weight of species α, respectively. The unclosed scalar-temperature correlation term is most commonly neglected. Further discussion on modeling the unclosed terms for practical high-speed applications for RAS is offered by Baurle [67].

2.1 Mixture Fraction

All flamelet models rely on the mixture fraction as a means of parameterizing combustion physics. By definition, the mixture fraction represents a mass fraction of all material that originated in the fuel stream that is present locally in the mixture. The formal definition of the mixture fraction can be written as:

$$Z = \frac{\beta - \beta_O}{\beta_F - \beta_O} \tag{8}$$

where Z is the mixture fraction and β_F and β_O are the mass fractions of the fuel material in the fuel and oxidizer streams, respectively. The definition of β is:

$$\beta = \sum_i \gamma_i Z_i = \sum_i \gamma_i \sum_j \frac{a_{ij} W_i Y_j}{W_j}, \quad i = C, H, O, \quad j = 1, 2, \ldots, N, \tag{9}$$

where γ_i is a weight corresponding to each element present in the mixture, Z_i is elemental mass fraction (e.g. Z_C, Z_H, Z_O), a_{ij} is the number of atoms of element i in species j. It is clear from Eq. (8) that the mixture fraction takes values in the range of 0 to 1, which correspond to pure oxidizer and fuel streams, respectively. Equation (9) also shows that the mixture fraction is a linear combination of elemental mass fractions. By conservation of mass, the latter are conserved scalars, therefore, the mixture fraction must be a conserved scalar also. Specific values of γ_i define a particular mixture fraction. Table 1 shows commonly used definitions. The mixture fraction can also be used to calculate the fuel-to-oxidizer mass ratio. Since by definition, the mixture fraction represents the mass fraction of elements originating in the fuel stream, the fuel-to-oxidizer mass ratio becomes,

Table 1 Elemental mixture fraction weights

γ_C	γ_H	γ_O	Notes
$\frac{2}{W_C}$	$\frac{1}{2W_H}$	$-\frac{1}{W_O}$	Bilger's definition [68]
$\frac{2}{W_C}$	$\frac{1}{2W_H}$	0	Barlow's definition (for Sandia Flames) [69]
1	0	0	Elemental mixture fraction for C
0	1	0	Elemental mixture fraction for H

$$\frac{F}{O} = \frac{Z}{1-Z}, \tag{10}$$

where $1 - Z$ is the mass fraction of material in the mixture that originated in the oxidizer stream. When the oxidizer is air, Eq. (10) represents the fuel-to-air ratio. The fuel equivalence ratio can also be computed by dividing the fuel-to-air ratio by its value evaluated at the stoichiometric value of the mixture fraction.

The mixture fraction transport equation is derived by applying the definition of the mixture fraction, Eqs. (8) and (9), to the unaveraged transport equations for the mass fractions. The result is;

$$\frac{\partial \rho Z}{\partial t} + \frac{\partial \rho u_i Z}{\partial x_i} = \frac{\partial}{\partial x_i}\left(\frac{\mu}{Sc}\frac{\partial Z}{\partial x_i}\right) + \epsilon_{DD}, \tag{11}$$

where the source term ϵ_{DD} is a correction factor due to the differential diffusion (DD) [70],

$$\epsilon_{DD} = \frac{1}{\beta_F - \beta_O}\sum_n \gamma_n \sum_\alpha \frac{a_{n\alpha} W_n}{W_\alpha}\frac{\partial J_{\alpha i}}{\partial x_i} - \frac{\partial}{\partial x_i}\left(\frac{\mu}{Sc}\frac{\partial Z}{\partial x_i}\right), \tag{12}$$

where $J_{\alpha i}$ is the diffusive flux of species α in the i-th direction. Most commonly, the mixture fraction transport equation is derived assuming equal diffusivities among the species in the mixture, i.e., $J_{\alpha i} = J_i$. Under this assumption ϵ_{DD} is identically zero. Assuming equal diffusivities and applying time averaging operator to Eq. (11) yields,

$$\frac{\partial \overline{\rho}\widetilde{Z}}{\partial t} + \frac{\partial \overline{\rho}\widetilde{u_i}\widetilde{Z}}{\partial x_i} = \frac{\partial}{\partial x_i}\left(\frac{\widehat{\mu}}{\widehat{Sc}}\frac{\partial \widetilde{Z}}{\partial x_i}\right) - \underbrace{\frac{\partial}{\partial x_k}\left(\widetilde{\overline{\rho}u_k Z} - \overline{\rho}\widetilde{u_k}\widetilde{Z}\right)}_{\text{Turbulence Flux}}, \tag{13}$$

where the term inside the underbrace is the unclosed turbulence mixture fraction flux and must be modeled.

Many TCI models, including presumed and transport PDF models, utilize the mixture fraction variance as a key aggregate variable by which to quantify the turbulence intensity experienced by the species. The mixture fraction variance is defined as,

$$\widetilde{Z''^2} = \widetilde{Z^2} - \widetilde{Z}^2. \tag{14}$$

The transport equation for this quantity can be readily obtained by subtracting the transport equation for $\widetilde{Z}^2$ from the transport equation for $\widetilde{Z^2}$, both of which can be derived in a manner similar to that used to obtain Eq. (13). The result is,

$$\frac{\partial \overline{\rho}\widetilde{Z''^2}}{\partial t} + \frac{\partial \overline{\rho}\widetilde{u}_i \widetilde{Z''^2}}{\partial x_i} = \frac{\partial}{\partial x_i}\left(\frac{\widehat{\mu}}{\widehat{Sc}}\frac{\partial \widetilde{Z''^2}}{\partial x_i}\right) - 2\underbrace{\left(\widetilde{\rho u_i Z} - \overline{\rho}\widetilde{u}_i\widetilde{Z}\right)}_{\text{Turbulence Flux}}\frac{\partial \widetilde{Z}}{\partial x_i}$$
$$- 2\frac{\widehat{\mu}}{\widehat{Sc}}\underbrace{\left(\overline{\frac{\partial Z}{\partial x_i}\frac{\partial Z}{\partial x_i}} - \frac{\partial \widetilde{Z}}{\partial x_i}\frac{\partial \widetilde{Z}}{\partial x_i}\right)}_{\text{Dissipation}} - \frac{\partial}{\partial x_i}\underbrace{\left(\overline{\rho}\left(\widetilde{u_i Z^2} - \widetilde{u}_i\widetilde{Z^2}\right) - 2\overline{\rho}\widetilde{Z}\left(\widetilde{u_i Z} - \widetilde{u}_i\widetilde{Z}\right)\right)}_{\text{Turbulence Transport}}. \tag{15}$$

The terms on the right hand side represent molecular diffusion, production, dissipation, and turbulent transport, respectively, of the mixture fraction variance.

2.2 Flamelet Equations

Several approaches have been used to obtain flamelet manifolds for both non-premixed and premixed flames [26, 33]. All approaches involve solutions to the one-dimensional forms of partial differential equations that result from transforming the governing equations for mass, momentum, and energy into a flame adapted coordinate system. The original approach proposed by Peters [12], utilizes a Crocco-type transformation from spatial coordinates to the mixture fraction coordinate. Applying this transformation to the unaveraged transport equations for species mass fractions and energy produces a set of laminar flamelet equations,

$$\rho\frac{\partial Y_\alpha}{\partial t} = \frac{1}{2}\rho\chi_\alpha\frac{\partial^2 Y_\alpha}{\partial Z^2} + \dot{\omega}_\alpha, \tag{16}$$

$$\rho\frac{\partial h}{\partial t} = \frac{1}{2}\rho\chi\frac{\partial^2 h}{\partial Z^2} \tag{17}$$

where χ_α, and χ are the scalar dissipation for species α, and scalar dissipation for the mixture, respectively. The scalar dissipations are defined as,

$$\chi_\alpha = 2\frac{\mu}{\rho Sc_\alpha}\frac{\partial Z}{\partial x_j}\frac{\partial Z}{\partial x_j},\ \chi = 2\frac{\mu}{\rho Sc}\frac{\partial Z}{\partial x_j}\frac{\partial Z}{\partial x_j}. \tag{18}$$

It should be noted that the above equations account for the effect of differential diffusion and should be solved together with Eq. (11) containing a model for ϵ_{DD}. However, by assuming unity Lewis number, which also leads to constant values for Sc_α, a more common form of the flamelet equations that neglects the effect of differential diffusion is obtained. It should further be noted that the above flamelet equationsare derived using a low-Mach-number approximation form of the energy

equation, where the first term on the right hand side of Eq. (4) is neglected. As a consequence, the viscous heating effects, which may be important in high-speed flows, are not captured by the flamelet manifold obtained using Eqs. (16) and (17).

Equations (16) and (17) represent a boundary-value problem that can be solved by specifying the species composition and temperature for the fuel ($Z = 1$) and oxidizer ($Z = 0$) streams, and the pressure for the mixture. Although in high-speed flows the pressure can vary between fuel and oxidizer streams, this effect cannot be captured by the flamelet equations, however for thin flames, this variation can be neglected. The scalar dissipation rates must also be specified. For RAS, a few models for these quantities can be obtained following the analogy to the dissipation of turbulent kinetic energy [2], which results in the scalar dissipation rate being a function of the turbulence dissipation, turbulent kinetic energy, and the mixture fraction variance. Because mixture fraction is bounded between 0 and 1, for a given value of the mixture fraction, there exists a theoretical upper limit of the mixture fraction variance, which limits the scalar dissipation rate.

The scalar dissipation rate controls the extent to which the flame is burning. For χ values approaching zero, a near-equilibrium chemistry solution is obtained, whereas for values approaching infinity, the nonreacting solution is recovered. The intermediate flamelet solutions can be obtained by varying the value of the scalar dissipation rate within those limits. However, care must be taken when attempting to generate a sequence of flamelet manifolds in this way because there exist three distinct flamelet solutions, corresponding to nonreacting, unstable burning, and stable burning, for a single value of the scalar dissipation rate. This multivalued nature of the scalar dissipation requires special simulation approaches [71, 72] to obtain all possible solutions. This also complicates the scalar dissipation's role as a parameterizing quantity, which requires a unique parameterization of the thermochemical state for applications. For this reason, early applications omitted the unstable flamelet branch from the flamelet table. More recently, a progress variable quantity [26, 31] has been introduced to improve unique parameterization of all possible flamelet solutions.

2.3 Progress Variable Equation

Instead of using Z and χ to parameterize solutions of the flamelet equations, a progress variable, C, is introduced to replace the latter. The progress variable is defined such that it provides a correlation with the global progress of the combustion and is typically a linear combination of combustion-product species mass fractions. For example, Pierce and Moin [31] have proposed $C = Y_{CO_2} + Y_{H_2O}$ for hydrocarbon fuels. Unlike the mixture fraction, the progress variable is a reacting scalar. The progress variable is also typically normalized across all manifolds by its equilibrium value, such that $C = 1$ for equilibrium combustion [27]. For nonreacting solutions, $C = 0$. Most importantly, since C is defined to correlate with the reaction's progress, Z and C have the potential to uniquely parameterize all of the flamelet solutions. It should be noted, however, that because of the nonlinear nature of chemical kinet-

ics, the use of the progress variable does not guarantee a unique parameterization, and some limited nonuniqueness typically still exists. Any nonunique regions of the complete flamelet manifold must be "trimmed" to avoid spurious behaviors in applications. Alternately, Ihme et al. [27] have proposed a regularization technique that strives to enforce a unique parameterization of the progress variable, to the extent possible, by introducing and adjusting the weights of the mass fractions that compose the progress variable.

The application of the flamelet model parameterized using Z and C in a computational fluid dynamics (CFD) solver requires a solution of the time-averaged progress variable transport equation along with the transport equation for $\widetilde{Z}$, Eq. (13). Once the definition of the progress variable has been established, the transport equation can be readily derived and generally takes on the form;

$$\frac{\partial \overline{\rho}\widetilde{C}}{\partial t} + \frac{\partial \overline{\rho}\widetilde{u}_i\widetilde{C}}{\partial x_i} = \frac{\partial}{\partial x_i}\left(\frac{\widehat{\mu}}{\widehat{Sc}}\frac{\partial \widetilde{C}}{\partial x_i}\right) - \underbrace{\frac{\partial}{\partial x_k}\left(\widetilde{\overline{\rho}u_k C} - \overline{\rho}\widetilde{u}_k\widetilde{C}\right)}_{\text{Turbulence Flux}} + \dot{\omega}_C(\overline{p}, \widetilde{Z}, \widetilde{C}, \widetilde{T}) + \underbrace{\left(\widetilde{\dot{\omega}_C(p, Z, C, T)} - \dot{\omega}_C(\overline{p}, \widetilde{Z}, \widetilde{C}, \widetilde{T})\right)}_{\text{Turbulence Chemistry Interaction (TCI)}}, \quad (19)$$

where the terms inside the underbrace are unclosed and must be modeled. It should be noted that, in addition to the unclosed turbulence flux term, which can be modeled in conventional ways, the above transport equation includes an unclosed term for the turbulence and progress variable chemistry interactions. This term is analogous to the TCI term in Eq. (2) and is difficult to model and often simply neglected. The reaction source term, $\dot{\omega}_C$, is evaluated from the solution of the flamelet equations and added to the flamelet table.

3 Introduction to Supersonic Combustion

Supersonic combustion is defined as the conversion of reactants into products that takes place in the supersonic "background" flow. By this definition, a conventional ramjet engine, although capable of supersonic propulsion, does not exhibit supersonic combustion because the supersonic freestream air is compressed and slowed to subsonic speeds prior to injecting the fuel and energizing the engine via combustion. The subsonically-convected combustion products are then expanded to supersonic speeds through the converging-diverging (CD) thrust nozzle. In a ramjet engine, the combustion processes are quite similar to those found in a conventional gas turbine combustors, although the mechanics of compression, fuel injection and mixing, and expansion to produce thrust are different. Supersonic combustion typically occurs in a scramjet engine, where the high-speed freestream air is compressed in such a way that it still remains supersonic when entering the high-speed combustor. One marked

difference between subsonic and supersonic combustion is that the static pressure in the combustor decreases by a few percentage points in a subsonic combustor, whereas it can rise by an order of magnitude in the supersonic combustor. This characteristic pressure rise is a result of the chemical conversion of reactants to products under compressibility effects of a supersonic flow, and is conceptually similar to a Rayleigh flow, i.e., a supersonic model flow with heat addition. However, it should be noted that unlike Rayleigh flow, the total enthalpy of a reacting flow does not change due to combustion and can only be altered by heat addition (or cooling) through the combustor walls. It should also be noted that it is not appropriate to categorize supersonic combustion as either constant pressure or constant volume as is sometimes helpful with subsonic combustion. For example, a gas turbine combustor and internal combustion engine can be effectively phenomenologically modeled using constant pressure and constant volume reactor models, respectively. The pressure rise in a scramjet is a result of compressibility of the working fluid and a function of its Mach number. A recent overview is provided by Urzay [73].

The rising pressure in a supersonic combustor acts as a back-pressure to the upstream supersonic inflow further slowing it down, and steepening and increasing the strength of any shock waves. The combustion-induced pressure can continue to increase until the value of the combustor pressure is about equal to that corresponding to the normal shock pressure rise of the combustor entrance flow. Any further increase in the combustor pressure will cause the flow to become "unstarted," that is, any shock wave system that formed upstream of the combustor must move further upstream and out of the inlet in order to reduce the mass flow rate through the engine to match that which the combustor pressure rise could physically support.

For nonpremixed systems, the relative velocity of the reactant streams is quantified by the velocity difference parameter, and it could be subsonic or supersonic as further quantified by the convective Mach number. Both the velocity difference parameter and the convective Mach number are relevant to the reactant mixing process and therefore combustion rate control in canonical problems [74–76]. Both quantities are important rate-controlling parameters in subsonic and supersonic combustion, but large velocity differences and supersonic convective Mach numbers are more commonly encountered in supersonic reacting flows because parallel-moving supersonic reactant streams can more readily exhibit velocity differences with values close to the speed of sound. Nevertheless, high convective Mach numbers can still be achieved for subsonic reactant streams if they are traveling in opposite directions, which is rare in practice. The primary impact of high values of the velocity difference parameter is an increased turbulence mixing rate of the mixing layer between the reactant streams. The convective Mach number has a limited competing effect in that the mixing rate could be suppressed by as much as a factor of about five as the convective Mach number increases to supersonic values [77]. The high velocity differences between the reactant streams can also induce viscous heating, which can alter the local temperature of the reactants, and therefore, reduce the ignition delay time of the local reactive mixture.

The shock waves and expansions that form in a supersonic combustor also interact with the combustion processes through the pressure and temperature changes they impart to the reactants and the generation of the baroclinic torque as they pass across the reactant mixing layer. Similar to viscous heating, the changes to pressure and temperature alter the response of the chemical kinetics, whereas the baroclinic torque introduces large-scale mixing, which increases the fuel-air interface, allowing molecular diffusion to mix the fuel and air at the molecular level where reactions take place.

Because of the strong interdependence among these various compressible flow processes and chemistry, it is hard to envision how a flamelet manifold could be generated a priori for supersonic combustion and contain all the relevant reactant states.

4 Flamelets and Supersonic Combustion

Although the utility of the flamelet model, and especially the flamelet progress variable (FPV) model, has been demonstrated extensively for numerous low speed applications, these models in their original form are unable to account for many of the physical processes characteristic of high speed reacting flows, such as variable combustion pressure, viscous heating, significant heat transfer at the walls, and varying flow properties of the reactants due to the compressibility effects, e.g., shocks and expansions. Several attempts at extending the FPV model formulation to high-speed compressible flows have been made. These attempts focus primarily on addressing the pressure dependence [78–80] of the flamelet manifold, which is the simplest and most obvious way to proceed within the framework of the existing flamelet equations.

The most common way to partially, but efficiently, account for the varying pressure in a supersonic combustor is to scale the tabulated reaction source term of the progress variable, Eq. (19), by a ratio of the square of the local mean pressure to the square of the reference pressure of the tabulated flamelet table, i.e.,

$$\overline{\dot{\omega}}_C = \frac{\overline{p}^2}{p_{ft}^2}\overline{\dot{\omega}}_{C_{ft}}, \tag{20}$$

where the subscript ft denotes the quantity obtained from the flamelet table. The pressure scaling of the progress variable reaction rate is motivated by the fact that the majority of chemical reactions are second order. However, although this scaling offers a physically reasonable approximate way to relate reaction rates at two different combustion pressures, it does not account for the differences in the equilibrium flame temperature or changes to the mixture composition, and therefore mixture fraction and progress variable, that also occur when the finite rate kinetics are actually evaluated at different pressures. Nevertheless, this approach has been demonstrated to improve the pressure predictions of HyShot II experiments [81].

More recently, to improve the accuracy of the pressure scaling of the progress variable reaction source term with respect to a generic chemical kinetics mechanism, Saghafian et al. [80] introduced a generalized scaling that includes a density power scaling and an activation temperature scaling in the form:

$$\overline{\dot{\omega}}_C = \left(\frac{\overline{\rho}}{\rho_{ft}}\right)^{a_p} \exp\left(-T_a\left(\frac{1}{\widetilde{T}} - \frac{1}{T_{ft}}\right)\right)\overline{\dot{\omega}}_{C_{ft}}, \tag{21}$$

where a_p and T_a are scaling constants that can be optimized a priori to improve the pressure scaling method over the range of pressures of interest. In practical applications, reasonable values for a_p and T_a range from 2–3, and 10,000–20,000, respectively.

While the scaling approach is certainly a way to introduce some influence of the variable pressure via a progress variable source term, the most direct way to account for the varying pressure within a flamelet framework is simply to add the pressure as a parameterizing variable to the flamelet table. This approach increases the computer memory footprint of the flamelet table by as much as an order of magnitude and further increases the computational cost of lookup and retrieval; however, it eliminates the approximations associated with the pressure scaling approach and significantly improves the robustness of the progress variable in supersonic combustion applications such that some regularization procedures proposed by [27] may not be needed, as demonstrated by Quinlan [82].

5 HIFiRE Direct Connect Rig (HDCR)

To demonstrate some of the challenges of utilizing flamelet models for supersonic combustion applications, RAS of the HDCR combustor are performed for two flight conditions corresponding to flight Mach numbers of 5.84 and 8. The first condition is referred to as the dual-mode case and exhibits regions of both subsonic and supersonic combustion. The second condition corresponds to the scram-mode and exhibits primarily supersonic combustion, albeit in both nonpremixed and premixed combustion modes. The two flight conditions cover a range of combustion phenomena that could be reasonably expected to commonly occur in a scramjet engine during flight.

The HDCR was a ground-based direct-connect experiment conducted at NASA Langley Research Center (LaRC) in support of the HIFiRE 2 flight experiment [37, 39]. HIFiRE 2 was a hydrocarbon-fueled scramjet flowpath designed to demonstrate supersonic-combustion mode transition from dual-mode to scram-mode operation and to validate design and analysis tools. Based on the estimated flight trajectory, supersonic combustion mode transition was expected to occur between flight Mach numbers of about 6–8. The HDCR ground experiment was developed and performed prior to flight of the HIFiRE 2 article to validate the flowpath design and demonstrate combustor operability in the range of flight Mach numbers from 6 to 8.

The HDCR ground test article included the constant-area isolator, cavity-based combustor with multistage fuel injection, and a bifurcated exhaust nozzle. An inner mold line of the flowpath is shown in Fig. 1, in which relevant dimensions and injector locations are indicated. The HIFiRE 2 inlet was not included in the HDCR test article, instead, the HDCR isolator was connected directly to the ground test facility CD nozzle. The flow properties, including the Mach number, at the entrance of the isolator were obtained from two CFD simulations [83] of the HIFiRE 2 inlet at flight Mach numbers of 5.84 and 8. These inlet simulation results showed that the facility nozzles, with Mach numbers of 2.51 and 3.46, produced isolator flows appropriate for the dual-mode and scram-mode experiments, respectively. The total enthalpy of each of the two flows was set to match that of the corresponding flight Mach number. The HDCR combustor has five stages of fuel injectors; however, only the primary and secondary injectors located upstream and downstream of the cavity, respectively, were fueled during the experiments. In the HDCR experiments, dual-mode operation was marked by the leading combustion-induced shock anchoring upstream of the primary injectors. When this leading shock moved downstream of the primary injectors, the flowpath was operating in scram-mode. The fuel used was a JP-7 surrogate consisting of a gaseous mixture of 36% methane and 64% ethylene by volume [84]. The dual-mode and scram-mode cases were tested with a total equivalence ratio of 0.65, and 1.0, respectively. The total equivalence ratio was further split between the primary and secondary injectors, with values of 0.15 and 0.5 for the dual-mode case and 0.4 and 0.6 for the scram-mode case, respectively. These fuel splits were set to demonstrate on the ground one of the primary objectives of the HIFiRE 2 flight experiment, which was to reach combustion performance of burned equivalence ratio of 0.7 at Mach 8 [37]. Hereafter, simulation cases will be referenced using a case identifier that reflects the operational mode, the flight Mach number, and the imposed simulation wall boundary conditions, as shown in Table 2. For example, case *D584A* signifies dual-mode operation, *D*, at a flight Mach number of *5.84* with adiabatic walls, *A*. Similarly, case *S800I* signifies scram-mode operation, *S*, at a flight Mach number of *8.00* with isothermal walls, *I*. Data collected during the experiments included wall temperatures, heat fluxes, and wall static pressures. The flowpath was outfitted with 144 static pressure ports, 19 flowpath surface thermocouples, and 4 heat flux gauges.

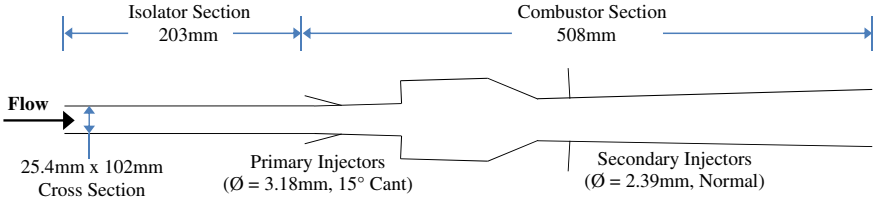

Fig. 1 Side view and key dimensions of the HDCR combustor flowpath, where ⊘ is internal diameter of the injectors

Table 2 Summary of simulated test cases, including flight Mach number, plenum total conditions, fuel equivalence ratios (Φ), and wall boundary conditions (BCs)

Case	Flt. mach	Tot. temp. (K)	Tot. pres. (atm)	Pri. inj. Φ	Sec. inj. Φ	Wall BC
D584A	5.84	1550	14.63	0.15	0.5	Adiabatic
D584I	5.84	1550	14.63	0.15	0.5	Isothermal
S800A	8.00	2570	42.19	0.40	0.6	Adiabatic
S800I	8.00	2570	42.19	0.40	0.6	Isothermal

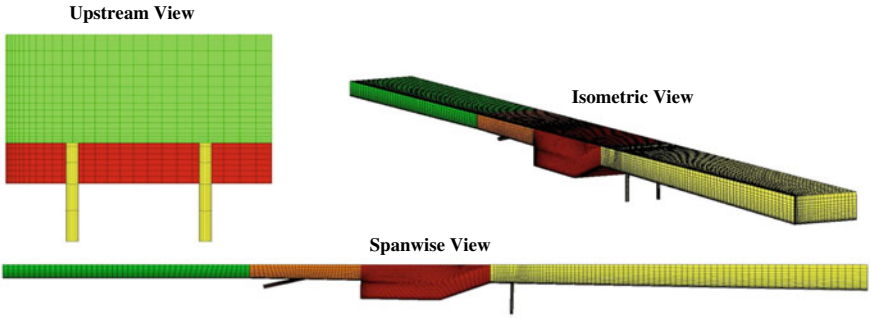

Fig. 2 Looking upstream, isometric, and side views of the structured, quarter-geometry, grid used for RAS of the HDCR combustor coarsened four times for visual clarity

5.1 Numerical Approach

To simulate the HDCR experiments, the Favré-averaged RAS equations were solved using VULCAN-CFD. VULCAN-CFD is a structured-grid finite-volume solver that is extensively used for high-speed combustion simulations using RAS techniques [85]. For the current study, a 6.6 million cell, quarter-geometry, structured grid was used, which is illustrated in Fig. 2. This grid included the facility nozzle, which is not shown. Wall spacing was set for the application of wall-matching functions [86] with y+ values not exceeding approximately 30. Symmetry was enforced at the appropriate boundaries, and an extrapolation of transported variables was applied at the outflow plane. Simulations were also performed using adiabatic and isothermal wall boundary conditions to determine the effect of wall heat losses. In the case of isothermal walls, a one-dimensional heat-conduction equation was solved for the heat transfer through solid surfaces given the wall external temperature and thermal conductivity, which were set to yield wall temperatures similar to those measured during the experiment [87]. The governing RAS equations were closed using the blended k-ω/k-ϵ turbulence model of Menter [88]. Inviscid fluxes were calculated using the low-dissipation flux-split scheme (LDFSS) of Edwards [89]. The van Leer

flux limiter was used, along with a monotone upstream-centered scheme for conservation laws (MUSCL) with an interpolation coefficient (κ) of 1/3. The equations were integrated in pseudotime using an implicit diagonalized approximate factorization (DAF) scheme [90] with a maximum local CFL number of 2.0.

Reaction chemistry was modeled using an 18-step reduced chemical reaction mechanism designed for the combustion of ethylene [38]. Transport equations for the 22 species comprising the reaction mechanism were solved implicitly, and no TCI model was used (aka laminar chemistry assumption). The turbulent Prandtl number was set to 0.89 for each case, and the turbulent Schmidt number was set to 0.325 for the dual-mode case and 0.25 for the scram-mode case, as suggested by Storch et al. [37]. Laminar Prandtl and Schmidt numbers were set to 0.72 and 0.22, respectively [37].

It should also be noted that no transport equation for the mixture fraction, mixture fraction variance or the progress variable were solved in the current work. Instead, these quantities were computed from the RAS data during the postprocessing and analysis step.

5.2 Simulations of the HDCR

Figures 3 and 4 show wall pressure vs. axial distance for simulations and the experiment for dual-mode (D584A and D584I) and scram-mode (S800A and S800I) cases, respectively. All simulations predict the general trends and values of the centerline experimental wall static pressure data. The pressure is slightly overpredicted throughout the isolator for the dual-mode cases and almost 20% for the scram-mode cases. This greater overprediction is due to the thermodynamic nonequilibrium effects [91], which were not modeled in the current simulations. Nevertheless, all simulations still captured the location of the leading oblique shock due to combustor pressure rise but overpredict somewhat the combustor and combustor peak pressures. The isothermal scram-mode case, S800I, overpredicts the combustor peak pressure the most. The differences in the isothermal and adiabatic solutions are a direct indication of the sensitivity of the flowfield to wall heat transfer, which increases for the scram-mode case because of the higher total temperature. Despite some of the noted discrepancies between the simulations and experiments, this qualitative level of agreement is likely sufficient for current analysis of the flamelet modeling assumptions.

Figures 5 and 6 show the contours of the Mach number in the spanwise center plane and through the middle of the injector centerline for the dual-mode and scram-mode cases, respectively. The black lines denote an isocontour of the sonic line. The leading shock due to combustor pressure rise resides upstream and downstream of the primary injectors for the dual- and scram-mode cases, respectively. The leading oblique shock serves to stabilize flames that anchor near the primary injector ports. The flow subsequently separates at the rearward-facing step corner, and a shear layer forms over the recirculating flow within the cavity. This shear layer reattaches near the point of cavity closeout. The mixture of air, partially reacted fuel from the primary

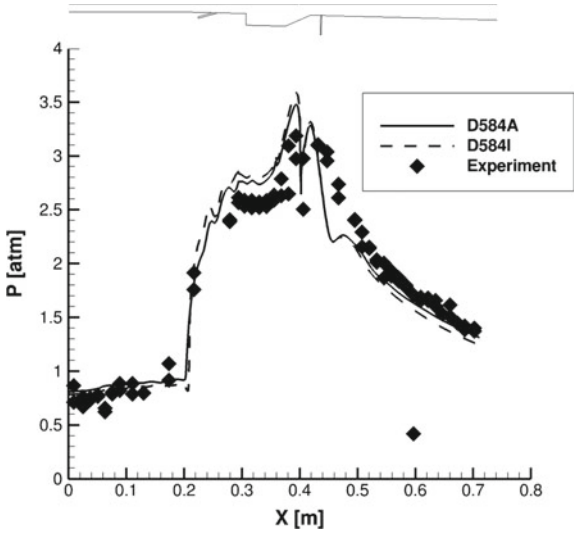

Fig. 3 Comparisons of streamwise (x) wall static pressure (p) data obtained from simulations D584A and D584I and experimentally for dual-mode operation of the HDCR combustor

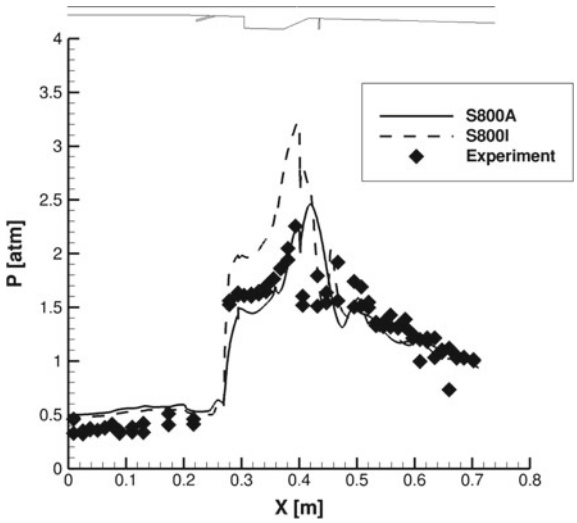

Fig. 4 Comparisons of streamwise (x) wall static pressure (p) data obtained from simulations S800A and S800I and experimentally for scram-mode operation of the HDCR combustor

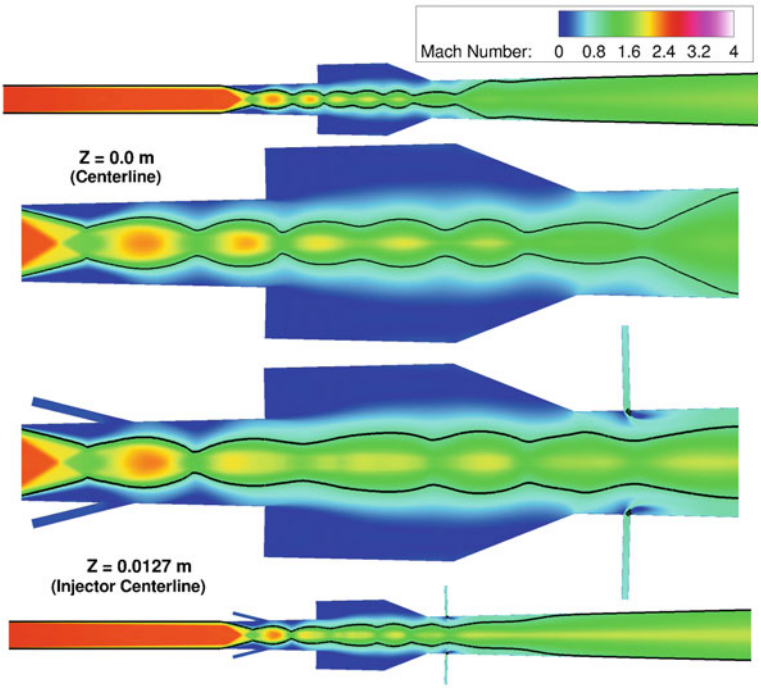

Fig. 5 Contours of the Mach number at spanwise (z) center plane and middle injector centerline for case D584A. Dark black lines correspond to the sonic isocontour

injectors, and some combustion products convect downstream where it further mixes with fresh fuel injected by the secondary injectors.

Because the majority of fuel for both flight conditions is delivered through the secondary injectors, the distribution of the heat release is shifted toward the secondary injectors. The normalized chemical heat release is shown in Figs. 7 and 8. For the dual-mode cases, the peak heat release occurs within the subsonic portions of the flowfield, whereas for the scram-mode cases, the combustion occurs predominantly at supersonic flow velocities. Of further note are the differences in flame location and structure. In the dual-mode case, the flame anchors directly outside of the primary injector ports, whereas in the scram-mode case, the primary injector fuel burns downstream of the injectors in a more distributed fashion. The flames anchored at the primary injection site reside behind the leading oblique shock and above the cavity region. The flames forming at the secondary injector site, for dual- and scram-mode cases, appear to be of a similar nature.

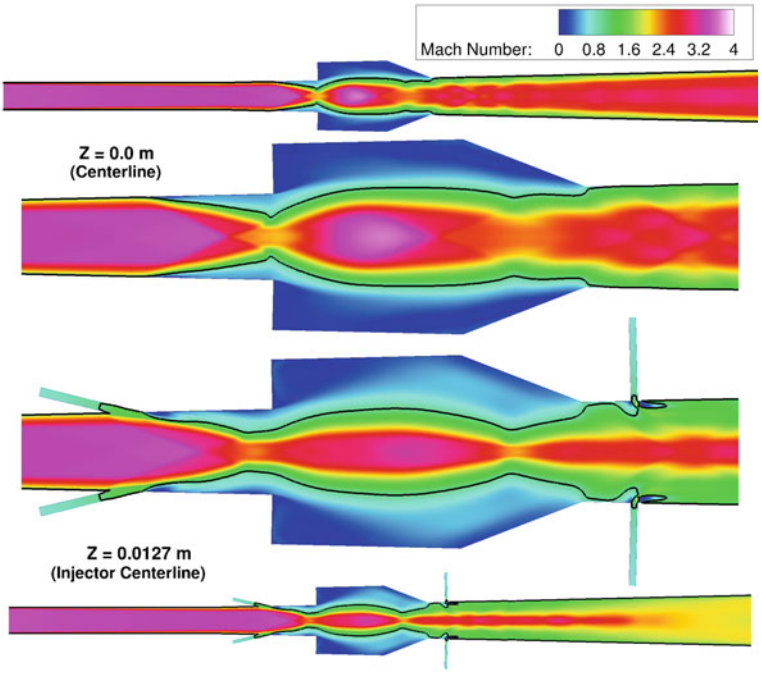

Fig. 6 Contours of the Mach number at spanwise (z) center plane and middle injector centerline for case S800A. Dark black lines correspond to the sonic isocontour

6 Combustion Mode Analysis for the HDCR

Assessing the applicability of flamelet models for a turbulent reacting flow requires one to consider the extent to which the flowfield meets the fundamental flamelet model assumptions. In the case of nonpremixed combustion, for which the flamelet resides near the surface of stoichiometric mixture fraction, and for which the scalar dissipation rate couples the flame dynamics to that of the fluid dynamics, the characteristic chemical time scale must be considerably smaller than that of the representative diffusive and turbulent transport processes. This means that the Damköhler number (Da), which is the ratio of a characteristic flow time scale, τ_{flow}, to that of chemistry, τ_{chem}, must be much greater than unity, indicating that the characteristic reaction chemistry times are much shorter than those of the characteristic flow processes.

In the case of premixed combustion, for which the flame can propagate normal to itself, the chemical time scale and thermal diffusivity effectively govern the flame thickness, which must be considerably smaller than the representative turbulent length scales under the flamelet assumption. This means that the Karlovitz number (Ka) defined as the ratio of a characteristic flame length scale to a characteristic tur-

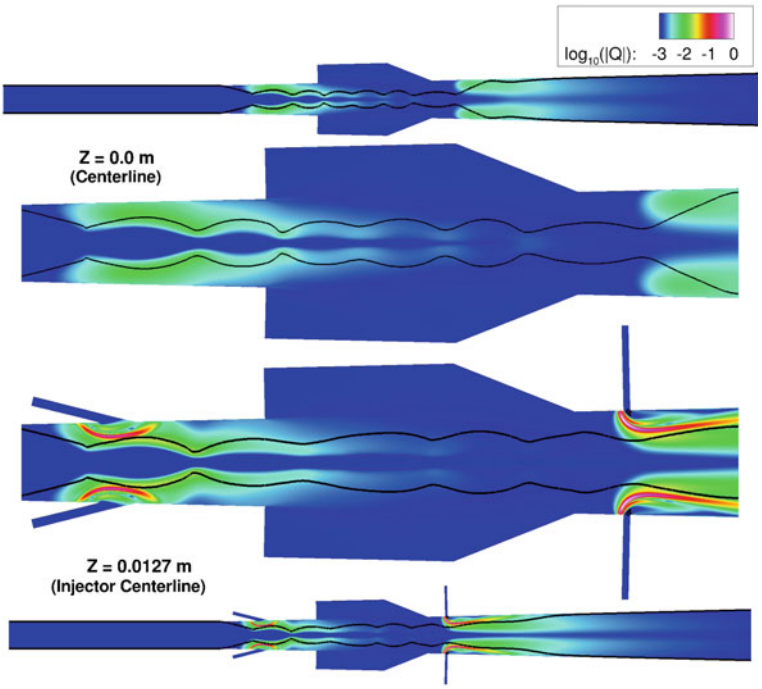

Fig. 7 Contours of the logarithm of chemical heat release (Q) normalized by its global maximum for simulation D584A. Dark black lines correspond to the sonic isocontour

bulence length scale, must be much less than unity. In most cases, the Kolmogorov scale is used as the representative turbulence length scale.

In the current work, the Favré-averaged RAS solutions for HDCR cases D584A and S800A are used to determine when the fundamental flamelet model assumptions are satisfied and/or violated for a scramjet combustor. To accomplish this, a flame index is first devised to identify regions of chemical activity. Once those regions are identified, a flame-weighted Takeno index is computed to identify regions of premixed and nonpremixed combustion. Local Da is subsequently estimated using the approach outlined by Poinsot and Veynante [2] and Peters [13]. Proxy combustion diagrams are devised for the nonpremixed combustion using the flame-weighted Takeno index and Da. Finally, a priori investigation of the effects of pressure and compressibility, wall heat transfer, and flamelet boundary condition variability on the HDCR flames is presented.

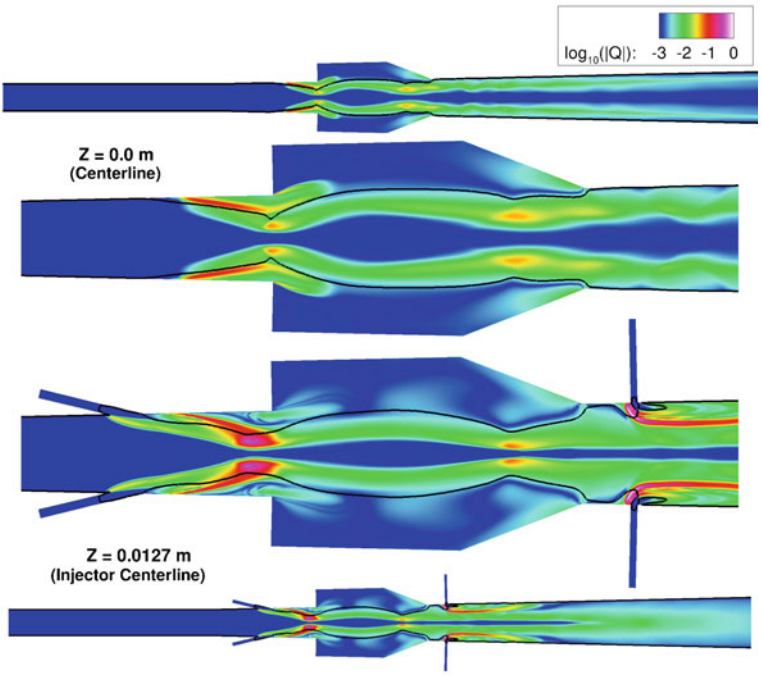

Fig. 8 Contours of the logarithm of chemical heat release (Q) normalized by its global maximum for simulation S800A. Dark black lines correspond to the sonic isocontour

6.1 Flame Index

The first step in characterizing the combustion fields is to devise a metric indicative of flame activity, which can be used to identify regions of combustion. The current study uses the approach of Lacaze et al. [92] and defines a flame index, f,

$$f(x, y, z) = \frac{\max_{\alpha}(\bar{\dot{\omega}}_{\alpha}(x, y, z))}{\max_{(x,y,z)}(|\bar{\dot{\omega}}_{\alpha}|)}, \tag{22}$$

where $\bar{\dot{\omega}}_{\alpha}$ is the Favré-averaged production rate of species α and x, y, and z are Cartesian coordinates. The subscript attached to the max operator indicates what quantity the max operation is applied to. The flame index is defined such that it indicates the level of maximum chemical production over all species in the finite-rate reaction mechanism used in the simulations. The index takes on a value between 0 and 1, where 0 corresponds to no chemical production and where 1 corresponds to a point at which at least one chemical species is produced at its global maximum.

Contours of $\log_{10}(f)$ for cases D584A and S800A are presented in Figs. 9 and 10, respectively. The flame index indicates that for dual-mode operation, case D584A,

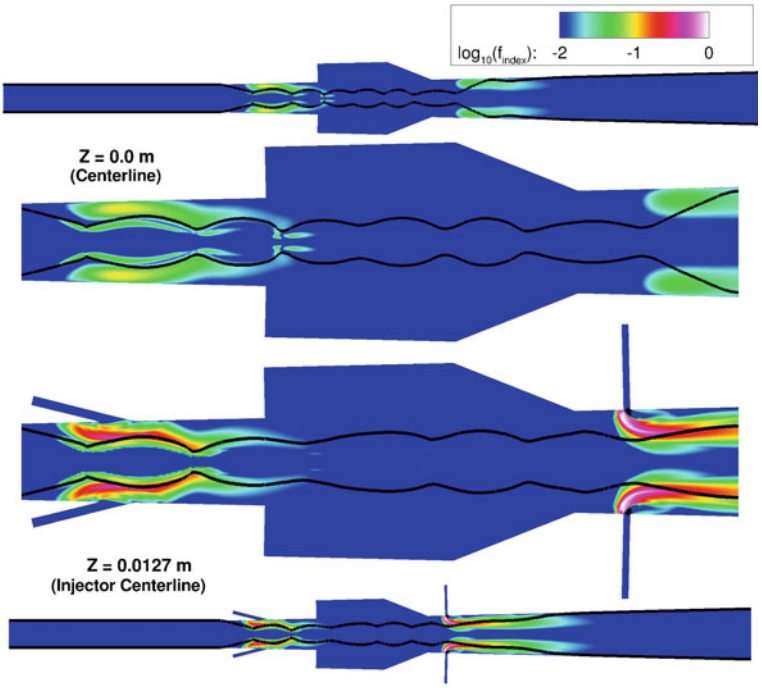

Fig. 9 Contours of the logarithm of flame index, f, for simulation D584A. Dark black lines correspond to the sonic isocontour

thin flames anchor near the primary injector orifices, which are stabilized by the leading oblique shock and recirculating fluid directly outside the injectors. Thin flames also burn outside the secondary injector orifices and extend downstream. For case S800A, the flames associated with the primary injectors appear to be fundamentally different than those of the secondary injectors. Although there does exist a thin region of combustion near the injectors stabilized by the fuel injection bow shock and fluid recirculation, most of the combustion appears to be distributed from the point of injection to just downstream of the cavity step corner. When compared to the Mach number contours in Fig. 6, the combustion appears to correlate with the leading shock until a pronounced increase in flame intensity is seen directly behind the point of the leading shock-shock interaction. This observation may suggest the occurrence of shock-induced combustion. Downstream of this intense region of combustion, a weak distributed flame is observed. However, it should be noted that some of the differences in the flame topology could be attributed to the difference in equivalence ratio at the primary injectors for the dual- and scram-mode cases. The secondary injector flames for the scram-mode are similar in nature to those observed in the dual-mode cases, which suggests a relatively thin flame that extends downstream past the injectors and is angled toward the wall.

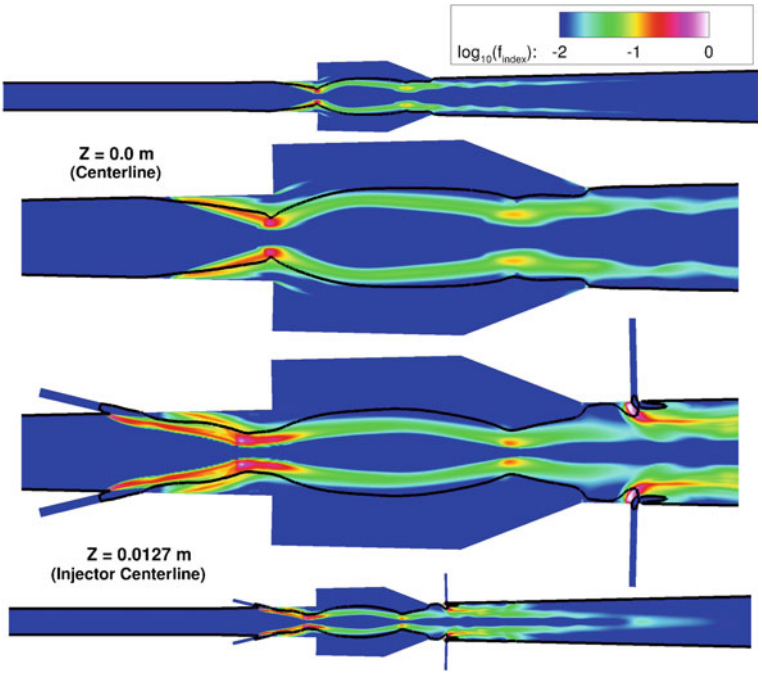

Fig. 10 Contours of the logarithm of flame index, f, for simulation S800A. Dark black lines correspond to the sonic isocontour

6.2 Combustion Mode

To isolate the nonpremixed combustion data from that of the premixed data, the approach of Yamashita et al. [93] is used. This method assumes that in nonpremixed flames, the gradients of oxidizer and fuel species are oriented in opposite directions, while in premixed flames, the gradients are oriented in the same direction. By taking the dot product of the gradients and normalizing, the Takeno index, Λ_T, can be obtained:

$$\Lambda_T = \frac{\nabla \widetilde{Y}_{oxidizer} \cdot \nabla \widetilde{Y}_{fuel}}{|\nabla \widetilde{Y}_{oxidizer} \cdot \nabla \widetilde{Y}_{fuel}|}, \tag{23}$$

where $\widetilde{Y}_{oxidizer}$ and $\widetilde{Y}_{fuel}$ are the Favré-averaged oxidizer and fuel species mass fractions, respectively. For the current work, the Takeno index is obtained using the oxidizer (O_2) and fuel (CH_4, C_2H_4) mass fractions. When the gradients of these mass fractions are aligned, the index returns 1.0, which indicates premixed combustion. Whereas, when these gradients are of opposite sign, the index returns -1.0, which indicates nonpremixed combustion. In the context of RAS, the Takeno index indicates the statistically-dominant combustion mode at a given location in the flowfield. Since the RAS solution is an averaged representation of the flowfield, either premixed

or nonpremixed regions of the RAS flowfield may in actuality exhibit periods of nonpremixed or premixed combustion. The effect of such intermittency can only be captured using LES or DNS.

By further weighting the Takeno index by the flame index, a new index, flame-weighted Takeno index, Λ_f, is formed:

$$\Lambda_f = f\Lambda_T \tag{24}$$

The value of Λ_f ranges from $-1.0 < \Lambda_f < 1.0$ and conveys both the flame intensity and dominant combustion mode at each point in the flowfield. Accordingly, Λ_f is used in subsequent analysis to identify the combustion character of the HDCR.

Additionally, the Da is also computed for both nonpremixed and premixed combustion. The Da is the ratio of a characteristic flow time scale, τ_{flow}, to that of the chemistry, τ_{chem}. When Da is large, there exists a separation of chemistry and flow scales such that the fundamental assumption of a flamelet model, i.e., that a thin laminar flame is only distorted by a background turbulent flowfield, is satisfied. However, when Da approaches unity, the flamelet assumptions break down as the turbulence and chemistry begin to interact and interfere with one another.

To compute the Da for nonpremixed combustion, the characteristic flow time scale is approximated using the scalar dissipation rate, χ (Eq. 18), which has the units of inverse time. The scalar dissipation rate is modeled using the approach of Poinsot and Veynante [2],

$$\chi_{modeled} = C_a \frac{\epsilon}{k} \widetilde{Z''^2}, \tag{25}$$

where ϵ, k, and C_a are the turbulence dissipation rate, turbulence kinetic energy, and a model constant set to unity [2]. When the mixture fraction variance is not available, its upper limit can still be computed, $\widetilde{Z''^2}_{max} = \widetilde{Z}(1 - \widetilde{Z})$, by using the boundedness property of the mixture fraction. This is useful when considering the limiting values of the Da. That is, using the maximum value of the mixture fraction variance to model the scalar dissipation rate and flow time scale lowers the value of the Da, which implies a conservative view of the applicability of the flamelet model. To estimate the characteristic time scale of the chemistry, a mass fraction and production rate of water are used,

$$\tau_{chem} = \frac{\bar{\rho}\widetilde{Y}_{\mathrm{H_2O}}}{\bar{\dot{\omega}}_{\mathrm{H_2O}}} \tag{26}$$

The Da is then computed as,

$$Da_{nonpremixed} = \frac{1}{\chi_{modeled}\tau_{chem}}. \tag{27}$$

For the case of premixed combustion, the Da is typically defined as the ratio of characteristic turbulence and flame time scales,

$$Da_{premixed} = \frac{\tau_{turb}}{\tau_{flame}} = \frac{l/u'}{l_F/s_L}, \tag{28}$$

where l_F, s_L, l, and u' are the laminar flame thickness and speed, integral turbulence length, and turbulence fluctuating velocity, respectively. However, the most appropriate turbulence scale for calculating the Da for premixed flames is unclear [2]. In the current work, the premixed Da is calculated using the integral turbulence length scale. The laminar flame thickness and laminar flame speed are estimated by solving freely-propagating premixed flames corresponding to the average temperature, pressure, and fuel equivalence ratio characterizing the premixed data within the flowfield, as identified by the flame-weighted Takeno index.

Scatter plots of the logarithm of the Da versus the flame-weighted Takeno index for the primary and secondary injector flames for case D584A are shown in Fig. 11. The same plots for case S800A are shown in Fig. 12. In each figure, the nonpremixed Da is used for data corresponding to $\Lambda_f < 0$, and the premixed Da is used for $\Lambda_f > 0$. The data points are sized by the chemical heat release rate and are colored by the production rate of water. Each figure includes only the data contained within the gray regions on the included flowpath diagram. These regions focus the analysis on the primary and secondary injection. The data within $0.03 < \Lambda_f < 0.03$ are omitted for clarity.

For case D584A, Fig. 11 suggests that, for both the primary and secondary injector flames, the combustion occurs primarily at high Das ($Da >> 1$) and in a nonpremixed mode ($\Lambda_f < 0$). Although limited regions of premixed combustion exist for this case, the heat release associated with those regions is small as compared to that of the nonpremixed combustion. These figures suggest that for case D584A, the fundamental assumptions made for nonpremixed flamelet models are likely satisfied and that such models may sufficiently predict the combustion physics governing dual-mode operation of the HDCR flowpath.

For case S800A, Fig. 12 suggests that the combustion is of a more complex nature. For the primary injectors, the combustion occurs over a range of Das and is split among both nonpremixed and premixed modes. A significant portion of the heat release due to the primary injectors corresponds to premixed regions of combustion occurring near $Da = 1$, suggesting that the characteristic flame time scale is on the same order of magnitude as that of the integral turbulence. However, a significant portion of the nonpremixed combustion occurs at high Da numbers as well. For the secondary injectors, the combustion occurs at a range of Das and primarily in a nonpremixed mode. Based on these data, a suitable simulation of the HDCR flowpath for scram-mode operation would likely require both premixed and nonpremixed flamelet models, and the fundamental assumptions made for these models may only be valid for limited regions of the combustion.

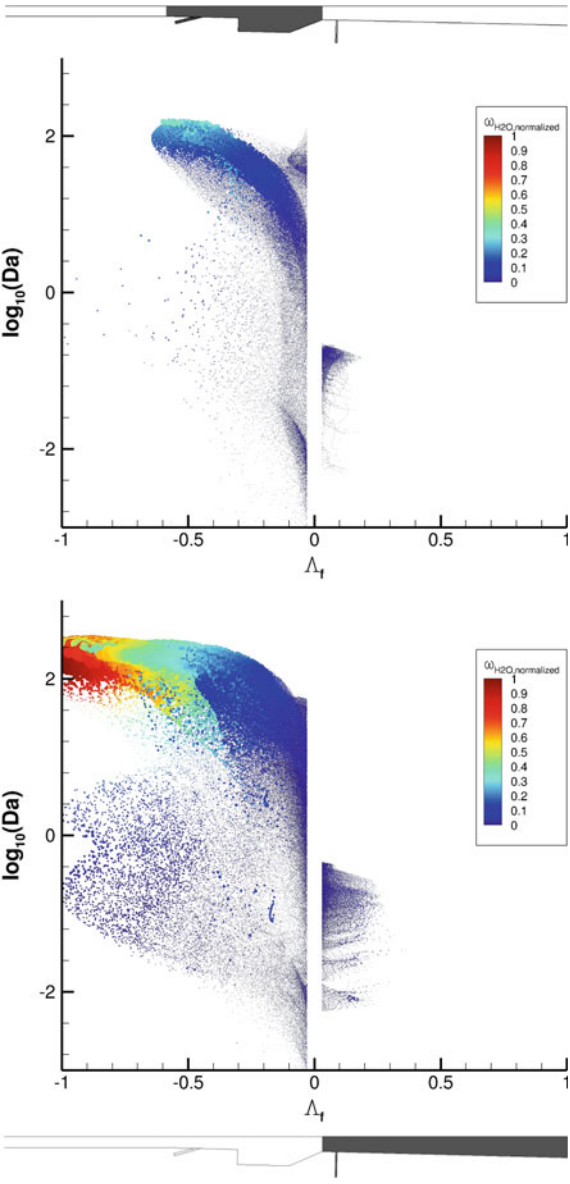

Fig. 11 Log of the *Da*, versus flame-weighted Takeno index, Λ_f, for case D584A. Data points are sized by chemical heat release, $\widetilde{Q}$, and colored by normalized production rate of water, $\tilde{\dot{\omega}}_{H_2O}$. Data are plotted for the primary injector (top) and secondary injector (bottom) portion of the flowpath as denoted by the gray regions on the included flowpath diagrams

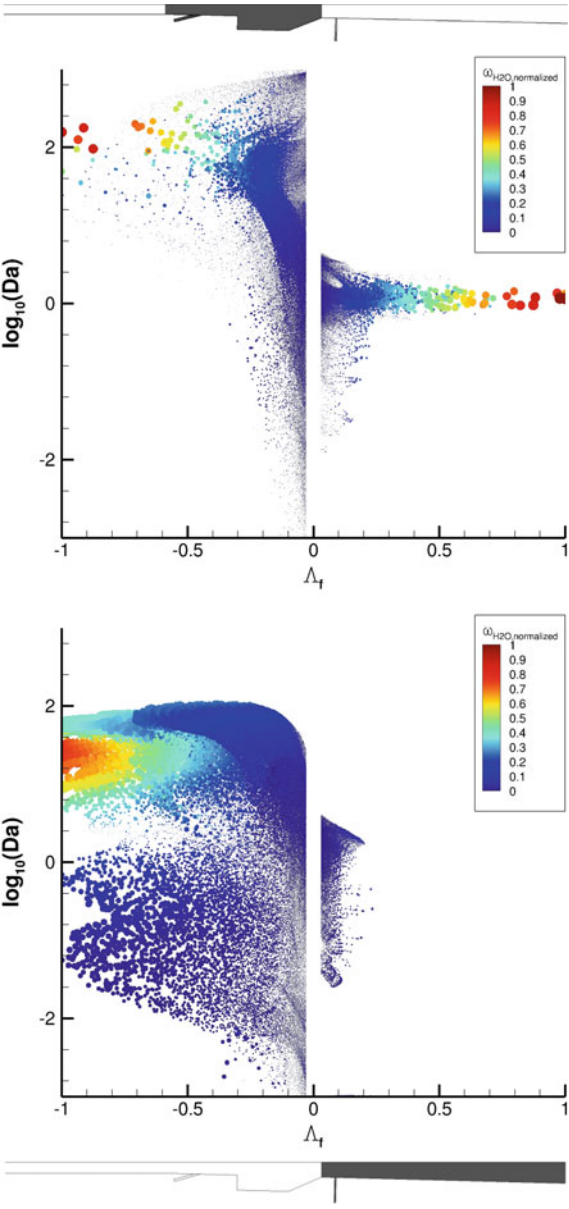

Fig. 12 Log of the Da, versus flame-weighted Takeno index, Λ_f, for case S800A. Data are sized by chemical heat release, $\widetilde{Q}$, and colored by normalized production rate of water, $\tilde{\dot{\omega}}_{H_2O}$. Data are plotted for the primary injector (top) and secondary injector (bottom) portion of the flowpath as denoted by the gray regions on the included flowpath diagrams

7 Effect of the Pressure

Figure 13 shows scatter plots of the mean static temperature vs. the Favré-averaged mixture fraction for cases D584A and S800A for both the primary and secondary injection regions. Since the majority of the combustion occurs in a nonpremixed mode, the mixture fraction provides a convenient parameterization of the three-dimensional flowfield data for visualizing the influence of the pressure on combustion. The scatter data are colored by the logarithm of the mean static pressure, which allows for identifying regions of significant variations in pressure. The variation in pressure appears to be generally higher for case S800A, although case D584A exhibits significant variation as well. The scram-mode data appear to span approx-

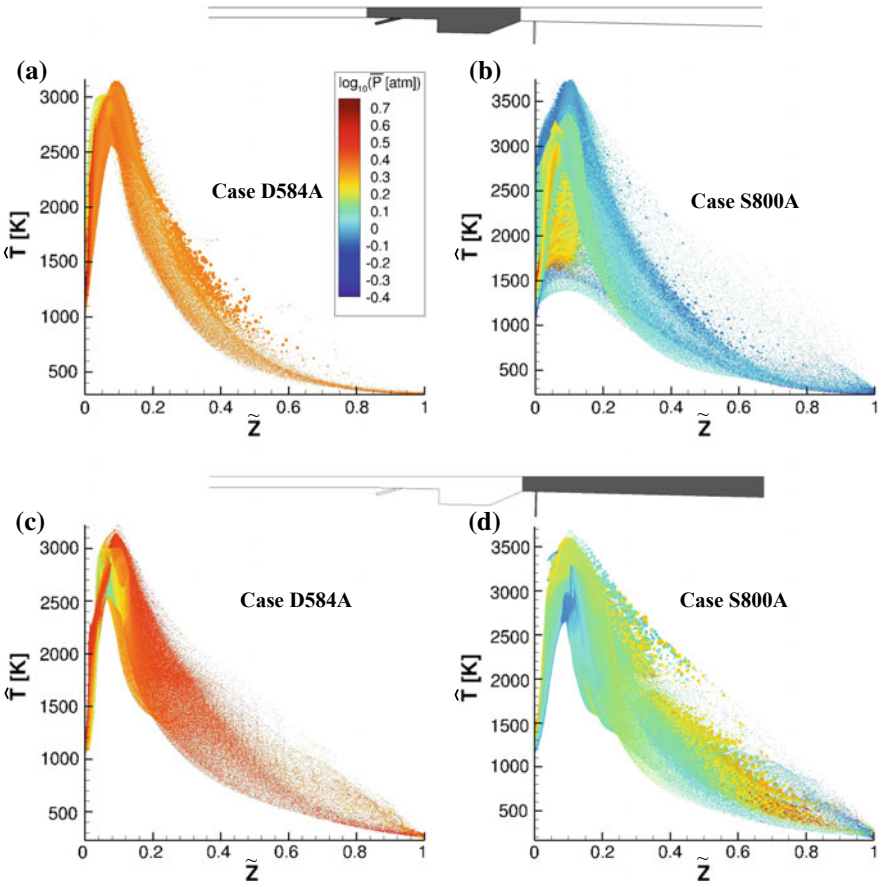

Fig. 13 Static temperature, $\widehat{T}$, versus mixture fraction, $\widetilde{Z}$, colored by the logarithm of static pressure, $\bar{P}$, and sized by chemical heat release rate, $\widetilde{Q}$, for **a** case D584A and **b** case S800A, primary injector flames and for **c** case D584A and **d** case S800A, secondary injector flames

imately half an order more of static pressure as compared to the dual-mode data, for which the static pressure spans nearly an entire order of magnitude. In addition, these pressure variations occur near stoichiometry, which is where the majority of heat is released as well. Thus, these observations indicate that any suitable flamelet model must account for pressure variations due to combustion and compressibility for application to a dual-mode scramjet combustor.

8 Effect of the Wall Heat Transfer

In addition to pressure variations and compressibility effects, recent efforts in developing flamelet models have been directed at including the effects of heat transfer. As with pressure, the focus has been on developing modifications to existing incompressible flamelet models to account for wall heat losses using various approaches [94–97]. In this section, the effect of heat loss on the flame structure is illustrated by analyzing the simulations computed with and without wall heat transfer. The primary mechanism by which wall heat transfer influences the combustion field is local quenching in the vicinity of the wall. For scramjet engines, in which the core flow is at high velocity and fuel is injected through the walls, a considerable amount of fuel is entrained in the slow-moving near-wall regions. As a result, the fuel has sufficient time to mix with oxidizer and react, thereby creating intense regions of combustion near the wall surfaces. Figure 14 shows scatter plots of the mean static temperature vs. the Favré-averaged mixture fraction for cases D584A and S800A (adiabatic), and D584I and S800I (isothermal) for the entire combustor section. The scatter data are colored by the logarithm of the velocity magnitude, V_s, which allows for identifying the near-wall regions denoted in dark blue. By examining the minimum velocity magnitude data, near-wall flame quenching by heat loss through the wall can be directly observed for the isothermal cases D584I and S800I. Nevertheless, these data show that relatively low temperature combustion is still taking place in the near-wall regions. For the adiabatic cases, D584A and S800A, the near-wall data exhibit high temperature, near-equilibrium values, which indicates fully burning flames. While these differences are striking and may suggest the requirement for inclusion of a heat loss model in a general compressible flamelet model, for the HDCR, the adiabatic simulations yielded more accurate solutions when compared to experimental static pressure data, suggesting that either the isothermal simulations significantly overpredicted the heat transfer, or the aggregate effect of wall heat transfer on the combustion and heat release is limited.

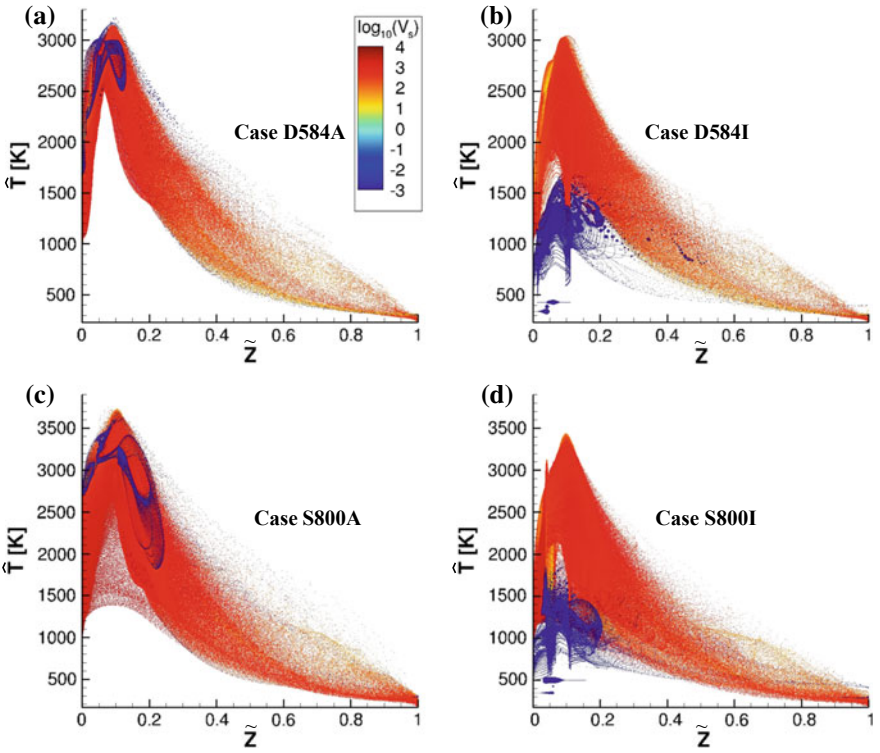

Fig. 14 Static temperature plotted in mixture fraction space and colored by logarithm of velocity magnitude, V_s, for cases **a** D584A, **b** D584I, **c** S800A, and **d** S800I, showing the effect of heat losses on the combustion

9 Effect of the Flamelet Model Boundary Conditions

The effect of the flamelet model boundary conditions is probably the least investigated and addressed issue facing flamelet models for compressible turbulent reacting flows. This is because the process of specifying applicable ranges for fuel and oxidizer temperatures and pressures a priori for flamelet equations is unclear. For example, since for supersonic flow pressure varies with flowpath geometry and across shocks and expansion waves, determining the appropriate pressures at which flames mix and react to build a flamelet table for a scramjet combustor is impossible without prior knowledge of the heat release rate and the flowfield. In this regard, a compressible flamelet model is fundamentally different from conventional incompressible flamelet models used in applications where the combustor pressure can typically be assumed to be approximately constant and known a priori, and where the pure fuel and oxidizer temperatures remain at their known injected values.

To obtain the information about the flamelet equation boundary conditions appropriate to a specific compressible flow, in general, one must perform a turbulent react-

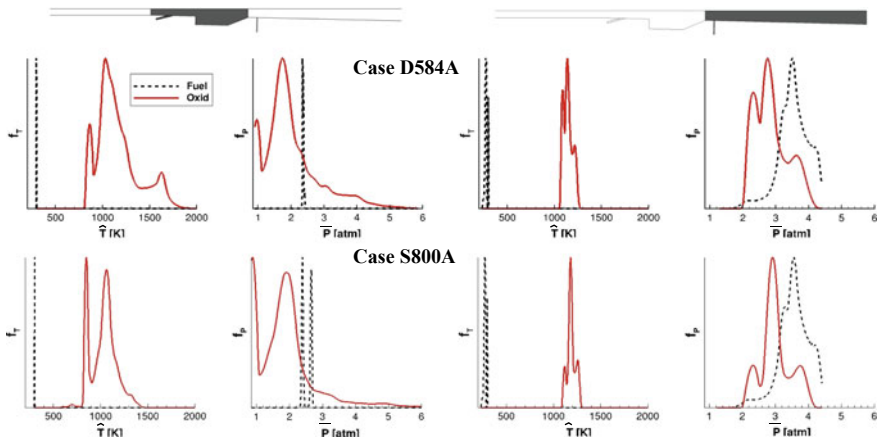

Fig. 15 PDFs of static temperature and pressure (f_T and f_P, respectively) for fuel ($Z > 0.99$) and oxidizer ($Z < 0.01$) conditions for cases D584A (top) and S800A (bottom). Regions from which the data are sampled are shown above the respective plots, with the leftmost representing the primary injector flames and the rightmost representing the secondary injector flames

ing flow simulation that does not utilize a flamelet model. After performing such a simulation, the simulation data must be analyzed and, at a minimum, fuel and oxidizer temperatures and pressures must be extracted for regions of the flowfield where a flame index indicates the presence of combustion. With this data, one may then construct PDFs to determine the range and the likelihood of specific flamelet boundary conditions required to model the combustion, and potentially use this information to select a most likely set of boundary conditions. The flamelet table is subsequently built by solving the flamelet equations for these conditions. Alternately, flamelet tables may be built for a range of boundary conditions as long as a unique parameterization for them can be developed. One such attempt is discussed by Quinlan [82]. Furthermore, for the case of multiple injectors, it is also prudent to tailor the analysis to each injector set independently and to determine whether a multiple mixture fraction approach may be appropriate [98, 99].

To estimate the range and likelihood of different flamelet equation boundary conditions in the HDCR combustor, all mixture fraction data less than 0.01 and greater than 0.99, for pure oxidizer and pure fuel, respectively, were isolated from the solution. These data were then split into two groups according to whether the data resided in the primary or secondary injector regions. PDFs were then constructed for pressure and temperature and are shown for cases D584A and S800A in Fig. 15. For both dual-mode and scram-mode operation, the fuel temperatures (dashed lines) remain about constant at their nominal values, while the oxidizer temperatures vary considerably and exhibit multimodal distributions. For the primary injectors, the fuel pressures are distributed tightly around their nominal values for the dual-mode case, whereas they exhibit some narrow-range bimodality for the scram-mode case. The oxidizer pressures exhibit broad multimodal distributions in all cases. For the sec-

ondary injectors, both the fuel and oxidizer pressures show multimodal distributions. However, these observations are not general and depend on whether the injected fuel flow is overexpanded, underexpanded or pressure matched. The observed pressure and temperature variations would be minimal for pressure matched conditions and much smaller for underexpanded than overexpanded flow conditions. This is because the flow contains only expansion waves for the fuel plumes undergoing underexpansion, whereas the same plumes contain internal shock waves during overexpansion. Therefore, because the fuel flumes are underexpanded, the fuel PDFs are narrow. On the other hand, because the oxidizer flow is always overexpanded, when the combustor provides sufficient back pressure, the oxidizer PDFs are broad.

10 Summary and Conclusions

Flamelet models have proven useful in enabling fast and accurate simulations of subsonic combustion because they can parameterize complex chemical state-space with as few as one scalar quantity, such as the mixture fraction. However, in supersonic combustion these models face many challenges. The current work presents an analysis of the steady flamelet model assumptions in supersonic combustion application. The HDCR [36, 37] dual-mode scramjet combustor is used for this purpose. Although designed for academic and collaborative purposes, the HDCR is representative of a practical cavity-stabilized scramjet combustor. The analysis uses 3D RAS data obtained using a finite-rate reaction mechanism at Mach 5.84 dual-mode and Mach 8 scram-mode flight conditions. Quantities, such as the mixture fraction and progress variable, typically used for parameterizing the flamelet models, are obtained from the RAS data in the postprocessing and analysis step. This analysis reveals that, for the HDCR, both nonpremixed and premixed combustion can be observed. Furthermore, although the majority of heat is released via nonpremixed, near-equilibrium combustion, for the Mach 8 scram-mode conditions, some heat enters the combustor via premixed combustion that includes significant finite-rate effects. These observations suggest that a multicombustion-mode flamelet model might be required to accurately simulate the Mach 8 flight conditions. Furthermore, to capture the finite-rate effects, a reaction progress variable is required in addition to the mixture fraction.

The effects of variable pressure, wall heat transfer, and flamelet equation boundary conditions were also evaluated. These three elements present key barriers to utilizing flamelets for supersonic combustion simulations. In the HDCR, the combustor pressure increases by about a factor of five. This rise is due to close coupling of thermodynamics with fluid mechanics that occurs at supersonic speeds, and occurs in the regions of the highest heat release. Several methods of accounting for rising pressure in flamelet models were discussed. The simplest is that of pressure scaling of the progress variable reaction source terms. This approach, however, neglects the pressure-induced differences in chemical composition and the adiabatic flame temperature. To account for these effects, pressure must be included as an additional parameterizing variable in the flamelet formulation.

The heat transfer to the walls can be significant at hypersonic speeds. For example, the total temperature for the HDCR ranges from about 1500–2500 K across the flight Mach number range, which would necessitate active cooling of the combustor for times longer than those for which this uncooled article was designed for. The heat transfer at the walls occurs because of two separate effects: due to slowing down and viscous heating of the flow in the boundary layers, and due to flame-wall interactions and convection of combustion products toward the wall. In the former, typically the oxidizer is cooled by the wall, thereby decreasing its enthalpy. In the latter, reacting fuel-oxidizer mixtures or hot combustion products are quenched or cooled by the walls, respectively. Both effects represent physics that are distinct from those embedded in the flamelet equations and therefore challenging to incorporate into the model.

Finally, the range of flamelet equation boundary conditions for the HDCR was quantified by plotting the PDFs of the pressure and temperature for the pure fuel and oxidizer streams. It should be noted that, although the oxidizer stream pressures are close to the combustor pressure, the fuel stream pressures are independent and a function of only the scramjet fuel injection system design, particularly whether the fuel streams are overexpanded, underexpanded, or pressure matched. If the injection pressure is pressure matched to the combustor, then parameterizing the flamelet using the combustor pressure offers a reasonable approach. However, even under the pressure matched injection conditions, the static temperature of the fuel and oxidizer streams will vary and therefore require further parameterization. Furthermore, these temperature differences will be due to completely different physical processes, i.e., shock train processes due to combustor back-pressuring for the oxidizer stream, and fuel injection system design and total temperature of the fuel (which may have been heated) when entering the combustor. Similar to the challenges associated with parameterizing the heat transfer, parameterizing the boundary condition effects is a nontrivial task.

Some of the challenges with using steady flamelet models for applications in supersonic combustion may be reduced or eliminated by using the unsteady flamelet [28] or representative interactive flamelet [30] approaches, albeit at the expense of higher computational cost. However, given the number of approximations and parameterizations needed to address all of the above issues, while still being constrained by the flamelet thin flame approximation and the fact that at least one non-flamelet simulation would generally be needed to provide information about the pressure range and the boundary conditions for the flamelet equations, it might be reasonable to revert to an alternate strategy, such as the optimized global reaction mechanisms [100], or specially tuned eddy dissipation concept models [101]. Although the fidelity to accurately represent the chemical kinetics would be diminished and the production of some minor species of interest would not be available, these simpler models may be sufficient for many practical applications and are simpler to implement and use. To fully take advantage of the benefits of flamelet models for supersonic combustion, further research is needed to overcome the challenges discussed in this work.

Acknowledgements Portions of this work were supported by a NASA Space Technology Research Fellowship (training grant NNX11AM86H) with additional support provided by the Virginia Space Grant Consortium, by a Virginia Commonwealth Fellowship, and by the Hypersonic Technology Project in the Advanced Air Vehicles Program of the NASA Aeronautics Research Mission Directorate (ARMD). Computational resources were provided by the NASA Advanced Supercomputing Division. Most importantly, the authors are grateful for the many helpful discussions with Dr. Johan Larsson (Univ. of Maryland) and Dr. Honest Mrema (Univ. of Minnesota).

References

1. W.H. Heiser, D.T. Pratt, *Hypersonic Airbreathing Propulsion* (AIAA, Washington, DC, 1994)
2. T. Poinsot, D. Veynante, *Theoretical and Numerical Combustion*, 2nd edn. (R.T. Edwards, Inc., Philadelphia, PA, 2005)
3. M. Conaire, H.J. Curran, J.M. Simmie, W.J. Pitz, C. Westbrook, A comprehensive modeling study of hydrogen oxidation. Int. J. Chem. Kinet. **36**(11), 603–622 (2004)
4. D.C. Wilcox, *Turbulence Modeling for CFD* (DCW Industries Inc, La Cañada, CA, 2006)
5. T. Lu, C. Law, Toward accommodating realistic fuel chemistry in large-scale computations. Prog. Energy Combust. Sci. **35**(2), 192–215 (2009)
6. R.J. Kee, M.E. Coltrin, P. Glarborg, Chemically reacting flow: theory and practice. Technical Report SAND2001-0143P (Sandia National Laboratories, Albuquerque, NM, 2001)
7. D.G. Goodwin, R.L. Speth, H.K. Moffat, B.W. Weber, Cantera: An object-oriented software toolkit for chemical kinetics, thermodynamics, and transport processes (2018). https://www.cantera.org. Version 2.4.0
8. K. Seshadri, F.A. Williams, Reduced chemical systems and their applications in turbulent combustion, in *Turbulent Reacting Flows*, ed. by P.A. Libby, F.A. Williams, Chap. 4, pp. 154–210 (Academic Press, London, UK, 1994)
9. B. Franzelli, E. Riber, M. Sanjosé, T. Poinsot, A two-step chemical scheme for kerosene-air premixed flames. Combust. Flame **157**, 1364–1373 (2010)
10. B.F. Magnussen, B.H. Hjertager, On mathematical modeling of turbulent combustion with special emphasis on soot formation and combustion, Proc. Combust. Inst. **16**(1), 719–729 (1977)
11. G. Esposito, M. Rahimi, H. Chelliah, V. Hiremath, S. Pope, D. Sheen, W. Tsang, Chemical kinetic model reduction and efficient implementation strategies for hypersonic propulsion applications, in *50th AIAA Aerospace Sciences Meeting Including the New Horizons Forum and Aerospace Exposition*, AIAA-2012-118 (AIAA, Nashville, TN, 2012)
12. N. Peters, Laminar diffusion flamelet models in non-premixed turbulent combustion. Prog. Energy Combust. Sci. **10**(3), 319–339 (1984)
13. N. Peters, Laminar flamelet concepts in turbulent combustion. Proc. Combust. Inst. **21**, 1231–1250 (1986)
14. N. Peters, *Turbulent Combustion* (Cambridge University Press, Cambridge Monographs on Mechanics, 2000)
15. F.A. Williams, Recent advances in theoretical description of turbulent diffusion flames, in *Turbulence in Mixing Operations*, ed. by R.S. Brodkey, pp. 189–209 (Academic Press, New York, 1975)
16. R.W. Bilger, The structure of diffusion flames. Combust. Sci. Technol. **13**, 155–170 (1976)
17. G. Dixon-Lewis, Structure of laminar flames, Proc. Combust. Ins. **23**(1), 305–324 (1991)
18. J. Larsson, I. Bermejo-Moreno, J. Bodart, R. Vicquelin, Predicting the operability limit of the HyShot II scramjet using LES, in *Center for Turbulence Research Annual Research Briefs* (2012)
19. J. Larsson, S. Laurence, I. Bermejo-Moreno, J. Bodart, S. Karl, R. Vicquelin, Incipient thermal choking and stable shock-train formation in the heat-release region of a scramjet combustor. Part II: large eddy simulations. Combust. Flame **162**(4), 907–920 (2015)

20. A.A.V. Perpignan, M.G. Talboom, Y. Levy, A.G. Rao, Emission modeling of an interturbine burner based on flameless combustion. Energy Fuels **32**, 822–838 (2018)
21. S. Pope, Computationally efficient implementation of combustion chemistry using in situ adaptive tabulation. Combust. Theor. Model. **1**, 41–63 (1997)
22. E.E. O'Brien, The probability density function (PDF) approach to reacting turbulent flows, in *Turbulent Reacting Flows*, ed. by P.A. Libby, F.A. Williams, vol. 44 of Topics in Applied Physics, Chap. 5, pp. 185–218 (Springer, Heidelberg, Germany, 1980)
23. R.L. Gaffney, J.A. White, S.S. Girimaji, J.P. Drummond, Modeling of turbulent/chemistry interactions using assumed PDF methods, in *28th AIAA/SAE/ASME/ASEE Joint Propulsion Conference and Exhibit*, AIAA-92-3638 (AIAA, Nashville, TN, 1992)
24. R.A. Baurle, G.A. Alexopoulos, H.A. Hassan, J.P. Drummond, An assumed joint-beta PDF approach for supersonic turbulent combustion, in *28th AIAA/SAE/ASME/ASEE Joint Propulsion Conference and Exhibit*, AIAA-92-3844 (AIAA, Nashville, TN, 1992)
25. S.H. Frankel, V. Adumitroaie, C.K. Madnia, P. Givi, Large eddy simulations of turbulent reacting flows by assumed PDF methods, in *Engineering Applications of Large Eddy Simulations*, ed. by S.A. Ragab, U. Piomelli, vol. 162, pp. 81–101 (ASME, Fluids Engineering Division, New York, 1993)
26. C.D. Pierce, Progress-variable approach for large eddy simulation of turbulent combustion. Ph.D. thesis, Stanford University, 2001
27. M. Ihme, L. Shunn, J. Zhang, Regularization of reaction progress variable for application to flamelet-based combustion models. J. Comput. Phys. **231**, 7715–7721 (2012)
28. M. Ihme, Y. Chee See, Prediction of autoignition in a lifted methane/air flame using an unsteady flamelet/progress variable model, Combust. Flame **157**, 1850–1862 (2010)
29. H. Pitsch, M. Chen, N. Peters, Unsteady flamelet modeling of turbulent hydrogen-air diffusion flames, Proc. Combust. Ins. **27**(1), 1057–1064 (1998)
30. S.-H. Keum, An improved representative interactive flamelet model accounting for evaporation effect in reaction space. Ph.D. thesis, University of Michigan, 2009
31. C.D. Pierce, P. Moin, Progress-variable approach for large-eddy simulation of non-premixed turbulent combustion. J. Fluid Mech. **504**, 73–97 (2004)
32. M. Ihme, C.M. Cha, H. Pitsch, Prediction of local extinction and re-ignition effects in non-premixed turbulent combustion using a flamelet/progress variable approach. Proc. Combust. Inst. **30**(1), 793–800 (2005)
33. J. van Oijen, L. de Goey, Modeling of premixed laminar flames using flamelet-generated manifolds. Combust. Sci. Technol. **161**, 113–137 (2000)
34. J.A. van Oijen, *Flamelet-generated manifolds: development and application to premixed laminar flames*. Ph.D. thesis, Eidenhoven Technical University, Eidenhoven, Netherlands, 2002
35. J.A. van Oijen, A. Donini, R.J.M. Bastiaans, J.H.M. ten Thije Boonkkamp, L.P.H. de Goey, State-of-the-art in premixed combustion modeling using flamelet generated manifolds. Prog. Energy Combust. Sci. **57**, 30–74 (2016)
36. N. Hass, K. Cabell, A. Storch, HIFiRE direct-connect rig (HDCR) phase I ground test results from the NASA Langley arc-heated scramjet test facility, in *JANNAF* (2010)
37. A. Storch, M. Bynum, J. Liu, M. Gruber, Combustor operability and performance verification for HIFiRE flight 2, in *17th AIAA International Space Planes and Hypersonic Systems and Technologies Conference* (San Francisco, CA, 2011)
38. Z. Luo, C.S. Yoo, E.S. Richardson, J.H. Chen, C.K. Law, T.F. Lu, Chemical explosive mode analysis for a turbulent lifted ethylene jet flame in highly-heated coflow. Combust. Flame **159**(1), 265–274 (2012)
39. K. Cabell, N.E. Hass, A. Storch, M. Gruber, HIFiRE direct-connect rig (HDCR) phase I scramjet test results from the NASA Langley arc-heated scramjet test facility, in *17th AIAA International Space Planes and Hypersonic Systems and Technologies Conference* (San Francisco, CA, 2011)
40. R.L. Panton, *Incompressible Flow* (Wiley, New York, 1984)
41. F.A. Williams, *Combustion Theory*, 2nd edn. (The Benjamin/Cummings Publishing Company, Menlo Park, CA, 1985)

42. S.R. Turns, *An Introduction to Combustion: Concepts and Applications*, 2nd edn. (McGraw Hill, 2000)
43. K.K. Kuo, *Principles of Combustion* (Wiley, Hoboken, N.J., 2005)
44. J. Warnatz, U. Maas, R.W. Dibble, *Combustion*, 4th edn. (Springer, Berlin, Germany, 2006)
45. C.K. Law, *Combustion Physics* (Cambridge University Press, 2006)
46. P. Gnoffo, R.N. Gupta, J.L. Shinn, *Conservation equations and physical modes for hypersonic air flows in thermal and chemical nonequilibrium, NASA Technical Paper 2867* (NASA, Hampton, VA, 1989)
47. C. Park, *Nonequilibrium Hypersonic Aerothermodynamics* (Wiley, New York, 1990)
48. G.M. Faeth, Evaporation and combustion in sprays. Prog. Energy Combust. Sci. **9**, 1–76 (1983)
49. J.P. Drummond, Supersonic reacting internal flow fields, in *Numerical Approaches to Combustion Modeling*, ed. by E.S. Oran, J.P. Boris, vol. 135 of Progress in Astronautics and Aeronautics, Chap. 12, pp. 365–420 (AIAA, Washington, D.C., 1991)
50. M. Safari, M.R.H. Sheikhi, M. Janbozorgi, H. Metghalchi, Entropy transport equation in large eddy simulation for exergy analysis of turbulent combustion systems. Entropy **12**(3), 434–444 (2010)
51. H. Tennekes, J.L. Lumley, *A First Course in Turbulence* (MIT Press, Cambridge, MA, 1972)
52. J.O. Hinze, *Turbulence* (McGraw Hill Book Company, New York, 1975)
53. P.A. Libby, F.A. Williams (eds.), *Turbulent Reacting Flows* (Academic Press, London, UK, 1994)
54. S.B. Pope, *Turbulent Flows* (Cambridge University Press, Cambridge, UK, 2000)
55. K.A. Hoffmann, S.T. Chiang, *Computational Fluid Dynamics*, vol. 1, 4th edn. (Engineering Education Systems, Wichita, KS, 2000)
56. K.A. Hoffmann, S.T. Chiang, *Computational Fluid Dynamics*, vol 2, 4th edn. (Endingeering Education System, Wichita, KS, 2000)
57. J.H. Ferziger, M. Perić, *Computational Methods for Fluid Mechanics*, 3rd edn. (Springer, Berlin, Germany, 2002)
58. J. Blazek, *Computational Fluid Dynamics: Principles and Applications*, 2nd edn. (Elsevier, Washington, D.C., 2005)
59. K. Masatsuka, *I Do Like CFD*, vol. 1, 2nd edn. (2013). http://www.cfdbooks.com/cfdbooks.html
60. R.H. Pletcher, J.C. Tannehill, D.A. Anderson, *Computational Fluid Mechanics and Heat Transfer*, 3rd edn. (CRC Press, Boca Raton, FL, 2013)
61. K.A. Hoffmann, S.T. Chiang, *Computational Fluid Dynamics*, vol. 3, 4th edn. (Engineering Education System, Wichita, KS, 2000)
62. D.C. Wilcox, *Turbulence Modeling for CFD* (DCW Industries Inc, La Cañada, CA, 2000)
63. P. Sagaut, *Large Eddy Simulation of Incompressible Flows: An Introduction*, 3rd edn. (Springer, Berlin, Germany, 2006)
64. E. Garnier, N. Adams, P. Sagaut, *Large Eddy Simulation for Compressible Flows* (Springer, Netherlands, 2009)
65. P.A. Durbin, B.A.P. Reif, *Statistical Theory and Modeling for Turbulent Flows*, 2nd edn. (Wiley Ltd., New York, 2011)
66. G.I. Taylor, Statistical theory of turbulence. Proc. Royal Soc. (A) **151**, 421–478 (1935)
67. R.A. Baurle, Modeling of high speed reacting flows: Established practices and future challenges, in *42nd AIAA Aerospace Sciences Meeting and Exhibit*, AIAA-2004-267 (AIAA, Reno, NV, 2004)
68. R.W. Bilger, S.H. Starner, R.J. Kee, On reduced mechanisms for methane-air combustion in nonpremixed flames. Combust. Flame **80**, 135–149 (1990)
69. R.S. Barlow, J.H. Frank, Effects of turbulence on species mass fractions in methane/air jet flames. Proc. Combust. Inst. **27**, 1087–1095 (1998)
70. H. Pitsch, N. Peters, A consistent flamelet formulation for non-premixed combustion considering differential diffusion effects. Combust. Flame **114**, 26–40 (1998)
71. T.F.C. Chan, H.B. Keller, Arc-length continuation and multi-grid techniques for nonlinear elliptic eigenvalue problems. SIAM J. Sci. Stat. Comput. **3**(2), 173–194 (1982)

72. H.F. Mrema, G.V. Candler, Large eddy simulation of supersonic combustion using the flamelet/progress-variable approach and the evolution-variable manifold approach, in *AIAA Scitech Forum* (San Diego, CA, 2019)
73. J. Urzay, Supersonic combustion in air-breathing propulsion systems for hypersonic flight. Ann. Rev. Fluid Mech. **50**, 593–627 (2018)
74. G.L. Brown, A. Roshko, On density effects and large structure in turbulent mixing layers. J. Fluid Mech. **64**, 775–816 (1974)
75. D.W. Bogdanoff, Compressibility effects in turbulent shear layers. AIAA J. **21**(6), 926–927 (1983)
76. D. Papamoschou, A. Roshko, The compressible turbulent shear layer: an experimental study. J. Fluid Mech. **197**, 453–477 (1988)
77. H. Foysi, S. Sarkar, The compressible mixing layer: An LES study. Theor. Comp. Fluid. Dyn. **24**, 565–588 (2010)
78. M. Oevermann, Numerical investigation of turbulent hydrogen combustion in a SCRAMJET using flamelet modeling. Aerosp. Sci. Technol. **4**, 463–480 (2000)
79. V.E. Terrapon, F. Ham, R. Pecnik, H. Pitsch, A flamelet-based model for supersonic combustion, in *Center for Turbulence Research Annual Research Briefs* (2009)
80. A. Saghafian, V.E. Terrapon, H. Pitsch, An efficient flamelet-based combustion model for compressible flows. Combust. Flame **162**(3), 652–667 (2015)
81. R. Pecnik, V. Terrapon, F. Ham, G. Iaccarino, H. Pitsch, Reynolds-averaged Navier Stokes simulations of the HyShot II scramjet. AIAA J. **50**, 1717–1732 (2012)
82. J.R. Quinlan, Flamelet/progress variable modeling for a dual-mode scramjet combustor. Ph.D. thesis, University of Virginia, Charlottesville, VA, 2015
83. P.G. Ferlemann, Forebody and inlet design for the HIFiRE 2 flight test, in *JANNAF Airbreathing Propulsion Subcommittee Meeting* (Boston, MA, 2008)
84. G.L. Pellett, S.N. Vaden, L.G. Wilson, Gaseous surrogate hydrocarbons for a HIFiRE scramjet that mimic opposed jet extinction limits for cracked JP fuels, in *55th JANNAF Propulsion Meeting, NTRS Report Number 20080020388* (Boston, MA, 2008)
85. Viscous Upwind ALgorithm for Complex Flow ANalysis (VULCAN): User manual (2010)
86. D.C. Wilcox, Wall matching, a rational alternative to wall functions, in *27th Aerospace Sciences Meeting* (Reno, NV, 1989)
87. V. Cuda, N.E. Hass, Heat flux and wall temperature estimates for the NASA Langley HIFiRE direct connect rig, in *JANNAF 43rd CS/31st APS/25th PSHS Joint Subcommittee Meeting* (La Jolla, CA, 2009)
88. F.R. Menter, Two-equation eddy-viscosity turbulence models for engineering applications. AIAA J. **32**, 1598–1605 (1994)
89. J.R. Edwards, A low-diffusion flux-splitting scheme for Navier-Stokes calculations. Comput. Fluids. **26**, 635–659 (1997)
90. T.H. Pulliam, D.S. Chaussee, A diagonal form of an implicit approximate-factorization algorithm. J. Comput. Phys. **39**, 347–363 (1981)
91. R. Baurle, Analysis of facility non-equilibrium thermodynamic effects on HIFiRE ground tests, in *JANNAF 46th CS/34th APS/34th EPSS/28th PSHS Joint Subcommittee Meeting* (Albuquerque, NM, 2014)
92. G. Lacaze, E. Richardson, T. Poinsot, Large eddy simulation of spark ignition in a turbulent methane jet. Combust. Flame **156**, 1993–2009 (2009)
93. H. Yamashita, M. Shimada, T. Takeno, A numerical study on flame stability at the transition point of jet diffusion flames. Proc. Combust. Inst. **26**, 27–34 (1996)
94. E. Sozer, E. Hassan, S. Yun, S. Thakur, J. Wright, M. Ihme, W. Shyy, Turbulence-chemistry interaction and heat transfer modeling of H2/O2 gaseous injector flows, in *48th AIAA Aerospace Sciences Meeting and Exhibit* (Orlando, FL, 2010)
95. D.J. Lee, M. Ihme, S. Thakur, W. Shyy, LES of a gaseous H2/O2 rocket injector: wall heat transfer modeling, in *13th International Conference on Numerical Combustion* (Corfu, Greece, 2011)

96. H. Wu, M. Ihme, Modeling of unsteady heat transfer in flame-wall interaction, in *66th Division of Fluid Dynamics Meeting of the American Physical Society* (Pittsburgh, PA, 2013)
97. P.C. Ma, H. Wu, M. Ihme, J.-P. Hickey, Nonadiabatic flamelet formulation for predicting wall heat transfer in rocket engines. AIAA J. **56**(6), 2336–2349 (2018)
98. H. Barths, C. Hasse, G. Bikas, N. Peters, Simulation of combustion in direct injection diesel engines using an Eulerian particle flamelet model. Proc. Combust. Inst. **28**(1), 1161–1167 (2000)
99. C. Felsch, M. Gauding, C. Hasse, S. Vogel, N. Peters, An extended flamelet model for multiple injections in DI diesel engines. Proc. Combust. Inst. **32**(1), 2775–2783 (2009)
100. C.K. Westbrook, F.L. Dryer, Simplified reaction mechanisms for oxidation of hydrocarbon fuels in flames. Combust. Sci. Technol. **27**, 31–43 (1981)
101. A.T. Norris, Tuning process for the modified Magnussen combustion model, in *AIAA Propulsion and Energy Forum* (Cincinnati, OH, 2018)

Filtered Density Function Implementation in a Discontinuous Spectral Element Method

Jonathan Komperda and Farzad Mashayek

Abstract An overview of the current state of progress in the large eddy simulation of turbulent combustion using the filtered density function (FDF) coupled with a discontinuous spectral element method is presented. It is assumed that the reader has some prior knowledge of the FDF method and its implementation in other codes. The unique challenges presented by the discontinuous spectral element method are outlined, and their solutions are described in the context of variable-density flows. Specifically, we discuss approaches for interpolating Eulerian quantities to particle locations, searching for particles on an unstructured grid, and constructing filtered quantities on collocation points. Sample results are presented to demonstrate the algorithm's efficacy and a discussion follows describing the future of the method.

Keywords Discontinuous spectral element method · Filtered density function · Large eddy simulation · Monte Carlo particle method · Unstructured grid

1 Introduction

Preservation of the environment has become a topic of intense debate in recent years. This debate has spurred the emergence of new technologies and policies in energy generation, energy utilization, and emissions. Although many market segments are seeing this drive, developments in modern vehicle technology are notable. Plug-in electric vehicles are rapidly entering the market, now contributing to 2.2% of the world share of vehicles [1, 2]. But, despite the growth of the alternative energy sources in recent years, the United States only generated 17.1% of electricity using renewables in 2018 [3]. A vast majority of energy is still produced from the combustion of fossil fuels, emphasizing the need to design more efficient and clean-burning

J. Komperda · F. Mashayek (✉)
Department of Mechanical and Industrial Engineering,
University of Illinois at Chicago, Chicago, IL 60607, USA
e-mail: mashayek@uic.edu

J. Komperda
e-mail: jonk@uic.edu

D. Livescu et al. (eds.), *Modeling and Simulation of Turbulent Mixing and Reaction*, Heat and Mass Transfer, https://doi.org/10.1007/978-981-15-2643-5_7

combustors. Modern advances in computing are allowing engineers to design and simulate combustors more rapidly than traditional experimental approaches; however, advances in numerical methods that can accurately predict the complex physics in supersonic turbulent combustion are still needed.

The simulation of turbulent combustion for real-world applications requires the development of accurate high-fidelity models that can perform detailed calculations in complex geometries. Accordingly, large eddy simulation (LES) has been replacing the commonly used Reynolds averaged Navier Stokes (RANS) methods due to its increased accuracy and a recent trend of increasing computational power allowing for large scale LES. One specific approach for LES of chemically reacting flows, the filtered density function (FDF), has gained particular attention due to the closed form of its chemical reaction source term, mathematical rigor, and ease of implementation using a particle mesh method. Active development of the FDF has included the extension to variable-density flows, the addition of compressibility effects, increasing the accuracy of the mixing models, simulation on massively parallel systems, and more recently the solution on unstructured grids [4–11]. For these reasons, we elect to implement the FDF methodology in the high-order discontinuous spectral element method.

In this chapter, we give a brief introduction to the implementation of the discontinuous spectral element method (DSEM) for the simulation of turbulent compressible flows coupled with the filtered density function for the prediction of chemical reaction. First, we briefly introduce the DSEM and describe its benefits along with the necessary considerations for the FDF. We then discuss the numerical approach for the implementation of FDF. We conclude with sample results using the coupled DSEM-LES/FDF approach.

2 Overview of the Discontinuous Spectral Element Method

The discontinuous spectral element method is a high-order approach for the solution of the compressible Navier-Stokes equations in non-dimensional form [12–15]. The equations we seek to solve are given as

$$\vec{Q}_t + \vec{F}_x^a + \vec{G}_y^a + \vec{H}_z^a = \frac{1}{\mathrm{Re}_f}(\vec{F}_x^v + \vec{G}_y^v + \vec{H}_z^v), \tag{1}$$

where $\vec{Q}$ is the solution vector; $\vec{F}$, $\vec{G}$, and $\vec{H}$ are flux vectors; and the superscripts a and v differentiate the inviscid and viscous fluxes, respectively [12, 13]. The non-dimensionalization also produces the reference Reynolds number, Prandtl number, and Mach number, which are defined as

$$\mathrm{Re}_f = \frac{U_f^* L_f^* \rho_f^*}{\mu_f^*}, \quad \mathrm{Pr}_f = \frac{c_p^* \mu_f^*}{\kappa^*}, \text{ and } \mathrm{Ma}_f = \frac{U_f^*}{\sqrt{\gamma R^* T_f^*}}.$$

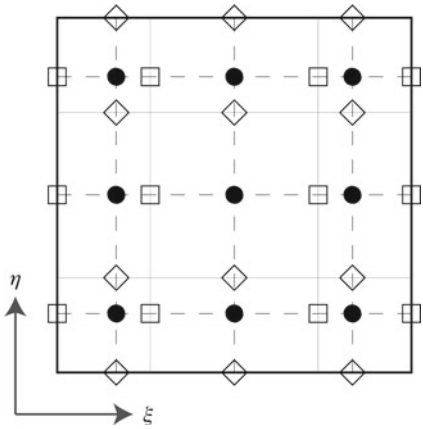

Fig. 1 Two-dimensional $\mathcal{P} = 3$ spectral element. Filled circles are Gauss/Gauss points, open squares are Lobatto/Gauss points, and open diamonds are Gauss/Lobatto points

The superscript * indicates dimensional variables and the subscript f shows reference values. Here, U, L, ρ, and μ are the velocity, length, density, and dynamic viscosity, respectively. The specific heat at constant pressure, thermal conductivity, ratio of specific heats, and gas constant are c_p, κ, γ, and R, respectively. The system of equations is completed by the equation of state, given by $p = \rho T/\gamma \mathrm{Ma}_f^2$.

The discretization in DSEM combines the geometric flexibility of finite elements with the high-order approximations of spectral functions [16, 17]. The decomposed domain consists of non-overlapping hexahedral elements that can be arbitrarily oriented on an unstructured grid. Additionally, the elements may have other complex features such as curved sides or faces, which is especially beneficial for the simulation of complex real-world geometries. The element itself employs a staggered grid formulation consisting of a nodal collocation of both Gauss and Lobatto quadrature points. The solution vector, $\vec{Q}$, is found on the Gauss collocation points and the inviscid and viscous fluxes are computed on the Lobatto points. A schematic of a two-dimensional element is shown in Fig. 1 to demonstrate the locations of the Gauss and Lobatto points.

DSEM utilizes high-order Lagrange polynomials in conjunction with particular quadrature rules, specifically Chebyshev-Gauss, to express the solution in the mapped space of the element as a series of polynomial basis functions, which can approximate the solution accurately as the polynomial degree tends to infinity [13, 17]. The governing equations are solved in the mapped space, and a parametric mapping operation is performed to convert the solution from the mapped space, over the interval [0, 1], to the physical space [14]. The solutions at any location within the mapped element may be approximated as the product of the Lagrange interpolating polynomials ($h_{\Xi+1/2}$) with the nodal solution vector on the Gauss-Gauss-Gauss grid as

$$Q(\xi,\eta,\zeta) = \sum_{i=0}^{N-1}\sum_{j=0}^{N-1}\sum_{k=0}^{N-1} Q^{ggg}_{i+1/2,j+1/2,k+1/2} h_{i+1/2}(\xi) h_{j+1/2}(\eta) h_{k+1/2}(\zeta), \quad (2)$$

where N is the number of Gauss points in the $\Xi = i, j, k$ directions, and ξ, η, ζ are the coordinates of interest in the mapped space. This feature of DSEM also allows for the construction of high-order spectral, or reduced-order Lagrange, interpolants based on the polynomial solution at a negligible cost [18]. Although the solution is smooth within the element, the values along the element interfaces are discontinuous. The flux values are patched along the interfaces using an approximate Riemann solver [14]. The temporal update of the solution is performed using a fourth-order explicit Runge Kutta scheme.

The formulation of this method leads to desirable computational properties compared to other numerical approaches. DSEM has the geometric flexibility of finite element and finite volume methods, which allows for the simulation of complex geometries; however, it also enables the user to utilize variable-order spectral approximations. Working with high-order spectral polynomials provides several benefits over traditional schemes, such as high-accuracy solutions, low numerical dissipation and dispersion, the ability to interpolate between grids of different resolutions at run-time, and efficient construction of filters for use in LES [19]. The formulation of DSEM also results in naturally diagonal mass matrices enabling efficient utilization of fast-tensor products. Additionally, the non-overlapping hexahedral elements allow for the solution within each element to be updated independently of the remainder of the grid. The combination of these features allows for computationally efficient implementation on massively parallel computer systems. The DSEM has been demonstrated to scale to tens of thousands of cores efficiently and is currently being optimized to run on systems of hundreds of thousands of cores. A sample of weak and strong scaling on the Argonne Leadership Computing Facility's Mira supercomputer is presented in Fig. 2.

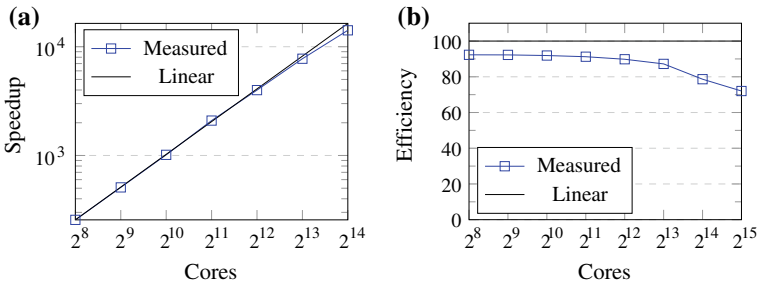

Fig. 2 **a** Strong scaling speedup for a simulation with 1.1 billion solution points and **b** weak scaling efficiency for a case with 20 P = 14 elements per core. Simulation performed using DSEM on Mira at Argonne Leadership Computing Facility

2.1 Considerations When Coupling Methods

The DSEM solver presents several unique challenges in the implementation of a joint FDF approach that are not present in other methods. Specifically, the joint FDF must be implemented in such a way that high computational efficiency on massively parallel systems is maintained. The FDF approach must also behave locally, within each element, and perform minimal inter-element operations to scale efficiently. The exchange of information between elements should be implemented in a manner consistent with the DSEM formulation, utilizing separate update and communication steps corresponding to the interior and interface solutions, respectively.

The unstructured nature of the grid as well as the nonuniform distribution of collocation points within the element present separate unique challenges. Tracking of particles on the unstructured grid complicates the particle search algorithm due to the unknown orientation, shape, and connectivity of the elements in the physical space. Additionally, the nonuniform distribution of the collocation points within the element must be accounted for when constructing mean particle estimates. In DSEM, there are two sets of points that may be considered for constructing mean quantities, the Gauss and Lobatto collocation points. The Gauss points are preferred, as the source term due to chemical reaction may be added to the energy equation without the need to interpolate from the Lobatto grid.

While significant challenges have been presented, the DSEM also contains features very beneficial to a particle-mesh approach. Firstly, the large size of the spectral elements at high polynomial orders results in particles residing in an element for longer durations, requiring fewer searches across the unstructured grid. Secondly, the known mapped location of collocation points in each element presents an opportunity to perform high-speed searches in a structured manner. Finally, the availability of high-accuracy interpolants reduces the overall cost of implementing a particle-based method for the solution of the FDF [20].

3 Coupled FDF Formulation

This section shall briefly summarize the governing equations of the filtered density function as well as describe the solution of the FDF in three dimensions with regards to DSEM. The modeled FDF transport equation we seek to solve is similar to previous work [20, 21], and includes the source term due to compressibility [22–24],

$$\frac{\partial F_L}{\partial t} + \frac{\partial \left[\langle u_i \rangle_L F_L\right]}{\partial x_i} = \frac{\partial}{\partial x_i}\left[(\gamma + \gamma_t)\frac{\partial (F_L/\langle \rho \rangle_l)}{\partial x_i}\right] + \frac{\partial}{\partial \psi_\alpha}\left[\Omega_m(\psi_\alpha - \langle \phi_\alpha \rangle_L) F_L\right] - \frac{\partial \left[\hat{S}_\alpha F_L\right]}{\partial \psi_\alpha} - \frac{\partial \left[\langle \tilde{S}_\alpha^{comp} \rangle_l F_L\right]}{\partial \psi_\alpha}. \tag{3}$$

where F_L is the filtered mass density function; $\langle u_i \rangle_L$ is the filtered velocity in the direction x_i; $\langle \rho \rangle_l$ is the filtered density; γ and γ_t are the molecular and sub-grid diffusivities, respectively; Ω_m is the sub-grid mixing frequency; ϕ_α is the scalar of interest; S_α^R is the reaction source term, and $\widetilde{S}_\alpha^{comp}$ is the compressibility source term. Formulation of the exact FDF transport equation and solution of the modeled FDF transport equation (Eq. 3) has been presented in great detail in other work [8, 21, 24–28], and therefore only the differences in the DSEM implementation will be outlined in detail.

3.1 Solution of the Coupled System

The solution of the FDF transport equation relies on the principle of *equivalent systems* [25]. A set of stochastic differential equations (SDEs), carrying identical statistics to the modeled FDF transport equation, is solved using a finite number of Monte Carlo particles in a Lagrangian frame of reference [21, 25]. Each point particle of the ensemble tracks a position vector $\vec{X}^+(t)$ and a set of scalar composition variables $\phi_\alpha \left(\vec{X}(t), t \right)$. Integration of the SDEs on each particle at each timestep updates its respective position and composition. Eulerian information, such as velocity and pressure, must be interpolated to the particle position. Finally, ensemble averaging of the particles is performed to determine the mean filtered quantities of this meshless solution on the DSEM grid.

The Lagrangian tracking of the particles consists of three stages per particle: searching, interpolation, and update. The search and interpolation algorithms implemented in the DSEM code are that of Jacobs et al. [18, 29, 30] with modifications for improved efficiency and scaling on large systems. To ensure consistency of Eulerian and Lagrangian methods, the interpolation step of the update procedure must utilize the same polynomial basis as the construction of the mean filtered particle quantities in the FDF [10, 31]. Ideally, the high-order spectral interpolant and basis, as opposed to a lower-order Lagrange interpolant or other function, should be used to preserve the high accuracy of the DSEM method. The calculation of the interpolant is a modified form of Eq. (2), where the polynomials ($h_{\Xi+1/2}$) are evaluated at the particle location ($\vec{X}^+(t)$). The coefficients ($h_{\Xi+1/2}$) must also be saved for later use in the construction of the Favre-filtered particle quantities on the element collocation points.

3.2 Considerations for Unstructured Grids

The construction of ensembles for the calculation of the Favre-filtered values of transport quantities ($\langle Q \rangle_L$) presents a substantial challenge on high-order finite element type grids. This challenge stems from the necessity to determine the nearest

collocation points to each particle. This step typically requires a search in the physical space, which is undesirable since such a search is computationally expensive. Alternatively, our group has proposed performing all FDF related computations in the mapped space of the element [17, 20]. The mapped space is selected in lieu of the physical space for two reasons: (1) at high polynomial orders the particle resides within the element for many timesteps, making it unnecessary to perform a physical search for tracking and update purposes, and (2) the non-uniform distribution of Gauss collocation points is well known and easily calculated in the mapped space regardless of the element orientation or shape [32].

The algorithm for calculating the filtered quantities can be summarized as follows. First, ensure that the mapped coordinate of the particle is in the range [0, 1]. Next, substitute the mapped particle location for each direction into the equation

$$j_i = \frac{N \cos^{-1}\left(1 - 2X_i^+\right)}{\pi} - \frac{1}{2}, \tag{4}$$

to determine the non-integer value of j_i. Then, all that is necessary to determine the Gauss quadrature points bounding the particle is to round the value of j_i both up and down in every direction, yielding a binary combination of eight points corresponding to the vertices of a cube [17]. Once the nearest eight Gauss points are known, the Favre-filtered value of a scalar at a Gauss point may be determined with

$$\langle Q \rangle_L \approx \frac{\sum_{n \in \Delta_E} \beta\left(\vec{X}^{(n)}\right) Q\left(\phi_\alpha\right) w^{(n)}}{\sum_\alpha \beta\left(\vec{X}^{(n)}\right) w^{(n)}}, \tag{5}$$

where β is the product of the interpolating polynomial, w is the mass weighting of the particle, and n is the index of particles in the domain (Δ_E) that contribute to the Gauss point [21]. The filtered quantities are constructed in the mapped space, then are projected onto the physical space using parametric mapping. The largest benefit of this approach is that the method functions on both skewed and non-skewed elements without additional processing.

3.3 Considerations for Compressible Flows

The DSEM solves the compressible Navier-Stokes equations and utilizes the so-called Entropy Viscosity (EV) method for shock capturing [33, 34]. The FDF implementation must account for compressibility effects (Eq. 3) as well as remain consistent with the scalar solution in the presence of compressible flow features, such as shockwaves. The EV method functions by applying numerical dissipation at the location of the shock [35]. This numerical dissipation must also be applied to the modeled FDF transport equation. Similarly, the diffusivity due to EV is calculated on the Eulerian grid, interpolated to the particle location, and used in conjunction with

the molecular and turbulent diffusivities for the particle update in the Lagrangian frame of reference.

4 Demonstration

The flow configuration selected to demonstrate the DSEM-LES/FMDF hybrid approach is the well established Taylor-Green Vortex (TGV) problem. The TGV has been studied extensively in literature and regularly serves as a benchmark problem for testing turbulence models [36–40]. The initial condition of the TGV is specified as an analytical solution in non-dimensional form for density, velocity, and pressure, given by

$$\rho = 1, \tag{6}$$

$$u_1 = \sin(x_1)\cos(x_2)\cos(x_3), \tag{7}$$

$$u_2 = -\cos(x_1)\sin(x_2)\cos(x_3), \tag{8}$$

$$u_3 = 0, \tag{9}$$

$$p = \frac{1}{16}\left[\cos(2x_1) + \cos(2x_2)\right]\left[\cos(2x_3) + 2\right], \tag{10}$$

respectively. The Mach number is set as $\mathrm{Ma}_f = 0.1$; the Reynolds number is $\mathrm{Re}_f = 1,400$, and the Prandtl number is $\mathrm{Pr}_f = 0.72$. The Reynolds number is calculated as the inverse of the reference kinematic viscosity, which means the product of the reference length and velocity is unity, $U_f^* L_f^* = 1$ [39, 41]. The temperature is calculated from the equation of state and all boundaries are specified to be periodic.

The computational domain is a three-dimensional cube with equal sides of length $L = 2\pi$. We specify an $11 \times 11 \times 11$-element mesh with polynomial order $\mathcal{P} = 5$, resulting in 287,496 solution points to ensure that DSEM-LES accurately predicts the kinetic energy dissipation rate. A total of 2.2 million particles are initialized in a uniformly random distribution in the domain. This quantity of particles results in approximately 62 particle contributions per Gauss point, sufficiently many to produce accurate statistics. The interpolant for the particles, as well as the basis for constructing Favre-filtered averages in the ensemble domains, is a $\mathcal{P} = 5$ spectral polynomial, consistent with the polynomial order of the element. The sub-grid scale model used for LES is the Smagorinsky model [14].

The TGV problem is intended to demonstrate the consistency of the FDF approach in conjunction with DSEM for the accurate prediction of filtered temperature. As the flow progresses, the initial condition goes through vortex breakdown from an anisotropic laminar phase to fully isotropic decaying turbulence [41]. Figure 3 shows $\langle T \rangle_L$ predicted by DSEM and FDF on isosurfaces of Q-criterion [42, 43] at time $t = 3.0$. The vortical structures are clearly apparent at this stage and the temperature variation in the domain is near its peak. The flow is mid-way to its maximum kinetic energy dissipation and exhibits strong three-dimensional effects. The consistency of

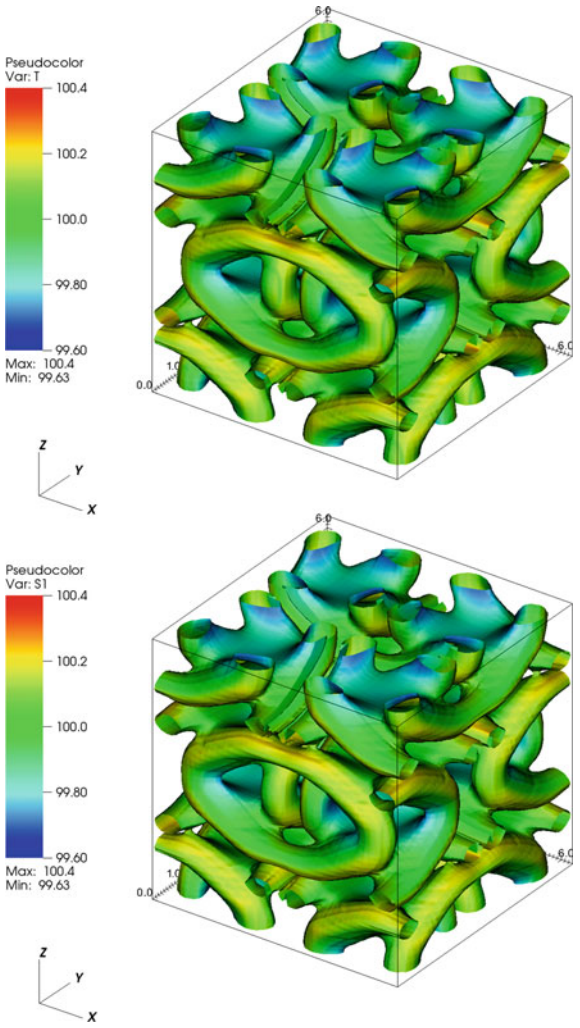

Fig. 3 Isosurfaces of Q-criterion ($Q = 0.1$) colored by **a** filtered temperature ($\langle T \rangle_{DSEM}$) as calculated by the DSEM solver and **b** filtered temperature ($\langle T \rangle_{FDF}$) as calculated by the filtered density function solver at time $t = 3.0$

the solver is assessed by comparing the filtered temperature obtained by DSEM and FDF, shown in Fig. 4. The correlation coefficient is $r = 0.9974$, which establishes excellent consistency of the method.

5 Concluding Remarks

The filtered density function methodology has proven to be effective for the large eddy simulation of turbulent chemically-reacting flows in the discontinuous spectral

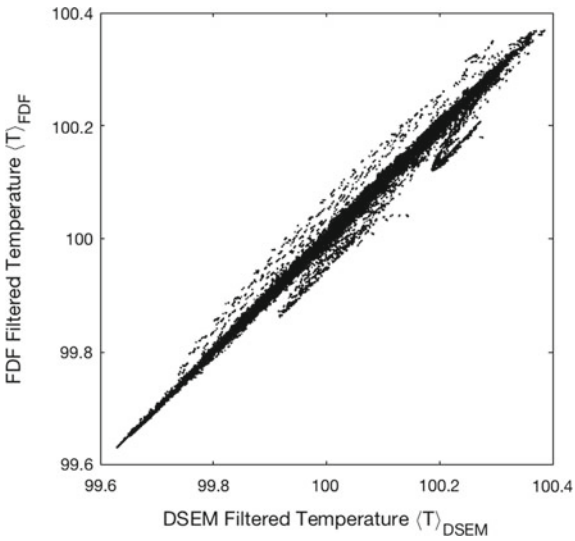

Fig. 4 Scatter plot of the scalar filtered temperature as predicted by FMDF versus that predicted by DSEM at time $t = 3.0$. The correlation coefficient is $r = 0.9974$

element method. The approach presented in this work has several desirable properties when compared to traditional approaches. It has an efficient particle search in spectral elements due to the use of the mapped space for computation of ensembles and parametric mapping for converting the solution to the physical space. Additionally, the mapping operation and use of mapped space grant the ability to handle unstructured grids without the need to adjust the search. The implementation of the entropy viscosity method allows for shock capturing in compressible flows. Finally, the solver allows the user to select the appropriate polynomial order for interpolation, construction of mean filtered quantities, and discretization of the element. The user is also able to use different order interpolants with high order discretizations.

Currently, the hybrid DSEM-LES/FDF method has successfully simulated several benchmark problems to establish consistency and determine accuracy. We expect the DSEM-LES/FDF approach to be able to perform LES of complex real-world geometries, such as scramjets and internal combustion engines, in the near future.

Acknowledgements The support for this work was provided by the U.S. Office of Secretary of Defense under contract FA8650-12-C-2247. The authors are also grateful to the Air Force Research Laboratory staff for program management support. This work used the Extreme Science and Engineering Discovery Environment (XSEDE), which is supported by National Science Foundation grant number ACI-1548562. This research used resources of the Argonne Leadership Computing Facility (ALCF), which is a DOE Office of Science User Facility supported under Contract DE-AC02-06CH11357. The simulation resources for this project were provided by UIC ACER, ALCF under a Director's Discretionary allocation titled "DSEM_SUPERSONIC," and the Extreme Science and Engineering Discovery Environment (XSEDE) Comet at SDSC through allocations TG-TRA180035 and CTS180014.

References

1. S.C. Davis, S.E. Williams, R.G. Boundy, S. Moore, 2016 vehicle technologies market report, Tech. Rep. (Oak Ridge National Laboratory, 2017)
2. R. Irle, Global EV sales for 2018 (2018) http://www.ev-volumes.com/country/total-world-plug-in-vehicle-volumes/. Last accessed on 1 Apr 2019
3. What is U.S. electricity generation by energy source? (2018) https://www.eia.gov/tools/faqs/. Last accessed on 1 Apr 2019
4. P.H. Pisciuneri, S.L. Yilmaz, P.A. Strakey, P. Givi, Massively parallel FDF simulation of turbulent reacting flows, in *Stochastic Equations for Complex Systems* (Springer, Berlin, 2015), pp. 175–192
5. N. Ansari, P.A. Strakey, G.M. Goldin, P. Givi, Filtered density function simulation of a realistic swirled combustor. Proc. Combust. Inst. **35**(2), 1433–1442 (2015)
6. A.G. Nouri, M.B. Nik, P. Givi, D. Livescu, S.B. Pope, Self-contained filtered density function. Phys. Rev. Fluids **2**(9), 094603 (2017)
7. M.B. Nik, P. Givi, C.K. Madnia, S.B. Pope, EPVS-FMDF for LES of high-speed turbulent flows, in *AIAA Paper 2012-0117* (2012)
8. T.G. Drozda, M.R.H. Sheikhi, C.K. Madnia, P. Givi, Developments in formulation and application of the filtered density function. Flow Turbul. Combust. **78**(1), 35–67 (2007)
9. N. Ansari, G.M. Goldin, M.R.H. Sheikhi, P. Givi, Filtered density function simulator on unstructured meshes. J. Comput. Phys. **230**(19), 7132–7150 (2011)
10. R. McDermott, S.B. Pope, A particle formulation for treating differential diffusion in filtered density function methods. J. Comput. Phys. **226** (2007)
11. C.K. Madnia, F.A. Jaberi, P. Givi, Handbook of numerical heat transfer, in *Large Eddy Simulation of Heat and Mass Transport in Turbulent Flows*, 2 edn. (Wiley, Hoboken, NJ, 2006), pp. 167–189
12. G.B. Jacobs, D.A. Kopriva, F. Mashayek, Validation study of a multidomain spectral code for simulation of turbulent flows. AIAA J. **43**(6), 1256–1264 (2005)
13. G.B. Jacobs, D.A. Kopriva, F. Mashayek, A conservative isothermal wall boundary condition for the compressible Navier-Stokes equations. J. Sci. Comput. **30**(2), 177–192 (2005)
14. K. Sengupta, G.B. Jacobs, F. Mashayek, Large-eddy simulation of compressible flows using a spectral multi-domain method. Intl J. Numer. Meth. Fluids **61**(3), 311–340 (2009)
15. Z. Ghiasi, D. Li, J. Komperda, F. Mashayek, Near-wall resolution requirement for direct numerical simulation of turbulent flow using multidomain Chebyshev grid. Int. J. Heat Mass Trans. **126**, 746–760 (2018)
16. D.A. Kopriva, *Implementing Spectral Methods for Partial Differential Equations: Algorithms for Scientists and Engineers* (Springer Science & Business Media, Berlin, 2009)
17. J. Komperda, Z. Ghiasi, D. Li, F. Mashayek, A. Irannejad, F.A. Jaberi, Simulation of the cold flow in a ramp-cavity combustor using a DSEM-LES/FMDF hybrid scheme, in *AIAA Paper 2016-1938* (2016)
18. G.B. Jacobs, D.A. Kopriva, F. Mashayek, Towards efficient tracking of inertial particles with high-order multidomain methods. J. Comp. Appl. Math. **206**, 392–408 (2007)
19. Z. Ghiasi, J. Komperda, D. Li, D. Nicholls, F. Mashayek, Modal explicit filtering for large eddy simulation in discontinuous spectral element method. J. Comput. Phys. **3**, 100024 (2019)
20. J. Komperda, Z. Ghiasi, F. Mashayek, A. Irannejad, F.A. Jaberi, Filtered mass density function for use in discontinuous spectral element method, in *AIAA Paper 2014-3471* (2014)
21. F.A. Jaberi, P.J. Colucci, S. James, P. Givi, S.B. Pope, Filtered mass density function for large eddy simulation of turbulent reacting flows. J. Fluid Mech. **401**, 85–121 (1999)
22. A. Irannejad, F. Jaberi, J. Komperda, F. Mashayek, Large eddy simulation of supersonic turbulent combustion with FMDF, in *AIAA Paper 2014-1188* (2014)
23. Z. Li, A. Banaeizadeh, S. Rezaeiravesh, F. Jaberi, Advanced modeling of high speed turbulent reacting flows, in *AIAA Paper 2012-116* (2012)
24. A. Banaeizadeh, Z. Li, F.A. Jaberi, Compressible scalar filtered mass density function model for high-speed turbulent flows. AIAA J. **49**(10), 2130–2143 (2011)

25. P.J. Colucci, F.A. Jaberi, P. Givi, S.B. Pope, Filtered density function for large eddy simulation of turbulent reacting flows. Phys. Fluids **10**, 499–515 (1998)
26. L.Y.M. Giscquel, P. Givi, F.A. Jaberi, S.B. Pope, Velocity filtered density function for large-eddy simulation of turbulent flows. Phys. Fluids **14**(3), 1196–1213 (2002)
27. M.R.H. Sheikhi, P. Givi, S.B. Pope, Velocity-scalar filtered mass density function for large eddy simulation of turbulent reacting flows. Phys. Fluids **19**(9), 095106 (2007)
28. M.R.H. Sheikhi, P. Givi, S.B. Pope, Frequency-velocity-scalar filtered mass density function for large eddy simulation of turbulent reacting flows. Phys. Fluids **21**(7), 075102 (2009)
29. G.B. Jacobs, D.A. Kopriva, F. Mashayek, A particle tracking algorithm for the multidomain staggered-grid spectral method, in *AIAA Paper 2001-0630* (2001)
30. G.B. Jacobs, J.S. Hesthaven, High-order nodal discontinuous Galerkin particle-in-cell method on unstructured grids. J. Comput. Phys. **214**, 96–121 (2006)
31. P. Jenny, S.B. Pope, M. Muradoglu, D.A. Caughey, A hybrid algorithm for the joint PDF equation of turbulent reactive flows. J. Comput. Phys. **166**, 218–252 (2001)
32. D.A. Kopriva, A staggered-grid multidomain spectral method for the compressible Navier-Stokes equations. J. Comput. Phys. **244**, 142–158 (1998)
33. H. Abbassi, F. Mashayek, G.B. Jacobs, Shock capturing with entropy-based artificial viscosity for staggered grid discontinuous spectral element method. Comput. Fluids **98**, 152–163 (2014)
34. A. Chaudhuri, G.B. Jacobs, W. Don, H. Abbassi, F. Mashayek, Explicit discontinuous spectral element method with entropy generation based artificial viscosity for shocked viscous flows. J. Comput. Phys. **332**, 99–117 (2017)
35. J.L. Guermond, R. Pasquetti, B. Popov, Entropy viscosity method for nonlinear conservation laws. J. Comput. Phys. **230**, 4248–4267 (2011)
36. G.I. Taylor, A.E. Green, Mechanism of the production of small eddies from large ones. Proc. R. Soc. Lond. A. Math. **158**(895), 499–521 (1937)
37. S.A. Orszag, Numerical simulation of the Taylor-Green vortex, in *Computing Methods in Applied Sciences and Engineering Part 2* (Springer, Berlin, 1974), pp. 50–64
38. M. Brachet, D.I. Meiron, S.A. Orszag, B.G. Nickel, R.H. Morf, U. Frisch, Small scale structure of the Taylor-Green vortex. J. Fluid Mech. **130**, 411–452 (1983)
39. M. Brachet, Direct simulation of three-dimensional turbulence in the Taylor-Green vortex. Fluid Dyn. Res. **8**(1–4), 1–8 (1991)
40. D. Drikakis, C. Fureby, F.F. Grinstein, D. Youngs, Simulation of transition and turbulence decay in the Taylor-Green vortex. J. Turbul. **8**(2), 1–12 (2007)
41. G.J. Gassner, A.D. Beck, On the accuracy of high-order discretizations for underresolved turbulence simulations. Theor. Comp. Fluid. Dyn. **27**(3–4), 221–237 (2013)
42. J.C.R. Hunt, A.A. Wray, P. Moin, Eddies, streams, and convergence zones in turbulent flows, Tech. Rep. (Center for Turbulence Research, 1988)
43. G. Haller, An objective definition of a vortex. J. Fluid Mech. **525**, 1–26 (2005)

Modern Developments in Filtered Density Function

Shervin Sammak, Zhuyin Ren and Peyman Givi

Abstract An overview is presented of recent developments in filtered density function (FDF) methodology as utilized for large eddy simulation (LES) of turbulent flows. The review is focused on computational and physical modeling of the FDF, along with a survey of some of the most recent results via LES-FDF.

Keywords Filtered density function · Large eddy simulation · Turbulent combustion

1 Introduction

Since its original conception [1–5], the popularity of the filtered density function (FDF) has been growing steadily. Within the past decade or so, there has been a significant increase in the number of investigators who have contributed to its continuing developments and utilization. The extent of the FDF popularity can be perhaps measured by the relatively large number of participants at a recent mini-symposium devoted to this methodology [6]. This is also reflected in the number of recent tutorials and survey articles devoted to the subject [7–13].

As for the fundamental developments of the methodology, Colucci et al. [14] are credited for the first demonstration of the FDF capability to provide a sys-

S. Sammak (✉)
Center for Research Computing,
University of Pittsburgh, Pittsburgh, PA 15213, USA
e-mail: shervin.sammak@pitt.edu

Z. Ren
Center for Combustion Energy/School of Aerospace Engineering,
Tsinghua University, Beijing 100084, China
e-mail: zhuyinren@tsinghua.edu.cn

P. Givi
Department of Mechanical Engineering and Materials Science, University of Pittsburgh,
Pittsburgh, PA 15261, USA
e-mail: pgivi@pitt.edu

D. Livescu et al. (eds.), *Modeling and Simulation of Turbulent Mixing and Reaction*, Heat and Mass Transfer, https://doi.org/10.1007/978-981-15-2643-5_8

tematic means of subgrid scale (SGS) closure. They develop and solve a modeled transport equation for the FDF of scalar variables (S-FDF) in incompressible turbulent flows. Jaberi and co-workers extend the methodology for LES of variable density flows by development of the scalar filtered mass density function (S-FMDF) for low Mach number [15] and high Mach number [16] flows. Gicquel et al. [17, 18] include the SGS closure of the velocity field for hydrodynamics-LES (V-FDF). This is further extended by Sheikhi et al. [19, 20] who construct the joint scalar-velocity FDF/FMDF, and the joint scalar-velocity-frequency FDF/FMDF [20]. Safari et al. [21–25] account for the entropy in FDF (en-FDF) to facilitate exergy analysis of reactive flows. The most sophisticated form of the model to date in single-phase, compressible, multi-species flow is in a "self-contained" manner to account for SGS modeling of all of the pertinent transport variables: "pressure-energy-velocity-composition filtered mass density function" (PEVC-FMDF) [26]. To account for multi-phase transport in the context of FDF, the pioneering work in Refs. [27, 28] constitutes the starting point.

Because of its demonstrated capabilities, the FDF is now being covered in contemporary textbooks, e.g. Ref. [29], and also serves as a powerful tool in many commercial combustion software, such as ANSYS [30]. Consequently, there has been a significant surge in its utilization worldwide. The objective of the chapter is to provide a survey of the most recent developments in FDF-based modeling and simulations. The scope of the review is limited to contributions made within the last decade or so, and is focused on the following constituents: (1) physical and computational modeling, and (2) simulations and practical applications. These are presented, in order, in this chapter.

2 Physical and Computational Modeling

The last decade has witnessed significant progress in fine tuning of the FDF subclosures, and the procedure by which the FDF is solved numerically. The modeling strategy is naturally influenced by the procedure by which the simulations are conducted.

Modeling of the SGS conditional expected diffusion and/or dissipation remains a challenging issue in FDF (and probability density function (PDF)) modeling [31–44]. Zhou et al. [40] compare the performances of several SGS mixing models, and investigate the sensitivities of combustion process to mixing and reaction. This issue is also considered by Zhang et al. [45]. They conduct a systematic analysis of various SGS closures by using direct numerical simulation (DNS) data of homogeneous isotropic turbulent mixing. Rieth et al. [46] develop a flamelet-FDF closure and Park and Echekki [47] and Gonzalez-Juez et al. [48] suggest a model constructed upon Kerstein's [49] one-dimensional turbulence (ODT) model.

Compressible FDF models have also been the subject of widespread attention [16, 50–59]. It is generally accepted that the joint velocity-composition-energy PDF provides the most systematic means of LES for such flows [57]. Koo et al. [54]

develop a compressible Eulerian model, termed the direct quadrature method of moments (DQMOM), in which the PDF is represented via a finite number of delta functions and then characterized by weight and location in composition space. De Almeida et al. [57] propose a joint scalar-enthalpy PDF and a joint velocity-scalar-energy PDF model using the Eulerian stochastic fields method. Some of the most recent results via LES-FDF of highly compressible flows are reported in Refs. [53, 60, 61].

There have been significant improvements in FDF computations in both Lagrangian and Eulerian contexts. In the former, the FDF is modeled via a set of Langevin stochastic differential equations (SDEs) which are composed to model the SGS effects. The Fokker-Planck corresponding to these SDEs would essentially be the modeled FDF transport equation [62–68]. In the Eulerian method, the FDF is represented by a set of modeled stochastic partial differential equations (SPDEs) solved on Eulerian grid points. The original idea for the latter is due to Sabel'nikov and Soulard [69] and Valiño [70]; and the methodology has proven very useful for LES of reactive flows as demonstrated in Refs. [71–90].

Due to relative simplicity of modeling in the Lagrangian framework, significant progress has been made in developments of advanced stochastic methods in this context [91–105]. As a notable example, Zhang and Wang [100] develop a mean shift (MS) particle model to account for accurate modeling of the differential diffusion effects. Zhou et al. [105] propose a modeling strategy to incorporate differential diffusion effects on both filter and subgrid scale in LES/FDF. Cleary et al. [93] introduce a sparse-Lagrangian multiple mapping conditioning (MMC) model for turbulent flames [106–108]. Sewerin and Rigopoulos [101, 102] introduce a population balance equation (PBE) for predicting the evolution of the soot particle size distribution.

Efficient implementations of chemistry integration in PDF/FDF simulation has also been the subject of broad investigations in both Eulerian and Lagrangian FDF solvers [109–115]. Hiremath et al. [116, 117] implement a combined dimension reduction/tabulation/redistribution algorithm to redistribute the chemistry workload among the computational cores. They report over 40% saving in the computational time. Parallelization of the chemistry solver in the Lagrangian FDF solver is significantly improved via development of temporally variant block decomposition in which the load imbalance problem is resolved by an irregularly portioned Lagrangian Monte Carlo solver (IPLMC) [118–120]. In this implementation, FDF employs MPI for inter-domain communication, and can scale up to 1000 s of segments via the adaptive partitioning [11, 118–122]. Tabulation of kinetic reactions via situ adaptive tabulation (ISAT) [123, 124] continues to be of significant importance in implementation of FDF methods. In 2013, ISAT was adapted to accelerate heterogeneous chemistry for transient simulations coupled with commercial CFD package ANSYS Fluent [125]. Contino et al. [126] propose a modification of ISAT to decrease the number of queries, resulting to have a retrieving process for a wide range of thermochemical conditions. More recently, Xie et al. [127] propose a dynamic adaptive acceleration method, in which ISAT or dynamic adaptive chemistry (DAC) is dynamically selected for chemistry integration based on the encountered composition inhomo-

geneity. These are particularly important for combustion simulation with unsteady applications such as the one in internal combustion engines. In order to decrease the overall error of the method, Hiremath et al. [128] develop a hybrid ISAT - rate controlled constrained-equilibrium (RCCE) method. Kumar and Mazumdar [129] introduce a variation of ISAT to consider the effect of surface reaction. Fooladgar et al. [130] present an efficient kinetic reaction solver using ISAT and an open source kinetic reaction package, Cantera [131] in OpenFOAM [132]. This will remove the dependence of ISAT to commercial chemical kinetic tool Chemkin II [133].

High-order CFD discretization schemes are gradually being introduced in FDF computations. An example of recent work is the use of discontinuous-Galerkin (DG) method coupled with the Lagrangian MC solver [134]. The hybrid methodology has shown to be particularly suitable for LES, as a larger portion of the resolved energy is captured with increase of the order of spectral approximation. Work is also in progress towards developments of spectral-element methods in hybrid MC simulations [135]. Associated with computational modeling is the accuracy and reliability of the simulated results. Some issues pertaining to resolution requirements of the FDF are discussed in Refs. [134, 136–141]. The primary objective of these studies is to examine the convergence of PDF/FDF to DNS by fine tuning the mesh size and LES filter width. Parallel to these are the sensitivity analysis [39, 40] and uncertainty quantification of PDF/FDF simulated results [142, 143]. Significant future work is expected in this regard. Adaptive mesh refinement (AMR) methods have also been successfully developed and have proven effective for FDF computations [62]. This is very encouraging as it facilitates the use of FDF for LES of complex flows.

Finally, for "futuristic" FDF/PDF computations, Xu et al. [144, 145] demonstrate that significant speed-up can be achieved via the use of "quantum computing" (QC). They demonstrate that the quantum algorithm provides a quadratic speedup over classical Monte Carlo methods in solving the PDF via the coalescence/dispersion model. More studies of this type are needed as QC seems to be more of a reality than fiction [146].

3 Simulations and Practical Applications

Within the past decade, there has been a noticeable surge in the implementation of FDF for a variety of LES predictions. The objective of these simulations is two-fold: (1) to appraise the performance of the various sub-closures in FDF, and (2) to understand some of the issues pertaining to turbulence and its interactions with chemistry.

FDF validation and assessment via comparison with laboratory data have been the subject of broad investigations in various flow configurations, such as premixed flames [83, 147–152], non-premixed flames [153–158], partially premixed flames [159–162], temporally and spatially developing mixing layers [163–165], turbulent jet flames [28, 166–174], and bluff-body stabilized flames [80, 175–178]. An example of the LES-FDF predictions of a swirling flame [179] is shown in Fig. 1. These

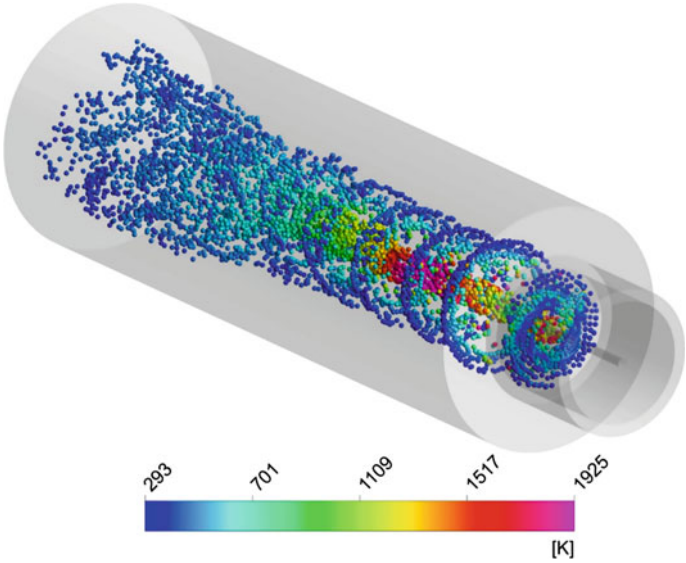

Fig. 1 Distribution of a fraction of fluid particles depicting swirl in Sydney swirl burner [179]. The particles are colored by temperature. Flow direction is from right to left. Reprinted from Ref. [30] with permission of the authors

results from Ref. [30] demonstrates the transport of the Lagrangian MC particles due to turbulence, and how such transport captures the dynamics of turbulence-chemistry interactions.

For spray combustion modeling and simulations, the focus is on the carrier-phase [27, 28, 77, 78, 81, 87, 91, 180–187], and the gas particles such as soot and coal [76, 188–196]. As an example, recently Wen et al. [189] develop a Lagrangian framework to track pulverized coal particles. Figure 2 shows the comparison of the velocity-FDF and the velocity-scalar joint FDF in predicting the droplet's axial mean velocity of an evaporating two-phase spray. The FDF is also employed to predict the droplet distribution in a turbulent methanol spray flame. The predictions are in good agreement with experimental data as shown in Fig. 3.

Due to its demonstrated capabilities, the PDF/FDF is being steadily built into commercial software and packages. As examples of computer codes currently in use are the ANSYS Fluent [197–200], the Siemens [201] in Ref. [202], the OpenFoam [132] in Refs. [97, 148, 203–205], and most recently the Nektar++ spectral/hp element [206, 207] in Ref. [135]. As an example of the the ANSYS/Fluent generated results, Fig. 4 show the iso-surface of the axial vorticity surrounded by velocity streamlines colored with the temperature for Delft jet in hot coflow burner [200]. These results are in excellent agreement with laboratory data. Another example based on the Open-Foam/FDF simulations in Figs. 5 and 6, in which the simulations capture many features of laboratory flames (Sandia flames D and H) [97, 204].

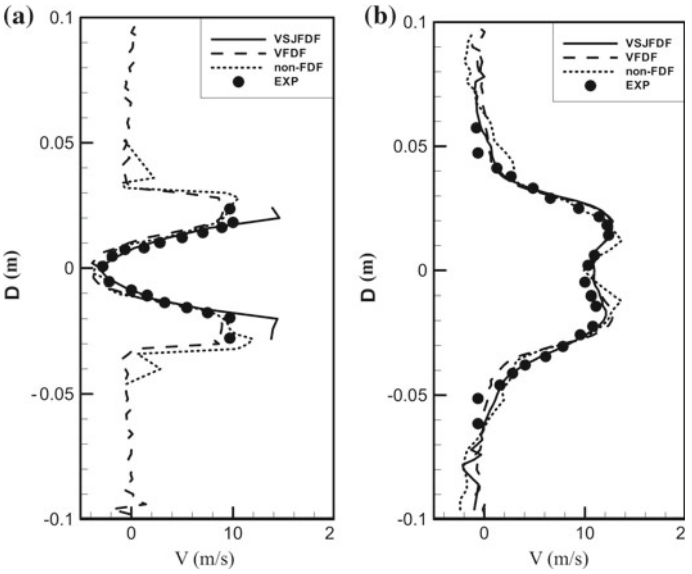

Fig. 2 Comparison of the droplets' axial mean velocity of an evaporating two-phase spray flow between numerical results and experimental data. **a** $x = 25$ and **b** $x = 100$. Here VSJFDF and VFDF represent velocity-scalar joint filtered density function and velocity filtered density function respectively. Reprinted from Ref. [180] with permission of the authors

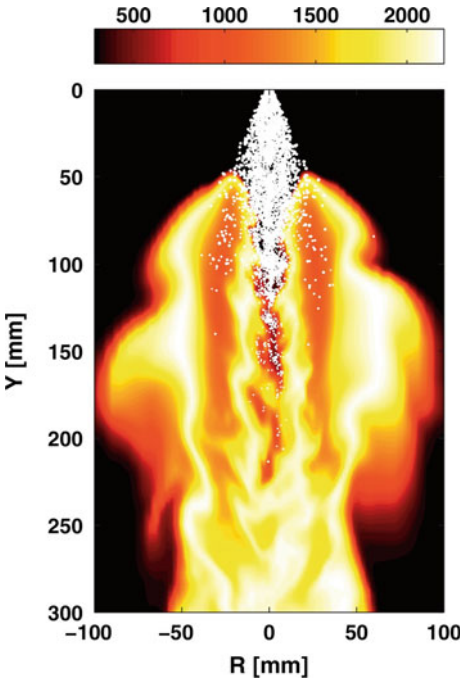

Fig. 3 A contour plot of the instantaneous gas-phase temperature with the reacting spray on turbulent methanol/air spray flame at the University of California, Irvine Combustion Laboratory. Reprinted from Ref. [181] with permission of the authors

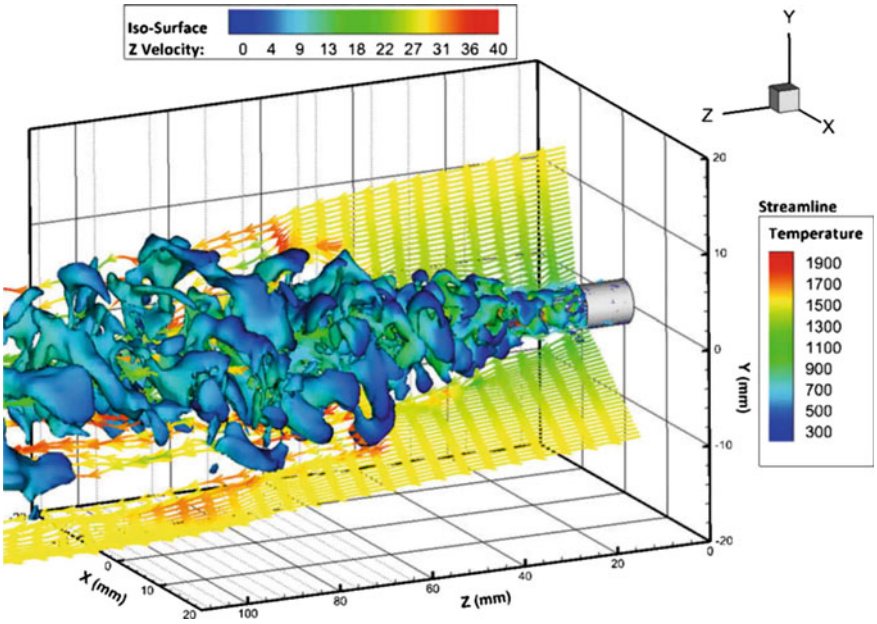

Fig. 4 Snapshot of the iso-surface of the axial vorticity colored with the axial velocity (m/s) surrounded by velocity streamlines colored with temperature for Delft jet in hot coflow burner. Reprinted from Ref. [200] with permission of the authors

Finally, some of the most recent implementation of FDF for predictions of practical (engineering) flows are LES of a rapid compression machine [208], a dump combustor with sudden expansion configuration (common for the jet engines and ramjet engines) [209–211], internal combustion engines [212, 213], oxy-natural gas combustion [214], and swirl combustors [30, 84, 85, 215–219].

4 Concluding Remarks

Thirty years after its conception, it is obvious that the FDF has successfully passed the test of time. The LES via FDF has proven very effective for reactive turbulent flow simulations, hence it is widely adopted in commercial software, as well as industry and government CFD codes. Because of this wide visibility, the method is now covered in modern textbooks in turbulence and combustion, and it usually has its own session at most conferences in these disciplines.

At this point, it is constructive to make some suggestions for future work pertaining to FDF:

- Accurate modeling of the SGS mixing term remains a challenge for FDF closure. Significant progress has been made in this regard, but more work is needed

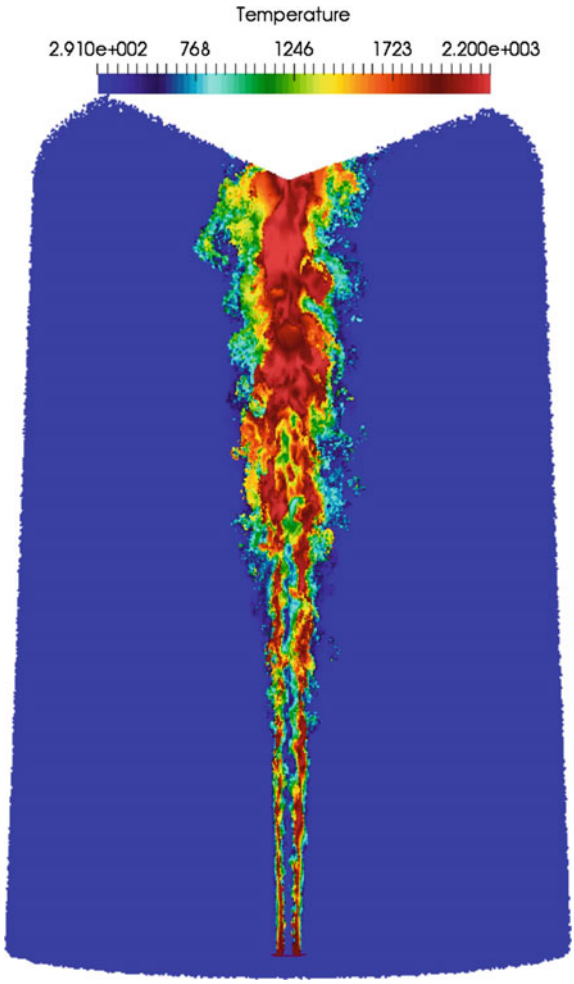

Fig. 5 3D plot of Lagrangian particles in the Sandia flame D simulations. Reprinted from Ref. [204] with permission of the authors

for developing models which can be trusted in various regimes of turbulent combustion.

- Much work remains to be done in improvements of the FDF for LES of multi-phase flows. This is needed to facilitate LES of practical combustors.
- More work is needed to have FDF implemented in high-order, unstructured CFD codes. Recent work in the development of discontinuous Galerkin and spectral-element codes has been very useful to allow LES-FDF of complex flows.
- A very large majority of the cases, the models in current use are based on FDF of the scalar compositions only. The joint velocity-scalar FDF should be more widely considered, so that the effects of SGS-convection can be more accurately modeled.

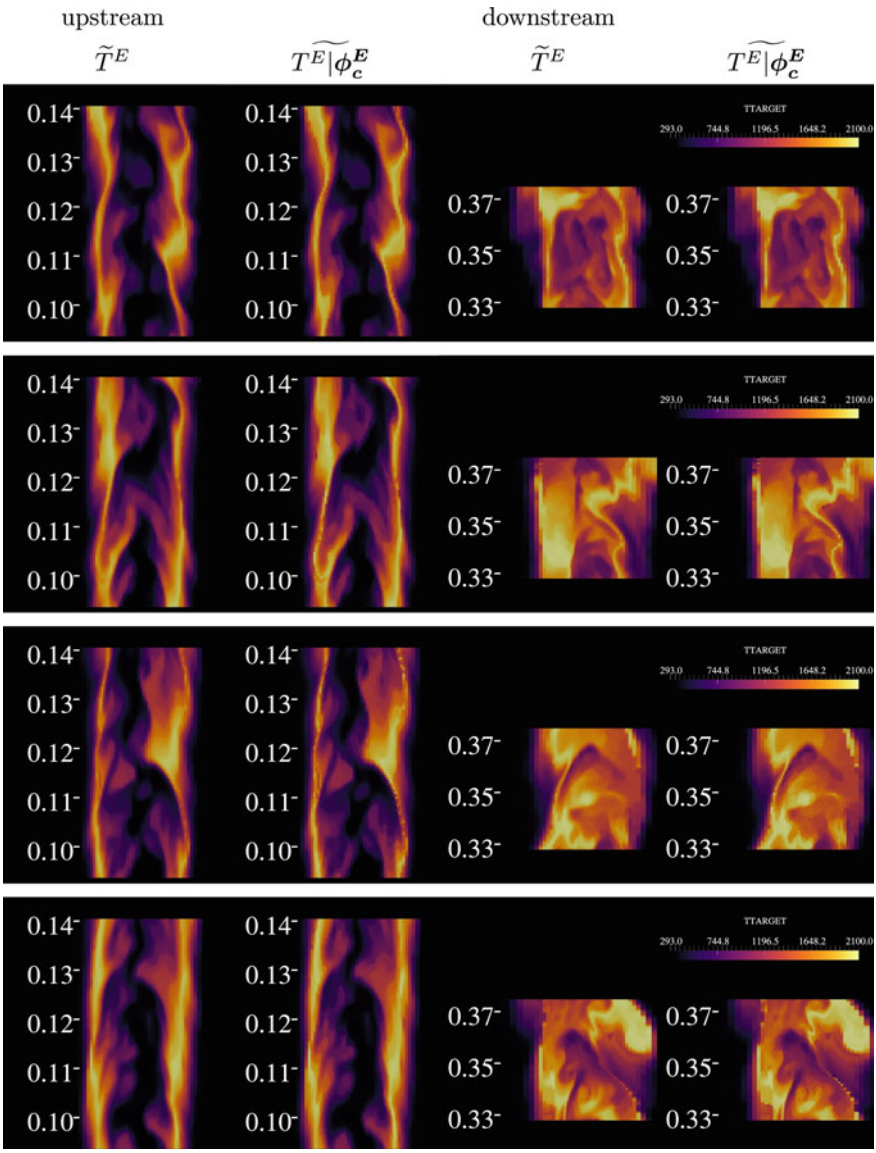

Fig. 6 Temperature fields in Sandia flame H at four different time steps (top to bottom) and two different axial zones. $\widetilde{T}^E$: Eulerian temperature, $\widetilde{T^E|\phi_c^E}$: smoothed Lagrangian temperature. Reprinted from Ref. [97] with permission of the authors

- Related to the previous item, modeling of the SGS viscous and pressure terms (similar to SGS mixing) need much more scrutiny.
- Parallel to the last three items, there is a need for developments of near-wall FDF closures. We are not aware of any significant work on this subject.
- As we move towards exascale computing, the use of GPU for FDF should be widely considered. Preliminary work in this regard shows a tremendous speed-up [220].
- Hybrid PDF-FDF methods [221] could be more broadly investigated to facilitate their use for hybrid Reynolds averaged Navier-Stokes (RANS)-LES predictions of large scale practical flows.
- At this present era of big-data, a combination of physics-based modeling and data-driven closure strategy is expected could prove to be effective. Preliminary work in this regard appears very promising [222].
- Finally, as we anticipate to reach the era of "quantum supremacy", it is suggested to think of relevant problems in PDF/FDF computation that can benefit from the use of algorithms that exhibit quantum speed-up.

Obviously, the FDF is here to stay. Therefore, it will surely benefit from all of the expected developments in all of the constituents of reactive flow modeling and simulation: numerical algorithms, computing platforms, discretization schemes, chemical kinetics, transport phenomena and more. The rate of progress within the past decade has been encouraging and growth within the next decade is expected to be even more glorious.

Acknowledgements The work at Pitt is part of an effort sponsored by the U.S. National Science Foundation, under Grant CBET-1603131 and Grant CBET-1609120. Computational resources are provided by the Center for Research Computing at Pitt. The work at Tsinghua is supported by the National Natural Science Foundation of China Grant 91841302.

References

1. P. Givi, Model free simulations of turbulent reactive flows. Prog. Energ. Combust. **15**, 1–107 (1989)
2. S.B. Pope, Computations of turbulent combustion: Progress and challenges. Proc. Combust. Inst. **23**, 591–612 (1990)
3. F. Gao, E.E. O'Brien, A large-eddy simulation scheme for turbulent reacting flows. Phys. Fluids A **5**(6), 1282–1284 (1993)
4. C.K. Madnia, P. Givi, Direct numerical simulation and large eddy simulation of reacting homogeneous turbulence, in *Large Eddy Simulations of Complex Engineering and Geophysical Flows*, vol. 5, Chap 15, ed. by B. Galperin, S.A. Orszag, (Cambridge University Press, Cambridge, 1993), pp. 315–346
5. S.H. Frankel, V. Adumitroaie, C.K. Madnia, P. Givi, Large eddy simulations of turbulent reacting flows by assumed PDF methods, in *Engineering Applications of Large Eddy Simulations*, FED-Vol. 162, ed. by S.A. Ragab, U. Piomelli (ASME, New York, NY, 1993), pp. 81–101
6. Seventeenth international conference on numerical combustion https://nc19.itv.rwth-aachen.de/ (2019)

7. P. Givi, Filtered density function for subgrid scale modeling of turbulent combustion. AIAA J. **44**(1), 16–23 (2006)
8. D.C. Haworth, Progress in probability density function methods for turbulent reacting flows. Prog. Energ. Combust. **36**(2), 168–259 (2010)
9. N. Ansari, F.A. Jaberi, M.R.H. Sheikhi, P. Givi, Filtered density function as a modern CFD tool, in *Engineering Applications of Computational Fluid Dynamics*, vol. 1, Chap. 1, ed. by A.R.S. Maher (International Energy and Environment Foundation, 2011), pp. 1–22
10. S.B. Pope, Small scales, many species and the manifold challenges of turbulent combustion. Proc. Combust. Inst. **34**(1), 1–31 (2013)
11. S.L. Yilmaz, N. Ansari, P.H. Pisciuneri, M.B. Nik, C.C. Otis, P. Givi, Applied filtered density function. J. Appl. Fluid Mech. **6**(3), 311–320 (2013)
12. Z. Ren, Z. Lu, L. Hou, L. Lu, Numerical simulation of turbulent combustion: Scientific challenges. Sci. China Phys., Mech. **57**, 1495–1503 (2014)
13. R.S. Miller, J.W. Foster, Survey of turbulent combustion models for large-eddy simulations of propulsive flowfields. AIAA J. **54**(10), 2930–2946 (2016)
14. P.J. Colucci, F.A. Jaberi, P. Givi, S.B. Pope, Filtered density function for large eddy simulation of turbulent reacting flows. Phys. Fluids **10**, 499–515 (1998)
15. F.A. Jaberi, P.J. Colucci, S. James, P. Givi, S.B. Pope, Filtered mass density function for large eddy simulation of turbulent reacting flows. J. Fluid Mech. **401**, 85–121 (1999)
16. A. Banaeizadeh, Z. Li, F.A. Jaberi, Compressible scalar filtered mass density function model for high-speed turbulent flows. AIAA J. **49**(10), 2130–2143 (2011)
17. L.Y.M. Gicquel, P. Givi, F.A. Jaberi, S.B. Pope, Velocity filtered density function for large eddy simulation of a turbulent mixing layer, in *DNS/LES-Progress and Challenges*, ed. by C. Liu, L. Sakell, R. Herklotz (Greyden Press, Columbus, OH, 2001), pp. 327–334
18. L.Y.M. Gicquel, P. Givi, F.A. Jaberi, S.B. Pope, Velocity filtered density function for large eddy simulation of turbulent flows. Phys. Fluids **14**(3), 1196–1213 (2002)
19. M.R.H. Sheikhi, T.G. Drozda, P. Givi, S.B. Pope, Velocity-scalar filtered density function for large eddy simulation of turbulent flows. Phys. Fluids **15**(8), 2321–2337 (2003)
20. M.R.H. Sheikhi, P. Givi, S.B. Pope, Frequency-velocity-scalar filtered mass density function for large eddy simulation of turbulent flows. Phys. Fluids **21**(7), 075102 1–14 (2009)
21. M. Safari, M.R.H. Sheikhi, M. Janbozorgi, H. Metghalchi, Entropy transport equation in large eddy simulation for exergy analysis of turbulent combustion systems. Entropy **12**(3), 434–444 (2010)
22. M.R.H. Sheikhi, M. Safari, H. Metghalchi, Large eddy simulation for local entropy generation analysis of turbulent flows. J. Energ. Resour.-ASME **134**(4), 041603 (2012)
23. M.R.H. Sheikhi, M. Safari, F. Hadi, Entropy filtered density function for large eddy simulation of turbulent flows. AIAA J. **53**(9), 2571–2587 (2015)
24. M. Safari, M.R.H. Sheikhi, Large eddy simulation for prediction of entropy generation in a nonpremixed turbulent jet flame. J. Energy Resour.-ASME **136**(2), 022002 (2014)
25. M. Safari, M.R.H. Sheikhi, Large eddy simulation-based analysis of entropy generation in a turbulent nonpremixed flame. Energy **78**, 451–457 (2014)
26. A.G. Nouri, M.B. Nik, P. Givi, D. Livescu, S.B. Pope, Self-contained filtered density function. Phys. Rev. Fluids **2**(9), 094603 (2017)
27. Z. Li, A. Banaeizadeh, F.A. Jaberi, Two-phase filtered mass density function for LES of turbulent reacting flows. J. Fluid Mech. **760**, 243–277 (2014)
28. A. Irannejad, F.A. Jaberi, Large eddy simulation of turbulent spray combustion. Combust. Flame **162**, 431–450 (2015)
29. K.K. Kuo, R. Acharya, *Fundamentals of Turbulent and Multi-Phase Combustion* (Wiley, Hoboken, NJ, 2012)
30. N. Ansari, P.H. Pisciuneri, P.A. Strakey, P. Givi, Scalar-filtered mass-density-function simulation of swirling reacting flows on unstructured grids. AIAA J. **50**(11), 2476–2482 (2012)
31. R. McDermott, S.B. Pope, A particle formulation for treating differential diffusion in filtered density function methods. J. Comput. Phys. **226**, 947–993 (2007)

32. S. Viswanathan, S.B. Pope, Turbulent dispersion from line sources in grid turbulence. Phys. Fluids **20**(10), 101514 (2008)
33. Z. Ren, M. Kuron, X. Zhao, T. Lu, E. Hawkes, H. Kolla, J.H. Chen, Micromixing models for PDF simulations of turbulent premixed flames. Combust. Sci. Technol. **191**(8), 1430–1455 (2019)
34. E.S. Richardson, J.H. Chen, Application of PDF mixing models to premixed flames with differential diffusion. Combust. Flame **159**, 2398–2414 (2012)
35. M. Kuron, Z. Ren, E.R. Hawkes, H. Zhou, H. Kolla, J.H. Chen, T. Lu, A mixing timescale model for TPDF simulations of turbulent premixed flames. Combust. Flame **177**, 171–183 (2017)
36. M. Kuron, E.R. Hawkes, Z. Ren, J.C. Tang, H. Zhou, J.H. Chen, T. Lu, Performance of transported PDF mixing models in a turbulent premixed flame. Proc. Combust. Inst. **36**(2), 1987–1995 (2017)
37. S.B. Pope, A model for turbulent mixing based on shadow-position conditioning. Phys. Fluids **25**(11), 110803 (2013)
38. Z. Ren, S.B. Pope, An investigation of the performance of turbulent mixing models. Combust. Flame **136**(1–2), 208–216 (2004)
39. Z. Ren, S.B. Pope, Sensitivity calculations in PDF modelling of turbulent flames. Proc. Combust. Inst. **32**(1), 1629–1637 (2009)
40. H. Zhou, S. Li, Z. Ren, D.H. Rowinski, Investigation of mixing model performance in transported PDF calculations of turbulent lean premixed jet flames through Lagrangian statistics and sensitivity analysis. Combust. Flame **181**, 136–148 (2017)
41. S. Viswanathan, H. Wang, S.B. Pope, Numerical implementation of mixing and molecular transport in LES/PDF studies of turbulent reacting flows. J. Comput. Phys. **230**, 6916–6957 (2011)
42. J.S. Miles, T. Echekki, A one-dimensional turbulence-based closure model for combustion LES. Combust. Sci. Technol. **192**(1), 78–111 (2020)
43. S. Liu, C. Tong, Subgrid-scale mixing of mixture fraction, temperature, and species mass fractions in turbulent partially premixed flames. Proc. Combust. Inst. **34**(1), 1231–1239 (2013)
44. H. Zhou, Z. Ren, M. Kuron, T. Lu, J.H. Chen, Investigation of reactive scalar mixing in transported PDF simulations of turbulent premixed methane-air Bunsen flames. Flow Turbul. Combust. **103**(3), 667–697 (2019)
45. J. Zhang, F. Gao, G. Jin, G. He, Conditionally statistical description of turbulent scalar mixing at subgrid-scales. Flow Turbul. Combust. **93**, 125–140 (2014)
46. M. Rieth, J.-Y. Chen, S. Menon, A.M. Kempf, A hybrid flamelet finite-rate chemistry approach for efficient LES with a transported FDF. Combust. Flame **199**, 183–193 (2019)
47. J. Park, T. Echekki, LES-ODT study of turbulent premixed interacting flames. Combust. Flame **159**(2), 609–620 (2012)
48. E.D. Gonzalez-Juez, R.C. Schmidt, A.R. Kerstein, ODTLES simulations of wall-bounded flows. Phys. Fluids **23**(12), 125102 (2011)
49. A.R. Kerstein, One-dimensional turbulence: Model formulation and application to homogeneous turbulence, shear flows, and buoyant stratified flows. J. Fluid Mech. **392**, 277–334 (1999)
50. M.B. Nik, P. Givi, C.K. Madnia, S.B. Pope, EPVS-FMDF for LES of high-speed turbulent flows, in *50th AIAA Aerospace Sciences Meeting including the New Horizons Forum and Aerospace Exposition* (Nashville, TN), pp. 1–12, AIAA, 2012. AIAA-2012-117
51. T.G. Drozda, J.R. Quinlan, P.H. Pisciuneri, S.L. Yilmaz, Progress toward affordable high fidelity combustion simulations for high-speed flows in complex geometries, in *48th AIAA/ASME/SAE/ASEE Joint Propulsion Conference & Exhibit*, (Atlanta, GA), pp. 1–16, AIAA, 2012. AIAA-2012-4264
52. N. Padmanabhan, R.S. Miller, Assessment of subgrid scale mixing models used in LES at high pressures. J. Turbul. **19**(8), 683–715 (2018)
53. L. Zhang, J. Liang, M. Sun, H. Wang, Y. Yang, An energy-consistency-preserving large eddy simulation-scalar filtered mass density function (LES-SFMDF) method for high-speed flows. Combust. Theor. Model. **22**(1), 1–37 (2018)

54. H. Koo, P. Donde, V. Raman, LES-based Eulerian PDF approach for the simulation of scramjet combustors. Proc. Combust. Inst. **34**(2), 2093–2100 (2013)
55. C. Otis, P. Ferrero, S.L. Yilmaz, G. Candler, P. Givi, SFMDF in US3D for LES of compressible flows on unstructured meshes, in *48th AIAA/ASME/SAE/ASEE Joint Propulsion Conference & Exhibit* (American Institute of Aeronautics and Astronautics, 2012)
56. S. Sammak, A.G. Nouri, M.J. Brazell, D.J. Mavriplis, P. Givi, Discontinuous Galerkin-Monte Carlo solver for large eddy simulation of compressible turbulent flows, in *55th AIAA Aerospace Sciences Meeting*, (Grapevine, TX), pp. 1–13, AIAA, 2017. AIAA-2017-0982
57. Y.P. de Almeida, S. Navarro-Martinez, Large eddy simulation of a supersonic lifted flame using the Eulerian stochastic fields method. Proc. Combust. Inst. **37**(3), 3693–3701 (2019)
58. J.P. Drummond, Methods for prediction of high-speed reacting flows in aerospace propulsion. AIAA J. **52**, 465–485 (2014)
59. H. Möbus, P. Gerlinger, D. Brüggemann, Comparison of Eulerian and Lagrangian Monte Carlo PDF methods for turbulent diffusion flames. Combust. Flame **124**(3), 519–534 (2001)
60. Y. Pei, E.R. Hawkes, M. Bolla, S. Kook, G.M. Goldin, Y. Yang, S.B. Pope, S. Som, An analysis of the structure of an n-dodecane spray flame using TPDF modelling. Combust. Flame **168**, 420–435 (2016)
61. Y. Yang, J. You, M. Sun, Modeling of turbulence-chemistry interactions in numerical simulations of supersonic combustion. Acta Aeronaut. Astronaut. Sin. **36**, 261–273 (2015)
62. M.M.R. Damasceno, J.G. de Freitas Santos, J.M. Vedovoto, Simulation of turbulent reactive flows using a FDF methodology–Advances in particle density control for normalized variables. Comput. Fluids **170**, 128–140 (2018)
63. P. Wang, F. Zieker, R. Schießl, N. Platova, J. Fröhlich, U. Maas, Large eddy simulations and experimental studies of turbulent premixed combustion near extinction. Proc. Combust. Inst. **34**(1), 1269–1280 (2013)
64. P. Donde, V. Raman, M.E. Mueller, H. Pitsch, LES/PDF based modeling of soot-turbulence interactions in turbulent flames. Proc. Combust. Inst. **34**(1), 1183–1192 (2013)
65. M.J. Cernick, S.W. Tullis, M.F. Lightstone, Particle subgrid scale modelling in large-eddy simulations of particle-laden turbulence. J. Turbul. **16**(2), 101–135 (2015)
66. J.M. Mejía, F. Chejne, A. Molina, A. Sadiki, Scalar mixing study at high-Schmidt regime in a turbulent jet flow using large-eddy simulation/filtered density function approach. J. Fluids Eng. **138**(2), 021205 (2016)
67. J.M. Mejía, A. Sadiki, F. Chejne, A. Molina, Transport and mixing in liquid phase using large eddy simulation: A review, in *Numerical Simulation-From Brain Imaging to Turbulent Flows*, Chap. 16, ed. by R. Lopez-Ruiz (IntechOpen, 2016), pp. 399–428
68. H. Wang, P. Zhang, T. Pant, Consistency and convergence of Eulerian Monte Carlo field method for solving transported probability density function equation in turbulence modeling. Phys. Fluids **30**(11), 115106 (2018)
69. V. Sabel'nikov, O. Soulard, Rapidly decorrelating velocity-field model as a tool for solving one-point Fokker-Planck equations for probability density functions of turbulent reactive scalars. Phys. Rev. E **72**(1), 016301 (2005)
70. L. Valiño, A field Monte Carlo formulation for calculating the probability density function of a single scalar in a turbulent flow. Flow Turbul. Combust. **60**(2), 157–172 (1998)
71. D. Fredrich, W. Jones, A. Marquis, Application of the Eulerian subgrid probability density function method in the large eddy simulation of a partially premixed swirl flame. Combust. Sci. Technol. **191**(1), 137–150 (2019)
72. S. Gallot-Lavallée, W. Jones, Large eddy simulation of spray auto-ignition under EGR conditions. Flow Turbul. Combust. **96**(2), 513–534 (2016)
73. W. Jones, M. Jurisch, A. Marquis, Examination of an oscillating flame in the turbulent flow around a bluff body with large eddy simulation based on the probability density function method. Flow Turbul. Combust. **95**(2–3), 519–538 (2015)
74. Y. Xia, D. Laera, W.P. Jones, A.S. Morgans, Numerical prediction of the flame describing function and thermoacoustic limit cycle for a pressurized gas turbine combustor. Combust. Sci. Technol. **191**(5–6), 979–1002 (2019)

75. D. Noh, E. Karlis, S. Navarro-Martinez, Y. Hardalupas, A. Taylor, D. Fredrich, W. Jones, Azimuthally-driven subharmonic thermoacoustic instabilities in a swirl-stabilised combustor. Proc. Combust. Inst. **37**(4), 5333–5341 (2019)
76. D. Noh, S. Gallot-Lavallée, W.P. Jones, S. Navarro-Martinez, Comparison of droplet evaporation models for a turbulent, non-swirling jet flame with a polydisperse droplet distribution. Combust. Flame **194**, 135–151 (2018)
77. W. Jones, A. Marquis, D. Noh, A stochastic breakup model for large eddy simulation of a turbulent two-phase reactive flow. Proc. Combust. Inst. **36**(2), 2559–2566 (2017)
78. S. Gallot-Lavallée, W. Jones, A. Marquis, Large eddy simulation of an ethanol spray flame under MILD combustion with the stochastic fields method. Proc. Combust. Inst. **36**(2), 2577–2584 (2017)
79. T. Brauner, W. Jones, A. Marquis, LES of the cambridge stratified swirl burner using a sub-grid PDF approach. Flow Turbul. Combust. **96**(4), 965–985 (2016)
80. W. Jones, A. Marquis, F. Wang, Large eddy simulation of a premixed propane turbulent bluff body flame using the Eulerian stochastic field method. Fuel **140**, 514–525 (2015)
81. W. Jones, A. Marquis, D. Noh, LES of a methanol spray flame with a stochastic sub-grid model. Proc. Combust. Inst. **35**(2), 1685–1691 (2015)
82. V.N. Prasad, M. Juddoo, A.R. Masri, W.P. Jones, K.H. Luo, Investigation of extinction and re-ignition in piloted turbulent non-premixed methane-air flames using LES and high-speed OH-LIF. Combust. Theor. Model. **17**(3), 483–503 (2013)
83. G. Bulat, W. Jones, A. Marquis, Large eddy simulation of an industrial gas-turbine combustion chamber using the sub-grid PDF method. Proc. Combust. Inst. **34**(2), 3155–3164 (2013)
84. W. Jones, A. Marquis, V. Prasad, LES of a turbulent premixed swirl burner using the Eulerian stochastic field method. Combust. Flame **159**(10), 3079–3095 (2012)
85. W. Jones, S. Lyra, S. Navarro-Martinez, Numerical investigation of swirling kerosene spray flames using large eddy simulation. Combust. Flame **159**(4), 1539–1561 (2012)
86. K. Vogiatzaki, A. Kronenburg, S. Navarro-Martinez, W. Jones, Stochastic multiple mapping conditioning for a piloted, turbulent jet diffusion flame. Proc. Combust. Inst. **33**(1), 1523–1531 (2011)
87. W. Jones, S. Lyra, S. Navarro-Martinez, Large eddy simulation of a swirl stabilized spray flame. Proc. Combust. Inst. **33**(2), 2153–2160 (2011)
88. G. Hauke, L. Valiño, Computing reactive flows with a field Monte Carlo formulation and multi-scale methods. Comput. Methods Appl. M. **193**(15–16), 1455–1470 (2004)
89. R. Mustata, L. Valiño, C. Jiménez, W. Jones, S. Bondi, A probability density function Eulerian Monte Carlo field method for large eddy simulations: Application to a turbulent piloted methane/air diffusion flame (Sandia D). Combust. Flame **145**(1–2), 88–104 (2006)
90. W. Jones, S. Navarro-Martinez, Large eddy simulation of autoignition with a subgrid probability density function method. Combust. Flame **150**(3), 170–187 (2007)
91. J. Minier, S. Chibbaro, S.B. Pope, Guidelines for the formulation of Lagrangian stochastic models for particle simulations of single-phase and dispersed two-phase turbulent flows. Phys. Fluids **26**(11), 113303 (2014)
92. J.-P. Minier, On Lagrangian stochastic methods for turbulent polydisperse two-phase reactive flows. Prog. Energ. Combust. **50**, 1–62 (2015)
93. M.J. Cleary, A.Y. Klimenko, J. Janicka, M. Pfitzner, A sparse-Lagrangian multiple mapping conditioning model for turbulent diffusion flames. Proc. Combust. Inst. **32**(1), 1499–1507 (2009)
94. Y. Ge, M.J. Cleary, A.Y. Klimenko, A comparative study of Sandia flame series (D-F) using sparse-Lagrangian MMC modelling. Proc. Combust. Inst. **34**(1), 1325–1332 (2013)
95. B. Sundaram, A.Y. Klimenko, M.J. Cleary, Y. Ge, A direct approach to generalised multiple mapping conditioning for selected turbulent diffusion flame cases. Combust. Theor. Model. **20**(4), 735–764 (2016)
96. S. Vo, O.T. Stein, A. Kronenburg, M.J. Cleary, Assessment of mixing time scales for a sparse particle method. Combust. Flame **179**, 280–299 (2017)

97. S. Galindo-Lopez, F. Salehi, M. Cleary, A. Masri, G. Neuber, O. Stein, A. Kronenburg, A. Varna, E. Hawkes, B. Sundaram et al., A stochastic multiple mapping conditioning computational model in OpenFOAM for turbulent combustion. Comput. Fluids **172**, 410–425 (2018)
98. Z. Huo, F. Salehi, S. Galindo-Lopez, M.J. Cleary, A.R. Masri, Sparse MMC-LES of a Sydney swirl flame. Proc. Combust. Inst. **37**(2), 2191–2198 (2019)
99. S. Galindo, F. Salehi, M. Cleary, A. Masri, MMC-LES simulations of turbulent piloted flames with varying levels of inlet inhomogeneity. Proc. Combust. Inst. **36**(2), 1759–1766 (2017)
100. P. Zhang, H. Wang, Variance consistent mean shift particle model for treating differential molecular diffusion in transported PDF methods for turbulent reactive flows. Comput. Fluids **170**, 53–76 (2018)
101. F. Sewerin, S. Rigopoulos, An LES-PBE-PDF approach for predicting the soot particle size distribution in turbulent flames. Combust. Flame **189**, 62–76 (2018)
102. F. Sewerin, S. Rigopoulos, An LES-PBE-PDF approach for modeling particle formation in turbulent reacting flows. Phys. Fluids **29**, 105105 (2017)
103. A. Varna, M.J. Cleary, E.R. Hawkes, A multiple mapping conditioning mixing model with a mixture-fraction like reference variable. Part 1: Model derivation and ideal flow test cases. Combust. Flame **181**, 342–353 (2017)
104. A. Varna, M.J. Cleary, E.R. Hawkes, A multiple mapping conditioning mixing model with a mixture-fraction like reference variable. Part 2: RANS implementation and validation against a turbulent jet flame. Combust. Flame **181**, 354–364 (2017)
105. H. Zhou, T. Yang, Z. Ren, Differential diffusion modeling in LES/FDF simulations of turbulent flames. AIAA J. **57**(8), 3206–3212 (2019)
106. M. Cleary, A.Y. Klimenko, A generalised multiple mapping conditioning approach for turbulent combustion. Flow Turbul. Combust. **82**(4), 477 (2009)
107. M.J. Cleary, A.Y. Klimenko, A detailed quantitative analysis of sparse-Lagrangian filtered density function simulations in constant and variable density reacting jet flows. Phys. Fluids **23**(11), 115102 (2011)
108. Y. Ge, M.J. Cleary, A.Y. Klimenko, Sparse-Lagrangian FDF simulations of Sandia flame E with density coupling. Proc. Combust. Inst. **33**(1), 1401–1409 (2011)
109. J. Kim, S.B. Pope, Effects of combined dimension reduction and tabulation on the simulations of a turbulent premixed flame using a large-eddy simulation/probability density function method. Combust. Theor. Model. **18**(3), 388–413 (2014)
110. P.P. Popov, H. Wang, S.B. Pope, Specific volume coupling and convergence properties in hybrid particle/finite volume algorithms for turbulent reactive flows. J. Comput. Phys. **294**, 110–126 (2015)
111. Y. Liang, S.B. Pope, P. Pepiot, A pre-partitioned adaptive chemistry methodology for the efficient implementation of combustion chemistry in particle PDF methods. Combust. Flame **162**(9), 3236–3253 (2015)
112. D.H. Rowinski, S.B. Pope, Computational study of lean premixed turbulent flames using RANS-PDF and LES-PDF methods. Combust. Theor. Model. **17**, 610–656 (2013)
113. I.A. Dodoulas, S. Navarro-Martinez, Large eddy simulation of premixed turbulent flames using the probability density function approach. Flow Turbul. Combust. **90**, 645–678 (2013)
114. V. Raman, H. Pitsch, R.O. Fox, Hybrid large-eddy simulation/Lagrangian filtered-density-function approach for simulating turbulent combustion. Combust. Flame **143**, 56–78 (2005)
115. J. You, Y. Yang, S.B. Pope, Effects of molecular transport in LES/PDF of piloted turbulent dimethyl ether/air jet flames. Combust. Flame **176**, 451–461 (2017)
116. V. Hiremath, S.R. Lantz, H. Wang, S.B. Pope, Computationally-efficient and scalable parallel implementation of chemistry in simulations of turbulent combustion. Combust. Flame **159**, 3096–3109 (2012)
117. V. Hiremath, S.R. Lantz, H. Wang, S.B. Pope, Large-scale parallel simulations of turbulent combustion using combined dimension reduction and tabulation of chemistry. Proc. Combust. Inst. **34**, 205–215 (2013)

118. S.L. Yilmaz, M.B. Nik, M.R.H. Sheikhi, P.A. Strakey, P. Givi, An irregularly portioned Lagrangian Monte Carlo method for turbulent flow simulation. J. Sci. Comput. **47**, 109–125 (2011)
119. S.L. Yilmaz, P.H. Pisciuneri, P. Givi, Towards petascale large eddy simulation of reacting flow, in *Seventh International Conference on Computational Fluid Dynamics (ICCFD7)* (Big Island, Hawaii) 2012. ICCFD7-2704
120. P.H. Pisciuneri, S.L. Yilmaz, P.A. Strakey, P. Givi, An irregularly portioned FDF simulator. SIAM J. Sci. Comput. **35**(4), C438–C452 (2013)
121. P.H. Pisciuneri, S.L. Yilmaz, P.A. Strakey, P. Givi, Massively parallel FDF simulation of turbulent reacting flows, in *Stochastic Equations for Complex Systems: Theoretical and Computational Topics* (Mathematical Engineering), Chap. 8, ed. by S. Heinz, H. Bessaih (Springer, Berlin, 2015), pp. 175–192
122. A. Maries, T. Luciani, P.H. Pisciuneri, M.B. Nik, S.L. Yilmaz, P. Givi, G.E. Marai, A clustering method for identifying regions of interest in turbulent combustion tensor fields, in *Visualization and Processing of Higher Order Descriptors for Multi-Valued Data* (Mathematics and Visualization), ed. by I. Hotz, T. Schultz (Springer, Berlin, 2015), pp. 323–338
123. S.B. Pope, Computationally efficient implementation of combustion chemistry using in situ adaptive tabulation, Tech. Rep. FDA 96-02 (Cornell University, Ithaca, NY, 1996)
124. L. Lu, S.B. Pope, An improved algorithm for in situ adaptive tabulation. J. Comput. Phys. **228**(2), 361–386 (2009)
125. Ansys Fluent Website https://www.ansys.com/products/fluids/ansys-fluent (2019)
126. F. Contino, H. Jeanmart, T. Lucchini, G. D'Errico, Coupling of in situ adaptive tabulation and dynamic adaptive chemistry: An effective method for solving combustion in engine simulations. Proc. Combust. Inst. **33**(2), 3057–3064 (2011)
127. W. Xie, Z. Lu, Z. Ren, G.M. Goldin, Dynamic adaptive acceleration of chemical kinetics with consistent error control. Combust. Flame **197**, 389–399 (2018)
128. V. Hiremath, Z. Ren, S.B. Pope, Combined dimension reduction and tabulation strategy using ISAT-RCCE-GALI for the efficient implementation of combustion chemistry. Combust. Flame **158**(11), 2113–2127 (2011)
129. A. Kumar, S. Mazumder, Adaptation and application of the in situ adaptive tabulation (ISAT) procedure to reacting flow calculations with complex surface chemistry. Comput. Chem. Eng. **35**(7), 1317–1327 (2011)
130. E. Fooladgar, C. Chan, K.-J. Nogenmyr, An accelerated computation of combustion with finite-rate chemistry using LES and an open source library for in-situ-adaptive tabulation. Comput. Fluids **146**, 42–50 (2017)
131. Cantera Website http://cantera.org (2019)
132. OpenFoam Website http://www.openfoam.org (2019)
133. Reaction Design, *CHEMKIN: A Software Package for the Analysis of Gas-Phase Chemical and Plasma Kinetics*, 3.6 edn (2000)
134. S. Sammak, M.J. Brazell, P. Givi, D.J. Mavriplis, A hybrid DG-Monte Carlo FDF simulator. Comput. Fluids **140**(13), 158–166 (2016)
135. A. Aitzhan, S. Sammak, A.G. Nouri, P. Givi, A hybrid spectral-hp element - FDF simulator, in *Modeling and Simulation of Turbulent Mixing and Reaction: For Power, Energy and Flight*, (Buffalo, NY, 2019), pp. 12–13
136. R.R. Tirunagari, S.B. Pope, LES/PDF for premixed combustion in the DNS limit. Combust. Theor. Model. **20**(5), 834–865 (2016)
137. R.R. Tirunagari, S.B. Pope, An investigation of turbulent premixed counterflow flames using large-eddy simulations and probability density function methods. Combust. Flame **166**, 229–242 (2016)
138. M.A. Picciani, E.S. Richardson, S. Navarro-Martinez, Resolution requirements in stochastic field simulation of turbulent premixed flames. Flow Turbul. Combust. **101**, 1103–1118 (2018)
139. A.Y. Klimenko, M.J. Cleary, Convergence to a model in sparse-Lagrangian FDF simulations. Flow Turbul. Combust. **85**, 567–591 (2010)

140. M. Nik, S. Yilmaz, M.R.H. Sheikhi, P. Givi, Grid resolution effects on VSFMDF/LES. Flow Turbul. Combust. **85**(3–4), 677–688 (2010)
141. S. Chibbaro, C. Marchioli, M.V. Salvetti, A. Soldati, Particle tracking in LES flow fields: Conditional Lagrangian statistics of filtering error. J. Turbul. **15**, 22–33 (2014)
142. X. Zhao, H. Kolla, P. Zhang, B. Wu, S. Calello, H.N. Najm, A transported probability density function method to propagate chemistry uncertainty in reacting flow CFD, in *57th AIAA Aerospace Sciences Meeting*, (San Diego, CA), pp. 1–12, AIAA, 2019. AIAA-2019-2007
143. W. Ji, Z. Ren, Y. Marzouk, C.K. Law, Quantifying kinetic uncertainty in turbulent combustion simulations using active subspaces. Proc. Combust. Inst. **37**(2), 2175–2182 (2019)
144. G. Xu, A.J. Daley, P. Givi, R.D. Somma, Turbulent mixing simulation via a quantum algorithm. AIAA J. **56**(2), 687–699 (2018)
145. G. Xu, A.J. Daley, P. Givi, R.D. Somma, Quantum algorithm for the computation of the reactant conversion rate in homogeneous turbulence. Combust. Theor. Model. (2019) (in press)
146. E. Grumbling, M. Horowitz (eds.), *Quantum Computing: Progress and Prospects* (National Academies of Sciences, Engineering, and Medicine, Washington, D.C., 2019)
147. S.L. Yilmaz, M.B. Nik, P. Givi, P.A. Strakey, Scalar filtered density function for large eddy simulation of a Bunsen burner. J. Propul. Power **26**(1), 84–93 (2010)
148. H. Turkeri, X. Zhao, S.B. Pope, M. Muradoglu, Large eddy simulation/probability density function simulations of the Cambridge turbulent stratified flame series. Combust. Flame **199**, 24–45 (2019)
149. R.P. Lindstedt, V.D. Milosavljevic, M. Persson, Turbulent burning velocity predictions using transported PDF methods. Proc. Combust. Inst. **33**(1), 1277–1284 (2011)
150. H. Wang, T. Pant, P. Zhang, LES/PDF modeling of turbulent premixed flames with locally enhanced mixing by reaction. Flow Turbul. Combust. **100**, 147–175 (2018)
151. W. Han, V. Raman, Z. Chen, LES/PDF modeling of autoignition in a lifted turbulent flame: Analysis of flame sensitivity to differential diffusion and scalar mixing time-scale. Combust. Flame **171**, 69–86 (2016)
152. H. Wang, P. Zhang, A unified view of pilot stabilized turbulent jet flames for model assessment cross different combustion regimes. Proc. Combust. Inst. **36**(2), 1693–1703 (2017)
153. E. van Vliet, J.J. Derksen, H.E.A. van den Akker, Turbulent mixing in a tubular reactor: Assessment of an FDF/LES approach. AIChE J. **51**(3), 725–739 (2005)
154. M.B. Nik, S.L. Yilmaz, P. Givi, M.R.H. Sheikhi, S.B. Pope, Simulation of Sandia flame D using velocity-scalar filtered density function. AIAA J. **48**, 1513–1522 (2010)
155. S. James, J. Zhu, M.S. Anand, Large eddy simulation of turbulent flames using the filtered density function model. Proc. Combust. Inst. **31**, 1737–1745 (2007)
156. M.R.H. Sheikhi, T.G. Drozda, P. Givi, F.A. Jaberi, S.B. Pope, Large eddy simulation of a turbulent nonpremixed piloted methane jet flame (Sandia flame D). Proc. Combust. Inst. **30**, 549–556 (2005)
157. I.A. Dodoulas, S. Navarro-Martinez, Analysis of extinction in a non-premixed turbulent flame using large eddy simulation and the chemical explosion mode analysis. Combust. Theo. Model. **19**(1), 107–129 (2015)
158. H. Wang, S.B. Pope, Large eddy simulation/probability density function modeling of a turbulent $CH_4/H_2/N_2$ jet flame. Proc. Combust. Inst. **33**(1), 1319–1330 (2011)
159. V. Raman, H. Pitsch, A consistent LES/filtered-density function formulation for the simulation of turbulent flames with detailed chemistry. Proc. Combust. Inst. **31**, 1711–1719 (2007)
160. N. Kim, K. Jung, Y. Kim, Large eddy simulation of piloted turbulent jet flames using the multi-environment PDF model based on the flamelet generated manifold. J. Mech. Sci. Technol. **32**, 2399–2406 (2018)
161. C. Yu, F. Minuzzi, U. Maas, Numerical simulation of turbulent flames based on a hybrid RANS/transported-PDF method and REDIM method. Eurasian Chem. Technol. J. **20**(1), 23–31 (2018)
162. W.P. Jones, V.N. Prasad, Large eddy simulation of the Sandia flame series (D-F) using the Eulerian stochastic field method. Combust. Flame **157**(9), 1621–1636 (2010)

163. C. Siklawi, R. Milane, Numerical prediction of isothermally reacting mixing layer using vortex-in-cell and filtered density function. Int. J. Numer. Meth. Flow. **66**(12), 1572–1586 (2011)
164. X.Y. Zhou, J.C.F. Pereira, Large eddy simulation (2D) of a reacting plane mixing layer using filtered density function. Flow Turbul. Combust. **64**, 279–300 (2000)
165. A. Innocenti, C. Marchioli, S. Chibbaro, Lagrangian filtered density function for LES-based stochastic modelling of turbulent particle-laden flows. Phys. Fluids **28**(11), 115106 (2016)
166. D. Wang, C. Tong, Conditionally filtered scalar dissipation, scalar diffusion, and velocity in a turbulent jet. Phys. Fluids **14**(7), 2170–2185 (2002)
167. A.G. Rajagopalan, C. Tong, Experimental investigation of scalar-scalar-dissipation filtered joint density function and its transport equation. Phys. Fluids **15**, 227–244 (2003)
168. W.P. Jones, V.N. Prasad, LES-PDF simulation of a spark ignited turbulent methane jet. Proc. Combust. Inst. **33**(1), 1355–1363 (2011)
169. H. Wang, S.B. Pope, LES/PDF studies of turbulent premixed jet flames, in *Fall Technical Meeting of the Eastern States Section of the Combustion Institute 2011* (Storrs, CT), pp. 1–8 (2011)
170. C. Le Ribault, S. Simoens, I. Vinkovic, Hybrid large eddy simulation/Lagrangian stochastic model for turbulent passive and reactive scalar dispersion in a plane jet. Chem. Eng. Commun. **199**(4), 435–460 (2012)
171. Y. Yang, H. Wang, S.B. Pope, J.H. Chen, Large-eddy simulation/probability density function modeling of a non-premixed CO/H_2 temporally evolving jet flame. Proc. Combust. Inst. **34**(1), 1241–1249 (2013)
172. P. Zhang, A.R. Masri, H. Wang, Studies of the flow and turbulence fields in a turbulent pulsed jet flame using LES/PDF. Combust. Theor. Model. **21**(5), 897–924 (2017)
173. M. Esmaeili, A. Afshari, F.A. Jaberi, Large-eddy simulation of turbulent mixing of a jet in cross-flow. J. Eng. Gas Turb. Power **137**(9), 091510 (2015)
174. H. Wang, H. Zhou, Z. Ren, C.K. Law, Transported PDF simulation of turbulent CH_4/H_2 flames under mild conditions with particle-level sensitivity analysis. Proc. Combust. Inst. **37**(4), 4487–4495 (2019)
175. M. Muradoglu, K. Liu, S.B. Pope, PDF modeling of a bluff-body stabilized turbulent flame. Combust. Flame **132**, 115–137 (2003)
176. W. Zhao, C. Zhang, C. Chen, Large eddy simulation of bluff-body stabilized flames using a multi-environment filtered density function model. Proc. Combust. Inst. **33**(1), 1347–1353 (2011)
177. S. Nambully, P. Domingo, V. Moureau, L. Vervisch, A filtered-laminar-flame PDF sub-grid scale closure for LES of premixed turbulent flames. Part I: Formalism and application to a bluff-body burner with differential diffusion. Combust. Flame **161**, 1756–1774 (2014)
178. P.P. Popov, S.B. Pope, Large eddy simulation/probability density function simulations of bluff body stabilized flames. Combust. Flame **161**, 3100–3133 (2014)
179. University of Sydney, Thermal Research Group Website, Swirl Flows and Flames Database http://web.aeromech.usyd.edu.au/thermofluids/database.php (2019)
180. X. Wen, H. Jin, K. Sun, J. Fan, Numerical investigation of droplet evaporation and transport in a turbulent spray with LES/VSJFDF model. Chem. Eng. Sci. **119**, 251–260 (2014)
181. W.P. Jones, A.J. Marquis, D. Noh, An investigation of a turbulent spray flame using large eddy simulation with a stochastic breakup model. Combust. Flame **186**, 277–298 (2017)
182. W.P. Jones, A. Tyliszczak, Large eddy simulation of spark ignition in a gas turbine combustor. Flow Turbul. Combust. **85**(3–4), 711–734 (2010)
183. H. Jin, S. Song, Y. Chen, C. Wang, J. Fan, Numerical investigation of evaporating isopropyl alcohol spray with LES-FDF model. Fuel **119**, 98–105 (2014)
184. C. Heye, V. Raman, A.R. Masri, Influence of spray/combustion interactions on auto-ignition of methanol spray flames. Proc. Combust. Inst. **35**(2), 1639–1648 (2015)
185. S. Navarro-Martinez, Large eddy simulation of spray atomization with a probability density function method. Int. J. Multiph. Flow **63**, 11–22 (2014)

186. P. Jenny, D. Roekaerts, N. Beishuizen, Modeling of turbulent dilute spray combustion. Prog. Energ. Combust. **38**, 846–887 (2012)
187. J.-P. Minier, Statistical descriptions of polydisperse turbulent two-phase flows. Phys. Rep. **665**, 1–122 (2016)
188. X. Wen, H. Jin, O.T. Stein, J. Fan, K. Luo, Large eddy simulation of piloted pulverized coal combustion using the velocity-scalar joint filtered density function model. Fuel **158**, 494–502 (2015)
189. X. Wen, K. Luo, H. Jin, J. Fan, Large eddy simulation of piloted pulverised coal combustion using extended flamelet/progress variable model. Combust. Theor. Model. **21**(5), 925–953 (2017)
190. M. Rieth, A.G. Clements, M. Rabacal, F. Proch, O.T. Stein, A.M. Kempf, Flamelet LES modeling of coal combustion with detailed devolatilization by directly coupled cpd. Proc. Combust. Inst. **36**(2), 2181–2189 (2017)
191. M. Rieth, F. Proch, A.G. Clements, M. Rabacal, A.M. Kempf, Highly resolved flamelet LES of a semi-industrial scale coal furnace. Proc. Combust. Inst. **36**(3), 3371–3379 (2017)
192. H. Jin, Y. Chen, J. Fan, K. Luo, LES/FDF simulation of a gas-particle backward-facing step flow. Chem. Eng. Sci. **66**, 3692–3700 (2011)
193. H. Jin, Y. Chen, Y. Chen, C. Wang, Numerical simulation of gas-particle dispersion in a backward-facing step flow with LES-FDF model. J. Visual. **15**, 343–352 (2012)
194. X.-Y. Zhao, D.C. Haworth, Transported PDF modeling of pulverized coal jet flames. Combust. Flame **161**(7), 1866–1882 (2014)
195. F. Sewerin, S. Rigopoulos, Algorithmic aspects of the LES-PBE-PDF method for modeling soot particle size distributions in turbulent flames. Combust. Sci. Technol. **191**(5–6), 766–796 (2019)
196. W. Han, V. Raman, M.E. Mueller, Z. Chen, Effects of combustion models on soot formation and evolution in turbulent nonpremixed flames. Proc. Combust. Inst. **37**(1), 985–992 (2019)
197. N. Ansari, G.M. Goldin, M.R.H. Sheikhi, P. Givi, Filtered density function simulator on unstructured meshes. J. Comput. Phys. **230**(19), 7132–7150 (2011)
198. A. Chandy, G.M. Goldin, S.H. Frankel, Modeling turbulent nonpremixed jet flames using Fluent's PDF transport model: Effect of mixing model on flame extinction, in *30th International Symposium on Combustion, Abstracts of Work-In-Progress Posters* (The Combustion Institute, Pittsburgh, PA, 2004), p. 447
199. D.J. Glaze, S.H. Frankel, J.C. Hewson, Non-premixed turbulent jet mixing using LES with the FMDF model, in *30th International Symposium on Combustion, Abstracts of Work-In-Progress Posters* (The Combustion Institute, Pittsburgh, PA, 2004), p. 79
200. R. Bhaya, A. De, R. Yadav, Large eddy simulation of mild combustion using PDF-based turbulence-chemistry interaction models. Combust. Sci. Technol. **186**(9), 1138–1165 (2014)
201. Star-ccm+ Website https://mdx.plm.automation.siemens.com/star-ccm-plus (2019)
202. Y. Zhang, D. Haworth, A general mass consistency algorithm for hybrid particle/finite-volume PDF methods. J. Comput. Phys. **194**(1), 156–193 (2004)
203. R. Mokhtarpoor, H. Turkeri, M. Muradoglu, A new robust consistent hybrid finite-volume/particle method for solving the PDF model equations of turbulent reactive flows. Comput. Fluids **105**, 39–57 (2014)
204. H. Turkeri, S.B. Pope, M. Muradoglu, A LES/PDF simulator on block-structured meshes. Combust. Theor. Model. **23**(1), 1–41 (2019)
205. X. Zhao, D. Haworth, E.D. Huckaby, Transported PDF modeling of nonpremixed turbulent $CO/H_2/N_2$ jet flames. Combust. Sci. Technol. **184**(5), 676–693 (2012)
206. C.D. Cantwell, D. Moxey, A. Comerford, A. Bolis, G. Rocco, G. Mengaldo, D. De Grazia, S. Yakovlev, J.-E. Lombard, D. Ekelschot et al., Nektar++: An open-source spectral/hp element framework. Comput. Phys. Commun. **192**, 205–219 (2015)
207. Nektar++ Website http://www.nektar.info (2019)
208. A.A. Validi, H. Schock, F. Jaberi, Turbulent jet ignition assisted combustion in a rapid compression machine. Combust. Flame **186**, 65–82 (2017)

209. A. Afshari, T. Almeida, K. Mehravaran, F.A. Jaberi, Large scale simulations of turbulent combustion and propulsion systems, in *Proceedings of the Seventeen ONR Propulsion Meeting*, pp. 41–46 (2004)
210. T. Almeida, A. Afshari, F.A. Jaberi, Modeling and large-scale simulations of complex combustion systems, in *Advances in Combustion and Noise Control*, Chap. 35, ed. by G.D. Roy, K.H. Yu, J.H. Whitelaw, J.J. Witton (Cranfield University Press, Cranfield, UK, 2006), pp. 551–564
211. A. Afshari, F.A. Jaberi, T.-H. Shih, Large-eddy simulation of turbulent flows in an axisymmetric dump combustor. AIAA J. **46**(7), 1576–1592 (2008)
212. A. Banaeizadeh, A. Afshari, H. Schock, F.A. Jaberi, Large eddy simulations of turbulent flows in IC engines, in *ASME Paper DETC2008-49788* (American Society of Mechanical Engineers, Brooklyn, NY, 2008)
213. A. Banaeizadeh, A. Afshari, H. Schock, F. Jaberi, Large-eddy simulations of turbulent flows in internal combustion engines. Int. J. Heat Mass Tran. **60**(1), 781–796 (2013)
214. X. Zhao, D. Haworth, T. Ren, M. Modest, A transported probability density function/photon Monte Carlo method for high-temperature oxy-natural gas combustion with spectral gas and wall radiation. Combust. Theor. Model. **17**(2), 354–381 (2013)
215. V. Moureau, P. Domingo, L. Vervisch, From large-eddy simulation to direct numerical simulation of a lean premixed swirl flame: Filtered laminar flame-PDF modeling. Combust. Flame **158**, 1340–1357 (2011)
216. G. Bulat, W.P. Jones, A.J. Marquis, NO and CO Formation in an industrial gas-turbine combustion chamber using LES with the Eulerian sub-grid PDF method. Combust. Flame **161**, 1804–1825 (2014)
217. W.P. Jones, A.J. Marquis, K. Vogiatzaki, Large-eddy simulation of spray combustion in a gas turbine combustor. Combust. Flame **161**, 222–239 (2014)
218. N. Ansari, P.A. Strakey, G. Goldin, P. Givi, Filtered density function simulation of a realistic swirled combustor. Proc. Combust. Inst. **35**(2), 1433–1442 (2015)
219. P. Wang, N.A. Platova, J. Fröhlich, U. Maas, Large eddy simulation of the PRECCINSTA burner. Int. J. Heat Mass Tran. **70**, 486–495 (2014)
220. M. Inkarbekov, A. Aitzhan, S. Sammak, P. Givi, P., A. Kaltayev, GPU accelerated DG-FDF large eddy simulator, in *Bulletin of the American Physical Society*, vol. 62 of *70th Annual Meeting of the APS Division of Fluid Dynamics* (Denver, CO, 2017), p. 412
221. S. Heinz, Unified turbulence models for LES and RANS, FDF and PDF simulations. Theor. Comp. Fluid Dyn. **21**, 99–118 (2007)
222. M. Raissi, H. Babaee, P. Givi, Deep learning of PDF turbulence closure, in *Bulletin of the American Physical Society*, vol. 63 of *71st Annual Meeting of the APS Division of Fluid Dynamics* (Atlanta, GA, 2018), p. 302

Large Eddy Simulations of Flows with Moving Boundaries

Iman Borazjani and Amir Akbarzadeh

Abstract Many important engineering and biological flows involve solid boundaries moving within a fluid at high Reynolds numbers, e.g., pumps, fish swimming, wind/hydrokinetic turbines. Simulating such flows requires dealing with moving boundaries and turbulence, which are two of the main challenges facing numerical methods today in computational fluid dynamics (CFD). In this chapter, the numerical methods that deal with moving boundaries in turbulent flows are reviewed and the recent advances are summarized. Some of the state-of-the-art simulations, their results, and the insights gained about the flow physics are discussed. Finally, some of the future developments, such as developing wall models over moving boundaries, required to advance large eddy simulations (LES) with moving boundaries are discussed.

Keywords Turbulent flow · Large eddy simulation (LES) · Moving boundary · Immersed boundary method · Arbitrary Lagrangian Eulerian

1 Introduction

Turbulent flows with moving boundaries are observed in many applications and such as engineering flows, e.g., rotary flows in turbines and compressors [1, 2], biological flows, e.g., swimming fish [3–5], and atmospheric/geophysical flows, e.g., interaction of ocean waves with the surrounding air [6]. Simulating flows with the combination of turbulence and the motion of boundaries is challenging even to the most advanced numerical methods.

Dealing with turbulence is one of the most difficult problems in fluid mechanics. The source of this difficulty is randomness, time dependency, and three dimen-

I. Borazjani (✉) · A. Akbarzadeh
J. Mike Walker '66 Department of Mechanical Engineering, Texas A&M University, College Station, TX 77843, USA
e-mail: iman@tamu.edu

A. Akbarzadeh
e-mail: amirmahd@tamu.edu

D. Livescu et al. (eds.), *Modeling and Simulation of Turbulent Mixing and Reaction*, Heat and Mass Transfer, https://doi.org/10.1007/978-981-15-2643-5_9

sionality of the flow [7], which has prohibited any simple analytical solution in nearly a century. In order to numerically solve turbulent flows, multiple numerical approaches have been developed. The most popular ones are direct numerical simulation (DNS), large eddy simulation (LES), and Reynolds averaged Navier-Stokes (RANS). Direct numerical simulation is the only method in which turbulence is not modeled but the full Navier-Stokes (N-S) equations are solved. Solving full N-S equations requires resolving the smallest length scale, i.e., the Kolmogorov scale which decreases as $Re^{-3/4}$. Therefore, DNS computational costs increase with Re^3, which limits its applications. Even though the computational power of the supercomputers has increased considerably in recent years, DNS is still restricted to moderate Reynolds numbers. Nevertheless, DNS results are required to tune models, e.g., LES and RANS, for specific applications in which turbulence models have not yet been developed. DNS has been applied to investigate turbulent shear layers [8], turbulent mixing layers [9–11], turbulent reacting flows [12], among others.

Due to the high cost of DNS, different turbulence modelings such as RANS and LES have been introduced. In the RANS modeling, which has the least grid requirement, the Reynolds closure stresses are modeled to solve the Reynolds averaged equations to determine the mean velocity [13]. The Reynolds averaged models can typically be categorized into: (i) turbulent viscosity model, and (ii) Reynolds stress model which is known to be more accurate [7]. Overall, since the RANS modeling is based on calculating the mean velocity, it is not suitable for unsteady flows, e.g., flows over a moving boundary [7], such as flows in turbo machinery applications [14, 15]. Nevertheless, there are many studies which has utilized RANS for turbulence modeling, including simulations of flow over marine propellers [16], wind turbines [17–20], vortex induced vibrations of a circular cylinder [21], flow over a vehicle [22] and sediment entrainment [23].

In LES modeling, the filtered velocity field which represents the large turbulent motion is solved. In fact, the effect of small scales on the large scale motion is modeled, whereas the large motions are solved directly. LES modeling is first introduced by Smagorinsky [24] to model atmospheric flows. Later, based on his model, several LES models were developed, including the dynamic Smagorinsky model [25, 26], the mixed model [27], and the implicit model [28]. To date, the LES modeling has become the most popular approach for simulations of unsteady three dimensional complex flows, e.g., separated flows, geophysical flows, and flows over moving boundaries. Although LES is less expensive than DNS, it is still confined to moderate Reynolds numbers as it is recommended that the filter size should be in the inertial range [7]. On the same note, the other challenge of LES modeling is in wall bounded flows, where a high resolution near the wall is required for capturing the boundary layer. Typically the first grid node for LES should be in the viscous sublayer, whose thickness scales with $(1/Re)$. To determine the velocity of the boundary layer without a high resolution grid, wall functions are employed. The wall functions, generally, obtain the velocity of the boundary layer with an algebraic model which is based on the turbulent boundary layer equation [29, 30]. Nevertheless, it is recognized that the wall functions show only good performance for attached boundary layers, e.g.,

flat channel flow, but the results for flows with separation and reattachment are not satisfactory.

By recent developments of LES and the increase in computational power, LES has become an applicable tool for simulating turbulent flow in complex geometries, particularly flows involving moving boundaries: incompressible flow in pumps with rotating blades at Reynolds numbers between 10^5 and 10^6 [14, 31, 32], compressible flow over an axial rotating fan and impeller [33–35], flow over a vertical axis wind turbine [36–39], flow over wind turbine arrays (wind farm) [40], and a hydrokinetic turbine [41] has been simulated using LES. In aerodynamic applications, the dynamic stall of a pitching airfoil/wing have been investigated with an implicit LES modeling (ILES) [42–44], and lift mechanism of a heaving airfoil/plate have been studied with a Smagorinsky LES model [45, 46]. In biological flows, the locomotion of swimming fish was modeled with a Smagorinsky LES [3, 47]. In geophysical flows, the flow over steady and unsteady waves has been modeled using a transport LES modeling along with a transformation to capture the moving boundary [48]. LES has also been applied in turbulent multiphase flow simulations, which can be categorized as a turbulent flow with a moving boundary. Such modeling (turbulent multiphase) is more frequent in combustion applications, e.g., the spray of fuel from a nozzle have been investigated via a compressible LES solver [49, 50], and the turbulent premixed flame has been modeled using levelset in conjunction with LES [51].

Generally the moving boundary/interface can be a solid or a fluid. When the moving boundary/interface is a fluid, the moving boundary/interface is typically called the moving interface. An example of a moving interface is in multiphase flows, e.g., interaction of two immiscible liquids [52–54] or gas-liquid interactions [55–57]. When the moving boundary/interface is a solid, it is typically called moving boundary which will be discussed further in this chapter. The problems involving moving boundary/interface, can generally be classified into (a) boundary conforming or interface tracking and (b) non-boundary conforming or interface capturing methods. The boundary conforming techniques can keep a high resolution near moving boundaries more efficiently, but suffer from highly skewed grids when deformations are large [58]. Such methods have been applied to simulate flows with moving boundaries [59–61], but typically require remeshing for large deformations. The most well known boundary conformed methods are arbitrary Lagrangian Eulerian (ALE) [62–64] and transformation [4, 65] methods. While the transformation method is only used in simulations where the motion of the moving boundary is prescribed and simple, e.g., heaving and pitching motion, the ALE method can track complex geometries. However, ALE is computationally expensive method since the mesh needs to be updated [66].

In non-boundary conforming methods, which are also called as Eulerian methods, the moving boundary moves over a fixed background mesh, i.e., does not conform to the moving boundary and there is no mesh deformation. One of the main non-boundary conforming methods is the immersed boundary method (IBM) [58, 67, 68] which can be implemented in different ways such as the Brinkman penalization [69], cut-cell, [70, 71], direct forcing [72, 73], and sharp-interface immersed boundary method [74, 75], among others.

This paper is organized as follows: in Sect. 2 different moving boundary methods including transformation, ALE, and immersed boundary are explained in Sects. 2.2, 2.1 and 2.3, respectively. Recent simulations and insight to flow physics are given in Sect. 3, and finally the future outlook is discussed in Sect. 4.

2 Numerical Methods

The governing equations are the 3D N-S equations. For incompressible flows, the filtered N-S equations for LES in Cartesian coordinates in tensor notation are as follows (i, j, k = 1, 2, 3 and repeated indices indicate summation):

$$\begin{aligned} &\frac{\partial \bar{u}_i}{\partial x_i} = 0, \\ &\frac{\partial \bar{u}_i}{\partial t} + \frac{\partial (\bar{u}_i \bar{u}_j)}{\partial x_j} = -\frac{1}{\rho}\frac{\partial \bar{p}}{\partial x_i} + \nu \frac{\partial^2 \bar{u}_i}{\partial x_j \partial x_j} + \frac{\partial \tau_{ij}}{\partial x_j}, \end{aligned} \tag{1}$$

where $\bar{p}$ and $\bar{u}$ are filtered pressure and velocity, respectively, and τ_{ij} is the subgrid-scale stress term that should be modeled. In many LES approaches, including Smagorinsky and mix models, the subgrid-scale stress tensor is modeled via an eddy viscosity (ν_t). For example in Smagorinsky model subgrid has a linear relation with the eddy viscosity as follows

$$\tau_{ij} = 2\nu_t S_{ij}, \tag{2}$$

where $S_{ij} = \frac{1}{2}(\frac{\partial \bar{u_i}}{\partial x_j} + \frac{\partial \bar{u_j}}{\partial x_i})$ is the rate of strain tensor. The eddy viscosity in Smagorinsy model is $\nu_t = (C_s \Delta)^2 (2 S_{ij} S_{ij})$, where Δ is the filter size, C_s is the Smagorinsky constant which can be a constant value [24] or computed dynamically [25, 26]. Subgrid-scale stress, τ_{ij}, can also be modeled with transport models similar to RANS modeling [76] which is more useful in atmospheric flows. Note that setting the eddy viscosity to zero recovers the original (unfiltered) N-S equations.

The governing equations are solved by imposing suitable initial and boundary conditions. This includes the no-slip condition at the moving boundaries. There are three main approaches to impose such conditions on the moving boundaries and handle the motion of the boundary:

1. Mapping the moving boundary into a stationary one using transformation,
2. Moving the grid with the boundary and imposing the boundary conditions on the grid points which are on the boundary,
3. Keeping the background grid fixed and imposing boundary conditions on the nodes near the moving boundary.

Each of the above approaches are discussed in Sects. 2.1, 2.2 and 2.3.

2.1 Transformation

In this method, a transformation is used to map the moving boundary into a stationary one. By this transformation, the governing equations (N-S) are also transformed by the mapping as well. Nevertheless, the transformation can introduce new terms to the N-S equation, which complicates solving it [4], e.g., in a pure rotation, rotational acceleration will be added to the equations. A simple example is using a non-inertial reference frame, which is attached to the center of mass of a moving rigid body, rather than an inertial reference frame [77]. In the non-inertial frame, the moving body is viewed as stationary. However, this method is confined to rigid body motion of a single geometry, e.g., a heaving/pitching airfoil [42, 43], flapping/revolving plate [78], or rotating blade of a propeller [79]. In addition to the non-inertial frame, Shen et al. [4] has also employed a transformation to model flow in a channel flow whose wall was undergoing a traveling wave oscillation. They have transformed the governing equation (N-S) from a Cartesian coordinate to a time-variant curvilinear coordinate by a mapping that maps a traveling wave to a fixed line. Such transformation enables solving the governing equations over a fixed grid rather than a moving one.

2.2 Arbitrary Lagrangian Eulerian (ALE) Method

This method was first introduced by Hirt et al. [62] in a finite difference discretization. Later a finite element discretization format of ALE was developed by Hughes et al. [80] and Donea et al. [63] for incompressible and compressible flow, respectively. To illustarte the ALE, a brief description of kinematics in Eulerian, Lagrangian and ALE are represented in Fig. 1. In Eulerian description, fluid domain is defined in a fixed frame (Fig. 1b), and all governing equations, including N-S are derived in this frame as given in Eq. (1). In a Lagrangian description, the non-conformed grid is attached to the moving boundary. Therefore, as the boundary in Fig. 1a moves upward the attached frame follows it as well, e.g., all points in the domain are shifting upward. In arbitrary Lagrangian Eulerian description, the flow problem is mapped to a moving reference domain such that points attached to the moving boundary (e.g., point q) are moved but the points on the domain which are far from the moving boundary are fixed (e.g., point p). Due to the grid motion a convection term is induced in the momentum equations.

By assuming that the grid is moving with velocity vector **w** the governing equation will be modified as follows due to the convection induced by the grid motion (see [81] for more detail of the derivation)

$$\begin{aligned} &\frac{\partial \bar{u}_i}{\partial x_i'} = 0, \\ &\frac{\partial \bar{u}_i}{\partial t}|_{x'} + \frac{\partial (\bar{u_j} - w_j)\bar{u}_i}{\partial x_j'} = -\frac{1}{\rho}\frac{\partial \bar{p}}{\partial x_i'} + \nu \frac{\partial^2 \bar{u}_i}{\partial x_j' \partial x_j'} + \frac{\partial \tau_{ij}}{\partial x_j'}, \end{aligned} \tag{3}$$

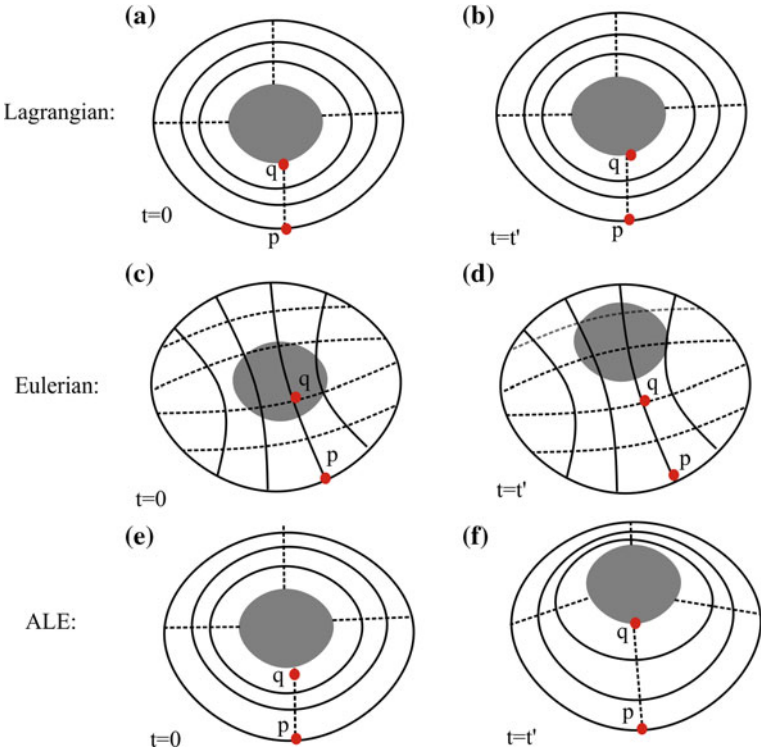

Fig. 1 Three configuration for a moving boundary problem, **a** Lagrangian: whole fluid mesh moves or rotates with the solid motion. **b** Eulerian: a fixed fluid (background) grid which is non-conformed to the moving boundary, *IBM*. **c** Arbitrary Lagrangian Eulerian (ALE): conformed to the moving boundary, some points on the mesh are moving to track the moving boundary, e.g., point p remains constant but point q moves with the moving boundary

where x' is the transformed grid. When $\mathbf{w}$ is 0, the representation is Eulerian, and when $\mathbf{w} = \mathbf{u}$, it is Lagrangian. Equation (3) is typically discretized based on a finite volume or finite element discretization [81]. These equation can be solved by imposing suitable boundary conditions. Generally, the boundary condition for the moving boundary is the no slip boundary condition. In addition, over the moving boundary, the displacement of the solid and fluid mesh should be the same as the fluid on the boundary. If the kinematic of the moving boundary is obtained by fluid-structure interaction, a dynamic boundary condition should be applied over the solid surface to enforce the force/stress on the solid to be the same as the fluid. There are two main methods to apply the above boundary conditions to the flow and structural solvers: the monolithic approach and the partitioned approach. In the monolithic approach both flow and structure equations are solved simultaneously with the boundary conditions in the same framework [82–84]. However, in the partitioned approach the domain is decomposed into two separate fluid and structure domains, which are discretized and

solved in time independently [85–87]. There is a large amount of studies on ALE methods for fluid-structure interaction (ALE-FSI solvers), see [81, 84, 87–89].

After advancing the FSI, the fluid mesh should be updated, which is the most challenging part of ALE, as required to track the solid boundary. In general, mesh update consists of mesh movement, as much as possible, and remeshing, i.e., creating a new mesh without changing connectivity of the nodes, and sometimes also a new set of nodes when the distortion is too high [90]. In some cases, the large deformation results in the distortion of the grid, where a mesh smoothing [91] can be applied to handle it. Once the mesh was updated, the solution should be projected from the old mesh to the new mesh. These procedures, mesh update and projection, are labor intensive and expensive part of this approach. Although ALE is a complex method in terms of implementation, but it can handle capturing the sharp corners, as well as the boundary layer, better compared to non-boundary conformed methods, e.g., the immersed boundary method.

ALE has been applied in many engineering and bioengineering applications. Here, we name few studies in which ALE has been used. It has been used in aeroelastic applications, e.g., in modeling flow over bridge [92], flapping of flexible wings with nonlinear elasticity [93, 94], and parachute inflation [95]. In biological flows, flow over mechanical heart valves and mitral heart valve [96, 97], and flow over aneurysmal arteries [98] is modeled. In turbulent flow, an ALE-finite element approach has been used to model flow over rotating blades of a wind turbine, which was compared against experimental results [99, 100]. In compressible flows, the hydrodynamics of a shock wave was modeled [64, 101–104]. In these problems the propagation of shock produced over a shock tube or a nozzle is captured by an ALE approach such that the mesh near the shock wave is highly resolved. In turbomachinery applications the flow over a flexible pump impeller has been modeled using OpenFOAM [105, 106].

2.3 Immersed Boundary Method (IBM)

Immersed boundary method was first introduced by Peskin [107–109] for modeling cardiovascular flow. In this method, a boundary condition is imposed, typically in the form of a forcing term, to model the effect of moving boundaries [58, 107]. Based on the implementation of the boundary condition, the immersed boundary method can be classified as a diffuse interface method or a sharp interface method [110]. In the diffuse interface method, the forcing term is distributed over several grid nodes in the vicinity of the immersed boundary, but in the sharp interface method the forcing term is applied only on the nodes adjacent to the moving boundary.

Diffuse Interface IBM

Based on the function and implementation of the forcing term, diffuse IBM methods can be classified as a classic IBM [108], Brinkman penalization [69], and fictitious domain method [111]. The classic IBM method proposed by Peskin [108] adds a force

term (**f**) to the right hand side of the N-S equation [(Eq. (1)]. The force term is defined by the deformation of the flexible immersed body using appropriate constitutive laws such as Hook's law. The force (**f**) is distributed on a few nodes around the moving boundary with a distribution function which is typically a discrete delta function, e.g., $f_i(x,t) = \int F(s,t)\delta(x - X(s,t))ds$ where $F(s,t)$ is the Lagrangian force density, δ is the Dirac delta function, x denotes the Cartesian coordinates, and $X(s,t)$ denotes the physical position of material point s at time t [108]. Since the forces depend on the deformation of the immersed body, this method is confined to elastic immersed bodies and it is not suitable for rigid immersed bodies. The other diffuse interface method is Brinkman penalization method. In Brinkman penalization or penalty methods the solid is treated as porous medium with very low permeability, i.e., there is low mass flux at the boundaries [112]. The other diffuse interface method is the fictitious domain method, which does not require remeshing and uses a Lagrange multiplier to weakly couple the fluid and structure domains [111]. This method is typically used for modeling particulate flows [113–115].

The diffuse interface methods require excessive resolution near the boundary because the force distribution smear the effect of boundaries over several grid nodes. To overcome this problem, these methods are being combined with adaptive mesh refinement [116–118].

Sharp Interface IBM

Sharp interface methods can be classified as direct forcing, and cut-cell methods [58, 110]. In direct forcing methods, a forcing term [119] is added discretely to the right hand side of N-S equation. This forcing term is applied to satisfy the no slip boundary condition on the interface. Later, Fadlun et al. [120] modified this method by enforcing the effect of forcing directly to the velocity and pressure of fluid near the interface by using ghost nodes. The ghost nodes are nodes in the solid that have at least one neighbor node in the fluid. In this approach, the velocity and pressure of the ghost nodes are interpolated such that the no slip boundary condition is applied on the moving boundary. Later, Gilmanov and Sotiropoulos [74] developed a hybrid Catersian/immersed boundary method, in which the velocity and pressure of the fluid nodes adjacent to the boundary, i.e., immersed nodes (Fig. 2a), are reconstructed using an interpolation along the normal direction of the interface. The method has been extended to curvilinear coordinates, i.e., the curvilinear immersed boundary (CURVIB) method, and the immersed nodes are identified using an efficient ray tracing method [75]. This method has been used in turbulent flow [121], biological flows such as aquatic locomotion [3, 122–124], cardiovascular flows [75, 125–131], and aneurysm blood flow [132–134]. Recently, Daghooghi and Borazjani [47, 135, 136] has performed fluid solid interaction simulations of irregular shape particles immersed in the fluid using the CURVIB method. This method (CURVIB) has also been used for modeling turbulent flow over rotating blades, e.g., wind turbine [137] and hydrokinetic turbines [41, 137] using an LES modeling.

The simulation of turbulent flow with the sharp interface IBM has been performed for compressible turbulent flows [68, 138–141]. de Tullio et al. [68] in their pioneering work have simulated subsonic to supersonic flows over stationary immersed

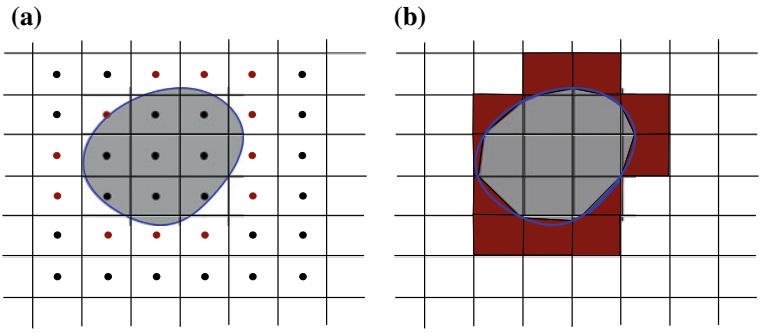

Fig. 2 Schematic configuration of a problem with two sharp immersed boundary approach: **a** Direct forcing (CURVIB), gray zone is the immersed body, immersed nodes are the fluid nodes adjacent to the immersed boundary (red points). **b** Cut-cell configuration, the immersed boundary is reshaped by the cut-cell (red cell)

bodies such as cylinders and airfoils in 2D and high Reynolds numbers using k–ω turbulence modeling. Ghias et al. [67] have simulated 3D flows over a stationary airfoil at Mach number 0.26. A large eddy simulation with an adaptive mesh was performed for modeling flow over rotorcraft [142, 143] where the motion was prescribed. Yu et al. [144] performed an LES modeling for flow over deformable parachute.

The simulations of turbulent flow with the sharp interface IBM have been performed for incompressible turbulent flow with moving boundaries as well. Tosi et al. [145] has modeled fluttering cantilever in a turbulent channel flow. Tsai et al. [146] investigated the Coriolis effect on dynamic stall of single blade of wind turbine with a 2D simulation. Ouro et al. [147] predicted the performance of a vertical tidal wind turbine using IBM-based LES. Posa et al. [148, 149] has simulated the wake of a submarine propeller with an LES modeling. This approach along with LES has also been used in weather research and forecasting model [150, 151].

In cut-cell methods the shape of the cells which are cut boundaries is modified to conform to the boundary. The fluxes across the faces of cut-cells are reconstructed from the surrounding fluid cells and immersed boundaries. The main advantage of cut-cell is its inherent conservation of mass and consequently, high accuracy near the interface. The major issue of cut-cells is the complexity of implementing in 3D. In addition, cut-cell requires smaller time steps because of the small cut-cell near the interface. Due to this drawback cut-cell is computationally expensive which makes it more suitable for two dimensional studies [152, 153]. Compressible flows over a rotating axial fan at a high Reynolds number of 10^6 has been modeled [33–35, 154]. Compressible flow in internal combustion engines has been modeled as well [155, 156].

3 Recent Large Eddy Simulations and Insights into Flow Physics

In this section, some large eddy simulations with moving boundaries performed by the CURVIB method are described.

3.1 Vortex Rings

Vortex rings are observed in both nature, e.g., ventricular flow, jellyfish wake, and engineering applications, e.g., pulsed jet engines. James and Madnia [157] carried out DNS of a laminar vortex ring and found that its circulation decays with non-dimensional time $t^{-0.33}$. Hewett and Madnia [158, 159] investigated the flame-vortex interaction in a reacting vortex ring. They found that the bulk of combustion is by a flame at the front of the vortex bubble when the ignition occurs during the formation phase of the ring, whereas it mostly occurs inside the vortex ring when ignition is delayed until after the formation phase. Asadi et al. [121] carried out LES of periodic vortex rings (Fig. 3). They validated their LES results on the location of the vortex ring at Reynolds number of 23,000 against experimental observations. Based on their LES, in addition, they found an empirical relationfor the location of vortex ring core (S) over time (t) as $S/D = 0.27\ T^{*\ 1+1.31Re^{-0.2}} t/T_s$ where Re is the Reynolds number based on the bulk flow velocity, T^* is the non-dimensional period based on the bulk flow velocity and equivalent to formation number, and T_s is the stroke time. This empirical relation collapses (scales) not only the LES results but also the results of experiments for non-periodic rings.

3.2 Hydrokinetic Turbine

Marine hydrokinetic energy from waves, tides, and currents compromise an important source of clean energies in the world. As mentioned in previous sections, flow

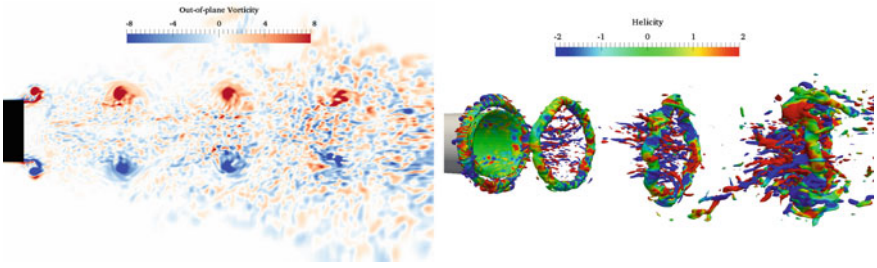

Fig. 3 LES of periodic vortex ring (Re = 11,500 and T^* = 2): The out-of-plane vorticity on the midplane (left) and iso-surfaces of q-criterion colored by helicity (right). Adopted from [121].

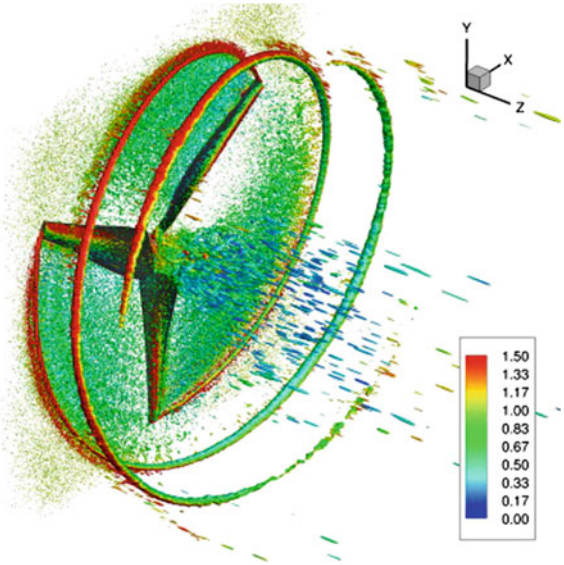

Fig. 4 Wake structure of an isolated rotor visualized by iso-surface of λ_2 colored by the magnitude of the velocity. Adopted from [41]

over hydrokinetic turbines is one of the turbulent flows involved with a moving boundary. Kang et al. [41] simulated the three dimensional turbulent flow past an axial-flow marine hydrokinetic (MHK) turbine for the first time. They modeled turbulent flow with a dynamic Smagorinsky subgrid-scale model for LES with a wall function to model the velocity near the wall because the Reynolds number was high, e.g., $Re \approx 10^7$. They carried out simulations of isolated rotor and the entire turbine configuration, including the pylon, nacelle and rotor. They found that the power predicted by both simulations are the same. The wake structure of the downstream of the turbine visualized by λ_2 shows the spiral tip vortices rotating in the same direction of the rotating blades (Fig. 4).

3.3 Aquatic Swimming

One of the interesting moving boundary problems in the nature is aquatic swimming. Aquatic swimmers typically propel themselves by deforming their body. This deformation, which is typically has the form of a backward traveling wave [160, 161], produces a thrust force that pushes them forward in the water. To simulate aquatic swimming, the motion of the fish body is typically imposed based on experimental data, and the fish swimming velocity is computed by FSI.

Daghooghi and Borazjani [47] performed LES simulations of fish schooling at high Reynolds number, i.e., $Re \approx 10^5$, to investigate the advantages of synchronized swimming in a rectangular pattern. Figure 5 shows the 3D wake structure, visualized by the iso-surface of q-criteria for different lateral spacing (w) between swimmers

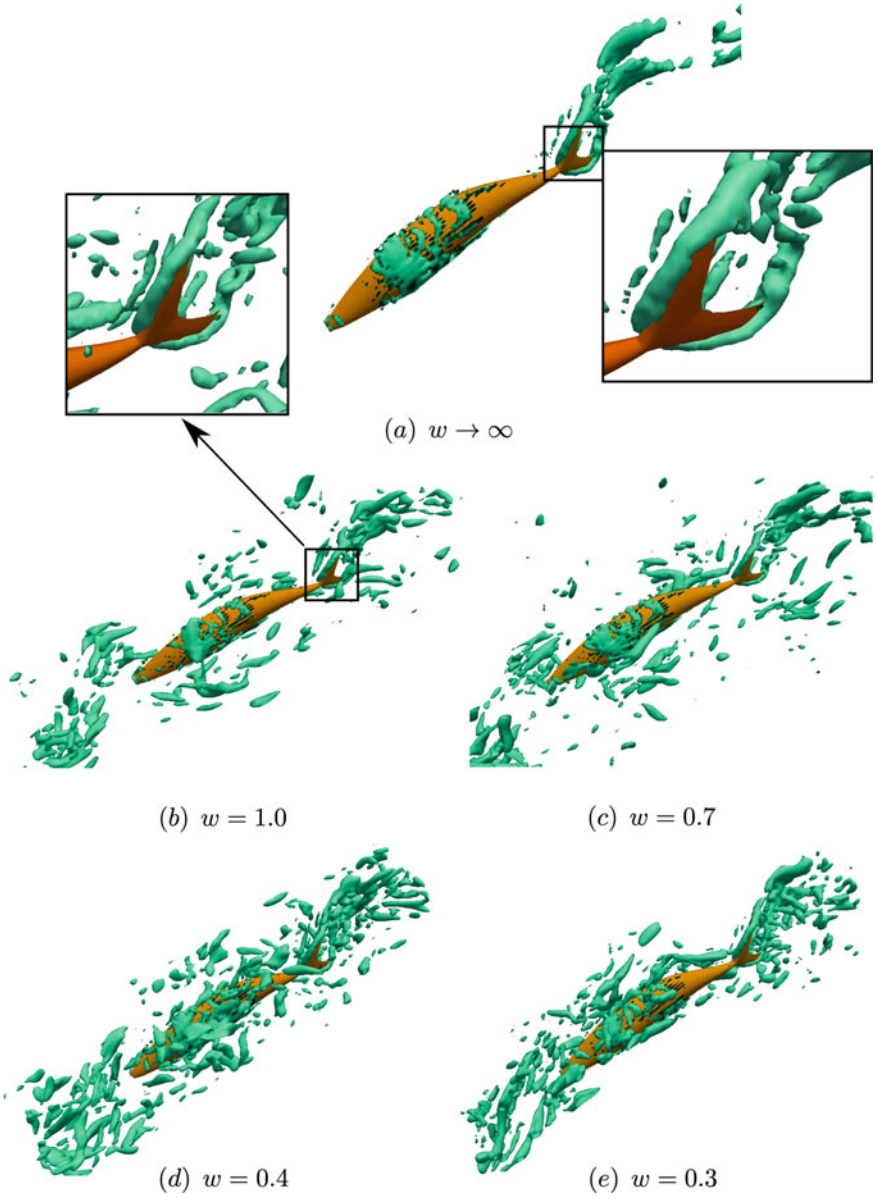

Fig. 5 3D wake structure visualized by the iso-surfaces of q-criterion for **a** a single swimmer; and a school of fish for different lateral distances (w): **b** w = 1.0, **c** w = 0.7, **d** w = 0.4, **e** w = 0.3. Adopted from [47]

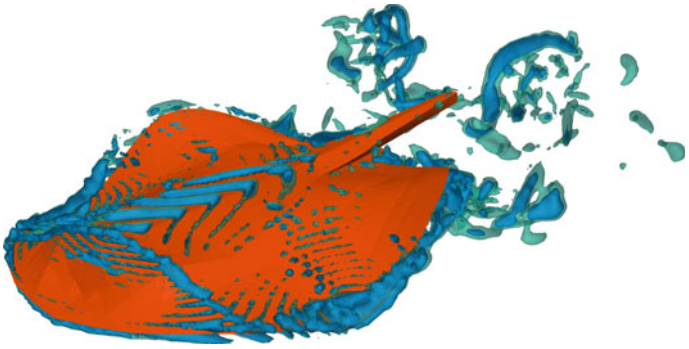

Fig. 6 Wake structure of a swimming stingray visualized by iso-surface of q-criteria reproduced from [3]

(Atlantic Mackerels). It was found that hydrodynamic performance of swimmers increases in synchronized swimming, i.e., they can achieve up to a 20% higher cruising speed than a single swimmer. These simulations revealed for the first time that the main mechanism for improved performance is the channeling effect rather than vortex interaction because the flow breaks into many small disorganized vortices (Fig. 5) which reduces the chance of positive vortex interaction [47].

Bottom et al. [3] simulated the locomotion of a stingray (Fig. 6), where the motion of stingray's body was prescribed from experiments. The Reynolds number for the fast swimming stingray was $Re = 23000$, and a dynamic Smagorinsky [26] LES along with a wall function was used to model the turbulent flow. The swimming speeds predicted by the simulations were within 12% of the nominal one. In addition, generation of a LEV was also reported over the stingray's body, while the LEV is typically generated over the leading edge of a flying/hovering wing [162]. The creation of LEV in aquatic swimming was first reported by Borazjani and Daghooghi [122] and later by Liu et al. [163]. Bottom et al. [3] observed that the presence of LEV in stingray's swimming can also increase its thrust. Figure 6 shows flow over stingray visualized by the iso-surface of q-criteria.

Another interesting phenomena in aquatic swimming, in addition to the generation of LEV, is flow reattachment on the swimmers' bodies during swimming [161], which is thought to be due to the traveling wave oscillation [4]. In fact, in addition to reattaching the flow, a backward traveling wave can also reduce the turbulent intensity of a turbulent boundary layer, i.e., it can relaminarize the boundary layer [4]. Inspired by these observations, e.g., flow reattachment by producing traveling wave [164], we have performed LES to reduce the flow separation over an airfoil and inclined wing using backward traveling waves. A few sample results of these studies are discussed in 3.4.

3.4 Bio-Inspired Flow Control

Flow separation is typically associated with a significant performance loss, e.g., increase in drag or decrease in lift. To overcome this drawback, passive flow control methods such as vortex generators [165], boundary layer trip [166], etc., and active flow control methods such as periodic excitation [167], synthetic jets [168] have been employed. With the development of smart materials, surface actuators are becoming practical as active flow control tools for low Re flows. Jones et al. [169] improved the aerodynamic performance via producing a standing wave oscillation on the suction side of an airfoil. Recently, traveling waves have been created experimentally on flexible structures using multiple piezoelectric actuators [170]. The amplitude of such traveling waves is low, which has motivated us to numerically investigate the effects of low amplitude traveling waves on flow separation and aerodynamic performance of an airfoil/wing in a low Re flow.

We have simulated the traveling wave oscillations on the suction side of the airfoil to reduce flow separation and enhance aerodynamic performance of a low Reynolds number airfoil ($Re = 50000$) at an angle of attack (AOA) of 10 degrees. Airfoil is a NACA18 which is shown within the fluid grid in Fig. 7. The simulations are performed for three cases as shown in Table 1. In case 1, the airfoil is static, and in cases 2 and 3 its suction oscillates with a traveling wave equation of the form:

$$Y(Z,t) = h(Z)\sin\left((2\pi)\left(\frac{fL}{U}t - \frac{Z}{\lambda}\right)\right) \tag{4}$$

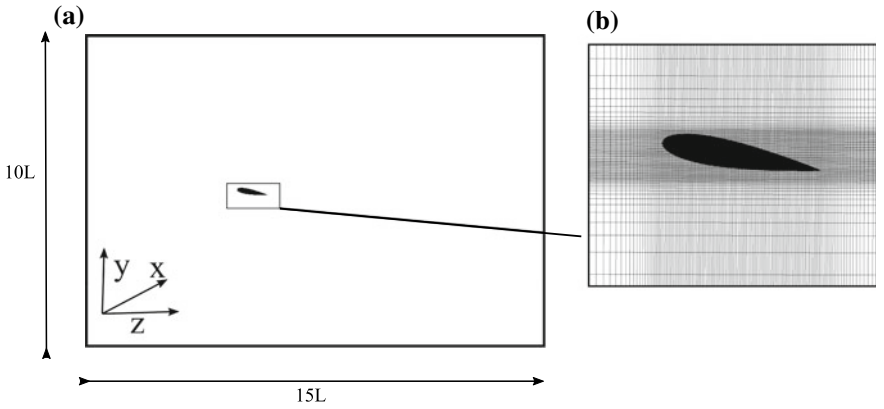

Fig. 7 The computational domain and immersed body. **b** 2D section of undulating airfoil in computational grid. The motion is defined in the rotated frame and then transformed in the flow frame. Every eighth grid line is shown in y direction and every fourth gridline is shown in z direction. The spanwise size is 0.3 L

Table 1 Values of drag coefficient C_D, lift coefficient C_L and power for morphing airfoil. All hydrodynamic forces are nondimensionalized with $\frac{1}{2}\rho U^2 L^2$, and power is nondimensionalized with $\rho U^2 L^3$

case	fL/U	a/L	C_D	C_L	$\Delta C_L(\%)$	Power
1	–	–	0.06	0.85	0.0	0.0
2	2.0	0.002	0.06	0.89	+4.5	0.001
3	2.0	0.01	0.06	0.89	+4.5	0.0001

where $fL/U = 20$ is the nondimensional frequency, and nondimensional wavelength is $\lambda = 0.2\,\mathrm{L}$, where L is the chord length. $h(Z)$ is the amplitude which increases linearly, and its maximum is $a = 0.002\,\mathrm{L}$ and $a = 0.01\,\mathrm{L}$ for cases 2 and 3, respectively (see Fig. 8 and Table 1). The results presented in Table 1 show that the traveling wave oscillation can increase the lift by 4.5% without any drag enhancement by consuming a negligible energy to produce the wave (see Table 1). It is observed that (Fig. 8) a large coherent structure which is formed near the leading edge, breaks down near the trailing edge and energizes the boundary layer and consequently, reduces separation near the trailing edge.

At a low Re and low angle of attack, boundary layer of an airfoil is laminar and attached, but as the angle of attack increases the boundary layer starts to separate from the trailing edge due to the reduction of kinetic energy by the viscous effect near the airfoil surface [167]. Over a thin plate/wing, however, flow separates from the leading edge due to the presence of a sharp leading edge. The boundary layer of the plate is highly separated and transition to a turbulent boundary layer as in the airfoil (Fig. 8) does not reduce separation. To reduce flow separation on an inclined plate, therefore, the streamwise momentum of the fluid should be increased with a high frequency undulation. Consequently, a high frequency traveling wave (Eq. (4)) with frequency $fL/U = 20$ and maximum amplitude $a/L = 0.01$ was simulated (Fig. 9). Note that in undulating plates both the suction and pressure sides undergo an undulatory motion, in contrast to the airfoil surface morphing simulation in which only the suction side oscillates (see Figs. 8 and 9).

Figure 9a shows the flow over a thin wing (flat plate) with aspect ratio 2 at an angle of attack (AOA=10°) visualized by the iso-surface of q-criteria. It shows the LEV and tip vortices along a motionless plate ($Re = 20000$). The impact of flow separation on the plate is presented in Fig. 9b to d for four different phase angles. The traveling wave generates clockwise and counter clockwise vortices on the suction side of the plate. Theses vortices are convected by the wave to the wake as it can be observed in phase-averaged results (Fig. 9b–d). It is observed that these traveling waves reduce the flow separation by injecting a streamwise momentum into the flow.

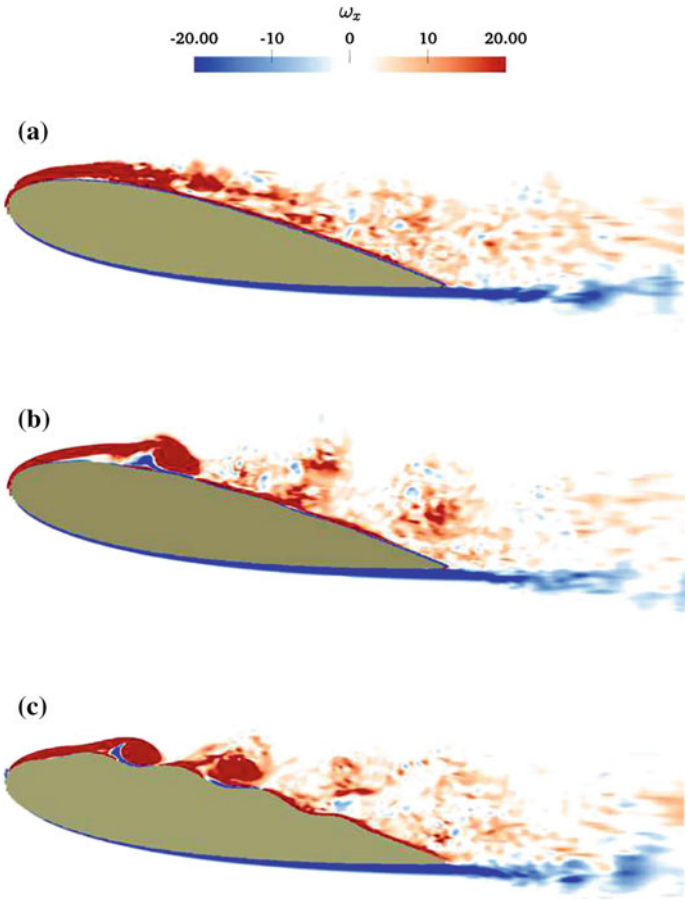

Fig. 8 Flow visualization of shear layer with spanwise-averaged out of plane vorticity, **a** static plate, **b** case 2: undulating airfoil with amplitude 0.002, and **c** case 3: undulating airfoil with amplitude 0.01

4 Future Outlook

ALE methods can keep a high resolution near the moving boundaries, but large deformation can lead to highly skewed grids. Immersed boundary methods, on the other hand, do not have any issue with mesh quality but require high resolution near the moving boundaries to capture the viscous sublayer for turbulent simulations. To increase the efficiency of the immersed boundary method, local grid refinement or moving overset grids, which can keep a high resolution grid near the moving boundaries while reducing the total grid number, might be useful. In addition, resolving the log-region rather the viscous sublayer near the moving boundaries is another way to reduce the computational cost of turbulent simulations. The law of the wall

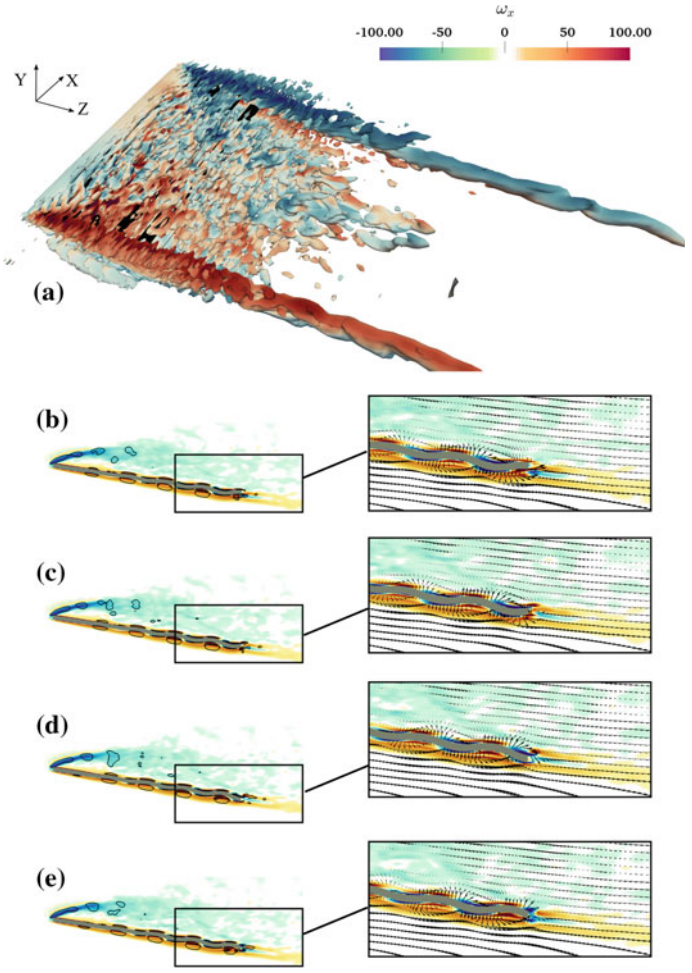

Fig. 9 Turbulent flow over a wing with aspect ratio of 2. **a** 3D wake of a motionless plate identified by q-criteria, (**b**–**d**) phase-averaged flow field of undulating plate in four different phase angles. The first column is the vorticity distribution and footprint of q-criteria with threshold $Q = 40$. The vorticity and velocity vector of flow close to the trailing edge is visualized in second column. The visualizations of first to fourth row is for phase-angle of: **b** $t/T = 0.0$; **c** $t/T = 0.25$; **d** $t/T = 0.5$; and **e** $t/T = 0.75$, respectively, where $T = 1/f$

is known for a turbulent boundary layer over flat surfaces, but it is not known how it changes with the movement of a surface. Therefore, developing law of the wall for turbulent boundary layer over moving surfaces is another avenue which can reduce the computational cost of such simulations.

Acknowledgements This work was partly supported by the National Science Foundation (NSF) CAREER Grant CBET 1453982. The computational resources were partly provided by the High Performance Research Computing (HPRC) facilities at Texas A&M University.

References

1. R. Howell, N. Qin, J. Edwards, N. Durrani, Wind tunnel and numerical study of a small vertical axis wind turbine. Renew. Energy **35**(2), 412–422 (2010)
2. D. Eckardt, Detailed flow investigations within a high-speed centrifugal compressor impeller. J. Fluids Eng. **98**(3), 390–399 (1976)
3. R. Bottom II, I. Borazjani, E. Blevins, G. Lauder, Hydrodynamics of swimming in stingrays: Numerical simulations and the role of the leading-edge vortex. J. Fluid Mech. **788**, 407–443 (2016)
4. L. Shen, X. Zhang, D.K.P. Yue, M.S. Triantafyllou, Turbulent flow over a flexible wall undergoing a streamwise travelling wave motion. J. Fluid Mech. **484**, 197–221 (2003)
5. E. Blevins, G. Lauder, Rajiform locomotion: Three-dimensional kinematics of the pectoral fin surface during swimming in the freshwater stingray potamotrygon orbignyi. J. Exp. Biol. **215**(18), 3231–3241 (2012)
6. S. Belcher, J. Hunt, Turbulent flow over hills and waves. Annu. Rev. Fluid Mech. **30**(1), 507–538 (1998)
7. S.B. Pope, *Turbulent Flows* (Cambridge University Press, 2000)
8. R. Jahanbakhshi, C.K. Madnia, Entrainment in a compressible turbulent shear layer. J. Fluid Mech. **797**, 564–603 (2016)
9. R. Jahanbakhshi, C.K. Madnia, Viscous superlayer in a reacting compressible turbulent mixing layer. J. Fluid Mech. **848**, 743–755 (2018)
10. R. Jahanbakhshi, C.K. Madnia, The effect of heat release on the entrainment in a turbulent mixing layer. J. Fluid Mech. **844**, 92–126 (2018)
11. C. Madnia, P. Givi, Direct numerical simulation and large eddy simulation of reacting homogeneous turbulence. Large Eddy Simul. Complex Eng. Geophys. Flows 315–346 (1993)
12. S.H. Frankel, V. Adumitroaie, C.K. Madnia, P. Givi, Large eddy simulations of turbulent reacting flows by assumed PDF methods, in Engineering Applications of Large Eddy Simulations, FED-Vol. 162, ed. by S.A. Ragab, U. Piomelli (ASME, New York, NY, 1993), pp. 81–101
13. D.C. Wilcox et al., *Turbulence Modeling for CFD*, vol. 2 (DCW industries La Canada, CA, 1998)
14. A. Posa, A. Lippolis, E. Balaras, Investigation of separation phenomena in a radial pump at reduced flow rate by large-eddy simulation. J. Fluids Eng. **138**, 121101 (2016)
15. R. Barrio, J. Parrondo, E. Blanco, Numerical analysis of the unsteady flow in the near-tongue region in a volute-type centrifugal pump for different operating points. Comput. Fluids **39**, 859–870 (2010)
16. T. Watanabe, T. Kawamura, Y. Takekoshi, M. Maeda, S.H. Rhee, Simulation of steady and unsteady cavitation on a marine propeller using a RANS CFD code, in *Proceedings of The Fifth International Symposium on Cavitation* (Cav, Citeseer, 2003)
17. G.V. Iungo, V. Santhanagopalan, U. Ciri, F. Viola, L. Zhan, M.A. Rotea, S. Leonardi, Parabolic RANS solver for low-computational-cost simulations of wind turbine wakes. Wind Energy **21**, 184–197 (2017)
18. D. Astolfi, F. Castellani, L. Terzi, A study of wind turbine wakes in complex terrain through RANS simulation and SCADA data. J. Sol. Energy Eng. **140**(3), 031001 (2018)
19. M. Shives, C. Crawford, Adapted two-equation turbulence closures for actuator disk RANS simulations of wind & tidal turbine wakes. Renew. Energy **92**, 273–292 (2016)

20. J. Thé, H. Yu, A critical review on the simulations of wind turbine aerodynamics focusing on hybrid RANS-LES methods. Energy **138**, 257–289 (2017)
21. Z. Pan, W. Cui, Q. Miao, Numerical simulation of vortex-induced vibration of a circular cylinder at low mass-damping using RANS code. J. Fluids Struct. **23**, 23–37 (2007)
22. J. Fröhlich, D. von Terzi, Hybrid LES/RANS methods for the simulation of turbulent flows. Prog. Aerosp. Sci. **44**, 349–377 (2008)
23. Z. Cheng, M. Koken, G. Constantinescu, Approximate methodology to account for effects of coherent structures on sediment entrainment in RANS simulations with a movable bed and applications to pier scour. Adv. Water Resour. **120**, 65–82 (2018)
24. J. Smagorinsky, General circulation experiments with the primitive equations: I. the basic experiment. Mon. Weather Rev. **91**(3), 99–164 (1963)
25. M. Germano, U. Piomelli, P. Moin, W.H. Cabot, A dynamic subgrid-scale eddy viscosity model. Phys. Fluids A: Fluid Dyn. (1989–1993) **3**(7), 1760–1765 (1991)
26. D.K. Lilly, A proposed modification of the Germano subgrid-scale closure method. Phys. Fluids A: Fluid Dyn. **4**(3), 633–635 (1992)
27. R.A. Clark, J.H. Ferziger, W.C. Reynolds, Evaluation of subgrid-scale models using an accurately simulated turbulent flow. J. Fluid Mech. **91**(1), 1–16 (1979)
28. M.R. Visbal, J.S. Shang, Investigation of the flow structure around a rapidly pitching airfoil. AIAA J. **27**, 1044–1051 (1989)
29. W. Cabot, P. Moin, Flow Turbul. Combust. **63**(1–4), 269–291 (2000)
30. M. Wang, P. Moin, Dynamic wall modeling for large-eddy simulation of complex turbulent flows. Phys. Fluids **14**(7), 2043 (2002)
31. C. Kato, M. Kaiho, A. Manabe, An overset finite-element large-eddy simulation method with applications to turbomachinery and aeroacoustics. J. Appl. Mech. **70**(1), 32–43 (2003)
32. N. Yamanishi, S. Fukao, X. Qiao, C. Kato, Y. Tsujimoto, LES simulation of backflow vortex structure at the inlet of an inducer. J. Fluids Eng. **129**(5), 587 (2007)
33. A. Pogorelov, M. Meinke, W. Schroder, Effects of tip-gap width on the flow field in an axial fan. Int. J. Heat Fluid Flow **61**, 466–481 (2016)
34. A. Pogorelov, M. Meinke, W. Schroder, Cut-cell method based large-eddy simulation of tip-leakage flow. Phys. Fluids **27**, 075106 (2015)
35. C. Li, X. Li, P. Li, X. Ye, Numerical investigation of impeller trimming effect on performance of an axial flow fan. Energy **75**, 534–548 (2014)
36. A. Posa, C.M. Parker, M.C. Leftwich, E. Balaras, Wake structure of a single vertical axis wind turbine. Int. J. Heat Fluid Flow **61**, 75–84 (2016)
37. X. Yang, K.B. Howard, M. Guala, F. Sotiropoulos, Effects of a three-dimensional hill on the wake characteristics of a model wind turbine. Phys. Fluids **27**, 025103 (2015)
38. D. Foti, X. Yang, M. Guala, F. Sotiropoulos, Wake meandering statistics of a model wind turbine: Insights gained by large eddy simulations. Phys. Rev. Fluids **1**(4), 044407 (2016)
39. S. Shamsoddin, F. Porté-Agel, A large-eddy simulation study of vertical axis wind turbine wakes in the atmospheric boundary layer. Energies **9**(5), 366 (2016)
40. X. Yang, F. Sotiropoulos, R.J. Conzemius, J.N. Wachtler, M.B. Strong, Large-eddy simulation of turbulent flow past wind turbines/farms: The virtual wind simulator (VWiS). Wind Energy **18**, 2025–2045 (2014)
41. S. Kang, I. Borazjani, J.A. Colby, F. Sotiropoulos, Numerical simulation of 3d flow past a real-life marine hydrokinetic turbine. Adv. Water Resour. **39**, 33–43 (2012)
42. M.R. Visbal, D.J. Garmann, Analysis of dynamic stall on a pitching airfoil using high-fidelity large-eddy simulations. AIAA J. 46–63 (2017)
43. M.R. Visbal, S.I. Benton, Exploration of high-frequency control of dynamic stall using large-eddy simulations. AIAA J. **56**, 2974–2991 (2018)
44. D.J. Garmann, M.R. Visbal, Numerical investigation of transitional flow over a rapidly pitching plate. Phys. Fluids **23**, 094106 (2011)
45. M. Rahromostaqim, A. Posa, E. Balaras, Numerical investigation of the performance of pitching airfoils at high amplitudes. AIAA J. 2221–2232 (2016)

46. J.A. Franck, K.S. Breuer, Unsteady high-lift mechanisms from heaving flat plate simulations. Int. J. Heat Fluid Flow **67**, 230–239 (2017)
47. M. Daghooghi, I. Borazjani, The hydrodynamic advantages of synchronized swimming in a rectangular pattern. Bioinspir. Biomim. **10**(5), 056018 (2015)
48. P.P. Sullivan, M.L. Banner, R.P. Morison, W.L. Peirson, Impacts of wave age on turbulent flow and drag of steep waves. Procedia IUTAM **26**, 174–183 (2018)
49. M. Ghiji, L. Goldsworthy, P. Brandner, V. Garaniya, P. Hield, Analysis of diesel spray dynamics using a compressible Eulerian/VOF/LES model and microscopic shadowgraphy. Fuel **188**, 352–366 (2017)
50. X.-S. Tian, H. Zhao, H.-F. Liu, W.-F. Li, J.-L. Xu, Three-dimensional large eddy simulation of round liquid jet primary breakup in coaxial gas flow using the VOF method. Fuel Process. Technol. **131**, 396–402 (2015)
51. V. Moureau, B. Fiorina, H. Pitsch, A level set formulation for premixed combustion LES considering the turbulent flame structure. Combust. Flame **156**, 801–812 (2009)
52. S. Balachandar, J.K. Eaton, Turbulent dispersed multiphase flow. Annu. Rev. Fluid Mech. **42**, 111–133 (2010)
53. V. Attari, S. Ghosh, T. Duong, R. Arroyave, On the interfacial phase growth and vacancy evolution during accelerated electromigration in Cu/Sn/Cu microjoints. Acta Mater. **160**, 185–198 (2018)
54. V. Attari, R. Arroyave, Phase field modeling of joint formation during isothermal solidification in 3DIC micro packaging. J. Phase Equilibria. Diffus. **37**, 469–480 (2016)
55. C.E. Brennen, C.E. Brennen, *Fundamentals of Multiphase Flow* (Cambridge University Press, 2005)
56. A.M. Akbarzadeh, A. Moosavi, A.M. Kheirabadi, Dewetting of evaporating thin films over nanometer-scale topographies. Phys. Rev. E **90**, 012409 (2014)
57. H. Asadi, M. Taeibi-Rahni, A.M. Akbarzadeh, K. Javadi, G. Ahmadi, Investigation of hydrodynamically dominated membrane rupture, using smoothed particle hydrodynamics-finite element method. Fluids **4**(3), 149 (2019)
58. R. Mittal, G. Iaccarino, Immersed boundary methods. Annu. Rev. Fluid Mech. **37**, 239–261 (2005)
59. M. Lesoinne, C. Farhat, Geometric conservation laws for flow problems with moving boundaries and deformable meshes, and their impact on aeroelastic computations. Comput. Methods Appl. Mech. Eng. **134**(1), 71–90 (1996)
60. A. Masud, T.J. Hughes, A space-time Galerkin/least-squares finite element formulation of the Navier-Stokes equations for moving domain problems. Comput. Methods Appl. Mech. Eng. **146**(1), 91–126 (1997)
61. P. Thomas, C. Lombard, Geometric conservation law and its application to flow computations on moving grids. AIAA J. **17**(10), 1030–1037 (1979)
62. C. Hirt, A. Amsden, J. Cook, An arbitrary Lagrangian-Eulerian computing method for all flow speeds. J. Comput. Phys. **14**, 227–253 (1974)
63. J. Donea, S. Giuliani, J. Halleux, An arbitrary Lagrangian-Eulerian finite element method for transient dynamic fluid-structure interactions. Comput. Methods Appl. Mech. Eng. **33**, 689–723 (1982)
64. J. Waltz, N. Morgan, T. Canfield, M. Charest, L. Risinger, J. Wohlbier, A three-dimensional finite element arbitrary Lagrangian-Eulerian method for shock hydrodynamics on unstructured grids. Comput. Fluids **92**, 172–187 (2014)
65. D. Yang, L. Shen, Simulation of viscous flows with undulatory boundaries. Part I: Basic solver. J. Comput. Phys. **230**, 5488–5509 (2011)
66. O. Hassan, K. Sørensen, K. Morgan, N. Weatherill, A method for time accurate turbulent compressible fluid flow simulation with moving boundary components employing local remeshing. Int. J. Numer. Methods Fluids **53**(8), 1243–1266 (2007)
67. R. Ghias, R. Mittal, H. Dong, A sharp interface immersed boundary method for compressible viscous flows. J. Comput. Physics **225**(1), 528–553 (2007)

68. M.D. de Tullio, P. De Palma, G. Iaccarino, G. Pascazio, M. Napolitano, An immersed boundary method for compressible flows using local grid refinement. J. Comput. Phys. **225**(2), 2098–2117 (2007)
69. A. Piquet, O. Roussel, A. Hadjadj, A comparative study of brinkman penalization and direct-forcing immersed boundary methods for compressible viscous flows. Comput. Fluids **136**, 272–284 (2016)
70. B. Muralidharan, S. Menon, A high-order adaptive cartesian cut-cell method for simulation of compressible viscous flow over immersed bodies. J. Comput. Phys. **321**, 342–368 (2016)
71. L. Schneiders, D. Hartmann, M. Meinke, W. Schröder, An accurate moving boundary formulation in cut-cell methods. J. Comput. Phys. **235**, 786–809 (2013)
72. M. Uhlmann, An immersed boundary method with direct forcing for the simulation of particulate flows. J. Comput. Phys. **209**, 448–476 (2005)
73. T. Kempe, J. Frohlich, An improved immersed boundary method with direct forcing for the simulation of particle laden flows. J. Comput. Phys. **231**, 3663–3684 (2012)
74. A. Gilmanov, F. Sotiropoulos, A hybrid cartesian/immersed boundary method for simulating flows with 3d, geometrically complex, moving bodies. J. Comput. Phys. **207**(2), 457–492 (2005)
75. I. Borazjani, L. Ge, F. Sotiropoulos, Curvilinear immersed boundary method for simulating fluid structure interaction with complex 3d rigid bodies. J. Comput. Phys. **227**(16), 7587–7620 (2008)
76. D.S. Henn, R.I. Sykes, Large-eddy simulation of flow over wavy surfaces. J. Fluid Mech. **383**, 75–112 (1999)
77. I. Borazjani, L. Ge, T. Le, F. Sotiropoulos, A parallel overset-curvilinear-immersed boundary framework for simulating complex 3D incompressible flows. Comput. Fluids **77**, 76–96 (2013)
78. L. Zheng, T. Hedrick, R. Mittal, A comparative study of the hovering efficiency of flapping and revolving wings. Bioinspir. Biomim. **8**(3), 036001 (2013)
79. J. Go, H. Yoon, J. Jung, Effects of a duct before a propeller on propulsion performance. Ocean Eng. **136**, 54–66 (2017)
80. T.J. Hughes, W.K. Liu, T.K. Zimmermann, Lagrangian-Eulerian finite element formulation for incompressible viscous flows. Comput. Methods Appl. Mech. Eng. **29**(3), 329–349 (1981)
81. J. Donea, A. Huerta, J.-P. Ponthot, A. Rodriguez-Ferran, *Arbitrary Lagrangian–Eulerian Methods*, ch. 14. (American Cancer Society, 2004)
82. M. Heil, A.L. Hazel, J. Boyle, Solvers for large-displacement fluid-structure interaction problems: Segregated versus monolithic approaches. Comput. Mech. **43**(1), 91–101 (2008)
83. A. Lozovskiy, M.A. Olshanskii, Y.V. Vassilevski, Analysis and assessment of a monolithic FSI finite element method. Comput. Fluids **179**, 277–288 (2019)
84. S. Basting, A. Quaini, S. Čanić, R. Glowinski, Extended ALE method for fluid-structure interaction problems with large structural displacements. J. Comput. Phys. **331**, 312–336 (2017)
85. J.W. Banks, W.D. Henshaw, D.W. Schwendeman, An analysis of a new stable partitioned algorithm for FSI problems. Part I: Incompressible flow and elastic solids. J. Comput. Phys. **269**, 108–137 (2014)
86. P. Le Tallec, J. Mouro, Fluid structure interaction with large structural displacements. Comput. Methods Appl. Mech. Eng. **190**(24–25), 3039–3067 (2001)
87. H.T. Ahn, Y. Kallinderis, Strongly coupled flow/structure interactions with a geometrically conservative ALE scheme on general hybrid meshes. J Comput. Phys. **219**, 671–696 (2006)
88. F. Casadei, J. Halleux, A. Sala, F. Chillè, Transient fluid-structure interaction algorithms for large industrial applications. Comput. Methods Appl. Mech. Eng. **190**, 3081–3110 (2001)
89. M. Heil, An efficient solver for the fully coupled solution of large-displacement fluid-structure interaction problems. Comput. Methods Appl. Mech. Eng. **193**, 1–23 (2004)
90. A. Johnson, T. Tezduyar, Mesh update strategies in parallel finite element computations of flow problems with moving boundaries and interfaces. Comput. Methods Appl. Mech. Eng. **119**, 73–94 (1994)

91. J. Hermansson, P. Hansbo, A variable diffusion method for mesh smoothing. Commun. Numer. Meth. Eng. **19**, 897–908 (2003)
92. T.A. Helgedagsrud, Y. Bazilevs, A. Korobenko, K.M. Mathisen, O.A. Oiseth, Using ALE-VMS to compute aerodynamic derivatives of bridge sections. Comput. Fluids **179**, 820–832 (2018)
93. V. K. Lakshminarayan, C. Farhat, Nonlinear aeroelastic analysis of highly flexible flapping wings using an ALE formulation of embedded boundary method, in *52nd Aerospace Sciences Meeting* (2014), p. 0221
94. C. Farhat, V.K. Lakshminarayan, An ALE formulation of embedded boundary methods for tracking boundary layers in turbulent fluid-structure interaction problems. J. Comput. Physics **263**, 53–70 (2014)
95. C. Farhat, CFD-based nonlinear computational aeroelasticity, *Encyclopedia of Computational Mechanics*, Second Edition (2017), pp. 1–21
96. K. Takizawa, T.E. Tezduyar, A. Buscher, S. Asada, Space-time fluid mechanics computation of heart valve models. Comput. Mech. **54**, 973–986 (2014)
97. D.M. Espino, D.E. Shepherd, D.W. Hukins, Evaluation of a transient, simultaneous, arbitrary Lagrange-Euler based multi-physics method for simulating the mitral heart valve. Comput. Methods Biomech. Biomed. Eng. **17**, 450–458 (2012)
98. M. Sharzehee, S.S. Khalafvand, H.-C. Han, Fluid-structure interaction modeling of aneurysmal arteries under steady-state and pulsatile blood flow: A stability analysis. Comput. Methods Biomech. Biomed. Eng. **21**, 219–231 (2018)
99. Y. Bazilevs, M.-C. Hsu, K. Takizawa, T.E. Tezduyar, ALE-VMS and ST-VMS methods for computer modeling of wind-turbine rotor aerodynamics and fluid-structure interaction. Math. Models Methods Appl. Sci. **22**, 1230002 (2012)
100. M.-C. Hsu, I. Akkerman, Y. Bazilevs, Finite element simulation of wind turbine aerodynamics: Validation study using NREL phase VI experiment. Wind Energy **17**, 461–481 (2013)
101. H. Luo, J.D. Baum, R. Lohner, On the computation of multi-material flows using ALE formulation. J. Comput. Phys. **194**, 304–328 (2004)
102. J. Waltz, J. Bakosi, A coupled ALE-AMR method for shock hydrodynamics. Comput. Fluids **167**, 359–371 (2018)
103. N. Takashi, ALE finite element computations of fluid-structure interaction problems. Comput. Methods Appl. Mech. Eng. **112**, 291–308 (1994)
104. A.J. Barlow, P.-H. Maire, W.J. Rider, R.N. Rieben, M.J. Shashkov, Arbitrary Lagrangian-Eulerian methods for modeling high-speed compressible multimaterial flows. J. Comput. Phys. **322**, 603–665 (2016)
105. R. Campbell, E. Paterson, Fluid-structure interaction analysis of flexible turbomachinery. J. Fluids Struct. **27**(8), 1376–1391 (2011)
106. J. Pei, H. Dohmen, S. Yuan, F.-K. Benra, Investigation of unsteady flow-induced impeller oscillations of a single-blade pump under off-design conditions. J. Fluids Struct. **35**, 89–104 (2012)
107. C.S. Peskin, Flow patterns around heart valves: A digital computer method for solving the equations of motion. Ph.D. thesis, Sue Golding Graduate Division of Medical Sciences, Albert Einstein College of Medicine, Yeshiva University, 1972
108. C.S. Peskin, Flow patterns around heart valves: A numerical method. J. Comput. Phys. **10**, 252–271 (1972)
109. C. Peskin, Numerical analysis of blood flow in the heart. J. Comput. Phys. **25**(3), 220–252 (1977)
110. F. Sotiropoulos, X. Yang, Immersed boundary methods for simulating fluid-structure interaction. Prog. Aerosp. Sci. **65**, 1–21 (2014)
111. R. Glowinski, T.-W. Pan, T.I. Hesla, D.D. Joseph, A distributed Lagrange multiplier/fictitious domain method for particulate flows. Int. J. Multiph. Flow **25**(5), 755–794 (1999)
112. P. Angot, C.-H. Bruneau, P. Fabrie, A penalization method to take into account obstacles in incompressible viscous flows. Numer. Math. **81**, 497–520 (1999)

113. A. Wachs, A. Hammouti, G. Vinay, M. Rahmani, Accuracy of finite volume/staggered grid distributed Lagrange multiplier/fictitious domain simulations of particulate flows. Comput. Fluids **115**, 154–172 (2015)
114. Z. Yu, Z. Lin, X. Shao, L.-P. Wang, A parallel fictitious domain method for the interface-resolved simulation of particle-laden flows and its application to the turbulent channel flow. Eng. Appl. Comput. Fluid Mech. **10**(1), 160–170 (2016)
115. P. Singh, D. Joseph, T. Hesla, R. Glowinski, T.-W. Pan, A distributed Lagrange multiplier/fictitious domain method for viscoelastic particulate flows. J. Nonnewton. Fluid Mech. **91**, 165–188 (2000)
116. B. Griffith, R. Hornung, D. McQueen, C. Peskin, An adaptive, formally second order accurate version of the immersed boundary method. J. Comput. Phys. **223**(1), 10–49 (2007)
117. B. Griffith, Immersed boundary model of aortic heart valve dynamics with physiological driving and loading conditions. Int. J. Numer. Method Biomed. Eng. **28**(3), 317–345 (2012)
118. R. Van Loon, P. Anderson, J. De Hart, F. Baaijens, A combined fictitious domain/adaptive meshing method for fluid-structure interaction in heart valves. Int. J. Numer. Meth. fluids **46**(5), 533–544 (2004)
119. R.J. LeVeque, Z. Li, The immersed interface method for elliptic equations with discontinuous coefficients and singular sources. SIAM J. Numer. Anal. **31**, 1019–1044 (1994)
120. E. Fadlun, R. Verzicco, P. Orlandi, J. Mohd-Yusof, Combined immersed-boundary finite-difference methods for three-dimensional complex flow simulations. J. Comput. Phys. **161**(1), 35–60 (2000)
121. H. Asadi, H. Asgharzadeh, I. Borazjani, On the scaling of propagation of periodically generated vortex rings. J. Fluid Mech. **853**, 150–170 (2018)
122. I. Borazjani, M. Daghooghi, The fish tail motion forms an attached leading edge vortex. Proc. Royal Soc. B **280**, 20122071 (2013)
123. I. Borazjani, F. Sotiropoulos, Why don't mackerels swim like eels? The role of form and kinematics on the hydrodynamics of undulatory swimming. Phys. Fluids **21**, 091109 (2009)
124. M. Daghooghi, I. Borazjani, Self-propelled swimming simulations of bio-inspired smart structures. Bioinspir. Biomim. **11**(5), 056001 (2016)
125. I. Borazjani, Fluid-structure interaction, immersed boundary-finite element method simulations of bio-prosthetic heart valves. Comput. Methods Appl. Mech. Eng. **257**, 103–116 (2013)
126. I. Borazjani, J. Westerdale, E. McMahon, P.K. Rajaraman, J. Heys, M. Belohlavek, Left ventricular flow analysis: Recent advances in numerical methods and applications in cardiac ultrasound. Comput. Math. Methods Med., Special Issue: Computational Analysis of Coronary and Ventricular Hemodynamics **2013**, 395081 (2013)
127. M. Hedayat, I. Borazjani, Comparison of platelet activation through hinge vs bulk flow in bileaflet mechanical heart valves. J. Biomech. **83**, 280–290 (2019)
128. M. Hedayat, H. Asgharzadeh, I. Borazjani, Platelet activation of mechanical versus bioprosthetic heart valves during systole. J. Biomech. **56**, 111–116 (2017)
129. Z. Song, I. Borazjani, The role of shape and heart rate on the performance of the left ventricle. J. Biomech. Eng. **137**(11), 114501 (2015)
130. I. Borazjani, A review of fluid-structure interaction simulations of prosthetic heart valves. Long Term Eff. Med. Implants. **25**(1–2), 75–93 (2015)
131. I. Borazjani, Numerical simulations of fluid/structure interaction problems in biological flows. Ph.D. thesis, University of Minnesota, 2008
132. H. Asgharzadeh, H. Asadi, H. Meng, I. Borazjani, A non-dimensional parameter for classification of the flow in intracranial aneurysms. II. Patient-specific geometries. Phys. Fluids **31**, 031905 (2019)
133. H. Asgharzadeh, I. Borazjani, A non-dimensional parameter for classification of the flow in intracranial aneurysms. I. Simplified geometries. Phys. Fluids **31**, 031904 (2019)
134. T.B. Le, I. Borazjani, F. Sotiropoulos, Pulsatile flow effects on the hemodynamics of intracranial aneurysms. J. Biomech. Eng. **132**, 111009 (2010)
135. M. Daghooghi, I. Borazjani, The influence of inertia on the rheology of a periodic suspension of neutrally buoyant rigid ellipsoids. J. Fluid Mech. **781**, 506–549 (2015)

136. M. Daghooghi, I. Borazjani, The effects of irregular shape on the particle stress of dilute suspensions. J. Fluid Mech. **839**, 663–692 (2018)
137. X. Yang, A. Khosronejad, F. Sotiropoulos, Large-eddy simulation of a hydrokinetic turbine mounted on an erodible bed. Renew. Energy **113**, 1419–1433 (2017)
138. C. Merlin, P. Domingo, L. Vervisch, Immersed boundaries in large eddy simulation of compressible flows. Flow Turbul. Combust. **90**(1), 29–68 (2013)
139. J. Nam, F. Lien, A ghost-cell immersed boundary method for large-eddy simulations of compressible turbulent flows. Int. J. Comput. Fluid Dyn. **28**(1–2), 41–55 (2014)
140. M. Al-Marouf, R. Samtaney, A versatile embedded boundary adaptive mesh method for compressible flow in complex geometry. J. Comput. Phys. **337**, 339–378 (2017)
141. C. Chi, B.J. Lee, H.G. Im, An improved ghost-cell immersed boundary method for compressible flow simulations. Int. J. Numer. Meth. Fluids **83**(2), 132–148 (2017)
142. Y.T. Delorme, S.H. Frankel, R. Jain, R. Strawn, High-order large eddy simulation and immersed boundary method on dynamic meshes: Application to rotorcraft aerodynamics, in *2018 AIAA Aerospace Sciences Meeting* (2018), p. 0599
143. Y.T. Delorme, S.H. Frankel, R. Jain, R. Strawn, Performance assessment of high-order large eddy simulation and immersed boundary method for rotorcraft hover, in *55th AIAA Aerospace Sciences Meeting* (2017), p. 0539
144. H. Yu, C. Pantano, F. Cirak, Large-eddy simulation of flow over deformable parachutes using immersed boundary and adaptive mesh, in *AIAA Scitech 2019 Forum* (2019), p. 0635
145. L.P. Tosi, T. Colonius, Modeling and simulation of a fluttering cantilever in channel flow. J. Fluids Struct. **89**, 174–190 (2019)
146. H.-C. Tsai, T. Colonius, Coriolis effect on dynamic stall in a vertical axis wind turbine. AIAA J. **54**, 216–226 (2016)
147. P. Ouro, T. Stoesser, An immersed boundary-based large-eddy simulation approach to predict the performance of vertical axis tidal turbines. Comput. Fluids **152**, 74–87 (2017)
148. A. Posa, R. Broglia, M. Felli, M. Falchi, E. Balaras, Characterization of the wake of a submarine propeller via large-eddy simulation. Comput. Fluids **184**, 138–152 (2019)
149. A. Posa, E. Balaras, Large-eddy simulations of a notional submarine in towed and self-propelled configurations. Comput. Fluids **165**, 116–126 (2018)
150. J. Bao, F.K. Chow, K.A. Lundquist, Large-eddy simulation over complex terrain using an improved immersed boundary method in the weather research and forecasting model. Mon. Weath. Rev. **146**, 2781–2797 (2018)
151. K.A. Lundquist, F.K. Chow, J.K. Lundquist, An immersed boundary method enabling large-eddy simulations of flow over complex terrain in the WRF model. Mon. Weath. Rev. **140**, 3936–3955 (2012)
152. H. Udaykumar, W. Shyy, M. Rao, Elafint: A mixed Eulerian-Lagrangian method for fluid flows with complex and moving boundaries. Int. J. Numer. Meth. Fluids **22**(8), 691–712 (1996)
153. T. Ye, R. Mittal, H. Udaykumar, W. Shyy, An accurate cartesian grid method for viscous incompressible flows with complex immersed boundaries. J. Comput. Phys. **156**, 209–240 (1999)
154. A. Pogorelov, M.H. Meinke, W. Schroeder, R. Kessler, Cut-cell method based large-eddy simulation of a tip-leakage vortex of an axial fan, in *53rd AIAA Aerospace Sciences Meeting* (2015), p. 1979
155. M. Meinke, L. Schneiders, C. Günther, W. Schroder, A cut-cell method for sharp moving boundaries in cartesian grids. Comput. Fluids **85**, 135–142 (2013)
156. L. Schneiders, C. Guenther, J.H. Grimmen, M.H. Meinke, W. Schroeder, Sharp resolution of complex moving geometries using a multi-cut-cell viscous flow solver, in *22nd AIAA Computational Fluid Dynamics Conference* (American Institute of Aeronautics and Astronautics, 2015)
157. S. James, C. Madnia, Direct numerical simulation of a laminar vortex ring. Phys. Fluids **8**(9), 2400–2414 (1996)
158. J.S. Hewett, C. Madnia, Flame-vortex interaction in a reacting vortex ring. Phys. Fluids **10**(1), 189–205 (1998)

159. J.S. Hewett, C.K. Madnia, Flame evolution in a reacting vortex ring, in *Advanced Computation & Analysis of Combustion*, eds. by G.D. Roy, S.M. Frolov, P. Givi (ENAS Publishers, Moscow, Russia, 1997), pp. 371–3871
160. M.S. Triantafyllou, G.S. Triantafyllou, D.K.P. Yue, Hydrodynamics of fishlike swimming. Ann. Rev. Fluid Mech. **32**, 33–53 (2000)
161. I. Borazjani, F. Sotiropoulos, Numerical investigation of the hydrodynamics of carangiform swimming in the transitional and inertial flow regimes. J. Exp. Biol. **211**, 1541–1558 (2008)
162. M.H. Dickinson, K.G. Gotz, Unsteady aerodynamic performance of model wings at low Reynolds numbers. J. Exp. Biol. **174**(1), 45–64 (1993)
163. G. Liu, Y. Ren, H. Dong, O. Akanyeti, J.C. Liao, G.V. Lauder, Computational analysis of vortex dynamics and performance enhancement due to body-fin and fin-fin interactions in fish-like locomotion. J. Fluid Mech. **829**, 65–88 (2017)
164. A. Akbarzadeh, I. Borazjani, A numerical study on controlling flow separation via surface morphing in the form of backward traveling waves, in *AIAA Aviation 2019 Forum* (American Institute of Aeronautics and Astronautics, 2019)
165. A.L. Braslow, R.M. Hicks, R.V. Harris, Use of grit-type boundary-layer-transition trips on wind-tunnel models (1966)
166. J.C. Lin, Review of research on low-profile vortex generators to control boundary-layer separation. Prog. Aerosp. Sci. **38**(4–5), 389–420 (2002)
167. D. Greenblatt, I.J. Wygnanski, The control of flow separation by periodic excitation. Prog. Aerosp. Sci. **36**(7), 487–545 (2000)
168. A. Glezer, M. Amitay, Synthetic jets. Annu. Rev. Fluid Mech. **34**(1), 503–529 (2002)
169. G. Jones, M. Santer, M. Debiasi, G. Papadakis, Control of flow separation around an airfoil at low Reynolds numbers using periodic surface morphing. J. Fluids Struct. **76**, 536–557 (2018)
170. M.A. Bani-Hani, M.A. Karami, Analytical structural optimization and experimental verifications for traveling wave generation in self-assembling swimming smart boxes. Smart Mater. Struct. **24**, 094005 (2015)

A Coupled Eulerian-Lagrangian Framework for the Modeling and Simulation of Turbulent Multiphase Flows

Everett A. Wenzel and Sean C. Garrick

Abstract Interfacial multiphase flows are challenging to simulate because they involve many spatio-temporal scales and discontinuous fluid properties. This chapter describes a new framework for simulating interfacial flows (with an emphasis on sprays) that is consistent and conservative. The framework is based on the coupling of point mass particles (PMPs) with an Eulerian grid. Three different simulation methods are derived by enforcing different levels of coupling between the PMPs and the Eulerian grid. We first develop an expression that relates the PMP velocity to the fluid velocity, and use this expression to define a methodology for tracking an arbitrary number of phases and scalars. Performance of this approach is demonstrated in the context of heated air blast atomization. Next, we derive a governing equation for the fluid velocity in the context of the PMP, and present a consistent and conservative framework for solving the multiphase Navier-Stokes equations. The chapter concludes with the development of a formulation for consistent and conservative large eddy simulation, with particular attention paid to the importance of closure models.

Keywords Sprays · Direct numerical simulation · Large eddy simulation

1 Introduction

Interfacial multiphase flows are fluid dynamic systems that involve at least two immiscible fluids. Familiar examples of interfacial flows include oil spills, splashing ocean waves, and emulsions. Liquid jet atomization (commonly known as spray) is one of the most important interfacial flows because it determines engine efficiency, exhaust gas composition, properties of particles synthesized via spray drying, and transfer

E. A. Wenzel · S. C. Garrick (✉)
Department of Mechanical Engineering, University of Minnesota,
Minneapolis, MN 55455, USA
e-mail: sgarrick@umn.edu

E. A. Wenzel
e-mail: wenz0081@umn.edu

D. Livescu et al. (eds.), *Modeling and Simulation of Turbulent Mixing and Reaction*, Heat and Mass Transfer, https://doi.org/10.1007/978-981-15-2643-5_10

efficiency of fertilizers, herbicides, paints, protective coatings and medicines. The ability to quantitatively predict atomization dynamics is therefore relevant for both economic and environmental reasons, but the physics of atomization make accurate modeling and simulation a significant challenge.

Primary atomization is the process by which ligaments and droplets are removed directly from the liquid core of a spray—the liquid core is the contiguous liquid jet expelled from the spray orifice. Primary atomization, while poorly understood, is known to depend on fluid property ratios, long and short wave interface instability, orifice shape, turbulence levels upstream of the orifice, collisions of separated droplets with the liquid core, and gas phase vortex interactions with the liquid core [1–6]. The dispersed droplets produced by primary atomization continue to breakup, undergoing secondary atomization, until achieving a stable droplet size. Automotive fuel injection can produce 10^7 dispersed droplets and a system length scale ratio of 10^5 [7]. Engine performance depends strongly on the droplet size distribution, and accurate predictions of engine performance therefore rely heavily on accurately modeling and simulating the multiphase dynamics involved in atomization.

Computational methods used for spray simulation include Reynolds averaged Navier-Stokes (RANS), large eddy simulation (LES), and direct numerical simulation (DNS). RANS, the most affordable approach, relies on linear stability theory and/or stochastic models to treat primary and secondary atomization [8–13]. The RANS approach fails to accurately describe the atomization process because it does not resolve transient dynamics [14]. In contrast to RANS solutions, DNS provides every spatio-temporal detail of the flow field, but requires orders of magnitude more computational effort [4, 15–22]. Only recently has DNS of primary atomization been possible, but the simulations span only a few injector diameters and generally remain under-resolved. The simulations require at least $O(10^5)$ CPU hours and serve almost exclusively for scientific discovery [3]. Multiple approaches have been used to perform LES of sprays, and perhaps the most common is to model the liquid phase as Lagrangian droplets [11, 14, 23–30]. Droplet motion is governed by a Lagrangian particle equation, such as the Basset-Bousinesq-Oseen equation [28, 30], and droplet temperatures and evaporation are treated by model expressions appropriate for the particular problem. Primary and secondary atomization are treated by a wide array of deterministic and stochastic breakup models [11, 14, 28–31]. These Lagrangian treatments perform well when the primary atomization is accurately described (either by prescribing the initial droplet size distribution or by tuning model parameters), but they cannot be used when the primary atomization process is poorly defined. This shortcoming renders the droplet-based spray LES incapable of modeling primary atomization, and therefore sprays, in a predictive manner.

This chapter describes a new framework for the modeling and simulation of interfacial flows with direct applicability to sprays. The framework is built upon the Lagrangian point mass particle (PMP) discretization, known in the simulation community for its use in smoothed particle hydrodynamics (SPH). The methodology is novel in that it couples the PMP discretization with an Eulerian grid. This coupling provides a number of simulation frameworks that address the principal challenges of simulating complicated interfacial flows, namely: (1) tracking the location of each

phase; (2) performing consistent transport of conserved quantities in the presence of discontinuities; and (3) resolving all relevant spatio-temporal scales present in the flow. The chapter begins with an introduction to the PMP, and a description of how it discretizes the fluid domain. A coupling framework is then derived and presented for performing phase and scalar transport, followed by a case study of heated air blast atomization. The PMP-Eulerian grid coupling is then extended to include consistent mass-momentum transport. Finally, an LES implementation is introduced with a discussion of future efforts.

2 The Point Mass Particle[1]

Consider a system comprised of N_ζ phases ζ^α, identified by $\zeta^1, \zeta^2, \ldots, \zeta^{N_\zeta - 1}, \zeta^{N_\zeta}$. The spatial distribution of phase is defined by a phase indicator function χ^α corresponding to each phase ζ^α. The phase indicator corresponding to phase ζ^α is a binary function given by

$$\chi^\alpha(t, \mathbf{x}) = \begin{cases} 1, & \mathbf{x} \in \zeta^\alpha, \\ 0, & \mathbf{x} \notin \zeta^\alpha, \end{cases} \tag{1}$$

where $\mathbf{x} = \{x, y, z\}$.

The subdomain $\mathbf{x} \in \zeta^\alpha$ is discretized by N_α Lagrangian particles. Each particle i is associated with a mass, such that the total mass of phase ζ^α is distributed amongst the N_α particles, satisfying

$$\int_V \rho^\alpha \chi^\alpha dV = \sum_{i=1}^{N_\alpha} M_i, \tag{2}$$

where ρ^α is the density of phase ζ^α, M_i is the mass of particle i, and V is the domain volume (summation is not implied by repeated superscripts in this expression). In addition to mass M_i, each particle is associated with a position $\mathbf{X}_i$ (capital to emphasize the position as a property of particle i) and a Lagrangian phase indicator for each phase: particles belonging to phase ζ^α are identified by $\chi_i^\alpha = 1$ and particles belonging to a different phase are identified by $\chi_i^\alpha = 0$. The PMPs are therefore a discretization of the mass and the associated phase in the domain.

The fluid density at point $\mathbf{x}$ is approximated by convolving the mass M_i of every particle near $\mathbf{x}$ with a compact weight function W according to

$$\rho(\mathbf{x}) = \sum_{i=1}^{N_p} W(\mathbf{x} - \mathbf{X}_i, h) M_i, \tag{3}$$

[1]Material from this section has been reproduced from Wenzel and Garrick [32]. The reader is directed to reference [32] for additional details.

where N_p is the total number of particles belonging to any phase ζ^α within the compact support radius h of position $\mathbf{x}$ [33, 34]. The weight function $W(\mathbf{x} - \mathbf{X}_i, h)$ is defined as compact because $W(\mathbf{x} - \mathbf{X}_i, h) = 0$ for $|\mathbf{x} - \mathbf{X}_i| \geq h$. N_p appearing in Eq. (3) is therefore the total number of particles of any phase ζ^α whose position $\mathbf{X}_i$ satisfies $|\mathbf{x} - \mathbf{X}_i| < h$, where h is the "compact support radius" of the weight function W. In other words, N_p is the number of particles who make a non-zero contribution to the summation in Eq. (3); the position $\mathbf{X}_i$ of each of these particles satisfies $|\mathbf{x} - \mathbf{X}_i| < h$.

Particles move with velocity $\mathbf{U}_i$ and accelerate due to pressure gradients and surface tension according to

$$\frac{d\mathbf{U}_i}{dt} = \mathbf{P}_i + \mathbf{F}_i, \tag{4}$$

where $\mathbf{P}_i$ is the acceleration vector due to pressure and $\mathbf{F}_i$ is the acceleration vector due to surface tension. The specific form of $\mathbf{P}_i$ considered here is widely used to compute pressure acceleration in SPH simulations [35], and is derived from Eq. (3), an equation of state for pressure $P_i = f(\rho_i)$, and the principle of least action:

$$\mathbf{P}_i = -\sum_{j=1}^{N_p} \left(\frac{P_i}{\rho_i^2} + \frac{P_j}{\rho_j^2} \right) M_j \nabla W_{ij}, \tag{5}$$

where $\nabla W_{ij} = \nabla W\left(\mathbf{X}_i - \mathbf{X}_j, h\right)$ is the gradient of the weight function W evaluated at $\mathbf{X_j}$ relative to $\mathbf{X_i}$ [33, 34].

Immiscible multiphase systems include surface tension arising from molecular-scale interactions at the phase interface, resulting in acceleration $\mathbf{F}_i$. A variety of models are available to define $\mathbf{F}_i$, but here the pairwise force method is advised because it is conservative and well–validated in the context of SPH [36]. The surface force acceleration is given by

$$\mathbf{F}_i = \sum_{j=1}^{N_p} -F^{int}_{\zeta_i\zeta_j}\left(\left|\mathbf{r}_{ij}\right|\right) \frac{\mathbf{r}_{ij}}{\left|\mathbf{r}_{ij}\right|}, \tag{6}$$

where $\mathbf{r}_{ij} = \mathbf{X}_i - \mathbf{X}_j$, and the subscript $\zeta_i\zeta_j$ indicates that the inter-particle function $F^{int}_{\zeta_i\zeta_j}$ depends on the phases of particles i and j. The function $F^{int}_{\zeta_i\zeta_j}$ is defined to produce the surface tension coefficient corresponding to a specific multiphase system [36].

3 Coupled Eulerian-PMP for Phase Tracking[2]

A significant challenge of performing interfacial flow simulations is tracking the location of each phase, primarily because the phase indicator function, Eq. (1), is a heavyside function. Many different methods have been successfully implemented for determining the location of each phase, most prominently front-capturing [15, 16, 37–43], including modern implementations of the level set method [43–48] and the volume of fluid (VOF) method [49–52]. Front-tracking [53–57], particle-based [58–61], and fully Lagrangian methods [33, 36, 62–65] are also widely used. Each of these techniques have shortcomings which may include reinitialization, regularization, conservation error, prohibitive compute times, inaccurate description of surface tension, restrictions on the number of fluids considered, or numerical diffusion near interfaces [3, 4, 43, 45, 55]. This section couples the PMP discretization to a grid for the purpose of tracking the local phase.

We consider a multiphase system where the fluid velocity $\mathbf{u}$ is known at a set of Eulerian grid points and the phase information and mass has been discretized by a set of PMPs. The particles move with velocity $\mathbf{U}_i$ (defined by Eq. (4)) over a small time increment dt according to

$$d\mathbf{X}_i = \mathbf{U}_i dt. \tag{7}$$

An approximation of the velocity $\mathbf{U}_i$ of particle i located at $\mathbf{X}_i$ can be made by tri-linearly interpolating the fluid velocity $\mathbf{u}$ from the surrounding grid points to the location $\mathbf{x} = \mathbf{X}_i$. We denote the interpolated velocity by $\overline{\mathbf{u}}_i = \mathbf{G}(\mathbf{u}, \mathbf{X}_i)$, where $\mathbf{G}$ is the interpolation operator. The velocity $\overline{\mathbf{u}}_i$ approximates the velocity of an infinitesimal fluid particle or a tracer particle, rather than a PMP. Only in the limit as the particle mass goes to zero does a point mass particle behave as an infinitesimal fluid particle:

$$\lim_{M_i \to 0} \mathbf{U}_i \to \mathbf{u}(\mathbf{X}_i). \tag{8}$$

We decompose $\mathbf{U}_i$ into the interpolated velocity $\overline{\mathbf{u}}_i$ and a residual velocity $\mathbf{u}'_i$:

$$\mathbf{U}_i = \overline{\mathbf{u}}_i + \mathbf{u}'_i. \tag{9}$$

The interpolated velocity $\overline{\mathbf{u}}_i$ describes the velocity field resolved on the Eulerian mesh interpolated to the particle location. It includes errors associated with the interpolation scheme. The residual velocity, $\mathbf{u}'_i$, is comprised of the negative of the errors introduced by interpolation, and the motions required to satisfy the particle acceleration equation, Eq. (4). Assuming the interpolated velocity and the point mass velocities are smooth functions in time, and therefore differentiable, we substitute the decomposed velocity into the acceleration equation for the PMP, Eq. (4), to yield

[2]Material from this section has been reproduced from Wenzel and Garrick [32]. The reader is directed to reference [32] for additional details.

$$\frac{d\mathbf{U}_i}{dt} = \frac{d\overline{\mathbf{u}}_i}{dt} + \frac{d\mathbf{u}'_i}{dt} = \mathbf{F}_i + \mathbf{P}_i. \tag{10}$$

Further, we assume residual acceleration terms for pressure $\mathbf{P}'_i$ and surface tension $\mathbf{F}'_i$ exist such that

$$\frac{d\mathbf{u}'_i}{dt} = \mathbf{F}'_i + \mathbf{P}'_i, \tag{11}$$

and

$$\frac{d\mathbf{U}_i}{dt} = \frac{d\overline{\mathbf{u}}_i}{dt} + \mathbf{F}'_i + \mathbf{P}'_i. \tag{12}$$

Having decomposed the particle acceleration into Eulerian and Lagrangian terms, we proceed to develop an expression for velocity $\mathbf{U}_i$ as a function of time. Performing a backward Taylor series expansion between time levels n and $n-1$ separated by Δt yields

$$\mathbf{U}_i^{n-1} = \mathbf{U}_i^n - \frac{d\mathbf{U}_i}{dt}^n \Delta t - O\left(\Delta t^2\right), \tag{13}$$

or

$$\mathbf{U}_i^n = \mathbf{U}_i^{n-1} + \frac{d\mathbf{U}_i}{dt}^n \Delta t + O\left(\Delta t^2\right). \tag{14}$$

Substituting the velocity and acceleration decompositions into the right-hand-side relates the point mass velocity $\mathbf{U}_i$ to the interpolated and residual velocities,

$$\mathbf{U}_i^n = \overline{\mathbf{u}}_i^{n-1} + \frac{d\overline{\mathbf{u}}_i}{dt}^n \Delta t + \mathbf{u}_i'^{n-1} + \frac{d\mathbf{u}'_i}{dt}^n \Delta t + O\left(\Delta t^2\right). \tag{15}$$

After collapsing all time derivatives of the interpolated velocity and substituting Eq. (11), we arrive at an expression for the point mass particle velocity as a function of the interpolated velocity plus residual acceleration and residual velocity terms

$$\mathbf{U}_i^n = \overline{\mathbf{u}}_i^n + \left(\mathbf{F}'_i + \mathbf{P}'_i\right)^n \Delta t + \mathbf{u}_i'^{n-1} + O\left(\Delta t^2\right). \tag{16}$$

Given an Eulerian velocity field, the interpolated velocity term $\overline{\mathbf{u}}_i$ is known. The residual acceleration terms for pressure $\mathbf{P}'_i$ and surface tension $\mathbf{F}'_i$, and the residual velocity $\mathbf{u}'_i$ require closure models. Wenzel and Garrick [32] present a closure based on simplified expressions for the PMP pressure acceleration Eq. (5) and surface tension acceleration Eq. (6). Readers interested in implementation details of the phase tracking PMP method, such as numerical parameters and closures, are directed to reference [32]. With the addition of appropriate closures, Eq. (16) governs the motion of a field of particles that define the local phase and any other scalars assigned to the particles.

3.1 Case Study: Air Blast Atomization with Heat Transfer

We demonstrate the capability of the PMP tracking scheme by simulating the air blast atomization of a low temperature droplet in hot gas. Thermal energy transport is treated in the PMP framework by discretizing the system thermal energy with the PMPs, performing convection with Eq. (16), and performing thermal diffusion in the paradigm of SPH [66]. This heat transfer methodology conserves energy and boundedness in the presence of property discontinuities, and enforces consistency between the convection of thermal energy and fluid properties.

Problem Description

Air blast atomization describes the scenario where fast moving air flows over a low speed or stationary liquid, resulting in breakup of the liquid phase. Single droplet air blast atomization dynamics depend on the Reynolds number $Re = \rho_g D_o U_\infty / \mu_g$, the aerodynamic Weber number $We = \rho_g U_\infty^2 D_o / \sigma$, and the liquid Ohnesorge number $Oh = \mu_L / \sqrt{\rho_L D_o \sigma}$, where subscript g references the gas phase, subscript L references the droplet phase, U_∞ is the free-stream velocity, D_o is the initial droplet diameter, σ is the surface tension coefficient, ρ is the density, and μ is the dynamic viscosity. Breakup occurs above a critical Weber number of approximately $We_c \approx 12$ for large Reynolds numbers and low Ohnesorge numbers [67]. To promote breakup, we consider a flow configuration with $Re = 1341$, $Oh = 0.039$, and $We = 101$. These parameters are achieved by assigning the following gas phase properties

$$\rho_g = 1 \text{ kg/m}^3, \qquad \mu_g = 1.81 \times 10^{-5} \text{ kg/ (m} \cdot \text{s)}, \tag{17}$$

and property ratios of

$$\rho_L / \rho_g = 15, \qquad \mu_L / \mu_g = 20. \tag{18}$$

The surface tension coefficient is set to $\sigma = 0.006$ N/m and the initial droplet diameter is set to $D_o = 971$ μm. The droplet is initially stationary, and the surrounding gas is impulsively accelerated to a free-stream velocity of $U_\infty = 25$ m/s.

The dimensionless numbers relevant for thermal transport are the Reynolds number and the Prandtl number $Pr = c\mu / k$, where c is the specific heat capacity and k is the thermal conductivity. The Prandtl numbers of the droplet phase and gas phase are set to $Pr_L = 3.6$ and $Pr_g = 0.36$, respectively. The droplet is initially cool with a temperature of $T_{L_o} = 300$ K and the gas is initially hot with a temperature of $T_{g_o} = 500$ K.

Results

Temporal evolution of the droplet deformation, breakup, and heating process is shown in Fig. 1 (the ambient air flows from left to right). The figure shows the droplet surface colored by the local temperature. Panel (a) shows the droplet in its initial condition, panel (b) shows the drop at $t = 0.08$ ms, and panel (c) shows the drop at $t = 0.3$ ms. The droplet in panel (a) is initially spherical and cool. As the fast moving

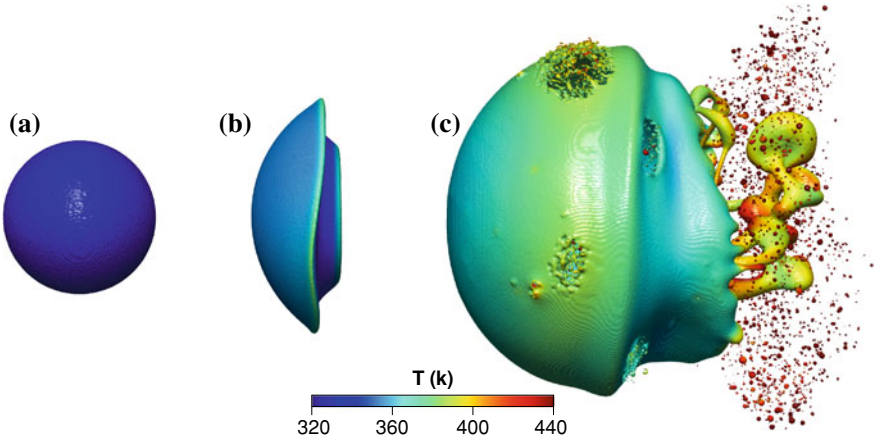

Fig. 1 Temporal evolution of the heated air blast atomization of a droplet. Hot ambient air flows over the droplet from left to right. **a** $t = 0$; **b** $t = 0.08$ ms; **c** $t = 0.3$ ms

gas passes over the droplet surface from left to right, a variety of dynamics evolve. Panel (b) shows that the droplet is simultaneously deformed and heated. At this early time, variations in temperature within the droplet phase are small, but slightly higher temperatures do appear at the outer-most surfaces on the downstream (right) side of the drop. At low density ratios, such as the present case with $\rho_L/\rho_g = 15$, a "bag" deformation is formed when the droplet wraps itself around a low pressure, recirculating wake. The early development of this bag deformation is apparent in panel (b), and the bag is fully developed at the later time in panel (c). The apparent size of the droplet has increased significantly because it has been stretched into a thin film. As the droplet thins, holes form in the surface, resulting in the sheet breakup mechanism. Sheet breakup produces the small droplets that are prominent at the downstream side of the drop in panel (c). Holes produced by sheet breakup grow radially under capillary forces, eventually merging with other nearby holes to form ligaments. The ligaments, also visible at the downstream side of the droplet, breakup under capillary forces, producing larger droplets. At the later time in panel (c), significant temperature variations are apparent in the droplet phase. The smallest droplets produced by sheet breakup are very hot (>440 k), while parts of the large structure remain relatively cool (<360 k). This results from a variety of fluid-thermal interactions related to droplet and ligament surface areas and volumes, boundary layer thicknesses, and recirculation. We note that these temperatures determine evaporation rates in combustion systems, and therefore accurate thermal modeling in sprays is critical to predictive combustion simulation.

To emphasize that this arblast simulation was performed with the PMP method, we compare the droplet phase PMPs to their corresponding Eulerian representation on the mesh. Figure 2 panel (a) shows the droplet phase PMPs colored by temperature, and panel (b) shows the corresponding Eulerian data. The PMPs in panel (a) are

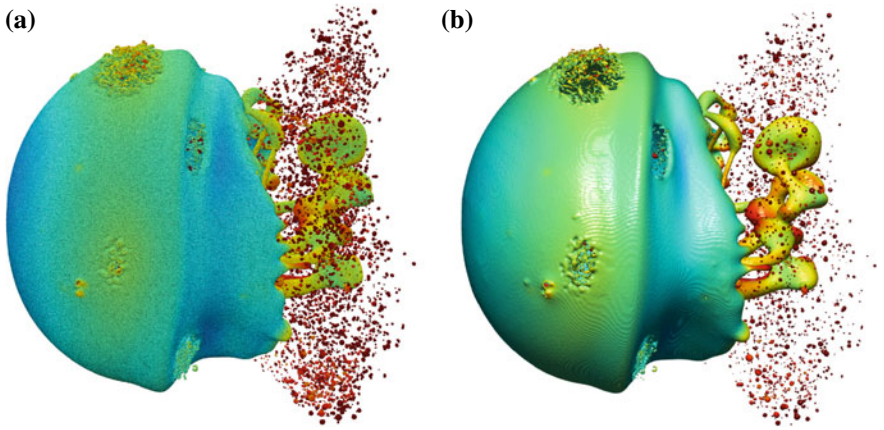

Fig. 2 Comparison between droplet phase PMPs colored by temperature and the corresponding Eulerian data at time $t = 0.3$ ms. **a** PMP field; **b** Eulerian field

the data used in the simulation to compute phase and thermal transport, while the Eulerian data in panel (b) is computed as a function of the PMPs on the Eulerian grid (this can be done in a variety of ways that we do not elaborate upon here [32]). In this simulation, each Eulerian control volume is discretized by two point mass particles. The particles are therefore a higher resolution discretization of the fluid system than the Eulerian grid. The capability of the PMPs to resolve more length scales than the Eulerian grid is made apparent by the larger number of small droplets in panel (a) than in panel (b). In order to fully leverage the small scale data provided by the PMP method in multiphase simulations with large property variations, we require a mass-momentum formulation that is consistent and conservative.

4 A Fully Consistent PMP[3]

Inconsistencies in the transport of fluid properties and conserved quantities near fluid interfaces generate numerical instabilities [52, 69]. Inconsistent transport arises from using different numerical schemes to compute the transport of different quantities. Inconsistent transport occurs, for example, when using a geometric VOF scheme to transport phase and density, and a centered scheme to transport momentum. In this section, we extend the PMP method to a conservative and consistent mass-momentum formulation by associating the particles with the fluid velocity.

Consider a particle that moves in space according to

$$d\mathbf{X} = \mathbf{u}dt + \mathbf{U}dt + \frac{1}{2}\mathbf{A}dt^2, \tag{19}$$

[3]Material from This Section Has Been Reproduced from Wenzel [68].

where $\mathbf{X}$ is the location of the particle, $\mathbf{u}$ is the fluid velocity at the location of the particle, and $\mathbf{U}$ and $\mathbf{A}$ are the particle velocity and acceleration vectors (defined by the PMP method). The fluid velocity does not entirely determine the particle trajectory, and therefore the particle is *not* a fluid particle. The local fluid velocity $\mathbf{u}$ changes as the particle moves. In order to determine how the fluid velocity changes as the particle moves through space and time, we follow the derivation principles of Dreeben and Pope [70]. We consider a small increment of fluid velocity resulting from a small displacement of the particle in space and time:

$$d\mathbf{u} = \frac{\partial \mathbf{u}}{\partial t} dt + \nabla \mathbf{u} \cdot d\mathbf{X} + \left[\frac{\partial \mathbf{u}}{\partial t} dt \right] [\nabla \mathbf{u} \cdot d\mathbf{X}] + H.O.T. \tag{20}$$

Substituting Eq. (19) into Eq. (20), retaining terms up to $O\left(dt^2\right)$ if they are multiplied by a component of acceleration $\mathbf{A}$, and up to $O\left(dt\right)$ if they are multiplied by a component of either velocity $\mathbf{U}$ or $\mathbf{u}$, returns

$$d\mathbf{u} = \frac{\partial \mathbf{u}}{\partial t} dt + \nabla \mathbf{u} \cdot \left[\mathbf{u} dt + \mathbf{U} dt + \frac{1}{2} \mathbf{A} dt^2 \right]. \tag{21}$$

The rationale for retaining different time orders for accelerations and velocities follows from Eq. (19), where spatial displacement depends on velocity to first-order and on acceleration to second-order with respect to time. Partially expanding the right-hand-side of Eq. (21) returns

$$d\mathbf{u} = \frac{\partial \mathbf{u}}{\partial t} dt + \mathbf{u} \cdot \nabla \mathbf{u} dt + \nabla \mathbf{u} \cdot \left[\mathbf{U} dt + \frac{1}{2} \mathbf{A} dt^2 \right]. \tag{22}$$

Again following [70], we consider the Navier-Stokes equations, expressed here in non-conservative form as

$$\frac{\partial \mathbf{u}}{\partial t} + \mathbf{u} \cdot \nabla \mathbf{u} = -\frac{1}{\rho} \nabla p + \frac{1}{\rho} \nabla \cdot \left(\mu \left(\nabla \mathbf{u} + \nabla^T \mathbf{u} \right) \right). \tag{23}$$

Interfacial dynamics enter the Navier-Stokes equations through the jump condition on pressure at the phase interface,

$$[p] = \sigma \kappa + 2 [\mu] \hat{\mathbf{n}}^T \cdot \nabla \mathbf{u} \cdot \hat{\mathbf{n}}, \tag{24}$$

where $[p]$ is the pressure jump at the interface, σ is the surface tension coefficient, κ is the interfacial curvature, $[\mu] = \mu_L - \mu_g$ is the difference in fluid viscosities, and $\hat{\mathbf{n}}$ is the interfacial unit normal vector. The left-hand-side of Eq. (23) is proportional to the first two terms on the right-hand-side of Eq. (22). In Eq. (22) we substitute the pressure and viscous terms for the temporal and convective terms, resulting in

$$d\mathbf{u} = \left[-\frac{1}{\rho}\nabla p + \frac{1}{\rho}\nabla \cdot \left(\mu \left(\nabla \mathbf{u} + \nabla^T \mathbf{u}\right)\right) + \nabla \mathbf{u} \cdot \left[\mathbf{U} + \frac{1}{2}\mathbf{A}dt\right]\right] dt. \tag{25}$$

Equation (25) is a first-order evolution equation for the fluid velocity $\mathbf{u}$ evaluated at the location $\mathbf{X}$ of a particle that moves in space according to Eq. (19). In order to leverage Eq. (25) in a coupled Eulerian-Lagrangian computational scheme, we require procedures to conservatively transfer information between the particles and an Eulerian grid.

4.1 Eulerian-Lagrangian Communication

Each particle i has a mass M_i, a phase ζ_i^α, a position $\mathbf{X}_i$ that evolves according to Eq. (19), and a fluid velocity $\mathbf{u}_i$ that evolves according to Eq. (25). The momentum of particle i is then

$$\mathbf{G}_i = M_i \mathbf{u}_i, \tag{26}$$

where the momentum of the fluid system is defined by the sum of particle momenta.

Eulerian density and momentum fields are computed from the particles. Each particle distributes its mass and momentum to an Eulerian grid using a spatially-compact distribution function $\mathcal{G}$. The function $\mathcal{G}$ is compact in that it only distributes mass and momentum to Eulerian cells within a cut-off distance h_d of particle i. In order to ensure consistency on a staggered Eulerian flow solver grid, mass and momentum must be defined at the same spatial locations [52, 69]. Similar to prior work [52, 69], we utilize a sub-grid with twice the resolution of the flow solver grid—in three dimensions, every Eulerian control volume contains eight sub-grid nodes. Unlike prior work, the sub-grid is a collocated grid, rather than a staggered grid. Each of the collocated sub-grid nodes gathers mass and momentum information from the particles, and then transfers the mass and momentum to the parent staggered-grid control volume. The details of these communications are described in this section.

The mass distributed from particle i to sub-grid node k, denoted by $M_{i\to k}$, is computed according to

$$M_{i\to k} = \frac{M_i \mathcal{G}\left(\mathbf{X}_i - \mathbf{x}_k, h_d\right)}{\sum_{j=1}^{N_j} \mathcal{G}\left(\mathbf{X}_i - \mathbf{x}_j, h_d\right)}. \tag{27}$$

The denominator on the right-hand-side is a scaling factor that ensures the totality of M_i is distributed amongst the N_j sub-grid nodes within the non-zero distribution radius h_d of particle i. The total mass distributed from particles to sub-grid node k, $\overline{m}_k$, is computed by summing the mass contributions from all particles,

$$\overline{m}_k = \sum_{i=1}^{N_i} M_{i\to k} = \sum_{i=1}^{N_i} \frac{M_i \mathcal{G}\left(\mathbf{X}_i - \mathbf{x}_k, h_d\right)}{\sum_{j=1}^{N_j} \mathcal{G}\left(\mathbf{X}_i - \mathbf{x}_j, h_d\right)}, \tag{28}$$

where N_i is the number of particles for which $M_{i\to k} \neq 0$. An identical distribution is performed for the momentum

$$(\overline{m\mathbf{u}})_k = \sum_{i=1}^{N_i} (M\mathbf{u})_{i\to k} = \sum_{i=1}^{N_i} \frac{M_i \mathbf{u}_i \mathcal{G}\left(\mathbf{X}_i - \mathbf{x}_k, h_d\right)}{\sum_{j=1}^{N_j} \mathcal{G}\left(\mathbf{X}_i - \mathbf{x}_j, h_d\right)}, \tag{29}$$

where $(\overline{m\mathbf{u}})_k$ is the momentum distributed from the particles to sub-grid node k. Mass and momentum are next transferred from the sub-grid to the flow solver grid.

Each sub-grid node falls within the bounds of a momentum control volume. The density and momentum are computed at the centroid of each momentum control volume by volume-averaging the sub-grid nodal values. This procedure returns the density according to

$$\rho = \frac{1}{V} \sum_{k=1}^{N_k} \overline{m}_k = \frac{1}{V} \sum_{k=1}^{N_k} \sum_{i=1}^{N_i} \frac{M_i \mathcal{G}\left(\mathbf{X}_i - \mathbf{x}_k, h_d\right)}{\sum_{j=1}^{N_j} \mathcal{G}\left(\mathbf{X}_i - \mathbf{x}_j, h_d\right)}, \tag{30}$$

where $V = \Delta x^3$ is the volume and $N_k = 8$ is the number of sub-grid nodes within the control volume (in three-dimensions). The momentum on the flow solver grid is similarly computed,

$$\mathbf{g} = \frac{1}{V} \sum_{k=1}^{N_k} (\overline{m\mathbf{u}})_k = \frac{1}{V} \sum_{k=1}^{N_k} \sum_{i=1}^{N_i} \frac{M_i \mathbf{u}_i \mathcal{G}\left(\mathbf{X}_i - \mathbf{x}_k, h_d\right)}{\sum_{j=1}^{N_j} \mathcal{G}\left(\mathbf{X}_i - \mathbf{x}_j, h_d\right)}. \tag{31}$$

Equations (30) and (31) provide an Eulerian density and momentum as a function of the particle field.

We now consider communication in the opposite direction—from the grid to the particles. Consider an increment of momentum $\delta\mathbf{g}$ computed on the Eulerian grid. We require a conservative mechanism to increment the momenta of the particles. For this purpose we again consider a distribution function. The momentum increment on the flow solver grid is first conservatively transferred to the sub-grid nodes. A simple approach is to divide the momentum increment uniformly over the sub-grid nodes N_k that were originally used to generate $\mathbf{g}$ in Eq. (31)

$$\delta\left(\overline{m\mathbf{u}}\right)_k = \delta\mathbf{g}/N_k. \tag{32}$$

The sub-grid nodal momenta can then be distributed to the particles in proportion to the mass the particles contributed to each sub-grid node

$$\delta\mathbf{u}_i = \sum_{k=1}^{N_k} \frac{\delta\left(\overline{m\mathbf{u}}\right)_k M_{i\to k}}{M_i \overline{m}_k}. \tag{33}$$

The communication procedures described in this section allow for conservative and consistent transfer of mass and momentum information between the particle field and a staggered Eulerian grid. These procedures are the building blocks of a coupled Eulerian-Lagrangian flow solving scheme that is conservative and consistent.

4.2 Discrete Mass and Momentum Integration

The fluid velocity $\mathbf{u}_i$, and the particle position $\mathbf{X}_i$, velocity $\mathbf{U}_i$, and acceleration $\mathbf{A}_i$ are known at time level n. The objective is to advance the solution to time level $n+1$, a finite increment in time of Δt, while conserving mass and momentum for arbitrary property variations amongst the phases. The solution is advanced with a combination of Lagrangian and Eulerian operations described in this section.

The particles move from $\mathbf{X}_i^n$ to $\mathbf{X}_i^{n+1}$ with the known fluid velocity $\mathbf{u}_i^n$ according to Eq. (19). After the particles have been moved to their new location, the Eulerian density at time level $n+1$ is computed according to Eq. (30)

$$\rho^{n+1} = \frac{1}{V}\sum_{k=1}^{N_k} \overline{m}_k^{n+1} = \frac{1}{V}\sum_{k=1}^{N_k}\sum_{i=1}^{N_i} \frac{M_i \mathcal{G}\left(\mathbf{X}_i^{n+1} - \mathbf{x}_k, h_d\right)}{\sum_{j=1}^{N_j} \mathcal{G}\left(\mathbf{X}_i^{n+1} - \mathbf{x}_j, h_d\right)}. \tag{34}$$

Moving the particles naturally accounts for convection of momentum through the Lagrangian operation C, represented here by

$$C = \mathbf{g}^n - \nabla \cdot (\rho \mathbf{u} \otimes \mathbf{u})^n \, \Delta t. \tag{35}$$

As the particles move from $\mathbf{X}_i^n$ to $\mathbf{X}_i^{n+1}$, the fluid velocity they carry is modified due to displacement from the particle velocity $\mathbf{U}_i^n$ and acceleration $\mathbf{A}_i^n$. This modification is accounted for by the last two terms on the right-hand-side of Eq. (25). These terms are non-conservative with respect to momentum. They are made conservative by considering an ensemble of N_e particles, comprised of the particles contained in a control volume that belong to the same phase. The mean $\mathbf{E}_{nc}$ of the non-conservative terms is computed amongst the ensemble

$$\mathbf{E}_{nc} = \frac{1}{N_e}\sum_{j=1}^{N_e} \left(\mathbf{U}_j^n + \frac{1}{2}\mathbf{A}_j^n \Delta t\right) \cdot \nabla \mathbf{u}^n \left(\mathbf{X}_j^n\right) \Delta t, \tag{36}$$

where $\nabla \mathbf{u}^n \left(\mathbf{X}_j^n\right)$ is the gradient of Eulerian velocity at time level n interpolated to the particle location at time level n. Subtracting $\mathbf{E}_{nc}$ from the non-conservative terms negates the conservation error. The resultant expression for fluid velocity on particle i at position $\mathbf{X}_i^{n+1}$ is

$$\mathbf{u}_i^* = \mathbf{u}_i^n + \left(\mathbf{U}_i^n + \frac{1}{2}\mathbf{A}_i^n \Delta t\right) \cdot \nabla \mathbf{u}^n \left(\mathbf{X}_i^n\right) \Delta t - \mathbf{E}_{nc}, \tag{37}$$

where $\mathbf{u}_i^*$ is the fluid velocity at time level n, augmented by the displacement in space due to $\mathbf{U}_i^n$ and $\mathbf{A}_i^n$. The Lagrangian convection operator C is then computed according to

$$\begin{aligned} C =& \mathbf{g}^n - \nabla \cdot (\rho \mathbf{u} \otimes \mathbf{u})^n \, \Delta t \\ =& \frac{1}{V} \sum_{k=1}^{N_k} (\overline{m\mathbf{u}})_k^* = \frac{1}{V} \sum_{k=1}^{N_k} \sum_{i=1}^{N_i} \frac{M_i \mathbf{u}_i^* \mathcal{G}\left(\mathbf{X}_i^{n+1} - \mathbf{x}_k, h_d\right)}{\sum_{j=1}^{N_j} \mathcal{G}\left(\mathbf{X}_i^{n+1} - \mathbf{x}_j, h_d\right)}. \end{aligned} \tag{38}$$

Moving the particles to $\mathbf{X}_i^{n+1}$ and updating $\mathbf{u}_i^n$ to $\mathbf{u}_i^*$ only partially advances the solution to time level $n+1$: viscous, pressure, and surface tension effects are treated with the Eulerian grid.

Consider an explicit, first-order discretization of the momentum equation with respect to time

$$\frac{\mathbf{g}^{n+1} - \mathbf{g}^n}{\Delta t} = -\nabla \cdot (\rho \mathbf{u} \otimes \mathbf{u})^n + \nabla \cdot (2\mu \mathbf{S} - p\mathbf{I})^n \,, \tag{39}$$

where the effects of surface tension have been absorbed by the pressure p according to Eq. (24). Solving for the momentum at time level $n+1$ returns

$$\mathbf{g}^{n+1} = \mathbf{g}^n - \nabla \cdot (\rho \mathbf{u} \otimes \mathbf{u})^n \, \Delta t + \nabla \cdot (2\mu \mathbf{S} - p\mathbf{I})^n \, \Delta t. \tag{40}$$

The effects of convection have already been computed via the Lagrangian operator C, allowing us to write

$$\mathbf{g}^{n+1} = C + \nabla \cdot (2\mu \mathbf{S} - p\mathbf{I})^n \, \Delta t. \tag{41}$$

We also choose to re-cast the remaining terms as a function of an intermediate velocity $\mathbf{u}^{**}$, defined by the most up-to-date particle information

$$\mathbf{u}^{**} = \frac{C}{\rho^{n+1}}, \tag{42}$$

resulting in

$$\mathbf{g}^{n+1} = C + \nabla \cdot (2\mu \mathbf{S} - p\mathbf{I})^{**} \, \Delta t. \tag{43}$$

This equation is solved for an incompressible flow with standard discretizations for the viscous term, operator splitting for pressure, and a ghost-fluid method for surface tension.

After the Eulerian momentum is updated to $\mathbf{g}^{n+1}$, a final modification of the fluid velocity carried by the particles is required. Referencing Eq. (25), we note that the last two terms on the right-had side have already been accounted for during the particle

displacement. Velocity changes due to pressure, surface tension, and viscous forces must be considered next. Using Eqs. (25) and (32), the relevant momentum increment for the sub-grid nodes is

$$\delta\left(\overline{m}\overline{\mathbf{u}}\right)_k^{n+1} = \nabla \cdot \left(2\mu\mathbf{S} - p\mathbf{I}\right)^{**} \Delta t / N_k. \tag{44}$$

The increment to particle velocity, according to Eq. (33), is

$$\delta\mathbf{u}_i^{n+1} = \sum_{k=1}^{N_k} \frac{\delta\left(\overline{m}\overline{\mathbf{u}}\right)_k^{n+1} M_{i\to k}^{n+1}}{M_i \overline{m}_k^{n+1}}, \tag{45}$$

and the updated particle velocity is given by

$$\mathbf{u}_i^{n+1} = \mathbf{u}_i^n + \delta\mathbf{u}_i^{n+1}. \tag{46}$$

The procedures outlined in this section provide a conservative and consistent method for integrating the multiphase Navier-Stokes equations with an arbitrary number of phases and arbitrary property variations. Simple multiphase flows can be fully-resolved on the Eulerian mesh. Complicated turbulent flows, however, contain a wide range of spatio-temporal scales. These flows require the use of LES.

5 Multiphase LES with the PMP[4]

Large eddy simulation reduces the computational cost of predicting fluid motion by solving filtered transport equations. The filtered fields have—ideally—a statistical relation to a filtered realization of the turbulent flow [71]. The Reynolds filtering operator, denoted by $\langle\rangle_\ell$, is defined by

$$\langle f\left(\mathbf{x}, t\right)\rangle_\ell = \int_{-\infty}^{\infty}\int_{-\infty}^{\infty} f\left(\mathbf{x}', t'\right) G\left(\mathbf{x} - \mathbf{x}', t - t'\right) dt' d\mathbf{x}', \tag{47}$$

where f is a function of space and time and G is the filter. The filter must satisfy a number of properties, and information pertinent to multiphase filtering operators can be found throughout the literature [72–74]. The Favre filtering operator is defined by

$$\langle f\rangle_L = \frac{\langle\rho f\rangle_\ell}{\langle\rho\rangle_\ell}, \tag{48}$$

where ρ is the fluid density. Favre filtering therefore produces a function that is both filtered and density-weighted. The purpose of the Favre filter is to decompose the

[4]Material from This Section Has Been Reproduced from Wenzel [68].

filtered momentum into a Favre filtered velocity and a filtered density according to the relation

$$\langle \rho \mathbf{u} \rangle_\ell = \langle \rho \rangle_\ell \frac{\langle \rho \mathbf{u} \rangle_\ell}{\langle \rho \rangle_\ell} = \langle \rho \rangle_\ell \langle \mathbf{u} \rangle_L, \tag{49}$$

where $\mathbf{u}$ is the velocity vector.

The Favre filtered governing equations for multiphase fluid dynamics are derived by first operating a Reynolds filter on the multiphase Navier-Stokes equations, followed by manipulating the equations to express all velocities as Favre filtered velocities [73]. The resultant expression for mass conservation is

$$\frac{\partial \langle \rho \rangle_\ell}{\partial t} + \nabla \cdot (\langle \rho \rangle_\ell \langle \mathbf{u} \rangle_L) = 0, \tag{50}$$

where (in the case of an incompressible fluid) the divergence of the Favre filtered velocity field is constrained by

$$\nabla \cdot \langle \mathbf{u} \rangle_L = \tau_{un}, \tag{51}$$

where

$$\tau_{un} = \frac{\langle \mathbf{u} \cdot \nabla \rho \rangle_\ell - \langle \mathbf{u} \rangle_L \cdot \nabla \langle \rho \rangle_\ell}{\langle \rho \rangle_\ell}. \tag{52}$$

The filtered momentum equation is given by

$$\begin{aligned} \frac{\partial \langle \rho \rangle_\ell \langle \mathbf{u} \rangle_L}{\partial t} + \nabla \cdot (\langle \rho \rangle_\ell \langle \mathbf{u} \rangle_L \otimes \langle \mathbf{u} \rangle_L) = \\ \nabla \cdot (2 \langle \mu \rangle_\ell \langle \mathbf{S} \rangle_L - \langle p \rangle_\ell \mathbf{I}) - \nabla \cdot \left(\boldsymbol{\tau}_{\rho uu} - \boldsymbol{\tau}_{\mu \mathbf{S}} \right) + \langle \mathbf{F}^s \rangle_\ell, \end{aligned} \tag{53}$$

where μ is the dynamic viscosity, $\mathbf{S}$ is the strain rate tensor, p is the pressure, and $\mathbf{I}$ is the identity matrix. The sub-filter and multiphase terms are the residual convective stress tensor

$$\tau_{\rho uu} = \langle \rho \rangle_\ell \left[\langle \mathbf{u} \otimes \mathbf{u} \rangle_L - \langle \mathbf{u} \rangle_L \otimes \langle \mathbf{u} \rangle_L \right], \tag{54}$$

the residual viscous stress tensor

$$\boldsymbol{\tau}_{\mu \mathbf{S}} = 2 \left[\langle \mu \mathbf{S} \rangle_\ell - \langle \mu \rangle_\ell \langle \mathbf{S} \rangle_L \right], \tag{55}$$

and the filtered surface tension

$$\langle \mathbf{F}^s \rangle_\ell = \langle \sigma \kappa \hat{\mathbf{n}} \delta \rangle_\ell, \tag{56}$$

where sub-filter notation is taken from [73]. The filtered surface tension acts at the interface δ in the normal direction $\hat{\mathbf{n}}$, and is proportional to the surface tension coefficient σ and the interfacial curvature κ. The final multiphase transport equation is for the phase indicator function of phase ζ^α

$$\frac{\partial \langle \chi^\alpha \rangle_\ell}{\partial t} + \nabla \cdot (\langle \chi^\alpha \rangle_\ell \langle \mathbf{u} \rangle_L) = -\nabla \cdot \tau_{\chi^\alpha}, \tag{57}$$

where χ^α is the phase indicator, and

$$\tau_{\chi^\alpha} = \langle \chi^\alpha \mathbf{u} \rangle_\ell - \langle \chi^\alpha \rangle_\ell \langle \mathbf{u} \rangle_L \tag{58}$$

is the residual flux of the phase indicator.

The multiphase LES equations, as expressed here, include five sub-grid scale terms: τ_{un}, $\tau_{\rho uu}$, $\tau_{\mu \mathbf{S}}$, $\langle \mathbf{F}^s \rangle_\ell$, and τ_{χ^α}. Unlike single phase fluid dynamics, multiphase interfacial dynamics are not cascades; the small scale features are not necessarily functions of resolved features. This topic is considered in depth by Herrmann and Gorokhovski [75], who argue that a fully-resolved interface is required for predictive LES of multiphase systems because breakup processes in the sub-grid cannot be informed by the resolved scales. In other words, Herrmann and Gorokhovski [75] argue it is insufficient to simply close the SGS terms. Rather, it is as important to maintain a physical representation of the sub-grid scales because the smallest scales in multiphase flows are typically of interest in applications. In the following sections, we extend the PMP approach to LES by leveraging concepts used in probability density function and filtered density function methods.

5.1 PMP Turbulence Modeling with the Langevin Equation

Decompose the fluid particle velocity equation, given by Eq. (25), into filtered and residual components

$$\begin{aligned} d\mathbf{u} = &-\frac{1}{\langle \rho \rangle_\ell} \nabla \langle p \rangle_\ell dt + \frac{1}{\langle \rho \rangle_\ell} \nabla \cdot \left(\langle \mu \rangle_\ell \left(\nabla \langle \mathbf{u} \rangle_L + \nabla^T \langle \mathbf{u} \rangle_L \right) \right) dt + \\ &\nabla \langle \mathbf{u} \rangle_L \cdot \left[\mathbf{U} + \frac{1}{2} \mathbf{A} dt \right] dt + \\ &\tau_1 dt + \tau_2 dt + \tau_3 dt, \end{aligned} \tag{59}$$

where τ_1, τ_2, and τ_3 are residual terms defined by

$$\tau_1 = -\frac{1}{\rho} \nabla p + \frac{1}{\langle \rho \rangle_\ell} \nabla \langle p \rangle_\ell, \tag{60}$$

and

$$\tau_2 = \frac{1}{\rho} \nabla \cdot \left(\mu \left(\nabla \mathbf{u} + \nabla^T \mathbf{u} \right) \right) - \frac{1}{\langle \rho \rangle_\ell} \nabla \cdot \left(\langle \mu \rangle_\ell \left(\nabla \langle \mathbf{u} \rangle_L + \nabla^T \langle \mathbf{u} \rangle_L \right) \right), \tag{61}$$

and

$$\tau_3 = \nabla \mathbf{u} \cdot \left[\mathbf{U} + \frac{1}{2} \mathbf{A} dt \right] - \nabla \langle \mathbf{u} \rangle_L \cdot \left[\mathbf{U} + \frac{1}{2} \mathbf{A} dt \right]. \tag{62}$$

The principal challenge of performing LES with the PMP method is closing each of these residual terms—this remains an open problem with a variety of potential solutions. One solution is to use fractal interpolation [76] to produce a synthetic velocity field at the resolution of the particle field. This approach has been proposed in the context of Eulerian VOF simulations, and requires the phase interface to be fully-resolved [77]. A second potential solution is to model the residual terms using the accelerations acquired from the PMP method, or stochastic models for fluid particle acceleration (such as those discussed in [78]). In this section, in order to adhere to prior work in probability density function methods [70, 79], we close the unknown residual quantities with the Generalized Langevin Equation

$$(\tau_1 + \tau_2 + \tau_3)\, dt = \mathbf{G} \left(\mathbf{u} - \langle \mathbf{u} \rangle_L \right) dt + \sqrt{C_0 \epsilon} d\mathbf{W} \tag{63}$$

where $\mathbf{G}$, C_0, and ϵ are parameters of the Generalized Langevin Equation (to be defined shortly), and $d\mathbf{W}$ is an increment of the Wiener vector process. The governing equations for the modeled particles are then

$$d\mathbf{X} = \mathbf{u} dt + \mathbf{U} dt + \frac{1}{2} \mathbf{A} dt^2 \tag{64}$$

and

$$\begin{aligned} d\mathbf{u} = & -\frac{1}{\langle \rho \rangle_\ell} \nabla \langle p \rangle_\ell dt + \frac{1}{\langle \rho \rangle_\ell} \nabla \cdot \left(\langle \mu \rangle_\ell \left(\nabla \langle \mathbf{u} \rangle_L + \nabla^T \langle \mathbf{u} \rangle_L \right) \right) dt + \\ & \nabla \langle \mathbf{u} \rangle_L \cdot \left[\mathbf{U} + \frac{1}{2} \mathbf{A} dt \right] dt + \\ & \mathbf{G} \left(\mathbf{u} - \langle \mathbf{u} \rangle_L \right) dt + \sqrt{C_0 \epsilon} d\mathbf{W}, \end{aligned} \tag{65}$$

which determine the evolution of particle position and fluid velocity in time. The system of equations can be closed by specifying the simplified Langevin model, where

$$\mathbf{G} = -\omega \left(\frac{1}{2} + \frac{3}{4} C_0 \right) \mathbf{I}, \tag{66}$$

$$\omega = \frac{\epsilon}{k}, \tag{67}$$

$$\epsilon = C_\epsilon \frac{k^{3/2}}{\Delta x}, \tag{68}$$

$$k = \frac{1}{2} \left[\langle \mathbf{u} \cdot \mathbf{u} \rangle_L - \langle \mathbf{u} \rangle_L \langle \mathbf{u} \rangle_L \right], \tag{69}$$

where C_0 and C_ϵ are model parameters.

5.2 Discrete Mass and Momentum Integration

The solution procedure for the filtered equations is similar to that outlined in Sect. 4.2 for the non-filtered equations. This section outlines some notable exceptions and caveats.

The particles, which are significantly more numerous than the number of Eulerian grid points, are advanced from position $\mathbf{X}_i^n$ to $\mathbf{X}_i^{n+1}$ with velocity $\mathbf{u}_i^n$ (and $\mathbf{U}_i^n$ and $\mathbf{A}_i^n$), and the filtered density is computed at $n+1$

$$\langle \rho \rangle_\ell^{n+1} = \frac{1}{V} \sum_{k=1}^{N_k} \langle \overline{m}_k \rangle_\ell^{n+1} = \frac{1}{V} \sum_{k=1}^{N_k} \sum_{i=1}^{N_i} \frac{M_i \mathcal{G}\left(\mathbf{X}_i^{n+1} - \mathbf{x}_k, h_d\right)}{\sum_{j=1}^{N_j} \mathcal{G}\left(\mathbf{X}_i^{n+1} - \mathbf{x}_j, h_d\right)}. \tag{70}$$

The intermediate fluid velocities $\mathbf{u}_i^*$ are computed next. In the context of LES, the intermediate fluid velocity includes the spatial corrections due to displacement via particle velocity, in addition to residual terms introduced by the Langevin equation. The last term on the right-hand-side of Eq. (65) is a non-conservative, random walk in velocity space. This term is included in the non-conservative correction

$$\mathbf{E}_{nc} = \frac{1}{N_e} \sum_{j=1}^{N_e} \left[\left(\mathbf{U}_j^n + \frac{1}{2} \mathbf{A}_j^n \Delta t \right) \cdot \nabla \langle \mathbf{u} \rangle_L^n \left(\mathbf{X}_j^n \right) \Delta t + \sqrt{C_0 \epsilon} d\mathbf{W}_j \right], \tag{71}$$

where $\nabla \langle \mathbf{u} \rangle_L^n \left(\mathbf{X}_j^n \right)$ is the gradient of the Favre-filtered Eulerian velocity at time level n interpolated to the particle location at time level n. The resultant expression for fluid velocity on particle i at position $\mathbf{X}_i^{n+1}$ is

$$\begin{aligned} \mathbf{u}_i^* =& \mathbf{u}_i^n + \left(\mathbf{U}_i^n + \frac{1}{2} \mathbf{A}_i^n \Delta t \right) \cdot \nabla \langle \mathbf{u} \rangle_L^n \left(\mathbf{X}_i^n \right) \Delta t + \\ & \mathbf{G}\left(\mathbf{u}_i^n - \langle \mathbf{u} \rangle_L^n \right) \Delta t + \sqrt{C_0 \epsilon} d\mathbf{W}_i - \mathbf{E}_{nc}. \end{aligned} \tag{72}$$

The filtered Lagrangian convection operator $\langle C \rangle_\ell$ is then computed according to

$$\langle C \rangle_\ell = \frac{1}{V} \sum_{k=1}^{N_k} \langle \overline{m\mathbf{u}} \rangle_{\ell k}^* = \frac{1}{V} \sum_{k=1}^{N_k} \sum_{i=1}^{N_i} \frac{M_i \mathbf{u}_i^* \mathcal{G}\left(\mathbf{X}_i^{n+1} - \mathbf{x}_k, h_d\right)}{\sum_{j=1}^{N_j} \mathcal{G}\left(\mathbf{X}_i^{n+1} - \mathbf{x}_j, h_d\right)}. \tag{73}$$

The filtered momentum equation is again considered in discrete, first-order fashion with respect to time

$$\frac{\langle \rho \mathbf{u} \rangle_\ell^{n+1} - \langle \rho \mathbf{u} \rangle_\ell^n}{\Delta t} = -\nabla \cdot \langle \rho \mathbf{u} \otimes \mathbf{u} \rangle_\ell^n + \nabla \cdot \left(2 \langle \mu \rangle_\ell \langle \mathbf{S} \rangle_L - \langle p \rangle_\ell \mathbf{I} \right)^n + \nabla \cdot \boldsymbol{\tau}_{\mu \mathbf{S}}^n + \langle \mathbf{F}^s \rangle_\ell^n. \tag{74}$$

The residual inertial term $\tau_{\rho uu}$ that typically requires modeling does not appear here because the filtered momentum has not been decomposed into velocity and density components. Instead, the effects of this term have been absorbed into the filtered Lagrangian convection operator by means of the Langevin equation. Solving for the filtered momentum at $n+1$ and substituting the filtered Lagrangian convection operator returns

$$\langle \rho \mathbf{u} \rangle_\ell^{n+1} = \langle C \rangle_\ell + \nabla \cdot (2\langle \mu \rangle_\ell \langle \mathbf{S} \rangle_L - p\mathbf{I})^{**} + \nabla \cdot \boldsymbol{\tau}_{\mu \mathbf{S}}^n + \langle \mathbf{F}^s \rangle_\ell^n, \tag{75}$$

where the Favre-filtered velocity used in the strain rate tensor is computed by

$$\langle \mathbf{u} \rangle_L^{**} = \frac{\langle C \rangle_\ell}{\langle \rho \rangle_\ell^{n+1}}. \tag{76}$$

The residual inertial term $\tau_{\rho uu}$ has been closed, but we have arrived at a series of challenges:

1. Closure of the SGS viscous term $\boldsymbol{\tau}_{\mu \mathbf{S}}^n$ requires modeling decisions. This term is much less important than all of the other SGS terms, and it is only non-zero at the interface [73]. For now, without a rational closure strategy, this term is simply neglected.
2. Closure of the filtered surface tension $\langle \mathbf{F}^s \rangle_\ell$ is required for solution of the Poisson equation for pressure. A number of potential closures are available. Following the work of [75], one could compute the surface tension on every PMP near the interface via the Finite Particle Method [80], followed by an explicit filtering operation, resulting in $\langle \mathbf{F}^s \rangle_\ell$. This is a mathematically rigorous closure (if the particle field is sufficiently resolved, as is required by [75]). The open question is how well the approach works in practice. Alternatively, the surface tension computed from the pairwise force method could be used for the same purpose. Evaluating the relative merits of these closures as a function of mesh resolution and filter size is an area of future work.
3. The Favre-filtered velocity field is not divergence-free at the interface, which precludes the use of the standard Poisson approach for identifying the pressure.

An immediate solution is simply to neglect $\boldsymbol{\tau}_{\mu \mathbf{S}}^n$, compute $\langle \mathbf{F}^s \rangle_\ell$ via explicit filtering, and to assume the Favre-filtered velocity field is divergence-free everywhere. Equation (75) is then solved with the standard operator splitting approach for pressure, coupled with the ghost fluid method for surface tension. Momentum increments are then transferred to the particles with expressions analogous to Eqs. (44)–(46). This LES framework enforces conservative and consistent transport of all conserved quantities.

6 Summary

This chapter has outlined a new framework for simulating interfacial flows, with a particular emphasis on sprays. The framework is based on the coupling of point mass particles (PMPs) with an Eulerian grid, and aims to address the three principle challenges of spray simulation: (1) tracking the location of each phase; (2) performing consistent transport of conserved quantities in the presence of discontinuities; and (3) resolving all relevant spatio-temporal scales present in the flow. An implementation appropriate for tracking the location of an arbitrary number of phases was derived by discretizing the system mass and phase information with the PMPs. By leveraging techniques from smoothed particle hydrodynamics, this method was extended to perform conservative, consistent, and bounded simulation of thermal transport. Performance of the phase tracking PMP coupled with thermal transport was demonstrated via simulation of heated air blast atomization. In order to address the consistency and stability challenges of spray simulation, we extended the formulation to a completely consistent and conservative mass-momentum implementation. This required the derivation of a governing equation for fluid velocity in the context of the PMP, as well as a discrete integration strategy for the Naiver-Stokes equations. Finally, in order to address the challenge of resolving the spatio-temporal scales in a spray, we extended the consistent mass-momentum framework to a large eddy simulation implementation. The LES implementation is favorable because it preserves all of the conservation and consistency properties of the PMP. With appropriate selection of closure models, the LES implementation has the potential to become the first method for performing predictive LES of sprays.

References

1. G. Faeth, Structure and atomization properties of dense turbulent sprays, in *Twenty-Third Symposium (International) on Combustion/The Combustion Institute*, (1990), pp. 1345–1352
2. G. Faeth, L.-P. Hsaing, P.-K. Wu, Structure and breakup properties of sprays. Int. J. Multiphas. Flow **21**, 99–127 (1995)
3. M. Gorokhovski, M. Herrmann, Modeling primary atomization. Annu. Rev. Fluid Mech. **40**, 343–366 (2008)
4. J. Shinjo, A. Umemura, Simulation of liquid jet primary breakup: Dynamics of ligament and droplet formation. Int. J. Multiphas. Flow **36**(7), 513–532 (2010)
5. D. Zuzio, J. Estivalezes, P. Villedieu, G. Blanchard, Numerical simulation of primary and secondary atomization. C. R. Macanique **341**, 15–25 (2013)
6. F. Xiao, M. Dianat, J. McGurik, LES of turbulent liquid jet primary breakup in turbulent coaxial air flow. Int. J. Multiphas. Flow **60**, 103–118 (2014)
7. T. Fansler, S. Parrish, Spray measurement technology: A review. Meas. Sci. Technol. **26**, 01002 (2015)
8. R. Reitz, Modeling atomization processes in high-pressure vaporizing sprays. Atomiz. Spray Technol. **3**, 309–337 (1987)
9. P. O'Rourke and A. Amsden, The TAB method for numerical calculation of spray droplet breakup, in *SAE Paper 872089* (1987)

10. P. Senecal, D. Schmidt, I. Nouar, C. Rutland, R. Reitz, M. Corradini, Modeling high-speed viscous liquid sheet atomization. Int. J. Multiphas. Flow **25**, 1073–1097 (1999)
11. S. Apte, M. Gorokhovski, P. Moin, LES of atomizing spray with stochastic modeling of secondary breakup. Int. J. Multiphas. Flow **29**, 1503–1522 (2003)
12. M. Gorokhovski, V. Saveliev, Analysis of Kolmogorov's model of breakup and its application to Lagrangain computation of liquid sprays under air-blast atomization. Phys. Fluids **15**(1), 184–191 (2003)
13. S. Sazhin, S. Martynov, T. Kristyadi, C. Crua, M. Heikal, Diesel fuel spray penetration, heating, evaporation and ignition: Modelling versus experimentation. Int. J. Eng. Syst. Model. Simul. **1**(1), 1–19 (2008)
14. A. Iannetti and J. Moder, Comparing spray characteristics from Reynolds averaged Navier-Stokes (RANS) national combustion code (NCC) calculations against experimental data for a turbulent reacting flow, in *48th Aerospace Sciences Meeting*, (AIAA–2010–578, 2010)
15. T. Menard, S. Tanguy, A. Berlemont, Coupling level set/VOF/ghost fluid methods: Validation and application to 3D simulation of the primary break-up of a liquid jet. Int. J. Multiphas. Flow **33**(5), 510–524 (2007)
16. O. Desjardins, V. Moureau, H. Pitsch, An accurate conservative level set/ghost fluid method for simulating turbulent atomization. J. Comput. Phys. **227**(18), 8395–8416 (2008)
17. M. Pai, O. Desjardins, H. Pitsch, Detailed simulations of primary breakup of turbulent liquid jets in crossflow Tech. Rep. Cent. Turbul. Res. (2008)
18. R. Lebas, T. Menard, P. Beau, A. Berlemont, F. Demoulin, Numerical simulation of primary break-up and atomization: DNS and modelling study. Int. J. Multiphas. Flow **35**, 247–260 (2008)
19. D. Fuster, A. Bague, T. Boeck, L. Moyne, A. Leboissetier, S. Popinet, P. Ray, R. Scardovelli, S. Zaleski, Simulation of primary atomization with an octree adaptive mesh refinement and VOF method. Int. J. Multiphas. Flow **35**, 550–565 (2009)
20. M. Herrmann, Detailed numerical simulations of the primary atomization of a turbulent liquid jet in crossflow. J. Eng. Gas Turb. Power **132**, 061506 (2010)
21. B. Duret, J. Reveillon, T. Menard, F. Demoulin, Improving primary atomization modeling through DNS of two-phase flows. Int. J. Multiphas. Flow **55**, 130–137 (2013)
22. C. Zhu, M. Ertl, B. Weigand, Numerical investigation on the primary breakup of an inelastic non-Newtonian liquid jet with inflow turbulence. Phys. Fluids **25**, 083102 (2013)
23. K. Mahesh, G. Constantinescu, S. Apte, G. Iaccarino, P. Moin, Large-eddy simulation of gas turbine combustors. Tech. Rep. Cent. Turbul. Res. (2001)
24. F. Ham, S. Apte, G. Iaccarino, X. Wu, M. Herrmann, G. Constantinescu, K. Mahesh, P. Moin, Unstructured LES of reacting multiphase flows in realistic gas turbine combustors. Tech. Rep. Cent. Turbul. Res. (2003)
25. R. Kurose, O. Desjardins, M. Nakamura, F. Akamatsu, H. Pitsch, Numerical simulations of spray flames. Tech. Rep. Cent. Turbul. Res. (2004)
26. T. Lederlin, H. Pitsch, Large-eddy simulation of an evaporating and reacting spray, Tech. Rep. Cent. Turbul. Res. (2008)
27. M. Chrigui, A. Masri, A. Sadiki, J. Janicka, Large eddy simulation of a polydisperse ethanol spray flame. Flow Turbul. Combust **90**, 813–832 (2013)
28. A. Irannejad, F.A. Jaberi, Large eddy simulation of turbulent spray breakup and evaporation. Int. J. Multiphas. Flow **61**, 108–128 (2014)
29. C. Gong, M. Jangi, T. Lucchini, G. D'Errico, X.-S. Bai, Large eddy simulation of air entrainment and mixing in reacting and non-reacting diesel sprays. Flow Turbul. Combust. **93**, 385–404 (2014)
30. A. Irannejad, A. Banaeizadeh, F. Jaberi, Large eddy simulation of turbulent spray combustion. Combust. Flame **162**, 431–450 (2015)
31. M. Turner, S. Sazhin, J. Healey, C. Crua, S. Martynov, A breakup model for transient diesel fuel sprays. Fuel **97**, 288–305 (2012)
32. E.A. Wenzel, S.C. Garrick, A point-mass particle method for the simulation of multiphase flows on an Eulerian mesh, J. Comput. Phys. **397**, 108835 (2019)

33. M.B. Liu, G.R. Liu, Smoothed particle hydrodynamics (SPH): An overview and recent developments. Arch. Comput. Methods Eng. **17**(1), 25–76 (2010)
34. D.J. Price, Smoothed particle hydrodynamics and magnetohydrodynamics. J. Comput. Phys. **227**(3), 759–794 (2012)
35. J.J. Monaghan, Smoothed particle hydrodynamics. Annu. Rev. Astron. Astrophys. **30**, 543–574 (1992)
36. A.M. Tartakovsky, A. Panchenko, Pairwise force smoothed particle hydrodynamics model for multiphase flow: Surface tension and contact line dynamics. J. Comput. Phys. **305**, 1119–1146 (2016)
37. C.W. Hirt, B.D. Nichols, Volume of fluid (VOF) method for the dynamics of free boundaries. J. Comput. Phys. **39**(1), 201–225 (1981)
38. S. Osher, J.A. Sethian, Fronts propagating with curvature-dependent speed: Algorithms based on Hamilton-Jacobi formulations. J. Comput. Phys. **79**(1), 12–49 (1988)
39. M. Sussman, P. Smereka, S. Osher, A level set approach for computing solutions to incompressible two-phase flow. Phys. Fluids A **114**(1), 146–159 (1994)
40. M. Sussman, E.G. Puckett, A coupled level set and volume-of-fluid method for computing 3D and axisymmetric incompressible two-phase flows. J. Comput. Phys. **162**(2), 301–337 (2000)
41. E. Olsson, G. Kreiss, A conservative level set method for two phase flow. J. Comput. Phys. **210**(1), 225–246 (2005)
42. E. Olsson, G. Kreiss, S. Zahedi, A conservative level set method for two phase flow II. J. Comput. Phys. **225**(1), 785–807 (2007)
43. M. Herrmann, A balanced force refined level set grid method for two-phase flows on unstructured flow solver grids. J. Comput. Phys. **227**(4), 2674–2706 (2008)
44. O. Desjardins, H. Pitsch, A spectrally refined interface approach for simulating multiphase flows. J. Comput. Phys. **20**, 1658–1677 (2009)
45. D. Enright, R. Fedkiw, J. Ferziger, I. Mitchell, A hybrid particle level set method for improved interface capturing. J. Comput. Phys. **183**(1), 83–116 (2002)
46. D. Enright, F. Losasso, R. Fedkiw, A fast and accurate semi-Lagrangian particle level set method. Comput. Struct. **83**, 479–490 (2005)
47. Z. Li, F.A. Jaberi, T.I.-P. Shih, A hybrid Lagrangian-Eulerian particle-level set method for numerical simulations of two-fluid turbulent flows. Int. J. Numer. Meth. Fluids **56**, 2271–2300 (2008)
48. R. Bermejo, J.L. Prieto, A semi-Lagrangian particle level set finite element method for interface problems. SIAM J. Sci. Comput. **35**(4), A1815–A1846 (2013)
49. G. Weymouth, D. Yue, Conservative volume-of-fluid method for free-surface simulations on cartesian-grids. J. Comput. Phys. **229**(8), 2853–2865 (2010)
50. A. Cervone, S. Manservisi, R. Scardovelli, An optimal constrained approach for divergence-free velocity interpolation and multilevel VOF method. Comput. Fluids **47**, 101–114 (2011)
51. M. Owkes, O. Desjardins, A computational framework for conservative, three-dimensional, unsplit, geometric transport with application to the volume-of-fluid (VOF) method. J. Comput. Phys. **270**, 587–612 (2014)
52. M. Owkes, O. Desjardins, A mass and momentum conserving unsplit semi-Lagrangian framework for simulating multiphase flows. J. Comput. Phys. **332**, 21–46 (2017)
53. G. Moretti, Computation of flows with shocks. Ann. Rev. Fluid Mech. **19**, 313–337 (1987)
54. S.O. Unverdi, G. Tryggvason, A front-tracking method for viscous, incompressible, multi-fluid flows. J. Comput. Phys. **100**, 25–37 (1992)
55. D.J. Torres, J.U. Brackbill, The point-set method: Front-tracking without connectivity. J. Comput. Phys. **165**, 620–644 (2000)
56. J.P. Gois, A. Nakano, L.G. Nonato, G.C. Buscaglia, Front tracking with moving-least-squares surfaces. J. Comput. Phys. **227**, 9643–9669 (2008)
57. H. Terashima, G. Tryggvason, A front-tracking/ghost-fluid method for fluid interfaces in compressible flows. J. Comput. Phys. **228**, 4012–4037 (2009)
58. F.H. Harlow, J.E. Welch, Numerical calculation of time-dependent viscous incompressible flow of fluid with a free surface. Phys. Fluids **8**, 2182–2189 (1965)

59. F.H. Harlow, The particle-in-cell computing method for fluid dynamics. Methods Comput. Phys. **3**, 319–343 (1963)
60. J. Liu, S. Koshizuka, Y. Oka, A hybrid particle-mesh method for viscous, incompressible, multiphase flows, J. Comput. Phys. **202**(1), 65–93 (2005)
61. E. Edwards, R. Bridson, A high-order accurate particle-in-cell method. Int. J. Numer. Meth. Eng. **90**, 1073–1088 (2012)
62. J. Morris, Simulating surface tension with smoothed particle hydrodynamics. Int. J. Numer. Meth. Fl. **33**, 333–353 (2000)
63. N. Nishio, K. Yamana, Y. Yamaguchi, T. Inaba, K. Kuroda, T. Nakajima, K. Ohno, H. Fujimura, Large-scale SPH simulations of droplet impact onto a liquid surface up to the consequent formation of Worthington jet. Int. J. Numer. Methods Fluids **63**(12), 1435–1447 (2010)
64. F.V. Sirotkin, J.J. Yoh, A new particle method for simulating breakup of liquid jets. J. Comput. Phys. **231**, 1650–1674 (2012)
65. H. Lei, C.J. Mundy, G. Schenter, Modeling nanoscale hydrodynamics by smoothed dissipative particle dynamics. J. Chem. Phys. **142**, 194504 (2015)
66. P. Cleary, J. Monaghan, Conduction modelling using smoothed particle hydrodynamics. J. Comput. Phys. **148**, 227–264 (1999)
67. M. Jain, R. Prakash, G. Tomar, R. Ravikrishna, Secondary breakup of a drop at moderate Weber numbers. Proc. R. Soc. A **471**, 20140930 (2018)
68. E.A. Wenzel. *Methods for the Modeling and Simulation of Sprays and Other Interfacial Flows*. Ph.D. thesis, University of Minnesota - Twin Cities (2019)
69. M. Rudman, A volume-tracking method for incompressible multifluid flows with large density variations. Int. J. Numer. Methods Fluids **28**(2), 357–378 (1998)
70. T. Dreeben, S. Pope, Probability density function and Reynolds-stress modeling of near-wall turbulent flows. Phys. Fluids **9**, 154–163 (1997)
71. S. Pope, Ten questions concerning the large-eddy simulation of turbulent flows. New J. Phys. **6**(35), 2–23 (2003)
72. M. Herrmann, M. Gorokhovski, A large eddy simulation subgrid model for turbulent phase interface dynamics, in *Proceedings of the 11th Triennial International Conference on Liquid Atomization and Spray Systems* (Vail, CO, USA, 2009)
73. J. Larocque, S. Vincent, D. Lacanette, P. Lubin, J.-P. Caltagirone, Parametric study of LES subgrid terms in a turbulent phase separation flow. Int. J. Heat Fluid Fl. **31**, 536–544 (2010)
74. J. Chesnel, J. Reveillon, F. Demoulin, T. Menard, Subgrid analysis of liquid jet atomization. Atomization Spray **21**(1), 41–67 (2011)
75. M. Herrmann, M. Gorokhovski, An outline of an LES subgrid model for liquid/gas phase interface dynamics, in *Proceedings of the 2008 CTR Summer Program* (Stanford CA, 2008), pp. 171–181
76. A. Scotti, C. Meneveau, A fractal model for large eddy simulation of turbulent flow. Physica D **127**, 198–232 (1999)
77. D. Kedelty, J. Uglietta, M. Herrmann, A volume of fluid dual scale approach for modeling turbulent liquid/gas phase interfaces, in *Proceedings of the 29th Annual Conference on Liquid Atomization and Spray Systems* (Atlanta, GA, USA, 2017)
78. S. Pope, Simple models of turbulent flows. Phys. Fluids **23**, 011301 (2011)
79. D. Haworth, S. Pope, A generalized Langevin model for turbulent flows. Phys. Fluids **29**(2), 387–405 (1986)
80. E.A. Wenzel, S.C. Garrick, Finite particle methods for computing interfacial curvature in volume of fluid simulations. At. Sprays **28**(2), 141–160 (2018)

Turbulent Suppression in Swirling Sprays

Nasser Ashgriz, Siyu Chen, Viktor Nikulin and Serguei Savtchenko

Abstract Effect of swirl on turbulent surface fluctuations in swirl nozzle atomizers is investigated based on a model of fluid elements moving in Lagrangian frame. The model indicates turbulence can be suppressed by swirl. The model is verified by performing a set of experiments on swirl nozzles, which keeps the internal turbulence level relatively constant and changes only the level of swirl. This is achieved by using nozzles with different swirl inserts to change the tangential inlet velocities and keep the jet velocity at the nozzle exit constant. It is shown that increasing the swirl suppresses surface fluctuations.

Keywords Turbulent suppression · Swirling turbulent flows · Swirling sprays

1 Introduction

Swirl nozzles are commonly used in industry to deliver high liquid flow rates with relatively small droplet sizes at low inlet pressures. They are used in gas turbines and gasoline direct injection engines among a wide range of other applications. A swirl nozzle has one or more inlet ports, a swirl chamber that usually has a converging spin section, and a discharge orifice at the exit. The swirling motion of liquid can be formed by either tangential inlet ports or a swirler [1]. The length of the swirl chamber and the diameter of the discharge hole are the main parameters that control

N. Ashgriz (✉) · S. Chen · S. Savtchenko
Department of Mechanical and Industrial Engineering, University of Toronto, Toronto M5S 3G8, Canada
e-mail: ashgriz@mie.utoronto.ca

S. Chen
e-mail: siyuchen@mie.utoronto.ca

S. Savtchenko
e-mail: serguei@mie.utoronto.ca

V. Nikulin
Lavrentyev Institute of Hydrodynamics SB RAS, Novosibirsk 630090, Russia
e-mail: nikulin@hydro.nsc.ru

D. Livescu et al. (eds.), *Modeling and Simulation of Turbulent Mixing and Reaction*, Heat and Mass Transfer, https://doi.org/10.1007/978-981-15-2643-5_11

the swirl action in swirl nozzles. Comprehensive reviews of the swirl nozzles are provided by Lefebvre [1], Vijay et al. [2], and Kang et al. [3].

In swirl nozzles, the fluid is forced to swirl and generates a conical liquid sheet. As the conical liquid sheet expands, the sheet thickness reduces. Generally, the generated droplet sizes correlate with the liquid sheet thickness. Therefore, swirl nozzles can generate small droplets even with large orifice sizes. As the swirl is increased, the emerging conical sheet may expand more, which will reduce the sheet thickness, and consequently generate smaller droplets. The swirl can be increased by simply increasing the tangential inlet velocity. On the other hand, higher liquid velocities may result in higher turbulence in the flow. Higher turbulence may cause faster breakup of the conical sheet, and therefore, generate larger droplets. However, experiments show that spray droplet sizes reduce with increasing swirl. Therefore, the expected turbulence effect is not observed. The conditions and character of the internal flow has a significant effect on the character of the liquid sheet and its breakup [4, 5]. Prior studies have investigated the cone sheet characteristics at different inlet pressures and show the change in surface fluctuations with pressure [6]. However, since both the turbulent characteristics of the nozzle internal flow as well as the level of the swirl change with changing the pressure, the effect of swirl on turbulence cannot be distinguished in such studies. Here we have performed a set of experiments to distinguish the effect of swirl on the turbulence levels on the liquid sheet emerging from a nozzle.

Turbulent suppression by swirling and vortex flows has been observed in single phase flows [7]. It has also been shown that the development of turbulence in an originally non-swirling inner jet is suppressed by an externally swirling flow [8]. One of the notable features of this effect is that even relatively small swirls can cause significant suppression of turbulence. This was observed in axially rotating tubes [9–11], where it was shown that all components of turbulent fluctuations decrease with increasing rotation rate, and the momentum transfer by turbulent motion is suppressed in the rotating pipe.

Once the liquid exits the nozzle, the flow turbulence causes fluctuations on the cone sheet. The relationship between the turbulence in the flow and the interface fluctuations at a liquid-gas interface has been extensively studied. One notable study is that of Madnia and Bernal [12]. They measured the turbulent levels in the internal flow and related them to fluctuations on the liquid-gas interface. They observed surface deformations at distances starting from one to two times the jet diameter. They also noted that waves propagate at an angle with respect to the flow direction. It is therefore expected that interface fluctuations due to turbulence in the liquid be observable close to the nozzle. The interaction of the liquid sheet with the external air will also cause sheet fluctuations. However, in order to investigate the effect of swirl on turbulence, the fluctuations close to the nozzle need to be considered.

In our previous work [13], we developed a relationship for the turbulent length scale in a swirl flow. We used a Lagrangian model to derive the motion of a fluid element in a swirling flow. This relationship showed that the turbulent length scale is inversely proportional to the angular velocity of the flow. This indicates that the turbulent fluctuations reduce as the swirl increases. In this work, we have applied

this model to turbulent fluctuation at a liquid-gas interface as observed at the surface of a swirling liquid sheet emerging from a swirl nozzle. We have also performed a set of experiments to show the validity of this model as it applies to swirl nozzles.

In §2, we describe the experimental setup, followed by the experimental results in §3 that shows the effect of swirl on the suppression of surface fluctuations in a swirl nozzle. In §4 we describe a model that shows the effect of swirl on the suppression of turbulence. A comparison between the prediction of model and experimental results is shown in §5, followed by conclusions in section §6.

2 Experimental Setup

The pressure swirl nozzle used in this experiment had a straight spray body with a swirl insert. The spray swirl is changed by changing the inserts in the same nozzle body. Two inserts, one with two grooves and the other with six grooves, are used to generate different levels of swirl. The nozzle assembly and the two different used inserts are shown in Fig. 1.

The swirl nozzle assembly includes an inlet, a swirl insert, a swirl chamber and an outlet. As the liquid flows through the grooves on the swirl insert, it swirls inside the nozzle chamber before it exits the nozzle orifice. As this rotating flow exits the axial orifice, a conical swirling sheet is formed. The conical sheet spreads out and finally breaks into small droplets.

The swirling processes result in the formation of an air core at the center surrounded by the conical liquid sheet as shown in Fig. 2. The air core is formed when the centrifugal force of the swirling flow overcomes the viscous force and a low-pressure area near the injector exit is created by the centrifugal motion of liquid within the swirl chamber [1].

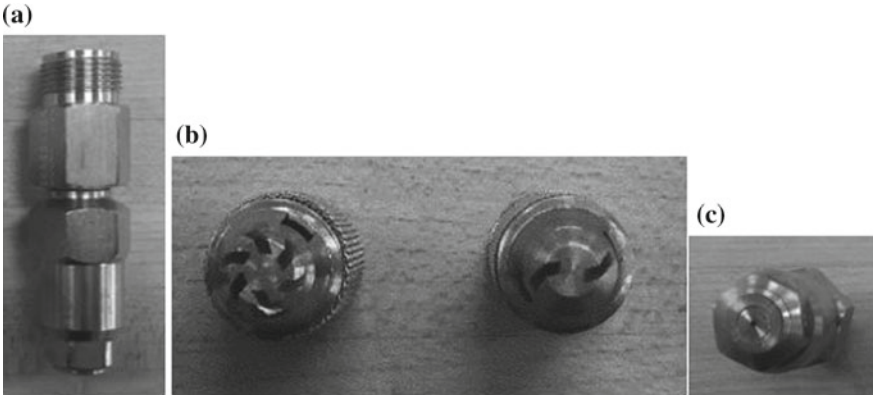

Fig. 1 The swirl nozzles used; the parts are (from left to right): **a** nozzle assembly **b** 6-groove insert and 2-groove insert **c** nozzle top view

Fig. 2 Schematic of the air core formation

The ratio between the area of the air core and the area of the nozzle, X, is related to the spray half angle θ, according to Lefebvre [1]:

$$\cos^2\theta = \frac{1-X}{1+X}, \tag{1}$$

where $X = A_a/A_o$ with A_a being the air core area and A_o the nozzle area.

Since the objective of this study was to determine the effect of swirl on the turbulence characteristics, the Reynolds number, which reflects the turbulence behavior, had to be properly controlled. The Reynolds number for a nozzle is defined as $\mathrm{Re} = UD/\nu$, where U is the outlet velocity, D is the orifice diameter and ν is the kinematic viscosity of the fluid. For the same test fluid and same nozzle body, the Reynolds number can only be changed by changing the outlet velocity U, which can be measured by the mass flow rate and the area of liquid flow at the outlet. The mass flow rate for a pressure-swirl nozzle assembly is determined by the inlet pressure. However, as the swirl increases for different nozzle inserts, the area of the air core increases and the area of the liquid flow at the nozzle exit reduces, increasing the liquid flow velocity for the same mass flow rate. Therefore, in order to keep the exit Reynolds number constant, the liquid flow area needs to be determined, and the mass flow rates for different swirl conditions need to be changed to keep the same velocity for different swirl conditions.

The nozzles used in the present study had a diameter of $D = 1.067\,\mathrm{mm}$. The liquid used was a 30% aqueous glycerol solution with a density of $\rho = 1072\,\mathrm{kg/m^3}$ and a viscosity of $\mu = 0.00219\,\mathrm{Pa \cdot s}$. In this experiment, the volumetric mass flow rate at the exit Q and the half spray angle are measured to tune the Reynolds number for different nozzle assemblies. The jet velocity is given by

Table 1 The operating conditions and Reynolds number for the two nozzle assemblies

Insert type	Orifice diameter (mm)	Pressure (psi)	Spray angle (∘)	Volumetric flow rate (ml/s)	Reynolds number
2 grooves	1.067	90	70	9.39	6829
6 grooves		45	42	10.78	6760

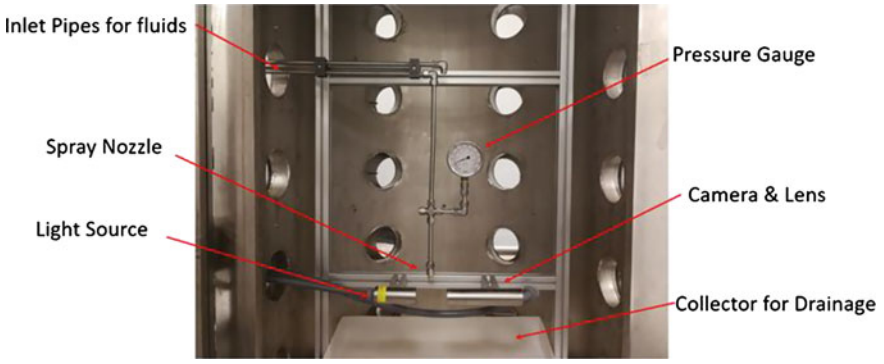

Fig. 3 Experimental setup in the testing chamber

$$U = \frac{\dot{Q}}{\frac{\pi}{2}\frac{\cos^2\theta}{1+\cos^2\theta}D^2}. \tag{2}$$

The determined operating conditions and the Reynolds numbers for the two nozzle assemblies are shown in Table 1.

The swirl nozzles are tested in a chamber equipped with a high-speed imaging system (Mazlite Spray Sizer [mazlite.com]) as shown in Fig. 3. The imaging system can generate flash lights with flash duration at as low as 50 nanoseconds. Images with a resolution of 1μm per pixel are taken at 20 frames per second. This system is used to take close-up images of the spray cone. The spray images are then analyzed using an image analyzing system to determine the contours and surface fluctuations.

3 Experimental Results and Discussions

3.1 Atomization Mechanism of a Pressure-Swirl Nozzle

In a pressure-swirl nozzle, a tangential velocity is induced on the fluid by the grooves on the swirl insert. As the fluid rotates in the chamber, the walls of the chamber support the rapidly swirling flow by providing a centrifugal force. The flow eventually forms a cylindrical liquid sheet and is ejected from the nozzle.

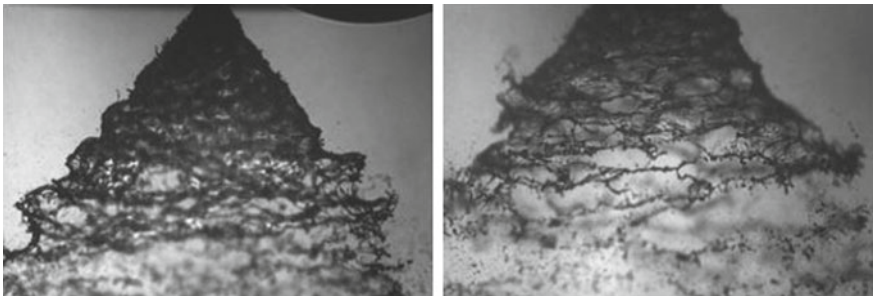

Fig. 4 Surface disturbance caused by the turbulence at the nozzle exit (left) and breakup of the sheet caused by the formation of perforation on the cone downstream (right)

After the liquid leaves the nozzle, there are two effects that influence sheet characteristics. One effect is the absence of centrifugal force due to the absence of the chamber walls. The radius of the orbit where the fluid swirls increase as the fluid moves downstream, which will reduce the sheet thickness. The other effect is the turbulence. At high pressures, the flow velocity rapidly increases. This will result in a very high Reynolds number, which indicates a highly turbulent flow. The turbulence will cause violent surface disturbances. At the position where the cone is thin enough, perforation will occur on the cone. The sheet of cone breaks up into the ligaments and then ligaments breaks up into fine droplets whose diameters are at the order of the sheet thickness. As shown in Fig. 4, the image on the left taken right at the nozzle exit indicates the violent surface disturbances caused by turbulence and the image on the right taken at 1.07 mm downstream shows the breakup of the sheet due to the formation of perforation.

3.2 Effect of Swirl on Turbulence

Fig. 5 shows images of two different swirling liquid sheets from two different nozzles. Since the cross-sectional area of the insert with 6 grooves is roughly 3 times of that of the insert with 2 grooves, the tangential velocity of the flow generated by the 2-groove insert is faster, which results in more swirl and larger spray angle. The degree of turbulence is reflected by the displacement of a fluid element from its equilibrium position, which can be shown by the waviness of the edge of the spray cone on the image. A less wavy edge indicates that the fluid elements hardly move away from the equilibrium orbit, which implies a more laminar behavior of the flow. The images are processed to extract the edges of the spray cone. Typical results are shown in Table 2. The edge of the spray cone generated by 2-groove insert is much smoother (smaller disturbance and less waviness) compared to the one generated by the 6-groove insert, which clearly indicates that the turbulence is suppressed with a larger swirl.

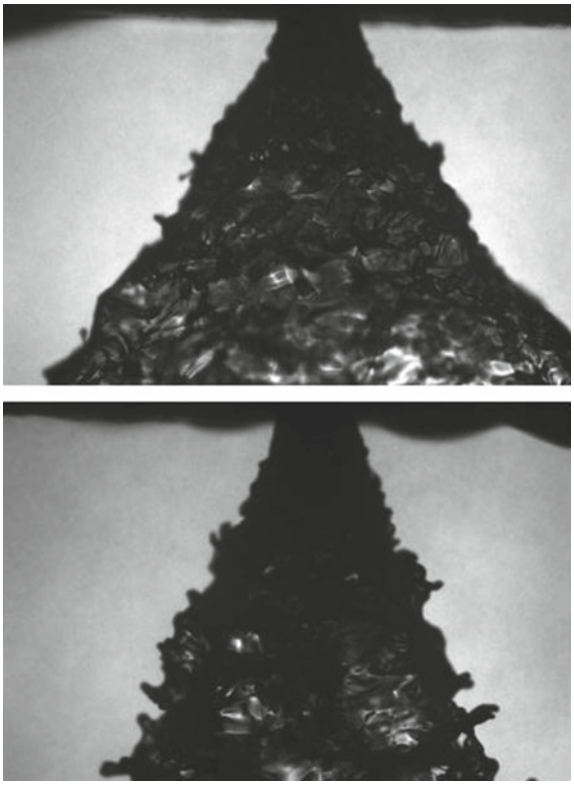

Fig. 5 The images taken at the nozzle exit for the nozzle assembly with 2-groove insert (top) and 6-groove insert (bottom)

Table 2 The amplitudes of fluctuation on the edge of the cone for the flows generated by the two inserts. The profile for nozzle with 2-groove insert shows less turbulence due to more swirl

Insert type	Edge profile
2 grooves	
6 grooves	

Table 3 Images of nozzle assemblies at different pressures

Inlet pressure (psi)	2-groove nozzle insert	6-groove nozzle insert
40		
60		
80		
100		

Another set of experiment was carried out with water to investigate the effect of inlet pressure on the turbulence characteristics. Four different inlet pressures (40 psi, 60 psi, 80 psi and 100 psi) are applied to each of the two nozzle assemblies. The near-nozzle images are taken and shown in Table 3. The extracted edges are shown in Table 4 for the nozzle assembly with 2 grooves and 6 grooves, respectively. For the same nozzle assembly, the level of turbulence increases as the pressure increases as shown by the increasing number of waves on the edge close to the nozzle exit. At the same pressure, the nozzle with 6-groove insert is exhibiting more wave with larger amplitude on the edge, indicating a higher turbulence level.

4 Theoretical Analysis

The flow generated from a pressure-swirl nozzle can be analyzed in a cylindrical coordinate. As shown in Fig. 6, the movement of a fluid element ejected from a pressure swirl nozzle is equivalent to a superposition of two independent motions: a linear motion in z-direction and a circular motion in r-θ plane.

Table 4 The amplitudes of fluctuation for the flows generated by different inserts at different inlet pressures

Inlet pressure (psi)	2-groove nozzle insert	6-groove nozzle insert
40		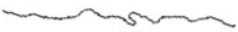
60		
80		
100	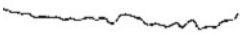	

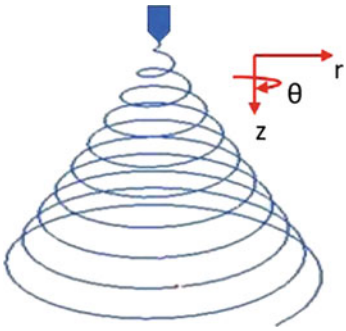

Fig. 6 The movement of a fluid element from a pressure-swirl nozzle can be decomposed into two independent motions: linear motion in z-direction, and circular motion in r-θ plane

For an inviscid fluid, assuming that the velocity fluctuation is very small comparing to the mean flow and mean flow is steady and axisymmetric, the Navier-Stokes equation in radial direction can be written as

$$\frac{1}{\rho}\frac{dP}{dr} = \frac{U_\theta^2(r)}{r}, \tag{3}$$

where ρ is the density of the fluid, P is the mean pressure and $U_\theta(r)$ is the mean velocity in θ-direction at a specific radial position r. For a fluid element which has a mass m and is small compared to the length scale, according to Newton's second law

$$m\vec{a} = f_r\vec{e}_r + f_\theta\vec{e}_\theta, \tag{4}$$

where $\vec{a}$ is the acceleration vector, $\vec{e}_r$ is the unit vector in r-direction and $\vec{e}_\theta$ is the unit vector in θ-direction. The acceleration in r-direction in polar coordinate is

$$\vec{a} = \left(\frac{d^2r}{dt^2} - r\omega^2\right)\vec{e}_r + \left(2\omega\frac{dr}{dt} - r\frac{d\omega}{dt}\right)\vec{e}_\theta, \tag{5}$$

where ω is the instantaneous angular velocity and r is the radial position of the fluid element. The centrifugal force in r-direction for a fluid element with volume V is

$$F = -mr\omega^2 = -V\frac{dP}{dr}. \tag{6}$$

As a result,

$$f_r = F = -V\frac{dP}{dr} = m\left(\frac{d^2r}{dt^2} - r\omega^2\right), \tag{7}$$

and

$$\frac{d^2r}{dt^2} = -\frac{1}{\rho}\frac{dP}{dr} + r\omega^2, \tag{8}$$

Since there is no external tangential force applied to the fluid element,

$$f_\theta = 0 = m\left(2\omega\frac{dr}{dt} - r\frac{d\omega}{dt}\right) = m\frac{d\left(\omega r^2\right)}{dt}. \tag{9}$$

As a result,

$$\omega r^2 = u_\theta r = Constant, \tag{10}$$

where u_θ is the instantaneous velocity of the fluid element in θ-direction. If a fluid element is disturbed only in radial direction from its equilibrium position $r = r_1$ (Fig. 7), at the equilibrium position r_1,

$$U_\theta\left(r_1\right) r_1 = u_\theta r. \tag{11}$$

As a result,

$$\frac{d^2r}{dt^2} = -\frac{1}{\rho}\frac{dP}{dr} + \frac{U_\theta^2\left(r_1\right) r_1^2}{r^3} = -\frac{U_\theta^2(r)r^2 - U_\theta^2\left(r_1\right) r_1^2}{r^3}. \tag{12}$$

Apply Taylor expansion at the equilibrium position,

$$\frac{d^2r}{dt^2} \approx -\frac{1}{r_1^3}\frac{d\Gamma^2\left(r_1\right)}{dr}\left(r - r_1\right). \tag{13}$$

where $\Gamma(r) = U_\theta(r)r$. The equation indicates that movement of the fluid element around the equilibrium orbit is analogous to Hook's Law as shown in Fig. 6, with

$$\mathrm{k} \approx -\frac{1}{r_1^3}\frac{d\Gamma^2\left(r_1\right)}{dr}. \tag{14}$$

Since

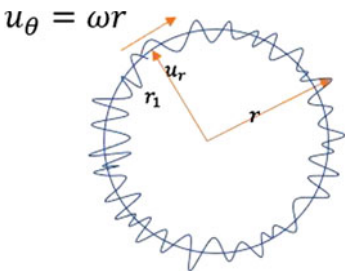

Fig. 7 The circular motion of a fluid element in r-θ plane at an arbitrary z-position. The movement of the fluid element is a superposition of a circular motion around z-axis due to the angular velocity and a circular motion around the equilibrium orbit due to the turbulence. u_r: instantaneous radial velocity, u_θ: instantaneous tangential velocity

$$\frac{d^2r}{dt^2} = \frac{d\frac{v_r^2}{2}}{dr}, \tag{15}$$

where $v_r = \frac{dr}{dt}$. For a solid body rotation, $U_\theta(r) = \Omega r$, where Ω is the mean value of angular velocity. If integrating from r to r_1,

$$\frac{v_r^2}{2} - \frac{v_{r1}^2}{2} = -\frac{1}{2}\Omega^2\left(r^2 - r_1^2\right) - \frac{1}{2}\Omega^2 r_1^4\left(r^{-2} - r_1^{-2}\right). \tag{16}$$

At the maximum displacement position, $v_r = 0$ and if the disturbance is $r = r_1 + \lambda$,

$$v_{r1}^2 = \Omega^2\left((r_1+\lambda)^2 - 2r_1^2 + r_1^4(r_1+\lambda)^{-2}\right), \tag{17}$$

and

$$\lambda = r_1\left(\sqrt{1 + \frac{v_{r1}^2}{2\Omega^2 r_1^2} \pm \sqrt{\left(1 + \frac{v_{r1}^2}{2\Omega^2 r_1^2}\right)^2 - 1}} - 1\right). \tag{18}$$

Since the velocity fluctuation in r-direction is small compared to the mean flow,

$$v_{r1} \ll U_\theta(r_1). \tag{19}$$

As a result,

$$\lambda \approx \frac{v_{r1}}{2\Omega}. \tag{20}$$

The equation indicates that the magnitude of the spatial fluctuation of fluid element in r-direction is decreasing as the rotational speed of the swirl increasing, which shows that the turbulence is suppressed due to the swirl.

5 Comparison of Model with Experiments

The magnitude of the disturbance λ can be measured from the image directly with the given resolution. The angular velocity at a specific position downstream can be estimated by the angular momentum conservation, since there is no support of the wall and thus no tangential force applied. The angular velocity is given by

$$\Omega(z) = \frac{v_\theta}{r(z)} = \frac{\dot{Q}\cos\varphi}{n\,\mathrm{Ar}(z)}, \tag{21}$$

where v_θ is the tangential velocity at the exit of nozzle insert, φ is the angle of the groove, n is the number of groove and A is the cross-sectional area of each groove.

The velocity of fluctuation in r-direction, v_{r1}, can be estimated using the empirical correlation for pipe flows

$$v_{r1} = 0.16 Re_{Dh}^{-0.125} v_{avg}, \tag{22}$$

where Re_{Dh} is the Reynolds number with the hydraulic diameter and v_{avg} is the average velocity in radial direction. In this work, the hydraulic diameter is estimated as the diameter of nozzle exit D and v_{avg} is estimated using the velocity U and half spray angle θ. As a result,

$$v_{r1}(z) = 0.16\left(\frac{\rho U \mathrm{D}}{\mu}\right)^{-0.125} U\sin(\theta), \tag{23}$$

Then the magnitude of disturbance can be calculated and the values are compared in Table 5.

As shown in Table 5, both the measured and calculated values indicate a decrease in λ as the swirl increases. The magnitudes of the measured and calculated value of the disturbance are matched well. It is worth noticing that both calculated values are smaller than the measured values. Such differences may be caused by the correlation used to estimate v_{r1}, which may not be the proper one for this case.

Table 5 Comparison of the calculated disturbance with the measured result at 0.12 mm (100 pixels) from the nozzle exit

Insert type	λ (measured) (μm)	Ω (s^{-1})	v_{r1} (m/s)	λ (calculated) (μm)
2 grooves	9.76	20584.5	0.398	9.66
6 grooves	17.7	8219.7	0.249	15.12

6 Conclusions

This work presents a model for the relationship between the turbulence and the degree of swirl in a pressure-swirl nozzle. The model indicates that the surface disturbances decrease as the mean angular velocity increases, indicating a suppression of the turbulence due to swirl. The experimental results generated with two different nozzle inserts are in accordance with the theory prediction qualitatively. Moreover, the predictions of the model on surface disturbance match the measured results from close-up images at the nozzle exit. The relationship between the swirl and turbulence is important in the design of the nozzle to generate better atomization quality.

References

1. A.H. Lefebvre, *Atomization and Sprays* (Hemisphere Publishing Corporation, 1989)
2. G.A. Vijay, N.S.V. Moorthi, A. Manivannan, Internal and external flow characteristics of swirl atomizers: A review. Atomization Sprays **25**(2), 153–188 (2015)
3. Z. Kang, Z. Wang, Q. Li, P. Cheng, Review on pressure swirl injector in liquid rocket engine. Acta Astronaut. **145**, 174–198 (2018)
4. G. Amini, Liquid flow in a simplex swirl nozzle. Int. J. Multiphas. Flow **79**, 225–235 (2016)
5. J. Jedelsky, M. Maly, N. Pinto del Corral, G. Wigley, L. Janackova, M. Jicha, Air-liquid interactions in a pressure-swirl spray. Int. J. Heat Mass Tran. **121**, 788–804 (2018)
6. J.-W. Ding, G.-X. Li, Y.-S. Yu, The instability and droplet size distribution of liquid-liquid coaxial swirling spray: An experimental investigation. Exp. Therm. Fluid Sci. **82**, 166–173 (2017)
7. S. Eskinazi, H. Yeh, An investigation on fully developed turbulent flows in a curved channel. J. Aeronaut. Sci. **75**, 23–34 (1956)
8. S. Savtchenko, N. Ashgriz, C. Jolliffe, L. Cousins, H. Gamble, Effect of a swirling desolvation gas flow on atmospheric pressure ion sources. J. Am. Soc. Mass Spectr. **25**(9), 1549–1556 (2014)
9. S. Imao, M. Itoh, T. Harada, Turbulent characteristics of the flow in an axially rotating pipe. Int. J. Heat Fluid Fl. **17**(5), 444–451 (1996)
10. S. Imao, M. Itoh, Y. Yamada, Q. Zhang, The characteristics of spiral waves in an axially rotating pipe. Exp. Fluids **12**(4–5), 277–285 (1992)
11. S. Imao, Q. Zhang, Y. Yamada, The laminar flow in the developing region of a rotating pipe. JSME Int. J. **32**, 317–323 (1989)
12. C.K. Madnia, L.P. Bernal, Interaction of a turbulent round jet with the free surface. J. Fluid Mech. **261**, 305–332 (1994)
13. V. Nikulin, S. Savtchenko, N. Ashgriz, A model for the turbulent suppression in swirling flows. Phys. Lett. A **381**, 3989–3995 (2017)